Connection between hot tearing and cold cracking in DC-casting of AA7050: Experiments and computer simulations

Tungky Ariwibowo SOSRO SUBROTO

The research described in this thesis was carried out in the Department of Materials Science and Engineering of Delft University of Technology in the Netherlands.

This research was carried out under project number M42.5.09340 in the framework of the Research Program of the Materials innovation institute (M2i) in the Netherlands (www.m2i.nl).

Connection between hot tearing and cold cracking in DC-casting of AA7050: Experiments and computer simulations

Proefschrift

ter verkrijging van de graad van doctor
aan de Technische Universiteit Delft,
op gezag van de Rector Magnificus prof. ir. K.C.A.M. Luyben,
voorzitter van het College voor Promoties,
in het openbaar te verdedigen op dinsdag 25 november 2014 om 12.30 uur

door

Tungky Ariwibowo SOSRO SUBROTO

Master of Science in Applied Physics
geboren te Bandung, Indonesië

Dit proefschrift is goedgekeurd door de promotoren:
Prof. ir. L. Katgerman
Prof. dr. D. G. Eskin

Samenstelling promotiecommissie:

Rector Magnificus,	voorzitter
Prof. ir. L. Katgerman,	Technische Universiteit Delft, promotor
Prof. dr. D. G. Eskin,	Brunel University, U.K., promotor
Dr. A. Miroux,	Materials innovation institute (M2i), currently at: Aleris Aluminium Duffel, Belgium
Prof. dr. P. D. Lee,	The University of Manchester, U.K.
Prof. dr. J. Th. M. de Hosson,	Rijksuniversiteit Groningen
Dr.-Ing. R. Sauermann,	Aleris Rolled Products, Germany
Prof. dr. ir. J. Sietsma,	Technische Universiteit Delft
Prof. dr. I. M. Richardson,	Technische Universiteit Delft, reservelid

Keywords: Aluminum, AA7050, Solidification, Hot tearing, Cold cracking, Direct-chill casting simulation, Tensile constitutive parameters, Semi-solid testing

Front and back: Designed by S. Heru Prabowo

ISBN: 978-94-91909-19-1

Printed in the Netherlands

To my beloved family

Table of Contents

Chapter 1
INTRODUCTION

1.1 High strength aluminum alloys

Aluminum is a versatile material that has applications in many aspects of our daily life. We can find its application in our surrounding starting from food packaging, structural and civil-engineering application up to transportation and aerospace-related applications [1]. This is not only because aluminum is abundant in earth but also because it has useful material properties such as good strength to weight ratio, high corrosion resistance properties and excellent formability [2] which are very important in many applications, e.g. in transportation and construction. High-strength and lightweight are two of the key properties of material in aerospace-related industries. One family of aluminum alloys, namely 7XXX series is known to have very high tensile strength and good fracture toughness, thus it is a primary choice in such an industry [3, 4].

Despite its advantages, 7XXX series aluminum alloys are known as a 'hard to cast' alloys due to their propensity to defect formation during primary production process (i.e. casting). However, since there is increasing demand for such an application due to the rise in the global air transportation need [5, 6], it is important to optimize the alloy production process to have a good quality level of produced ingot while simultaneously maintaining a reasonable production fee [7].

1.1.1 Production process through direct-chill casting

Direct-chill (DC) casting is a semi-continuous casting process, invented in the 1930s [8, 9] and it is usually employed as the production process of aluminum wrought alloys. The main advantages of this method are its robustness and relative simplicity [10, 11]. Additionally, the solidification in DC casting could be well controlled [12].

Figure 1.1a shows a typical DC casting setup and Figure 1.1b shows example of round ingots (billets) produced by DC casting. The steps to produce an ingot through DC casting are as following: first, raw materials are melted in the furnace and then the melt is transported to the mold via launder and, finally, the melt is poured to a water-cooled mold (primary cooling). As the mold is filled and the shell of the ingot is solidified, the starting block that is connected with the withdrawal ram is moved downwards with a speed of v_z defined as the casting speed. Immediately as the ingot exits the mould, it is sprayed by water (secondary cooling), hence the name 'Direct-Chill' casting. This process is continued until the length of the billet reaches several meters and then the supply of liquid aluminum to the mold is stopped and the billet subsequently removed from the casting pit for further downstream processing route.

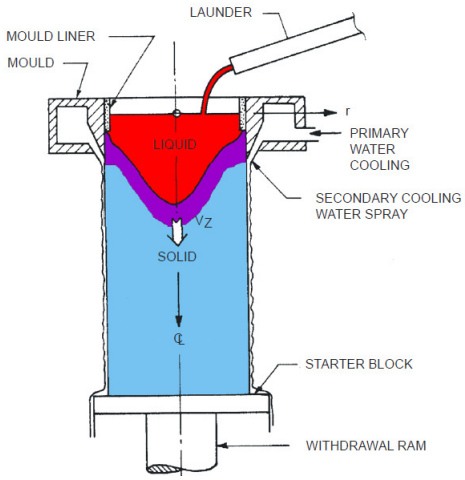

(a)

(b)

Figure 1.1 An example of a typical DC casting setup [13] (a) and example of DC cast billets [14] (b).

1.1.2 Thermo-physical properties of AA7050

AA7050 is a high-strength and heat-treatable commercial alloy and its properties are well known [15-18]. This alloy has three main alloying elements; zinc, copper and magnesium and several other minor alloying elements. The average chemical composition of the alloy is described in Table 1.1

Table 1.1 Average chemical composition of AA7050.

Elements, wt. pct.								
Zn	Cu	Mg	Zr	Fe	Mn	Si	Ti	Cr
6.15	2.2	2.1	0.13	0.07	0.04	0.04	0.03	< 0.01

Solidification and thermo-physical properties of the alloy are important for the consideration of casting variables selection to ensure the quality of the cast product. The summary of thermo-physical properties such as solidus ($T_{solidus}$) and liquidus temperature ($T_{liquidus}$), contraction onset temperature – defining the rigidity point of the alloy (T_{contr_onset}), thermal conductivity at 25 °C and average coefficient of thermal expansion (CTE) between 20°C and 100 °C of the alloy is given in the Table 1.2. Solidification properties such as solidus and liquids temperature and solidification path are calculated via JMat-Pro® software [19] (the calculation was provided by Tata Steel B.V. (IJmuiden, The Netherlands)). The solidification path from such a calculation is shown in Figure 1.2. Such a figure shows that the eutectic solidification starts from approximately 475 °C or approximately at solid fraction (f_s) = 0.94.

Table 1.2 Summary of thermo-physical properties of the alloy [18, 20].

$T_{liquidus}$	$T_{solidus}$	T_{contr_onset}	$CTE_{20°C-100°C}$	$\kappa_{25°C}$
635 °C	465°C	559 ± 5 °C	24.1 (10^{-6} /K)	157 (W/m·K)

From mechanical point of view, although between room temperature up to 400°C the mechanical properties have been well studied [17, 21] there are not much high temperature and semi-solid mechanical properties of this alloy readily available in the literature. Such properties are critical to produce sound cast products.

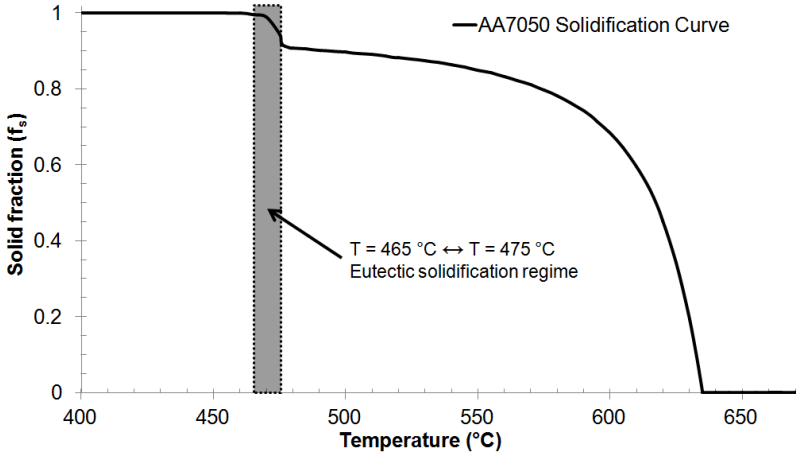

Figure 1.2 Solidification curve of AA7050 via JMat-Pro® calculation.

1.2 Defects during DC casting process

The DC casting process creates relatively high thermal gradient between the chill zone (water sprayed zone) and the center of the billet which is still in the semi-solid or even fully liquid state. This cooling condition relates to severe thermo-mechanical conditions inside the billet thus could produce defects in the cast product such as unwanted deformations in the ingot as shown in Figure 1.3 – pull-in, butt-swell and butt-curl. This excessive deformation eventually might leads to worse defects such as cracking. There are two types of crack that might occur during casting; hot tearing and cold cracking and they will be described in more detail in the subsequent part.

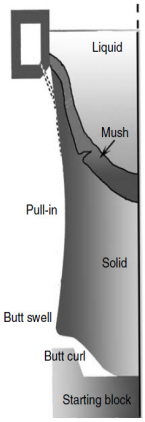

Figure 1.3 Unwanted deformations in cast product due to severe thermo-mechanical conditions during DC casting [8].

1.2.1 Hot tearing

Hot tearing (HT) or hot cracking is defined as cracking that occurs during casting when the material is still in its semi-solid state (above the solidus line). This type of crack is considered as one of the most critical defects in casting practice [22]. This is because excessive HT with a sub-critical dimension or micro HT (Figure 1.4a) might reduce the quality of the ingot while macroscopic HT that propagate in the axial direction and covers a substantial length of the cast (Figure 1.4b) makes the ingot useless for the subsequent process, requiring it to be scrapped. The term 'tearing' comes from the cracking in partially solid material, which resembles tearing in a weak material [23].

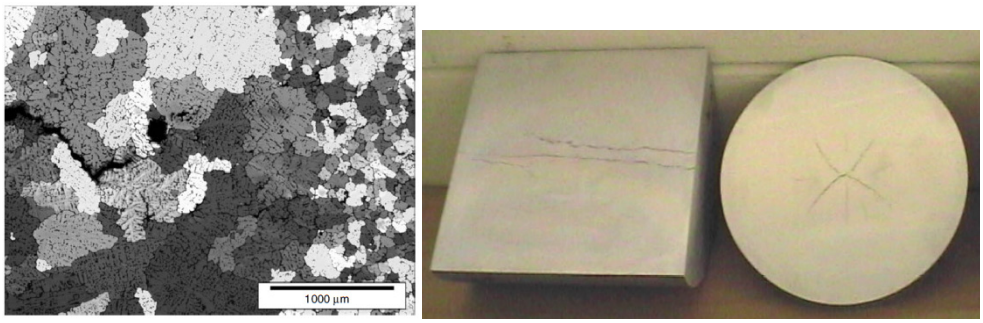

(a) **(b)**

Figure 1.4 Different levels of HT damage; Undeveloped HT or micro-HT which was arrested during propagation [8] (a) and macroscopic HT that propagates throughout the axial length of the billet [24] (b).

HT is easily recognizable since this defect has strong characteristics such as interdendritic propagation (Figure 1.5a) – usually through the liquid film that stays on grain boundaries during the last stage of solidification. Therefore, the fracture surface has a dendritic morphology. It is good to remember that HT susceptibility is dependent on process conditions, casting geometry and indeed on alloy composition. For example, Al-4% Cu does not have HT problem while Al-1% Cu is strongly susceptible to HT [24].

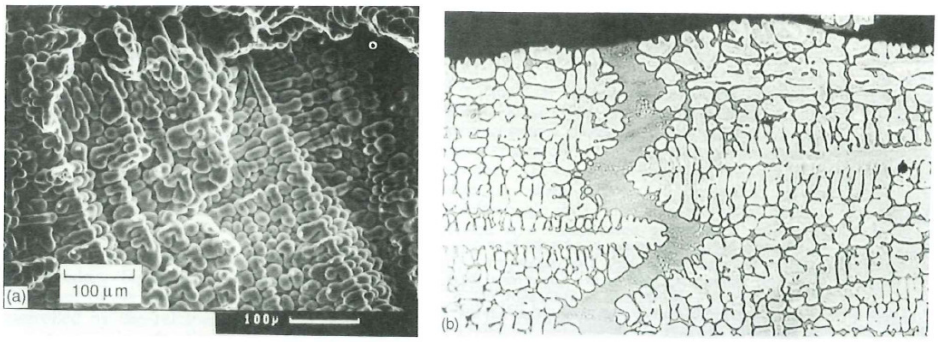

Figure 1.5 Interdendritic HT fracture surface observed in a scanning electron microscope (SEM) (a) and an example of healed HT by eutectics (b) [23].

HT usually occurs in a specific solid-fraction range during solidification; toward the end of solidification process. It commonly occurs below the rigidity temperature where the amount of solid fraction is relatively high and a continuous solid network has been established. This is because, above the rigidity temperature, the fraction of the liquid phase is still substantial thus liquid metal feeding is still active [8], and grains are more loosely connected so that they can accommodate thermal strain [25]. Therefore, if excessive tensile stresses or even HT forms in this regime, it may be healed by the liquid phase filling the initiated HT (Figure 1.5b). Moreover, due to the adequate amount of liquid phase, the grains might still be able to translate and/or rotate to compensate the deformation [25].

As mentioned earlier, HT occurs below the rigidity temperature which is defined as the temperature when the grains start to connect with each other and form a solid network, and the material starts to have mechanical strength. In this temperature regime, the volume between the already solidified grains forms a complex feeding path that leads to feeding difficulties. At the same time, there is solidification shrinkage due to the volume difference between solid and liquid phase of the alloy and, simultaneously, thermal contraction of the rigid solid skeleton. This thermal contraction occurs inhomogeneously due to the temperature gradient between the shell (directly in contact with cooling surface) and the center of the ingot which is still in semi-solid state. Because the shell of the ingot solidified earlier than the center of the billet, the semi-solid part contracts in the direction of the shell

region, thus producing tensile stress (thermal stress) in the center part of the billet which is still on semi-solid state. If this thermal tensile stress is larger than the strength of the alloy in the semi-solid state, then HT can form. In the semi-solid state, the fracture stress is quite low, because the liquid films has a very low stress threshold to hold the grains together [26]. Additionally, during the last stage of solidification when there is still some liquid in the grain boundaries, other mechanisms such as liquid metal embrittlement [27] might enhance the HT development. The conditions and mechanisms of HT have already been extensively discussed in the works of Eskin *et al.* [26, 27].

1.2.2 Cold cracking

Cold cracking (CC) is by definition cracking that occurs below the solidus temperature or when the material has fully solidified. This type of cracking usually occurs deep below the solidus temperature when the material is brittle [21] and often leads to a catastrophic failure making the ingot completely unusable [17]. Other than economic reasons, safety is another reason to study CC. The energy release during CC could be instantaneous and there is a possibility of spontaneous fragment ejection. This process could pose safety hazards to casting personnel or damage to equipment within the vicinity of the casting setup [28-31]. This type of cracking usually occurs in high strength aluminum alloys such as 2XXX series or 7XXX series alloy due to their brittleness below 300 °C [17, 28, 31].

Depending on the geometry of the ingot and location of cracking, various propagation paths may be observed. Figure 1.6 shows typical crack shapes in rectangular ingots [32]. Examples of typical CC in real ingots are shown in Figure 1.7. When the residual stresses built up and the ingot cooled down without any stress-relieving mechanisms, a relatively small amount of perturbation, for instance during the sawing process, may lead to catastrophic cracking [30, 31, 33]. The characteristics of the fracture surface of CC may be both intergranular and transgranular. Lalpoor *et al.* [34] reported that the crack propagation for the 7XXX series aluminum alloys are mainly intergranular, although fast cracks propagating through intermetallics also leave some transgranular features such as when they pass through interdendritic bridges. These findings are also supported by the result of Paramatmuni *et al.* [35] from the result of quench crack testing of AA2024, where this test is used to simulate CC condition through rapid cooling.

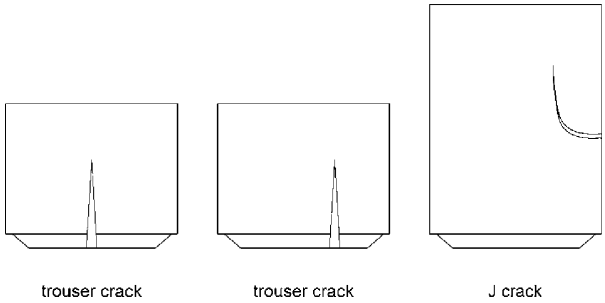

Figure 1.6 Common CC propagation paths in rectangular ingots; Trouser shaped and J-crack [32].

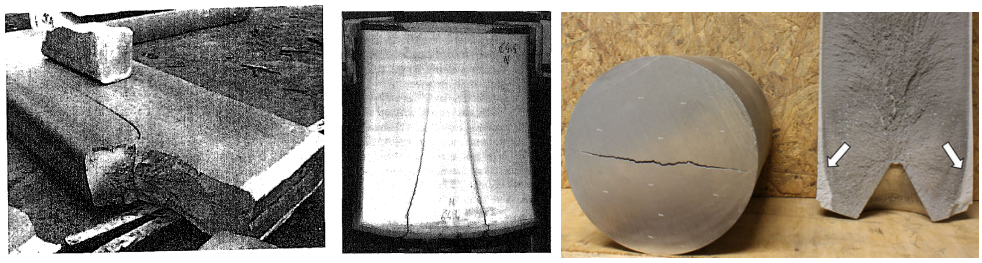

Figure 1.7 Examples of CC in 7XXX series alloys: J-crack (left) [31], trouser crack (center) [36] in rectangular ingots and trouser crack on a round billet (right) [37].

From previous studies, it is concluded that the main reason for CC is residual stresses [17, 21, 31, 32, 34-36, 38, 39]. The stresses are thermal stresses (explained in Section 1.2.1) that are mainly produced due to the uneven cooling throughout the ingot during the course of solidification and further cooling. Due to the nature of DC casting (cooling rate on surface is higher than in the center of the billet), different parts of the ingot receive different cooling conditions which results in different microstructural features. Moreover, the different phases between the solid (outer part of the ingot) and semi-solid (at the center of the billet) might also give a different thermal conductivity [40] which also worsens the uneven cooling condition. Although uncommon, inclusions [32, 41] may also acts as stress raisers that could promote CC.

1.2.3 Possible connection between the two cracks

Up to now, HT and CC are considered to be two different problems, thus they are treated separately. However, the research question that is yet to be answered is whether these two types of cracks are connected. If such a connection is possible, then there should be

different rules and constraints implemented during casting to minimize both cracking occurrence.

Previous research toward this problem showed there is a possible connection between defects that are formed during solidification (e.g. (micro) HT, pore and inclusion) and catastrophic CC [42, 43]. This research also found that in order for a catastrophic CC to occurs, it needs an initiation point. For example, it was proved that an inclusion that has a dimension exceeding a critical crack size could start a catastrophic CC. Figure 1.8 shows a cold-cracked billet and an Mg-oxide inclusion located at the initiation point of the CC. It was suggested that the CC was initiated by the defect that was created and survived throughout the solidification process. The significant change in the stress states of the billet as the material solidifies [38] makes the formed defect that initially has a dimension below the critical crack size (at higher temperature or semi-solid state) exceeding the critical crack size as the ingot temperature decreases.

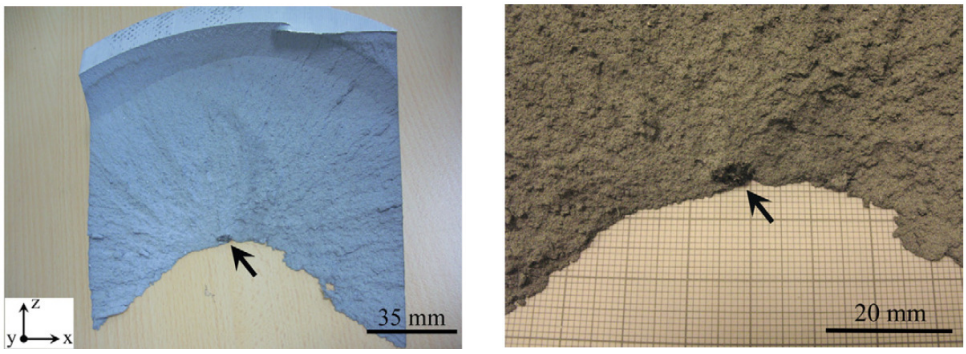

Figure 1.8 Picture of a catastrophically cold-cracked billet (left) with an Mg-oxide inclusion (dark spot pointed by arrow) as the initiation point for CC. The high-magnification picture of the initiation point of the same picture (right) [42].

From the summary of thermal and mechanical properties of AA7050 that is shown in Table 1.2, we can suggest that such an alloy is prone to HT as this alloy has a wide solidification range ($T_{liquidus} - T_{solidus}$ = 170 °C) compared to other wrought aluminum alloys that are considered not significantly susceptible to HT [20]. Moreover, the onset of thermal contraction in this alloy is at a relatively low solid fraction (around solid fraction of 0.8) compared to other alloys [18, 44, 45]. This condition widens the vulnerable solidification regime where alloy is prone to HT.

From the facts presented above, intuitively we can suggest that micro-HT could be formed during the casting process but it may stay dormant until the ingot cooled down. This micro-HT could serve as the initiation point for the CC due to the change in stress states. Since previous research has shown that AA7050 is prone to CC, then AA7050 is a perfect system to study the connection between HT and CC. Although it has been suggested that the

presence of HT might increase the susceptibility of CC occurrence [34], at the moment we do not have an experimental proof or detailed explanation of the mechanisms of such a connection. Thus, an experimental validation and detailed study of the mechanisms of such a connection needs to be carried out.

1.3 Means of predicting cracking during DC casting

The defects that are present in the produced cast range from those affecting the quality [46-48] up to those that cause catastrophic failure with scrapping of the cast product. This can affect the productivity of the cast house and eventually influence the profit level of the aluminum producer company [7].

In response to that situation, aluminum producers were looking at the ways to reduce the occurrence of cracking during DC casting. In the earlier days, the engineers in the cast houses were using trial and error methods to find a window of casting variables (for example the combination of casting speed and cooling rate during casting) to produce sound cast products. This window is indeed different for different alloy compositions; therefore, this approach is not very efficient as the demands for the alloy development for different applications are increasing rapidly.

1.3.1 Numerical modeling to support DC casting process

As the computational power of the desktop computers increases, the development of numerical model to simulate DC casting becomes popular. This is due to its efficiency in terms of time and resources for understanding and optimizing the casting process to produce a sound cast product [49, 50].

Multi-physics simulation packages such as ABAQUS, ANSYS and MSC Marc [51-55] are often used to simulate DC casting process. In this work, we use ALSIM to model the DC casting simulation. ALSIM is a semi-commercial multi-physics finite-element based model developed by the Norwegian Institute of Energy Technology (IFE) in collaboration with industrial and research partners [56, 57]. This model is continuously developed within an industrial consortium and it is specifically aimed at aluminum casting processes. Therefore, this model could capture unique and important phenomena during DC casting process, for instance utilizing coupled approach between thermal, fluid flow and mechanical phenomena, air-gap calculation, start-up stage of the process and cracking susceptibility [42, 56, 58-63]. To predict the result of DC casting of a certain alloy, ALSIM needs the physical properties reflecting such as thermal, mechanical, rheological as well as solidification behavior of such an alloy. We will discuss more details about modeling of DC casting using ALSIM in the next chapter of this thesis.

Result of DC casting simulation consists of physical field values for example: temperature, fluid-flow velocity and stress distribution. This information is adequate to predict general casting defects such as ingot deformation (pull in, butt curl and butt swell). However, to predict cracking susceptibility one have to go one step further in understanding the entire solidification process and interpreting the result of the produced physical fields according to a certain rule. Therefore, one usually uses a criterion to estimate cracking susceptibility of the ingot during DC casting. Different criteria are used to treat different types of cracks (HT and CC). The next section will show examples of existing criteria for each types of crack.

1.3.2 Criteria to predict cracking during casting

1.3.2.1 Hot tearing criteria

There are already a number of HT criteria developed so far and these criteria are built based upon different phenomena during solidification [26, 27]. The purpose of this section is to briefly review some examples of HT criteria to show different phenomena during solidification that could be used to build a HT criterion. In general, HT criteria are divided into two large groups: non-mechanical based criteria and mechanical based criteria.

The non-mechanical based criteria usually focus on feeding difficulties of the liquid metal as the main condition for HT to form. Feurer [64] stated that HT forms if the feeding mechanism or the melt flow at the last stage of solidification cannot compensate the shrinkage rate of the solidifying metal. Then, Clyne and Davies [65] expanded such a theory by developing a variable to quantify the HT susceptibility which is called hot-cracking susceptibility (HCS). They consider HCS to be based on the ratio between the time intervals that are available for HT development and for the stress-relief process – mass feeding of liquid metal. The higher value of HCS means higher susceptibility of the alloy to HT. Katgerman [66] integrated theoretical considerations from both ideas by introducing the critical time which is defined as the time when the feeding is just sufficient to compensate solidification shrinkage. Using this modified criterion, it is reported that the HT susceptibility is in better comparison with experimental data.

The mechanical-based criteria use stress, strain or strain-rate fields to define the susceptibility of HT during casting. Dickhaus [67] proposed a HT criterion which is based on the stress in the semi-solid region of the material. In this model, they assumed if the exerted tensile stress is higher than the strength of a liquid film that separates two grains when the material is in its semi-solid phase, then HT will occur.

Examples of HT criteria that are built upon strain-rate field are the ones developed by Rappaz [68] and Prokhorov [8]. The HT criterion made by Rappaz, Drezet and Gremaud or popularly known as the RDG criterion [68], is based on the critical pressure drop due to

both solidification shrinkage and deformation-induced pressure drop during solidification. However, the measure of HT susceptibility is based on the maximum strain-rate that can be sustained by the mush at the deepest part of the mush where the pressure is below the critical pressure drop, thus the susceptibility of the HT in this criterion is defined as an inverse of maximum strain-rate value that can be sustained by the mush. Prokhorov [8] on the other hand developed a criterion based on a temperature regime where ductility (δ) is very low – between rigidity temperature ($T_{rigidity}$) and solidus temperature ($T_{solidus.}$) – refer to Figure 1.9. This low ductility regime is usually called the brittle temperature range or BTR [26]. The parameter for HT sensitivity in this criterion is defined as the relation between the minimum ductility of the alloy in such a regime and the strain rate that occurs during solidification within such regime.

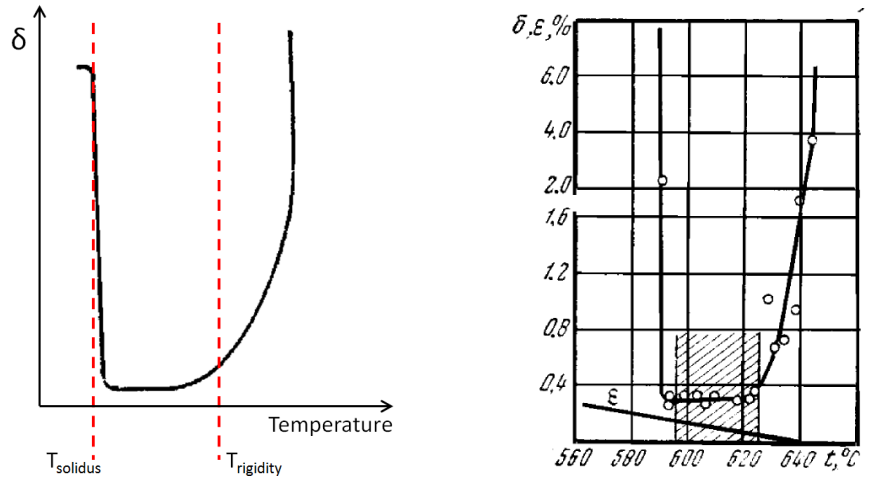

(a) (b)

Figure 1.9 The regime in material where ductility (δ) is very low – between $T_{rigidity}$ and $T_{solidus}$ or usually called BTR (a) and the dashed regime is an example of BTR from real alloy measurement (b) [26].

Novikov [8] developed a HT criterion that is similar to Prokhorov [8]. However, Novikov used strain instead of strain-rate as the measure of HT sensitivity. He proposed to use the reserve of plasticity (amount of strain available to compensate for deformation) as a measure of HT susceptibility [8]. The amount of this variable is defined as the area between the alloy ductility (ε_p) and the thermal contraction (ε_{th}) of the alloy or as S normalized to the width of BTR (ΔT_{br} in Figure 1.10a), see Figure 1.10. However for alloys that has two low-ductility regimes as in Figure 1.10b, S is defined as S_1 minus S_2.

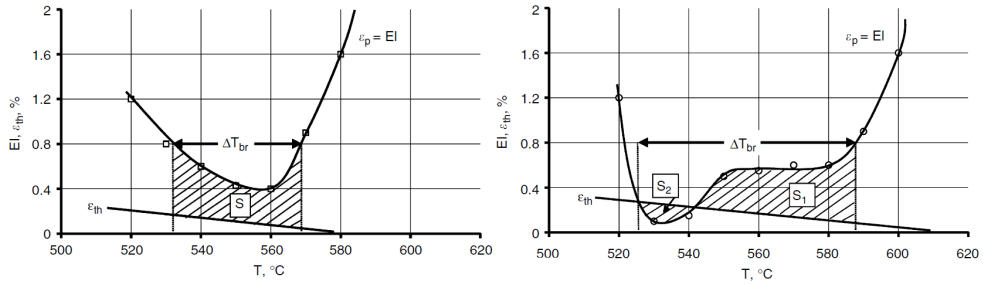

Figure 1.10 Amount of reserve plasticity when the alloy has more ductility than the linear contraction (a) and if the alloy has two low-ductility regimes within BTR (b) [8].

Magnin *et al.* [69] also developed a model to predict HT based on strain field. The HT susceptibility in this criterion is measured by the size of the overlapping area between the ductility curve and the greatest positive principal strain. It is reported that the greatest positive principal strain increases with the casting speed, which linearly increases the HT susceptibility [69].

Recently, a strain-based criterion is developed based upon a two-phase material model [61]. The criterion takes into account other variables during solidification to define the HT susceptibility of the alloy, because it uses critical pressure drop or a solid fraction value as a starting point for HT susceptibility calculation. It calculates the total deformation from such a starting condition up to when material is sufficiently strong to resist HT propagation. This is the HT criterion that is used in ALSIM, and it will be described in more detail later on in this thesis.

1.3.2.2 Cold cracking criteria

The criteria for CC are usually based on mechanical aspect. Livanov [70-72] proposed two different criteria for estimating CC propensity of alloys. The first criterion is based on the tensile strain of the alloy; if the alloy can be deformed more than 1.5% of tensile strain at room temperature, then CC will not occur. To produce his second criterion, he performed casting trials to study the connection between casting speed and cast geometry with respect to crack occurrence. He eventually built a relationship of casting parameters in order to minimize the crack occurrence. Additionally, he found experimentally that for rectangular ingots with a specific multiplicity (width to thickness ratio), decreasing casting speed could increase the propensity of CC occurrence whereas increasing casting speed will increase the susceptibility to HT. Therefore, in order to obtain a sound ingot, casting velocity must be optimized such that it is positioned at point '*a*' (Figure 1.11a).

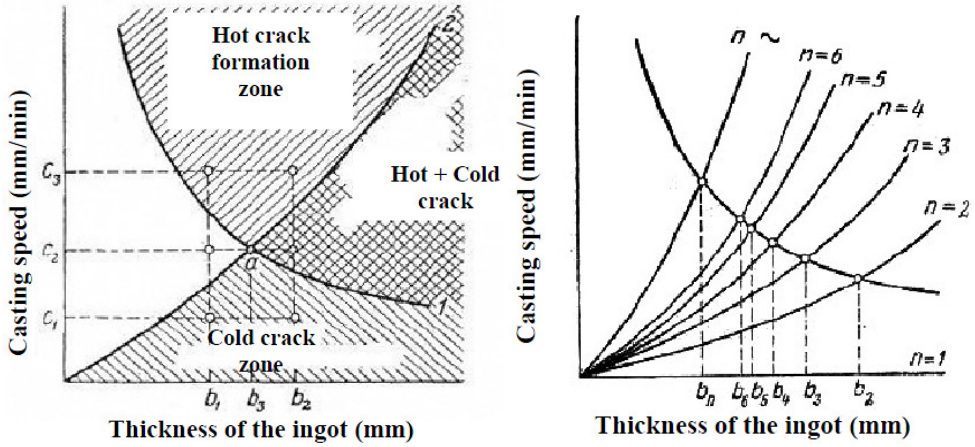

(a) (b)

Figure 1.11 Effect of casting speed (a) and geometry of the cast (b) related to cracking susceptibility during DC casting [70-72].

Figure 1.11b shows the relationship between the ingot geometry (ratio between ingot width and thickness or '*n*') and the optimum casting speed. It could also be suggested that rectangular ingots might have a higher susceptibility to CC than a cylindrical ingot (billet), because stresses tend to concentrate at ingot edges promoting crack initiation.

Boender [32] proposes two approaches to predict the CC susceptibility. The first approach is using principal-stress based calculation. Such as: If the first or maximum principal stress is greater than the uniaxial tensile strength, or the third or minimum principal stress reaches compressive strength of the alloy, then failure will occur. The second approach uses fracture mechanics – Griffith's criterion for brittle material. In the presence of a tensile field, a crack with an ideal sharpness and dimensions exceeding the calculated critical size will cause a catastrophic failure on the material [42]. The latter criterion is the criterion that is currently used to estimate CC susceptibility in ALSIM and it will be discussed in more detail in the next chapter.

1.3.3 Bottlenecks in the existing cracking prediction

After reviewing briefly the description and the available criteria of both types of crack, we can notice two missing points. First, HT and CC are treated separately while the possibility and connection mechanism between these two cracks is yet to be confirmed. Second, to the best of author's knowledge, the existing HT criterion only gives relative susceptibility and there is no measure such as numerical probability of crack likelihood and/or the extent of its occurrence (such as geometry, length and location of the produced crack within the cast product) [27].

Even though the CC criterion could provide an estimate of critical crack dimension to initiate a catastrophic failure, it says nothing about the origins of such a crack. And, as mentioned above, currently there is no HT criterion that could provide information regarding the dimension of the produced HT. Therefore, it is not possible to capture CC occurrence via fracture mechanics approach with HT as the crack initiator. Thus, to capture the connection between the two cracks, a criterion that can provide dimension of a HT is desired and this connection should be captured by the ALSIM model.

1.3.4 ALSIM prediction capability - current status

ALSIM contains crack susceptibility criteria for both HT and CC and to properly simulate a DC casting process for a certain alloy, it needs a set of physical properties of such an alloy. In our case, in the regime of the connection between HT and CC, there are not much mechanical data for AA7050 available from the literature. As a result of the incomplete database, the crack prediction accuracy is currently limited. The detailed condition of existing AA7050 database will be discussed in more detail in the next chapter.

Responding to the demand for ALSIM to be able to capture the connection between HT and CC, a criterion that could capture this connection should be developed and implemented in ALSIM. However, a criterion that would be able to capture undeveloped HT with a length scale of millimeters [8, 34] will require a model that is sufficiently sensitive with respect to different process variables such as casting parameters and material properties. At the moment, there is no study yet regarding the sensitivity of ALSIM model with respect to different process variables. Therefore, a sensitivity analysis of ALSIM model would be needed prior to the development of a criterion that could capture the dimension of undeveloped HT.

1.4 Objectives and the structure of the thesis

From the review of the current understanding and modeling of cracking mechanisms during casting of high strength aluminium alloys given in the previous sections, the objective of this thesis is four-fold:

1. We need to complete ALSIM database on AA7050 alloy in the temperature regime relevant for the connection between HT and CC.
2. We need to analyze the sensitivity of ALSIM DC casting model to the process variables and input parameters prior the development of the criterion that can estimate the dimension of HT.
3. We need to validate the phenomenon connecting HT and CC through a critical crack size criterion.
4. A concept of the new criterion that could provide us with a quantitative crack prediction, able to predict the extent of the produced HT, needs to be proposed.

To complete such objectives, this thesis is arranged as follows:

Chapter 2 presents the current ALSIM capability in DC casting simulation. In this chapter, we perform benchmarking between DC casting trials and simulations with casting variables resembling such trials. Moreover, we also show the method to estimate HT and CC susceptibility during DC casting using existing cracking criteria in ALSIM. We also discuss ALSIM sensitivity with respect to different casting variables and the comparison between the simulation results and the results in the casting trial.

Chapter 3 focuses on the experiment to obtain tensile mechanical properties of the alloy in the sub-solidus temperature regime (high temperature fully solid state). The strength and ductility from different temperatures and strain rates are discussed in this chapter. From the obtained data, we extract constitutive parameters for ALSIM database in this temperature range. Additionally, we also discuss the fracture behavior in this temperature range based on fracture surface analysis.

Chapter 4 focuses on the experiment to obtain tensile mechanical properties of the alloy in the super-solidus temperature regime (semi-solid state between the rigidity temperature and the solidus). The strength, ductility and fracture behavior of the alloy at different solid fractions and strain rates are discussed here. The parameter extraction for the constitutive model by ALSIM software is also performed in this chapter. Additionally, the HT susceptibility of the studied alloy is discussed.

Chapter 5 dicusses the ALSIM sensitivity analysis with respect to different mechanical properties databases which were obtained from the previous chapters. The analysis shows the comparison between the simulation results obtained in Chapter 2 and the same cases but with the updated materials properties database.

To experimentally validate the connection between HT and CC, we need first samples containing micro-HT. In **Chapter 6** we design an experimental procedure that enables us to produce such samples by controlling different solidification parameters. After the samples (henceforth called the pre-HT samples) are produced, we performed sub-surface imaging of the pre-HT samples to observe the produced HT. In this chapter, we also discuss the relationship between different solidification parameters and the amount of produced HT within the sample.

In **Chapter 7** we perform quantitative imaging on the pre-HT samples and subsequently carry out tensile mechanical testing of those samples at room temperature (where alloy is brittle and susceptible to CC). The purpose of the tensile test is to measure the remaining mechanical behavior (e.g. strength and ductility) of the pre-HT samples. We analyze the result to establish the relationship between the quantitative amount of the formed HT and

the remaining mechanical properties of the pre-HT sample and ultimately the connection between HT and CC.

In **Chapter 8**, we propose a new concept of HT criterion that is able to capture the location and dimension of the formed HT. This criterion is designed such that it could be used in a model connecting HT and CC. The mathematical framework of the criterion and the formulation of the connection between the two crack types is presented here. Finally, a mathematical-level implementation of the model on a simplified one dimensional case is presented in this chapter.

To close this thesis, in **Chapter 9** we provide the concluding remarks from this study and subsequently, the recommendation for future research.

References

[1] http://en.wikipedia.org/wiki/Aluminium, "Aluminium" (2014).
[2] Miller, W. S., Zhuang, L., Bottema, J., Wittebrood, A. J., De Smet, P., Haszler, A., Vieregge, A., "Recent development in aluminium alloys for the automotive industry", *Materials Science and Engineering A* (2000), 280, pp. 37-49.
[3] Earle, T. P., Robinson, J. S., Colvin, J. J., "Investigating the mechanisms that cause quench cracking in aluminium alloy 7010", *Journal of Materials Processing Technology* (2004), 153-154, pp. 330-7.
[4] Williams, J. C., Starke Jr, E. A., "Progress in structural materials for aerospace systems", *Acta Materialia* (2003), 51, pp. 5775-99.
[5] http://www.airbus.com/company/market/forecast/, "Airbus Global Market Forecast 2013-2032 Booklet" (2013).
[6] http://www.icao.int/publications/Pages/annual-reports.aspx, "Annual Reports of the Council - International Civil Aviation Organization" (2012).
[7] Research project proposal of Project number: 42.5.09340, Materials innovation institute (M2i), Delft, The Netherlands (2009).
[8] Eskin, D. G., "Physical Metallurgy of Direct Chill Casting of Aluminum Alloys (Advances in Metallic Alloys)", CRC Press, Taylor & Francis group, LLC (2008).
[9] Grandfield, J. F., McGlade, P. T., "DC casting of aluminium: Process behaviour and technology", *Materials Forum* (1996), 20, pp. 29-51.
[10] Emley, E. F., "Continuous casting of aluminium", *International metals reviews* (1976), 21, pp. 75-115.
[11] Phillion, A. B., "Hot tearing and constitutive behavior of semi-solid aluminum alloys", [Ph.D. thesis] (2007), The University of British Columbia.
[12] Eskin, D. G., Savran, V. I., Katgerman, L., "Effects of melt temperature and casting speed on the structure and defect formation during direct-chill casting of an Al-Cu alloy", *Metallurgical and Materials Transactions A* (2005), 36, pp. 1965-76.
[13] Zuidema, J., "Modelling of Flow Phenomena during DC Casting", [Ph.D. Thesis] (2005), Delft University of Technology.

[14] Mukhopadhyay, A. K., "Selection and design principles of wrought aluminium alloys for structural applications", In: *International Conference on Advances in Metallic Materials and Manufacturing Processes for Strategic Sectors (ICAMPS 2012)*, Trivandrum, India (2012), pp. 50-65.
[15] ASM International Handbook Committee, "ASM handbook, Volume 2", Materials Park, OH, USA, ASM International (1990).
[16] Lalpoor, M., Eskin, D., Katgerman, L., "Numerical simulation of residual thermal stresses in AA7050 alloy during DC-casting using ALSIM5", *Advanced Materials Research* (2010), 89-91, pp. 319-24.
[17] Lalpoor, M., Eskin, D. G., Katgerman, L., "Fracture behavior and mechanical properties of high strength aluminum alloys in the as-cast condition", *Materials Science and Engineering A* (2008), 497, pp. 186-94.
[18] Lalpoor, M., Eskin, D. G., Katgerman, L., "Thermal expansion/contraction behavior of AA7050 alloy in the as-cast condition relevant to thermomechanical simulation of residual thermal stresses", *International Journal of Materials Research* (2011), 102, pp. 1286-93.
[19] Sente Software Ltd., Surrey Technology Center, 40 Occam Road, GU2 7YG, UK.
[20] Alastuey, I., "Thermo-mechanical modeling to predict cold cracking in 7xxx aluminum alloys", [M.Sc. Thesis] (2009), Delft University of Technology.
[21] Lalpoor, M., Eskin, D. G., Katgerman, L., "Constitutive parameters, mechanical properties and failure mechanism in DC-cast AA7050 billets", In: *12th International Conference on Fracture (ICF-12)*, Ottawa, ON, Canada (2009), pp. 407-15.
[22] Rappaz, M., Danzig, J. A., "Solidification", CRC Press, Taylor & Francis group, LLC (2009).
[23] Campbell, J., "Casting", Butterworth-Heinemann Ltd. (1991).
[24] Suyitno, A., Eskin, D. G., Savran, V. I., Katgerman, L., "Effects of alloy composition and casting speed on structure formation and hot tearing during direct-chill casting of Al-Cu alloys", *Metallurgical and Materials Transactions A* (2004), 35 A, pp. 3551-61.
[25] Stangeland, A., Mo, A., Nielsen, Ø., Eskin, D., M'Hamdi, M., "Development of thermal strain in the coherent mushy zone during solidification of aluminum alloys", *Metallurgical and Materials Transactions A* (2004), 35 A, pp. 2903-15.
[26] Eskin, D. G., Suyitno, Katgerman, L., "Mechanical properties in the semi-solid state and hot tearing of aluminium alloys", *Progress in Materials Science* (2004), 49, pp. 629-711.
[27] Eskin, D. G., Katgerman, L., "A quest for a new hot tearing criterion", *Metallurgical and Materials Transactions A* (2007), 38A, pp. 1511-9.
[28] Drezet, J. M., Phillion, A. B., "As-cast residual stresses in an aluminum alloy aa6063 billet: Neutron diffraction measurements and finite element modeling", *Metallurgical and Materials Transactions A* (2010), 41, pp. 3396-404.
[29] Drezet, J. M., Evans, A., Pirling, T., Pitié, B., "Stored elastic energy in aluminium alloy AA 6063 billets: Residual stress measurements and thermomechanical modelling", *International Journal of Cast Metals Research* (2012), 25, pp. 110-6.
[30] Drezet, J. M., Ludwig, O., Heinrich, B., "Finite element modelling of the sawing of DC cast AA2024 aluminium alloy slabs", In: *10th Esaform Conference on Material Forming*, Zaragoza, Spain (2007), pp. 1257-62.

[31] Ludwig, O., Drezet, J. M., Commet, B., Heinrich, B., "Modelling of internal stresses in DC casting and sawing of high strength aluminum alloys slabs", In: *Modeling of Casting, Welding and Advanced Solidification Processes - XI.*, Opio, France (2006), pp. 185-92.
[32] Boender, W., Burghardt, A., Van Klaveren, E. P., Rabenberg, J., "Numerical simulation of DC casting; interpreting the results of a thermo-mechanical model", In: *Light Metals, TMS* Charlotte, NC, USA (2004), pp. 679-84.
[33] Drezet, J. M., Evans, A., Jaquerod, C., Phillion, A., "Measurement of as-cast residual stresses in an aluminium alloy AA6063 billet using neutron diffraction", In: *Jim Evans Honorary Symposium - TMS 2010 Annual Meeting and Exhibition*, Seattle, WA (2010), pp. 43-52.
[34] Lalpoor, M., Eskin, D. G., ten Brink, G., Katgerman, L., "Microstructural features of intergranular brittle fracture and cold cracking in high strength aluminum alloys", *Materials Science and Engineering A* (2010), 527, pp. 1828-34.
[35] Paramatmuni, R. K., Chang, K. M., Kang, B. S., Liu, X., "Evaluation of cracking resistance of DC casting high strength aluminum ingots", *Materials Science and Engineering A* (2004), 379, pp. 293-301.
[36] Hannart, B., Cialti, F., Van Schalkwijk, R., "Thermal Stresses in DC Casting of Aluminum Slabs: Application of a Finite Element Model", In: *Light Metals, TMS*, San Francisco, CA, USA (1994), pp. 879-87.
[37] Lalpoor, M., Eskin, D. G., Katgerman, L., "Cold cracking development in AA7050 direct chill-cast billets under various casting conditions", *Metallurgical and Materials Transactions A* (2010), 41A, pp. 2425-34.
[38] Lalpoor, M., Eskin, D. G., and Katgerman, L., "Cold-cracking assessment in AA7050 billets during direct-chill casting by thermomechanical simulation of residual thermal stresses and application of fracture mechanics", *Metallurgical and Materials Transactions A* (2009), 40A, pp. 3304-13.
[39] Fjær, H. G., Mo, A., "ALSPEN-A mathematical model for thermal stresses in direct chill casting of aluminum billets", *Metallurgical Transactions B* (1990), 21, pp. 1049-61.
[40] Bidwell, C. C., Hogan, C. L., "Thermal conductivity of aluminum; Solid and liquid states", *Journal of Applied Physics* (1947), 18, pp. 776-9.
[41] Lalpoor, M., Eskin, D. G., Fjær, H. G., Ten Cate, A., Ontijt, N., and Katgerman, L. , "Application of a criterion for cold cracking to casting high strength aluminium alloys", *Materials Science Forum* (2010), 654-656, pp. pp. 1432-5.
[42] Lalpoor, M., Eskin, D. G., Ruvalcaba, D., Fjær, H. G., Ten Cate, A., Ontijt, N., Katgerman, L., "Cold cracking in DC-cast high strength aluminum alloy ingots: An intrinsic problem intensified by casting process parameters", *Materials Science and Engineering A* (2011), 528, pp. 2831-42.
[43] Eskin, D. G., Lalpoor, M., Katgerman, L., "Cold cracking during direct-chill casting", In: *Light Metals, TMS*, San Diego, CA, USA (2011), pp. 669-74.
[44] Stangeland, A., Mo, A., Eskin, D., "Thermal strain in the mushy zone for aluminum alloys", *Metallurgical and Materials Transactions A* (2006), 37, pp. 2219-29.
[45] Zhang, L., Eskin, D. G., Lalpoor, M., Katgerman, L., "Factors affecting thermal contraction behavior of an AA7050 alloy", *Materials Science and Engineering A* (2010), 527, pp. 3264-70.

[46] Yi, J. Z., Gao, Y. X., Lee, P. D., Lindley, T. C., "Microstructure-based fatigue life prediction for cast A356-T6 aluminum-silicon alloys", *Metallurgical and Materials Transactions B* (2006), 37, pp. 301-11.
[47] Yi, J. Z., Lee, P. D., Lindley, T. C., Fukui, T., "Statistical modeling of microstructure and defect population effects on the fatigue performance of cast A356-T6 automotive components", *Materials Science and Engineering A* (2006), 432, pp. 59-68.
[48] Puncreobutr, C., Lee, P. D., Hamilton, R. W., Cai, B., Connolley, T., "Synchrotron tomographic characterization of damage evolution during aluminum alloy solidification", *Metallurgical and Materials Transactions A* (2013), 44, pp. 5389-95.
[49] Drezet, J. M., Rappaz, M., "Modeling of ingot distortions during direct chill casting of aluminum alloys", *Metallurgical and Materials Transactions A* (1996), 27, pp. 3214-25.
[50] Koric, S., Thomas, B. G., "Thermo-mechanical model of solidification processes : implementation in Abaqus and application to continuous casting casting of steel", Saarbrücken, VDM (2009).
[51] Drezet, J. M., Burghardt, A., Fjaer, H. G., Magnin, B., "Thermomechanical effects in DC casting of aluminum alloy: A numerical benchmark study", *Materials Science Forum* (2000), 329, pp. 493-500.
[52] Du, J., Kang, B. S. J., Chang, K. M., Harris, J., "Computational modeling of D. C. casting of aluminum alloy using finite element method", In: *Proceedings of the 127th TMS Annual Meeting*, San Antonio, TX, USA (1998), pp. 1025-30.
[53] Nagaumi, H., "Prediction of internal crack in high strength Al-Mg-Si alloy" In: Proceedings of The 8th International Conference on Aluminium Alloys (ICAA8), Gregson, P. J., Harris, S. (Eds.), Cambridge, (2002), pp. 71-6.
[54] Nagaumi, H., Umeda, T., "Prediction of internal cracking in a direct-chill cast, high strength, Al-Mg-Si alloy", *Journal of Light Metals* (2002), 2, pp. 161-7.
[55] Hongjun, H., Dingfei, Z., MingBo, Y., "Numerical simulation of thermal stress in cast billets made of AZ31 magnesium alloy during direct-chill casting", *Journal of Manufacturing Processes* (2008), 10, pp. 82-8.
[56] Mortensen, D., "A mathematical model of the heat and fluid flows in directchill casting of aluminum sheet ingots and billets", *Metallurgical and Materials Transactions B* (1999), 30, pp. 119-32.
[57] Mortensen, D., Fjær, H. G., Lindholm, D., Rudshaug, M., Sørheim, E. A., "The development of Alsim - A modelling tool for direct chill casting, twin roll casting, wheel and belt casting and chain conveyor casting", In: *12th International Conference and Exhibition, on Aluminium Cast House Technology*, Melbourne, VIC, Australia (2011), pp. 187-95.
[58] Fjaer, H. G., Mortensen, D., Hakonsen, A., Sorheim, E. A., "Coupled stress, thermal and fluid flow modelling of the start-up phase of aluminum sheet ingot casting", In: *Light Metals, TMS*, San Diego, CA, USA (1999), pp. 743-8.
[59] Gruen, G. U., Buchholz, A., Mortensen, D., "3-D modeling of fluid flow and heat transfer during the DC casting process - Influence of flow modeling approach", In: *Light Metals, TMS*, Nashville, TN, USA (2000), pp. 573-8.
[60] M'Hamdi, M., Benum, S., Mortensen, D., Fjær, H. G., Drezet, J. M., "The importance of viscoplastic strain rate in the formation of center cracks during the start-up phase of

direct-chill cast aluminum extrusion ingots", *Metallurgical and Materials Transactions A* (2003), 34 A, pp. 1941-52.
[61] M'Hamdi, M., Mo, A., Fjær, H. G., "TearSim: A two-phase model addressing hot tearing formation during aluminum direct chill casting", *Metallurgical and Materials Transactions A* (2006), 37, pp. 3069-83.
[62] M'Hamdi, M., Mo, A., Mortensen, D., Fjær, H. G., "Modelling of air gap development and associated surface macrosegregation in DC casting of aluminium sheet ingots", In: *131st TMS Annual Meeting*, Seattle, WA, USA (2002), pp. 695-701.
[63] Subroto, T., Miroux, A., Mortensen, D., M'Hamdi, M., Eskin, D. G., Katgerman, L., "Semi-quantitative predictions of hot tearing and cold cracking in aluminum DC casting using numerical process simulator", *IOP Conference Series: Materials Science and Engineering* (2012), 33, pp. 012068.
[64] Feurer, U., "Influence of Alloy Composition and Solidification Conditions on Dendrite Arm Spacing, Feeding and Hot Tearing Properties of Aluminum Alloys", In: *International Symposium of Quality Control of Engineering Alloys and the Role of Metals Science*, Delft, The Netherlands (1977), pp. 131-45.
[65] Clyne, T. W., Davies, G. J., "Influence of composition on solidification cracking susceptibility in binary alloy systems", *British Foundryman* (1981), 74, pp. 65-73.
[66] Katgerman, L., "A mathematical model for hot cracking of aluminum alloys during D.C. casting", *Journal of Metals* (1982), 34, pp. 46-9.
[67] Dickhaus, C. H., Ohm, L., Engler, S., "Mechanical Properties of Solidifying Shells of Aluminum Alloys", *Transactions of the American Foundrymen's Society* (1993), 101, pp. 677-84.
[68] Rappaz, M., Drezet, J. M., Gremaud, M., "A new hot-tearing criterion", *Metallurgical and Materials Transactions A* (1999), 30, pp. 449-55.
[69] Magnin, B., Maenner, L., Katgerman, L., Engler, S., "Ductility and rheology of an Al-4.5%Cu alloy from room temperature to coherency temperature", *Materials Science Forum* (1996), 217-222, pp. 1209-14.
[70] Lalpoor, M., "Study of cold cracking during DC-casting of high strength aluminum alloys", [Ph.D. Thesis] (2010), Delft University of Technology.
[71] Livanov, V. A., "Casting of Large Ingots for Sheet Production from Aluminum Alloys" In: Aluminum Alloys, Belov, A. F., Agarkov, G. D. (Eds.), Oborongiz, Moscow, (1955), pp. 128 - 68.
[72] Livanov, V. A., Gabidullin, R. M., Shipilov, V. S., "Continuous Casting of Aluminum Alloys", Metallurgiya, Moscow, (1977).

Chapter 2

CRACK SUSCEPTIBILITY ESTIMATION AND CASTING PARAMETERS SENSITIVITY STUDY OF DC CASTING SIMULATIONS

2.1 Introduction

The recent increase in computing power of tabletop has becomes widely accessible, making numerical simulation a preferred method to optimize DC casting process over the traditional trial-error casting. This is because numerical simulation is more effective in terms of time and resource efficiency [1, 2].

In this chapter, we use ALSIM to simulate the DC casting process and calculate the crack susceptibility of AA7050. As briefly mentioned in Chapter 1, ALSIM is a multi-physics process model that is focused on simulating the aluminum DC casting process [3-5]. A detailed description and study of ALSIM's capability to predict DC casting process of high strength aluminum alloy has been done in the previous work by Lalpoor [6]. Therefore, in this chapter, only a brief review of DC casting simulation from ALSIM is given.

In its current development release (ALSIM 6), ALSIM has the criteria to estimate the susceptibility of both hot tearing (HT) and cold cracking (CC). The HT criterion is based on a two-phase material model and developed in the TearSim model [7]. The CC criterion is based on the study of Lalpoor *et al*. [8-11].

The goal of this chapter is twofold; first is to show how ALSIM performs crack susceptibility estimation of both types of cracks (HT and CC). The second is to analyze the sensitivity of the ALSIM model with respect to different casting parameters. To achieve both of these points, we performed benchmarking simulations. Several experimental DC casting trials have been performed at Tata Steel (IJmuiden), which resulted in different cracking conditions: HT billet, CC billet and healthy billet. As a comparison, we ran ALSIM simulations with casting parameters mimicking those trial DC castings and analyzed the simulation output parameters such as temperature distribution, fluid flow pattern, mechanical calculation results and the susceptibility both to HT and to CC. Only two casting parameters were changed to achieve the different cracking state: Casting speed/water-flow rate and the feeding inlet geometry.

This chapter closes with a discussion on ALSIM's limitations and drawbacks with respect to its cracking estimation capability. Additionally, we also discuss whether ALSIM is able to capture the connection between HT and CC and what would be the next step of development towards this direction. The results in this chapter also provide a better understanding for the interpretation of crack susceptibility estimation in ALSIM and assist the modeling efforts for the connection between HT and CC.

Table 2.1 Nomenclature.

T	Temperature
g_s, g_l	Volume fraction; solid, liquid
p_s, p_l	Pressure in; solid, liquid
$\boldsymbol{\sigma}_s$	Solid stress tensor
$\boldsymbol{\tau}_s$	Deviatoric part of stress tensor
$\hat{\boldsymbol{\sigma}}_s$	Effective solid stress tensor
$\bar{\sigma}_s$	von Mises stress
J_1, J_2	First and second stress invariants
$\dot{\boldsymbol{\varepsilon}}_s^p$	Viscoplastic strain-rate tensor
$\dot{\varepsilon}_s^p$	Effective viscoplastic strain-rate
ε_s^p	Viscoplastic strain
X	Stress triaxiality
C	Partial cohesion strain rate
A_2, A_3	Function of solid fraction in closing relation
α, C^*	Internal variables function of g_s and X
p, α_0, α_1, X_0, Δx, Δg_s, k	Semi-solid parameters of cohesion model
σ_0, $\dot{\varepsilon}_0$, Q, n	Parameters of high-temperature solid-state creep law
K, r, m	Parameters in extended-Ludwik equation (ALSPEN) constitutive model
R	Molar gas constant
g_s^{coh}, g_s^{coal}	Coherency and coalescence solid fraction respectively
$\boldsymbol{I}$	Identity tensor

2.2 DC casting modeling in ALSIM

ALSIM is a finite element package with the capability of performing a coupled calculation between thermal, fluid flow and mechanical phenomena. A more detailed description regarding the ALSIM software, its physical model and the boundary condition definitions can be found elsewhere [3]. In order to predict the behavior of a certain alloy during DC casting, ALSIM needs several inputs, such as the solidification path of the alloy and specific information regarding the thermal, fluid and mechanical properties of the alloy. This information can be obtained either using model prediction software or through experiments [8].

2.2.1 Mechanical model and materials database

Mechanical properties of alloys are different at different temperature ranges. There is a dramatic change in the constitutive behavior of alloys in the vicinity of the solidus point due to the significant change in morphology (spatial distribution of the remaining liquid metal), strength and ductility of the alloy [12-14]. Because of this ALSIM uses different constitutive models for different temperature regimes. Below, we describe briefly the different constitutive mechanical models that are used by ALSIM. The details of used constitutive mechanical models in ALSIM have been explained elsewhere: for semi-solid and sub-solidus states the mechanical constitutive models are described in [15-19], while the fully solid state, i.e. below solidus and at lower temperatures, is described in [4].

As liquid aluminum is poured into the mold, the temperature of the melt reduces due to heat extraction and solidification starts to take place. While the temperature of the alloy is still above the rigidity temperature (temperature where alloy starts to transfer stress), there were no mechanical calculations performed because above this temperature the alloy does not have mechanical strength. As the temperature of the alloy falls below this point, grains forms interconnected network and the alloy gains mechanical strength. Equations (2.1) through (2.16) are used in ALSIM to represent the constitutive behavior of this regime. The constitutive equation is as follows and the description for each variable of the equation is shown in Table 2.1:

$$\dot{\boldsymbol{\varepsilon}}_s^p = \frac{\dot{\varepsilon}_0 \exp\left(-\frac{Q}{RT}\right)}{\left(C\sigma_0\right)^n}\left[-\frac{1}{9}A_2\left(g_s\right)J_1\boldsymbol{I} + \frac{3}{2}A_3\left(g_s\right)g_s\boldsymbol{\tau}_s\right]\left[\frac{1}{9}A_2\left(g_s\right)J_1^{\,2} + 3A_3\left(g_s\right)J_2\right]^{\frac{n-1}{2}} \tag{2.1}$$

$$\dot{C} = \alpha\left(g_s, X\right)\left(1 - \frac{C}{C^*\left(g_s, X\right)}\right)\dot{\varepsilon}_s^p \tag{2.2}$$

Where J_1 and J_2 are the first and stress invariants respectively, defined as follows:

$$J_1 = -\mathrm{tr}(\hat{\boldsymbol{\sigma}}_{\mathbf{s}}) = 3g_s(p_s - p_l) \tag{2.3}$$

$$J_2 = \frac{1}{2}\mathrm{tr}(g_s\boldsymbol{\tau}_{\mathbf{s}} : g_s\boldsymbol{\tau}_{\mathbf{s}}) = \frac{1}{3}\bar{\sigma}_s^{\,2} \tag{2.4}$$

Where the effective stress tensor $\hat{\boldsymbol{\sigma}}_s$ is defined as:

$$\hat{\boldsymbol{\sigma}}_s = \left(g_s\boldsymbol{\sigma}_s - g_l p_l\boldsymbol{I}\right) + p_l\boldsymbol{I} = g_s\boldsymbol{\tau}_s - g_s\left(p_s - p_l\right)\boldsymbol{I} \tag{2.5}$$

And the effective strain rate is given by:

$$\dot{\varepsilon}_s^p = \sqrt{\frac{2}{3}\mathrm{tr}\left(\dot{\boldsymbol{\varepsilon}}_s^p : \dot{\boldsymbol{\varepsilon}}_s^p\right)} \tag{2.6}$$

and the stress triaxiality is defined by:

$$X = J_1 \Big/ \left(3\sqrt{3J_2}\right) \tag{2.7}$$

As suggested by Martin *et al.* [19], the expression for $A_2(g_s)$ and $A_3(g_s)$, which characterizes the softening effect of liquid saturated pores in the mush, can be taken from the literature [20, 21]:

$$A_2\left(g_s\right) = \frac{9}{4}\left\{n\left[\left(1-g_s\right)^{-1/n} - 1\right]\right\}^{-2n/(n+1)} \tag{2.8}$$

$$A_3\left(g_s\right) = \left[1 + \frac{2}{3}\left(1-g_s\right)\right] g_s^{-2n/(n+1)} \tag{2.9}$$

The functions $\alpha(g_s, X)$ and $C^*(g_s, X)$ describe the evolution of the partial cohesion of the mush C and must be determined from careful rheological experiments at various fractions of solids and stress states. For grain-refined Al-Cu alloys, Ludwig *et al.* [16, 22] have shown that the following expressions provide a simplified good fit with experimental data. For all stress states (all X values) both functions are described as follows [6, 7, 16, 22-24]:

$$C^*(g_s, X) = C^*(g_s, X=0) + \frac{1 - C^*(g_s, X=0)}{1 + \exp\left[\dfrac{X_0 - X}{\Delta x}\right]} \tag{2.10}$$

$$\alpha(g_s, X) = \alpha(g_s, X=0) \tag{2.11}$$

Where:

$$C^*(g_s, X=0) = \frac{1-\left(1-g_s\right)^p}{1 + \exp\left(\dfrac{g_s^{coh} - g_s}{\Delta g_s}\right)} \tag{2.12}$$

$$\alpha(g_s, X=0) = \frac{\alpha_0 + \alpha_1 \frac{g_s^{1/3}}{1-g_s^{1/3}}}{1+\exp\left(\frac{g_s^{coh} - g_s}{\Delta g_s}\right)} \tag{2.13}$$

In the most recent version of the equations [16, 24], the model offers the option to take into account the effect of coalescence in the tensile stress state ($X < 0$) through $\alpha(g_s, X)$ function as follows:

$$\alpha(g_s, X<0) = \frac{\alpha_0 + \alpha_1 \frac{g_s}{1-g_s}\exp(k(g_s - g_s^{coal})}{1+\exp\left(\frac{g_s^{coh} - g_s}{\Delta g_s}\right)} \tag{2.14}$$

When the alloy becomes fully cohesive and reaches the fully solid state (at $g_s = 1$, $C = 1$), the alloy becomes ductile and follows the creep law behavior. Therefore, Eq. (2.1) and (2.2) simplify as follows [7, 24]:

$$\dot{\boldsymbol{\varepsilon}}_s^p = \frac{3}{2}\frac{\dot{\varepsilon}_s^p}{\bar{\sigma}_s}\boldsymbol{\tau}_s \tag{2.15}$$

with

$$\bar{\sigma}_s = \sigma_0 \exp\left(\frac{Q}{nRT}\right)\left(\frac{\dot{\varepsilon}_s^p}{\dot{\varepsilon}_0}\right)^{1/n} \tag{2.16}$$

This law governs the behavior of the alloy until the merge properties temperature (T_{merge}) which is usually a few ten of degrees below solidus temperature. From this point down to onset hardening temperature (T_0) the alloy is governed by extended Ludwik equation or ALSPEN model (Eq. 2.17) [4]. However, since the hardening effect in this temperature range is not significant, the hardening parameter (r(T)) is set to zero. Below T_0, the strain hardening of the alloy starts to become important [4, 8]. Hence, the full extended Ludwik equation is used to simulate the mechanical behavior of the alloy.

$$\sigma = \mathrm{K(T)}(\varepsilon_p + \varepsilon_p^0)^{\mathrm{r(T)}}(\dot{\varepsilon}_p)^{\mathrm{m(T)}} \tag{2.17}$$

Where K(T) is the consistency of the alloy (at $\varepsilon = 1$, $\dot{\varepsilon} = 1$ s^{-1}), r(T) is the hardening parameter and m(T) is the strain-rate sensitivity of the alloy. These parameters are temperature dependent. ε_p^0 is a constant equal to 0.001 [4, 8].

2.2.2 Criteria for crack prediction

2.2.2.1 Hot tearing criterion

In ALSIM, the HT susceptibility is measured by taking into account both the feeding difficulties and thermal deformation effect, as these two phenomena are well known to be the main driving forces for HT during DC casting [25]. This criterion is called the integrated critical strain, or ICS, and the formulation is as follows:

$$\Delta\varepsilon\left(w_v, w_d\right) = \begin{cases} 0 & \text{for } p_l \geq p_c \\ \int_{t(p_l < p_c)}^{t\left(g_s = g_s^{nof}\right)} \left(w_v \cdot \mathrm{tr}\left(\dot{\boldsymbol{\varepsilon}}_s^p\right) + w_d \cdot \bar{\dot{\varepsilon}}_s^p\right) dt & \text{for } p_l < p_c \end{cases} \quad \textbf{(2.18)}$$

ICS ($\Delta\varepsilon$) measures the cumulative strain (through the plastic strain rate or $\dot{\boldsymbol{\varepsilon}}_s^p$) that occurs when the mush is vulnerable to HT, namely when it is in a state of feeding difficulties and the pressure in the mushy zone (p_l) is below a certain critical pressure (p_c). This calculation is finished when the solid fraction of the mush (g_s) has passed through the advanced coalescence stage ($g_s > g_s^{nof}$), because at this solid fraction, we assume that coalescence and bridging between the grains are fairly advanced, therefore no continuous liquid films are present. Thus, the alloy has obtained sufficient ductility to prevent the formation of a HT. The parameters w_v and w_d enable us to tune the weight of the calculation between volumetric and deviatoric strain components, respectively. More details of this criterion can be found elsewhere [7]. Higher values of ICS mean higher susceptibility at that position on the billet to HT.

2.2.2.2 Cold cracking criterion

For CC, ALSIM measures the cracking susceptibility via the critical crack size or CCS. The principle idea of this criterion is as follows. If a defect (for instance micro hot-tear, inclusion or porosity) exists within the ingot and such a defect has a dimension exceeding the CCS when the alloy is brittle (below 200 °C for AA7050), then CC will occur. The formulation of CC criteria for different crack geometries [10] are shown in Table 2.2.

The parameter a_c, equal to half the CCS, takes into account the geometry of the initial defect; whether it is a volumetric crack (penny-shaped crack) or a surface crack (thumbnail shaped crack). This criterion also takes into account the plane strain fracture toughness (K_{Ic}) at several temperature points, which is obtained experimentally [8], and the first principal stress σ_{11}, which is readily available from ALSIM calculations. This criterion uses the assumption that the longest axis of the crack is perpendicular to the first principal stress direction. In summary, the lower the CCS value, the more susceptible that part of the billet is to CC.

Table 2.2 Geometrical factor of different types of cracks [10]. a_c is half of CCS, K_{Ic} is plane strain fracture toughness and σ_{11} is the first principal stress which is readily available from ALSIM calculation.

Penny-shaped crack		Thumbnail-shaped crack	
$a_c = \frac{\pi}{4}\left(\frac{K_{Ic}}{\sigma_{11}}\right)^2$	**(2.19)**	$a_c = \frac{\pi}{(2\times 1.13)^2}\left(\frac{K_{Ic}}{\sigma_{11}}\right)^2$	**(2.20)**

2.2.3 Model setting for numerical DC casting simulation

We performed benchmarking between 2D DC casting simulations and trial DC casting billets. Owing to the geometric symmetry, to reduce the calculation time, we only performed the simulation on half of the geometry with the centerline of the ingot as the symmetry axis.

The simulated geometries are built according to the trial setup, which includes the melt distributor, mold, water jet, bottom block and ingot part or cast domains, i.e. the Euler, expansion and Lagrange domains (see Figure 2.1a). These geometries are meshed using quadrilateral elements. When the casting starts and the first part of the billet has solidified, the bottom block will be retracted downwards and elements in the expansion zone will grow vertically at every time step until a new row of elements is split from the expansion zone and added to the Lagrange domain below. Subsequently, the ingot shell, which has just solidified, is sprayed with water at room temperature (20 °C) to let it cool down. Some additional simulations settings and AA7050 material properties that are used in the simulation are as follows: The solidification path of the AA7050 alloy was calculated using JMat-Pro® software with Scheil approximation. The solidification curve is shown in Figure 1.2., heat transfer coefficient to both mold and bottom block is 1000 W/m^2K [26], latent heat of fusion is $380.8 \cdot 10^3$ J/Kg, density for solid and liquid state are 2628 Kg/m^3 and 2491 Kg/m^3 respectively, and kinematic viscosity of liquid aluminum is $5.1 \cdot 10^{-7}$ m^2/s.

For the constitutive mechanical behavior prediction, the internal variable $\alpha(g_s, X)$ for all stress states (Eq. 2.13) [6, 22] was used in the semi-solid mechanical model. And for the materials database, an Al–2 wt% Cu database was used for the semi-solid state (Eq. 2.1 and 2.2) and high temperature fully solid temperature regime (Eq. 2.15 and 2.16) [16], since the AA7050 data in this temperature regime was not available at this stage of the project. For the fully solid and hardening temperature regime (Eq. 2.17) we used the database for the AA7050 alloy [8]. The merging property temperature where the mechanical model changes from a cohesion model (Eq. 2.1 up to Eq. 2.16) to the extended Ludwik equation (Eq. 2.17) is defined as T_{merge} = 410 °C. The onset of hardening temperature for Eq. 2.17 is defined as T_0 = 390 °C [8].

Other than varying the casting speed and water flow rate, we also use two different inlet geometries: a semi-horizontal feeding scheme (Figure 2.1b) – with an angle of 40° from the horizontal axis and a vertical feeding scheme (Figure 2.1c).

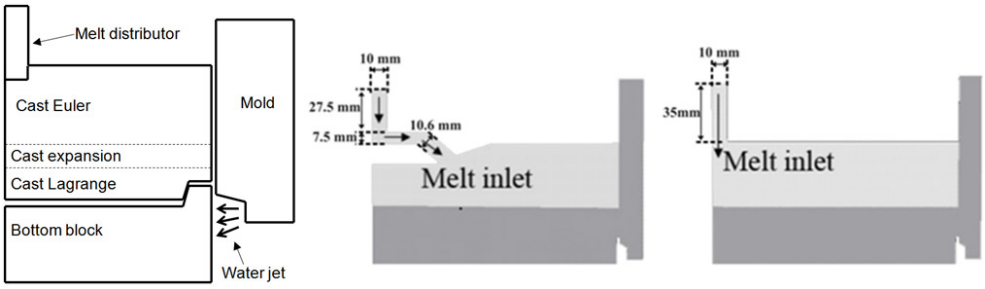

(a) (b) (c)

Figure 2.1 Generic casting setup geometry (a) and two different types of inlet flow geometry; semi-horizontal feeding scheme (b) and vertical feeding scheme (c).

For calculating the HT susceptibility, we used a critical pressure drop of –7000 Pa and a g_s^{nof} of 0.99 [26]. The weights for volumetric and deviatoric strain components were 1.0 and 0.0, respectively. For the CC susceptibility calculation, we used data from previous research [8] for the plane strain fracture toughness (K_{Ic}) of the AA7050 alloy and we assumed that the initial crack geometry was penny shaped.

Three different casting trials with different casting conditions were performed at DC casting facilities at Tata Steel (IJmuiden) and the results of those castings were billets with HT, CC and a healthy ingot without visible fracture. The details of the casting trials are described in the next section.

2.3 Procedure of DC casting trials

The cylindrical billets were DC cast at Tata Steel Research and Development center in IJmuiden, The Netherlands. The diameter of the billets was 315 mm and the average alloy composition is shown in Table 1.1. The melt was first degassed in the furnace at 730 °C and then cast with a conventional DC casting mold as schematically shown in Figure 2.1a. The casting temperature was approximately 680 °C. All of the billets were grain refined by using the same amount of Al5Ti1B (2.5 kg/ton) for each billet. Main casting parameters are shown in Table 2.3.

As a result, we have one billet with HT, one with CC and one healthy ingot that we use as a reference. The nominal casting speed and water flow rate correspond to the steady state casting conditions after the ramping up stage. These casting parameters (including the ramping procedure) are chosen based on the casting practice and personnel experience and

such parameters could reproduce the condition of the cast billet (high probability of HT for hot tear casting parameters and similar for the CC and healthy cases).

Table 2.3 Description of the casting process parameters for the AA7050 alloy.

Process parameter	Billet 1	Billet 2	Billet 3
Distributor/inlet geometry	Vertical	Semi-horizontal	Semi-horizontal
Nominal casting speed (mm/min)	50	90	50
Water flow rate (l/min)	40	110	40
Cracking status	Hot tear	Cold crack	Healthy

2.4 Results

2.4.1 Trial casting results

Figure 2.2 shows the cracked billets. The HT is shown in Figure 2.2a. One can see a centerline crack (between the arrow heads) that propagates as a plane along the longest axis of the ingot. This is the classical feature of a catastrophic HT in a round billet [27], because such a crack is produced through tensile-radial mechanical deformation of the semi-solid mush due to the high temperature gradient between the center and surface of the billet.

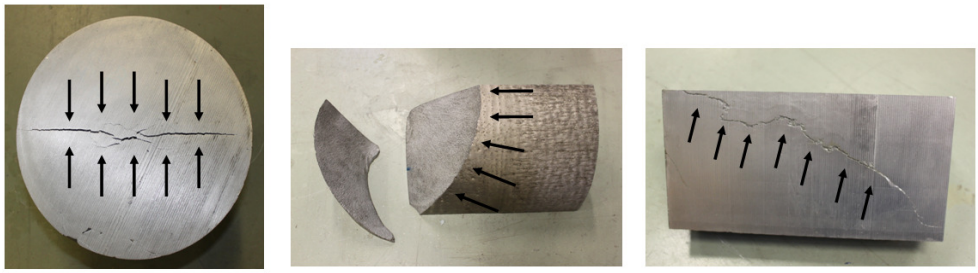

Figure 2.2 Ingot with HT (a) and ingot with CC which occurs throughout the ingot (b, c).

Figure 2.2b and 2.2c show the CC billet. These figures demonstrate that the cracks are propagating throughout the billet but not necessarily along the centerline. For instance, in Figure 2.2b, the crack that splits the billet open starts from the centerline and propagates to the surface (pointed by the arrows). In Figure 2.2c, one can see a crack path (pointed by the arrows) of a CC that has not split the billet apart.

2.4.2 DC casting simulation results

The results from the numerical simulations show that indeed, the change in casting parameters, both the inlet geometry and the casting speed, give significant changes to the temperature distribution across the billet (represented by color legend in Figure 2.3) and,

consequently, to the shape of the sump (isolines represent different solid fractions). In Figure 2.3, it is shown that the healthy case (Figure 2.3a) has the shallowest sump. As we increase the casting speed (90 mm/min) using the same inlet geometry to obtain the CC case (Figure 2.3b), the sump slope also steepened, which in turn also changes the temperature gradient across the billet. Although the shape of the sump does not change significantly, by increasing the casting speed, the sump depth is increased significantly. As we changed the inlet geometry to a vertical inlet (spout) but still use the low casting speed (50 mm/min) to obtain the HT case (Figure 2.3c), the shape of the sump changes significantly. In addition, the sump depth also increases compared to the healthy case. An interesting feature of the simulation run using the vertical inlet geometry (HT case) is that there are two sump slopes observed on the sump instead of one (when we use the semi-horizontal inlet geometry). In the HT case, the sump slope nearest to the billet center is very steep and as we move toward the billet surface, at approximately 40 mm from the billet center (marked with the black arrows at Figure 2.3c), the slope becomes shallower. In terms of sump depth as measured from metal level down to when the solid fraction of the alloy is 0.9, the deepest sump is achieved by the CC case (254 mm) and followed by the HT case (176 mm). The shallowest sump is obtained by the healthy case (139 mm).

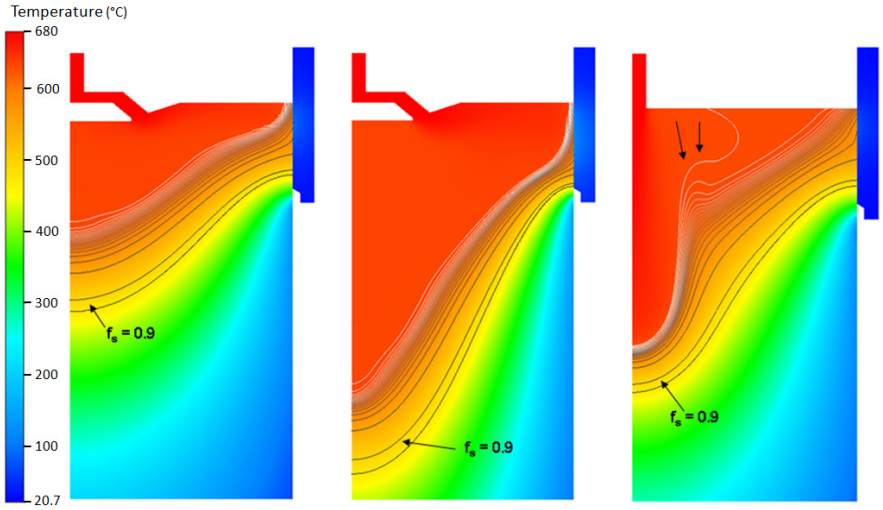

Figure 2.3 Comparison of temperature distribution in °C (color legend) and solid fraction isolines between 0 (fully liquid) and 1 (fully solid state) of different casting conditions: healthy case (a), CC case (b) and HT case (c). This image is taken when the billet already reached steady-state casting condition.

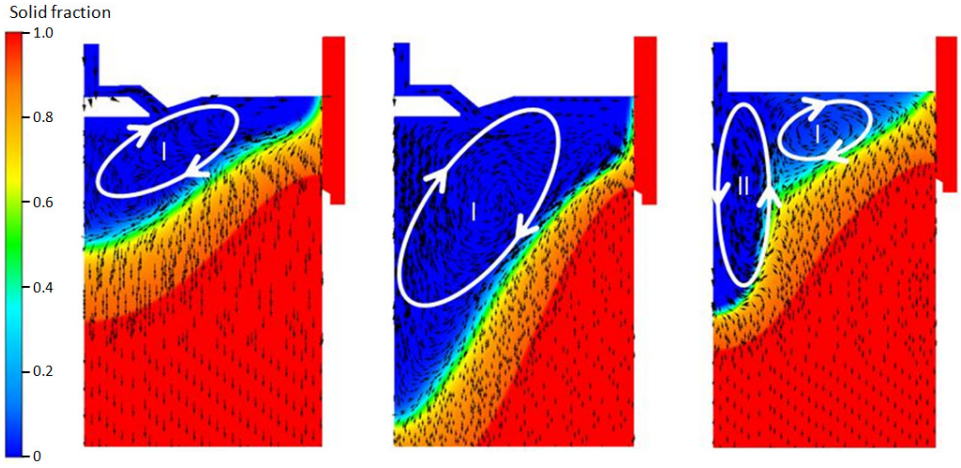

(a) (b) (c)

Figure 2.4 Comparison of solid fraction (color legend) and fluid flow patterns (arrows) in the sump for different cases – healthy case (a), CC case (b) and HT case (c). This image is taken when the billet already reached steady-state casting condition.

The change in the inlet geometry has a significant impact to the fluid flow pattern of the billet during DC casting. Figure 2.4 shows the results of fluid flow calculations in different casting cases. The color legend in the figure represents the solid fraction of the ingot; red is the fully solid state, blue is the fully liquid state and the transition colors represent the mushy zone. Figure 2.4a shows that in the healthy case, there is only one flow vortex with clockwise flow direction. When the casting speed is increased (CC case, Figure 2.4b), the flow pattern does not change significantly; there is only one flow vortex in a clockwise flow direction. However, by changing the inlet geometry (HT case, Figure 2.4c), although the used casting speed is similar to the healthy case, the fluid flow pattern changes significantly. In the HT case, there are two vortices in the ingot with flow directions opposite to each other; the vortex near to the billet center has a counter-clockwise direction, while the one closer to the billet surface has a clockwise direction. It is important to notice that these two flows meet at approximately 40 mm from the billet center. At this point, there is a zero horizontal flow speed but a positive (upward) vertical flow speed. It is also interesting to note that this meeting point is where the sump slope discontinuity occurs (black arrows in Figure 2.3c). This shows that the fluid flow has a significant effect on the shape of the sump.

In terms of stress calculation, in general, all of the cases have similar trends. In the radial direction, the maximum positive (tensile) value is found in the center of the billet and diminishes as we move to the surface. In the circumferential and axial direction, the stress state is highly positive in the center, but as we move towards the surface the value becomes

highly negative (compressive). However, by changing the casting parameters, the stress value and spatial distribution is modified in different stress directions. As a representation, a comparison of the first principal stress calculations for different cases is shown in Figure 2.5. The first principal stress value also has a similar trend. It is positive in the center and the stress value diminishes toward the surface of the billet.

In terms of stress value, the healthy case has the lowest maximum first principal stress (+140 MPa) as compared to HT (+169 MPa) and CC (+173 MPa) cases. The highest value appears in the center of the billet in all three cases. The lowest minimum first principal stress value is obtained in both healthy and HT case (–7 MPa) while the CC case has the minimum first principal stress value of –4 MPa. The lowest first principal stress values in all three cases are found in the subsurface area after the billet passed the water impingement zone (area that is hit directly by water as soon as the billet exits the mold). From the comparison in Figure 2.5, it seems that the CC case has the widest area with high first principal stress (area with red color), followed by HT case and healthy case.

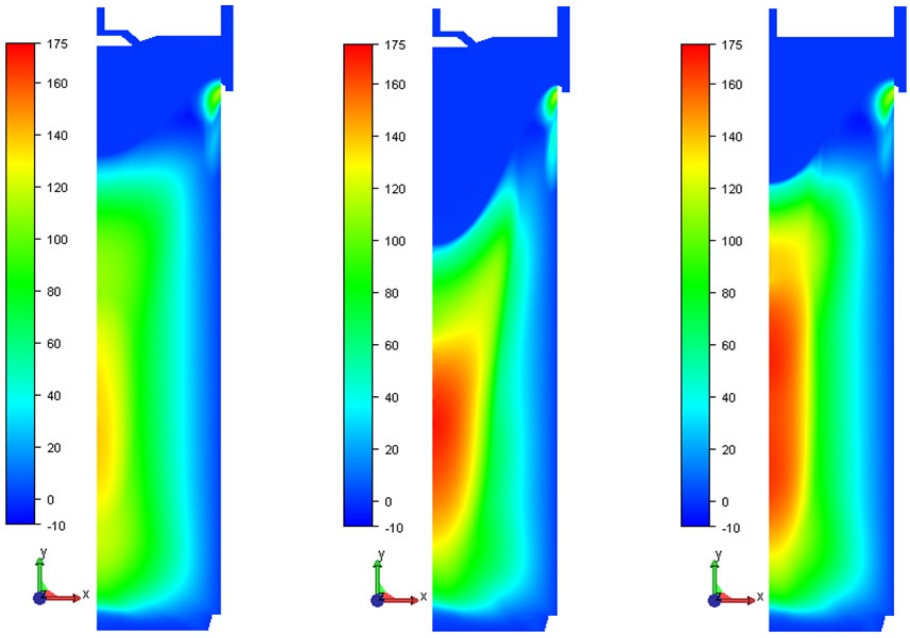

Figure 2.5 Comparison of first principal stress calculations (unit in MPa) from different casting cases at steady state casting condition; healthy (a), CC (b) and HT (c).

2.4.3 Crack susceptibility estimation results

We observed both the ICS and CCS values for all simulation cases when the DC casting simulation proceeded beyond the steady state condition. The distribution of ICS from different casting cases is shown on Figure 2.6. This figure shows that, in general, high ICS values are mostly concentrated on the centerline of the billet and the value drops dramatically as we move towards the surface of the billet. Moreover, we can also see that there is always a (local) peak ICS value at the start-up phase of the casting (high ICS value just above the bottom block) even though the value of the peak differs for different casting cases.

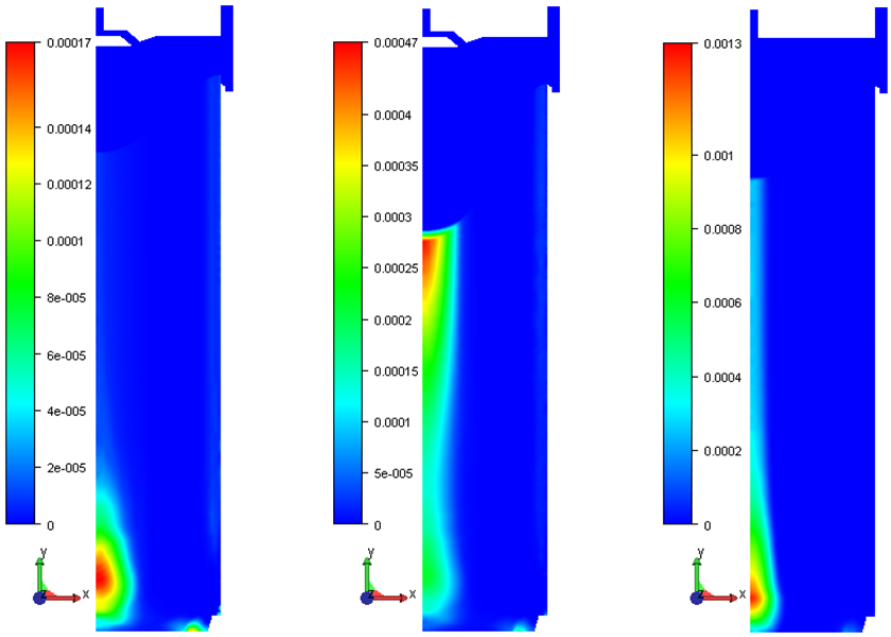

(a) (b) (c)

Figure 2.6 ICS distribution for different casting cases at steady state casting condition; healthy (a), CC (b) and HT (c).

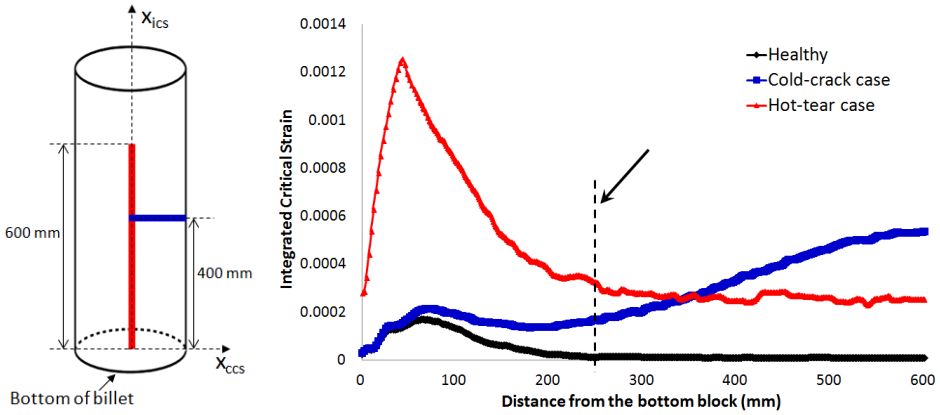

(a) (b)

Figure 2.7 Illustration of plot line position in the billet for different crack susceptibility estimation – red line for ICS and blue line for CCS (a). Comparison of ICS calculation from different casting conditions (b); HT (red line), CC (blue line) and healthy case (black line). The plot is taken at the centerline from just above the bottom block up to 600 mm above the bottom block.

Since the most significant ICS value is concentrated at the centerline, we plotted the ICS values on this line (red line in Figure 2.7a), from just above the bottom block up to 600 mm above the bottom block as given in Figure 2.7b. This figure shows that the highest ICS value is achieved by the HT case with the peak value at the start-up regime, which is around 0.0013, then followed by the CC case where the start-up peak is approximately 0.00022. The lowest ICS value is obtained by the healthy case, which the peak also occurs in the start-up phase with ICS value of around 0.00017. In all of the cases, the ICS value stabilizes after the peak in the start-up phase. For the healthy case, the ICS value is stabilizes at a very low value, while for HT case, the ICS value stabilizes at approximately 0.00025. The CC case produces a different trend than the other two cases. In this case, the highest ICS value is obtained in its steady-state condition; stabilizing at approximately 0.0006 after the cast length is beyond 600 mm.

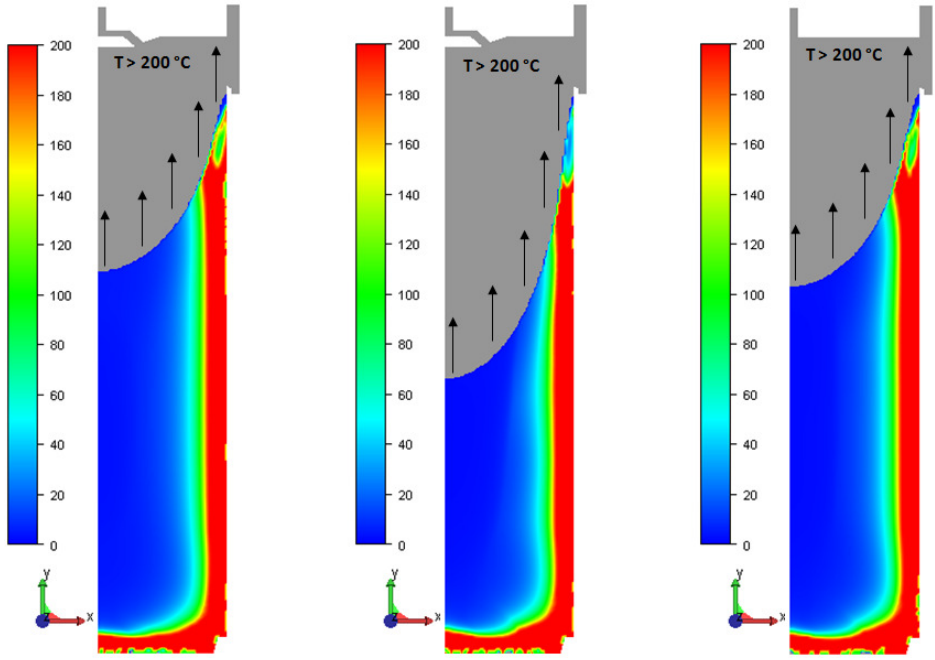

(a) (b) (c)

Figure 2.8 CCS distribution (unit in mm) for different casting cases at steady state casting condition; healthy (a), cold-crack (b) and HT (c).

From the CC side, Figure 2.8 shows that the trend of CCS distribution is similar for all casting cases. The lowest CCS values are concentrated in the center of the billet and the CCS value increases as we move to the surface of the billet. In short, the center of the billet is more susceptible to CC initiation compared to the surface of the billet. The grey area in each billet in Figure 2.8 shows the area in the ingot with temperatures above 200 °C. At this temperature, the alloy is ductile [8], thus significantly reducing the probability of CC occurrence.

To observe the radial CCS distribution in the steady state casting condition (at cast length of 400 mm above the bottom block), we plot CCS value from the center up to the surface of the billet – blue line in Figure 2.7a. From Figure 2.9, we see that in general the healthy case always has the highest CCS value as compared to both HT and CC cases, which means the healthy case has the least susceptibility to CC occurrence. The CC case always has the lowest CCS value throughout the billet except between the center and the quarter-radius of the billet where the value is slightly higher than the HT case. From this graph, it is also important to note that at around mid-radius, the CC case is approximately twice more susceptible to cold cracking as compared to the healthy case.

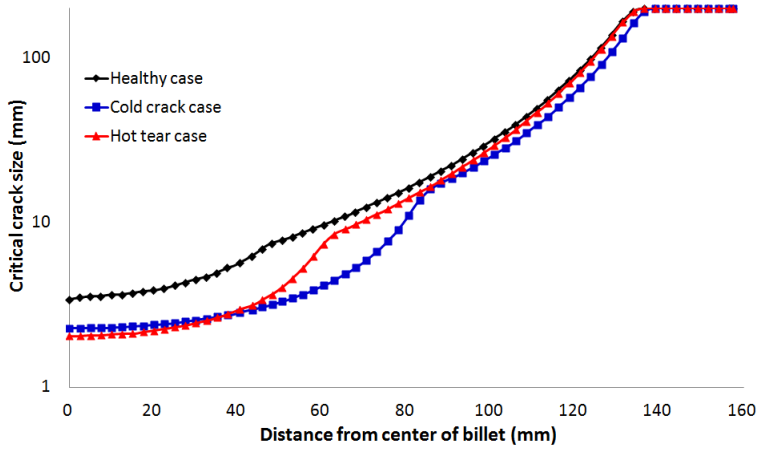

Figure 2.9 CCS comparison for the three different cases; HT case (red line), CC case (blue line) and healthy case (black line). The plot taken at the position of cast length of 400 mm above the bottom block, from the centerline to the surface of the billet.

2.5 Discussion

The results given in the previous section show that the ALSIM model is sensitive with respect to the change in casting variables such as casting speed and feeding inlet geometry. Varying both casting speed and inlet geometry changes the thermal gradient across the billet, which eventually changes cracking susceptibility for both the CC and HT cases.

ALSIM fluid flow calculations can capture interesting features caused by the change in fluid flow. It was reported by Zhang *et al.* [28], based on chemical composition analysis, that a peak of negative segregation occurs at the meeting point of the two flows (40 mm from ingot center, black arrows in Figure 2.3c) in the billet (Figure 2.10a) for the HT case. In the same location, Figure 2.10b shows that a thin layer of coarse grains (between the black dotted lines) is produced among the fine-grained structure. The formation of such a coarse grain layer is unlikely to occur providing the billets are grain refined. It was found from ALSIM simulations that this specific location has a significantly lower cooling-rate compared to the surrounding area of the billet [28]. This result supports the experimental finding shown in Figure 2.10. This example flaunts the considerable accuracy of the ALSIM fluid flow model. It is worth to note here that the local changes in chemical composition and structure may also have an impact to HT susceptibility due to local increase of solidification width [29, 30] and also to CC susceptibility due to the change in the amount of the brittle phases in the billet after it is fully solidified [31].

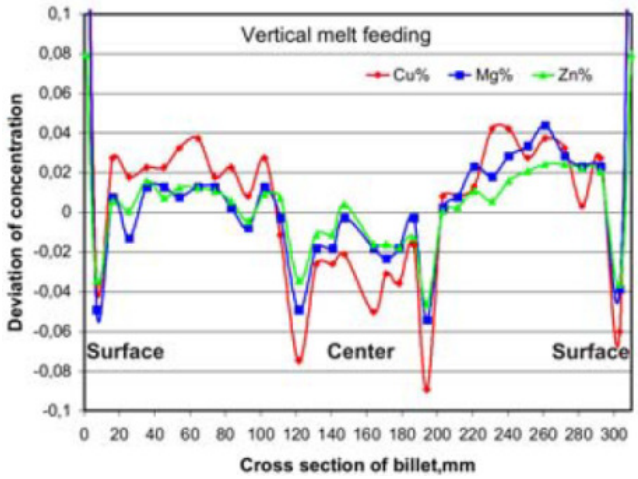

(a)

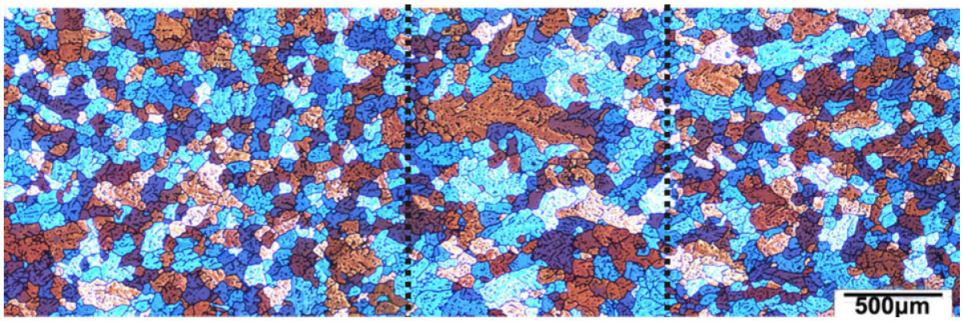

(b)

Figure 2.10 Chemical composition analysis across the HT billet (a) and an example of optical microstructure observation around the negative segregation peak (around 40 mm from billet center) (b). The thin layer of coarse grain is located approximately at the negative segregation peak [28].

From the mechanical calculation results, the general trends of the stress states (thermal stresses) on the billets are similar to the previous work [8]. The first principal stress calculation shows that the CC case has higher maximum stress value compared to the HT and the healthy cases. This is in good accordance with the fact that residual stress is the main driving force for CC [4, 8, 32-34]. Although the stress distribution is similar in all three cases, highly positive in the center and reducing toward the surface of the billet, the shape of the sump influences the stress distribution values. The CC case has the deepest sump, thus produces wider area with higher stress values (region with red color in Figure 2.5b). This condition eventually affects the CC susceptibility by widening the susceptible area to CC as compared to the healthy case (refer to Figure 2.9). Such a figure also shows

that the change of inlet geometry increases the CC susceptibility by widening the CC-prone area in the billet. However, from such a result, the effect of inlet geometry is less dominant compared to the increase in casting speed. This result shows that the sump shape and depth influences the stress distribution and also affects the CC susceptibility within the billet – deeper sump depth increases CC susceptibility.

Both Figure 2.6 and Figure 2.7b show that ALSIM captures the peak ICS value at the start-up phase of DC casting. This is in accordance with previous works that show HT usually occurs in the start-up phase since at the top of the starting block, not only is there a severe concentration of strain occurring at the end of solidification [35], but there is also a significant drop in the mushy-zone pressure [36]. Additionally, it was also reported that at the start-up phase of the casting, the sump depth and transition zone thickness are temporarily larger than in the steady state [37-39]. These conditions increase the susceptibility of HT during DC casting. This result shows that ALSIM can capture the important features related to HT during DC casting.

An important point to mention is that when comparing ICS calculations and trial casting for the HT case, when the cast length reached approximately 250 mm (black arrow and dashed line in Figure 2.7b), the billet had a catastrophic HT, as reported by the casting personnel. This result is counterintuitive considering the peak ICS value occurs when the cast length is approximately 50 mm. One possible explanation for this occurrence is that at the peak ICS value (at a cast length of 50 mm) the HT initiates and the ingot accumulates more (sub-critical) damage as the casting continues since the ICS value is still significant after 50 mm of cast length. Such damage accumulation eventually reaches a threshold as the cast length reaches 250 mm and the HT propagates catastrophically.

Figure 2.7b shows that the ICS value for the CC case in the steady state is quite significant (stable at approximately 0.0006 after 600 mm of cast length) but the HT does not occur and instead catastrophic CC occurs after the casting process is finished (when the billet has fully solidified). This could mean that there may be some underdeveloped HT formed in the billet but they remained dormant until a sufficiently significant increase in stress took place as the ingot cooled down [10] making the alloy brittle (below 200 °C) [8, 40]. Additionally, it is also known that a high casting speed also increases HT susceptibility during casting [29, 37]. This fact supports the hypothesis that an underdeveloped HT could initiate CC.

This result suggests that ALSIM has the potential to capture the possible connection between HT and CC, since the CC case not only generally has the lowest CCS value but also has a significant ICS value. The possible connection mechanism based on ALSIM simulation is that if a micro HT reaches a critical size, a catastrophic CC can be initiated.

Although it has been shown that ALSIM can provide a DC casting simulation with considerable accuracy, at the moment there are still critical drawbacks in ALSIM's ability to capture the connection between HT and CC. These drawbacks are as follows:

1. Although we demonstrated in Section 2.4.2 that ALSIM is sensitive to different casting parameters, at the moment we do not have any information about its sensitivity with respect to different material databases. In order to capture the delicate phenomenon of micro HT formation, we need to have a model that is sensitive with respect to different material properties such as alloy composition because it is one of the important parameters that dictates HT susceptibility during DC casting [25, 29, 37, 41]. Thus, a study regarding ALSIM's sensitivity to different alloy databases needs to be carried out. This study is the main focus of Chapter 5 of this thesis.
2. At this stage of the project, ALSIM does not have a complete constitutive mechanical behavior database of AA7050. It only have material database information AA7050 on the fully solid temperature regime (from room temperature up to 400 °C) and Al-2% Cu database at the semi solid state and high-temperature (creep-law dictated regime) fully solid temperature regime. This calls for the AA7050 database from 400 °C to the solidus point (sub-solidus temperature regime), which is an important regime for two reasons. Firstly, there is a significant change in mechanical properties of the alloy as it approaches solidus [42, 43]. Secondly, the behavior of the solid material near the solidus point represents the solid grain behavior in the semi-solid state. Additionally, we also need the AA7050 database on the semi-solid state temperature to replace the Al-2% Cu database. The incompleteness of this database might reduce crack prediction accuracy, especially since the missing data lies at the point where HT initiates (semi-solid regime) and the connection point between HT and CC (around solidus point and sub-solidus regime). Therefore, it is crucial to complete this constitutive behavior database. Chapter 3 focuses on constitutive mechanical behavior in the sub-solidus temperature regime, while Chapter 4 focuses on constitutive mechanical behavior in semi-solid temperature regime.
3. From the results in the Section 2.4.3, we observe that although ALSIM has crack susceptibility estimation for both HT (via ICS value) and CC (via CCS value), the measure only provides relative susceptibility and does not provide information as to whether cracks in either regime will occur. Therefore, a more quantitative crack prediction needs to be developed. This development is the main subject of Chapter 8.
4. At the current status of its development, although ALSIM can provide a critical dimension for CC occurrence, it cannot provide information on the size and geometry of the micro HT that acts as a crack initiation point. It is also mentioned in Chapter 1 that to the best of author’s knowledge, there are no criteria that can capture the size and dimension of the formed HT, because this phenomenon is complex and non-linear [44, 45]. Therefore, a new criterion that can capture the HT size is necessary to capture the

connection between these two types of cracks. Together with the problem mentioned in point 3, a concept for this new criterion will be discussed further in Chapter 8.

2.6 Conclusions

From the result of this work, we draw several conclusions as follows:

1. ALSIM is sensitive with respect to different casting parameters such as the melt feeding scheme and casting speed.
2. The melt feeding scheme affects the shape of the sump by distributing the hot melt and changing the temperature profile. This plays an important role in the susceptibility to HT in the billet.
3. Sump depth also increases with casting speed, which in turn increases the thermal gradient between the centre and the surface of the billet, and ultimately promotes HT and CC
4. The output of the simulation is in qualitative agreement with the experimental results of trial DC casting, which validates the cracking model used in ALSIM. The HT case results in the highest ICS value, the CC case generally has the lowest CCS value, and the healthy case always has the lowest cracking susceptibility in both cracking domains.
5. From the analysis and interpretation of ALSIM calculations, we obtained a supporting argument for the connection between the two cracks: CC could be initiated from non-critical micro HT.
6. ALSIM lacks data for the AA7050 constitutive mechanical database in the temperature regimes that are crucial to HT formation (as the cold-crack initiator), namely in the semi-solid state and in the connection regime between these two cracks (the solidus point and sub-solidus temperature regime). Therefore, it is important to obtain the complete AA7050 database as this incompleteness may reduce the DC casting simulation and cracking estimation accuracy. Additionally, a complete alloy database for the DC casting temperature range can also be used to analyze ALSIM's sensitivity with respect to different material databases.
7. ALSIM has the limitation of only being able to provide a qualitative susceptibility estimate (relative measures) for both HT and CC. Thus, a quantitative crack prediction is needed. Additionally, ALSIM cannot capture the dimension and orientation of the formed HT. Therefore, a modeling concept toward this direction is necessary for a quantitative crack prediction during DC casting.

References

[1] Drezet, J. M., Rappaz, M., "Modeling of ingot distortions during direct chill casting of aluminum alloys", *Metallurgical and Materials Transactions A* (1996), 27, pp. 3214-25.
[2] Koric, S., Thomas, B. G., "Thermo-mechanical model of solidification processes : implementation in Abaqus and application to continuous casting casting of steel", Saarbrücken, VDM (2009).
[3] Mortensen, D., "A mathematical model of the heat and fluid flows in directchill casting of aluminum sheet ingots and billets", *Metallurgical and Materials Transactions B* (1999), 30, pp. 119-32.
[4] Fjær, H. G., Mo, A., "ALSPEN-A mathematical model for thermal stresses in direct chill casting of aluminum billets", *Metallurgical Transactions B* (1990), 21, pp. 1049-61.
[5] Fjaer, H. G., Mortensen, D., Hakonsen, A., Sorheim, E. A., "Coupled stress, thermal and fluid flow modelling of the start-up phase of aluminum sheet ingot casting", In: *Light Metals, TMS*, San Diego, CA, USA (1999), pp. 743-8.
[6] Lalpoor, M., "Study of cold cracking during DC-casting of high strength aluminum alloys", [Ph.D. Thesis] (2010), Delft University of Technology.
[7] M'Hamdi, M., Mo, A., Fjær, H. G., "TearSim: A two-phase model addressing hot tearing formation during aluminum direct chill casting", *Metallurgical and Materials Transactions A* (2006), 37, pp. 3069-83.
[8] Lalpoor, M., Eskin, D. G., and Katgerman, L., "Cold-cracking assessment in AA7050 billets during direct-chill casting by thermomechanical simulation of residual thermal stresses and application of fracture mechanics", *Metallurgical and Materials Transactions A* (2009), 40A, pp. 3304-13.
[9] Lalpoor, M., Eskin, D. G., Fjær, H. G., Ten Cate, A., Ontijt, N., and Katgerman, L. , "Application of a Criterion for Cold Cracking to Casting High Strength Aluminium Alloys", *Materials Science Forum* (2010), 654-656, pp. 1432-5.
[10] Lalpoor, M., Eskin, D. G., Katgerman, L., "Cold cracking development in AA7050 direct chill-cast billets under various casting conditions", *Metallurgical and Materials Transactions A* (2010), 41A, pp. 2425-34.
[11] Lalpoor, M., Eskin, D. G., Ruvalcaba, D., Fjær, H. G., Ten Cate, A., Ontijt, N., Katgerman, L., "Cold cracking in DC-cast high strength aluminum alloy ingots: An intrinsic problem intensified by casting process parameters", *Materials Science and Engineering A* (2011), 528, pp. 2831-42.
[12] Fabrègue, D., Deschamps, A., Suéry, M., Poole, W. J., "Rheological behavior of Al-Mg-Si-Cu alloys in the mushy state obtained by partial remelting and partial solidification at high cooling rate", *Metallurgical and Materials Transactions A* (2006), 37, pp. 1459-67.
[13] Subroto, T., Miroux, A., Eskin, D. G., Ellingsen, K., Marson, A., M'Hamdi, M., Katgerman, L., "Tensile mechanical behavior of as-cast AA7050 alloy in the super-solidus temperature range", In: *13th International Conference on Fracture (ICF-13)*, Beijing, China (2013), pp. 2528-36.
[14] Giraud, E., Suery, M., Coret, M., "Mechanical behavior of AA6061 aluminum in the semisolid state obtained by partial melting and partial solidification", *Metallurgical and Materials Transactions A* (2010), 41, pp. 2257-68.

[15] Ludwig, O., Commet, B., Drezet, J. M., Martin, C. L., Suery, M., "Rheological behavior of partially solidified Al-Cu alloys: Experimental and numerical study", In: *Modeling of Casting, Welding and Advanced Solidification Processes - X*, Destin, FL, USA (2003), pp. 183-90.
[16] Ludwig, O., Drezet, J. M., Martin, C. L., Suéry, M., "Rheological behavior of Al-Cu alloys during solidification: Constitutive modeling, experimental identification, and numerical study", *Metallurgical and Materials Transactions A* (2005), 36, pp. 1525-35.
[17] Ludwig, O., Martin, C. L., Suéry, M., "Deformation behaviour under various stress states of al-cu alloys during solidification", *Materials Forum* (2004), 28, pp. 357-62.
[18] Martin, C. L., Braccini, M., Suéry, M., "Rheological behavior of the mushy zone at small strains", *Materials Science and Engineering A* (2002), 325, pp. 292-301.
[19] Martin, C. L., Ludwig, O., Suéry, M. "Modelling of the rheological behaviour of metallic alloys during solidification", *Fifth World Congress on Computational Mechanics (WCCM V)*, Vienna, Austria (2002).
[20] Duva, J. M., Crow, P. D., "The densification of powders by power-law creep during hot isostatic pressing", *Acta Metallurgica Et Materialia* (1992), 40, pp. 31-5.
[21] Michel, J. C., Suquet, P., "The constitutive law of nonlinear viscous and porous materials", *Journal of the Mechanics and Physics of Solids* (1992), 40, pp. 783-812.
[22] Ludwig, O., [Ph.D. Thesis] (2005), Institut National Polytechnique de Grenoble.
[23] "ALSIM 6 reference manual. release 105", (2013).
[24] Ludwig, O., Drezet, J. M., Ménésès, P., Martin, C. L., Suéry, M., "Rheological behavior of a commercial AA5182 aluminum alloy during solidification", *Materials Science and Engineering A* (2005), 413-414, pp. 174-9.
[25] Eskin, D. G., Suyitno, Katgerman, L., "Mechanical properties in the semi-solid state and hot tearing of aluminium alloys", *Progress in Materials Science* (2004), 49, pp. 629-711.
[26] Subroto, T., Miroux, A., Mortensen, D., M'Hamdi, M., Eskin, D. G., Katgerman, L., "Semi-quantitative predictions of hot tearing and cold cracking in aluminum DC casting using numerical process simulator", *IOP Conference Series: Materials Science and Engineering* (2012), 33, pp. 012068.
[27] Suyitno, A., Eskin, D. G., Savran, V. I., Katgerman, L., "Effects of alloy composition and casting speed on structure formation and hot tearing during direct-chill casting of Al-Cu alloys", *Metallurgical and Materials Transactions A: Physical Metallurgy and Materials Science* (2004), 35 A, pp. 3551-61.
[28] Zhang, L., Eskin, D. G., Miroux, A., Subroto, T., Katgerman, L., "Influence of Melt Feeding Scheme and Casting Parameters During Direct-Chill Casting on Microstructure of an AA7050 Billet", *Metallurgical and Materials Transaction B* (2012), 43B, pp. 1565- 73.
[29] Suyitno, Eskin, D. G., Savran, V. I., Katgerman, L., "Effects of alloy composition and casting speed on structure formation and hot tearing during direct-chill casting of Al-Cu alloys", *Metallurgical and Materials Transactions A* (2004), 35A, pp. 3551-61.
[30] Ellingsen, K., M'Hamdi, M., Mortensen, D., Fjær, H. G., "Analysis of the impact of macrosegregation on hot tearing conditions during DC casting of aluminium alloys", *International Journal of Cast Metals Research* (2009), 22, pp. 90-3.

[31] Lalpoor, M., Eskin, D. G., ten Brink, G., Katgerman, L., "Microstructural features of intergranular brittle fracture and cold cracking in high strength aluminum alloys", *Materials Science and Engineering A* (2010), 527, pp. 1828-34.
[32] Boender, W., Burghardt, A., Van Klaveren, E. P., Rabenberg, J., "Numerical simulation of DC casting; interpreting the results of a thermo-mechanical model", In: *Light Metals, TMS*, Charlotte, NC, USA (2004), pp. 679-84.
[33] Hannart, B., Cialti, F., Van Schalkwijk, R., "Thermal Stresses in DC Casting of Aluminum Slabs: Application of a Finite Element Model", In: *Light Metals, TMS*, San Francisco, CA, USA (1994), pp. 879-87.
[34] Ludwig, O., Drezet, J. M., Commet, B., Heinrich, B., "Modelling of internal stresses in DC casting and sawing of high strength aluminum alloys slabs", In: *Modeling of Casting, Welding and Advanced Solidification Processes - XI*, Opio, France (2006), pp. 185-92.
[35] Drezet, J. M., M'Hamdi, M., Benum, S., Mortensen, D., Fjær, H., "Hot tearing during the start-up phase of DC cast extrusion billets", In: *Proceedings of the 8th International Conference ICAA8*, Cambridge, UK (2002), pp. 59-64.
[36] M'Hamdi, M., Benum, S., Mortensen, D., Fjær, H. G., Drezet, J. M., "The importance of viscoplastic strain rate in the formation of center cracks during the start-up phase of direct-chill cast aluminum extrusion ingots", *Metallurgical and Materials Transactions A* (2003), 34 A, pp. 1941-52.
[37] Eskin, D. G., "Physical Metallurgy of Direct Chill Casting of Aluminum Alloys (Advances in Metallic Alloys)", CRC Press, Taylor & Francis group, LLC (2008).
[38] Grandfield, J. F., Wang, L., "Application of mathematical models to optimization of cast start practice for DC cast extrusion billets", In: *Light Metals, TMS*, Charlotte, NC, USA (2004), pp. 685-90.
[39] Grandfield, J. F., Goodall, K., Misic, P., Zhang, X., "Water cooling in direct chill casting: Part 2, effect on billet heat flow and solidification", In: *TMS Annual Meeting*, Orlando, FL, USA (1997), pp. 1081-90.
[40] Lalpoor, M., Eskin, D. G., Katgerman, L., "Fracture behavior and mechanical properties of high strength aluminum alloys in the as-cast condition", *Materials Science and Engineering A* (2008), 497, pp. 186-94.
[41] Farup, I., Mo, A., "Two-phase modeling of mushy zone parameters associated with hot tearing", *Metallurgical and Materials Transactions A* (2000), 31, pp. 1461-72.
[42] Subroto, T. A. S., Miroux, A. G., Eskin, D. G., Katgerman, L., "Constitutive behaviour of an as-cast AA7050 alloy in the sub-solidus temperature range", *IOP Conference Series: Materials Science and Engineering* (2011), 27, pp. 012074.
[43] Van Haaften, W. M., Kool, W. H., Katgerman, L., "Tensile behaviour of semi-solid industrial aluminium alloys AA3104 and AA5182", *Materials Science and Engineering A* (2002), 336, pp. 1-6.
[44] Eskin, D. G., Katgerman, L., "A quest for a new hot tearing criterion", *Metallurgical and Materials Transactions A* (2007), 38 A, pp. 1511-9.
[45] Van Haaften, W. M., Kool, W. H., Katgerman, L., "Hot tearing studies in AA5182", *Journal of Materials Engineering and Performance* (2002), 11, pp. 537-43.

Chapter 3

TENSILE MECHANICAL PROPERTIES AND CONSTITUTIVE PARAMETERS AT SUB-SOLIDUS TEMPERATURE REGIME

3.1 Introduction

As an alloy cools down and fully solidifies, it passes through the sub-solidus temperature range – from the solidus point (465 °C for our AA7050) to approximately 50 – 60 °C below solidus. In this temperature regime, stress inside the billet starts to build up rapidly [1] and additionally the mechanical properties of the alloy, such as strength, ductility [2, 3] and Young's modulus [4, 5], change significantly.

From the solidification point of view, the sub-solidus regime can be seen as the transition from the semi-solid state, where the alloy is weak due to the liquid phases present at the grain boundaries [6], to the fully solid state, which is stronger compared to the semi-solid state. As described in Chapter 1, our main objective is to observe the possible connection between hot tearing or HT (cracking that occurs at the end of solidification when there is still liquid phase at the grain boundaries) and cold cracking or CC (cracking that occurs when the material is in the fully solid state and usually occurs when the material has cooled to a brittle state, e.g. below 300°C). From the previous work, it was reported that in the sub-solidus temperature regime the material is quite weak and has low ductility [3], thus it may facilitate (sub-critical) propagation of the earlier formed solidification defects (e.g. micro HT and pores), which could subsequently increase the susceptibility to cold-cracking. Therefore, it is important to understand the constitutive behavior in such a transition zone.

We mentioned in Chapter 1 that we would like to capture the connection between HT and CC using ALSIM. In order to perform good DC casting, it is necessary to understand the constitutive behavior of the alloy at different temperature ranges [7]. We already noted that the constitutive behavior of AA7050 in a lower-temperature, fully solid-state regime (from room temperature up to 400 °C) is readily available from previous research [8]. However, ALSIM is still lacking constitutive behavior data in the sub-solidus temperature regime (between 400 °C and 465 °C). This is a critical drawback especially if we would like to capture the connection between HT and CC using ALSIM. Although it is important to understand the constitutive behavior in the sub-solidus temperature regime, there is not much data available in the literature for as-cast AA7050 [9, 10] and the available data might give different mechanical properties compared to the as-cast condition. Therefore, a systematic study of constitutive behavior on an as-cast AA7050 in the sub-solidus temperature regime needs to be done.

As explained in the previous chapter, during DC casting, thermal stresses and strains are generated due to a relatively high temperature gradient between the center and the surface of the billet that has direct contact with water at room temperature. From this situation, we can suggest that the main failure mode in the center of the billet (where HT often takes place) is in the tensile direction. Therefore, in this chapter we discuss the result of

isothermal tensile tests in the sub-solidus temperature regime (between 400 and 465 °C) with different strain rates and observe the repeatability of the tests. Additionally, we perform fracture surface analysis using scanning electron microscope (SEM) on the tensile tested samples to reveal the failure mechanisms of the alloy in this temperature range. Moreover, we fit the tensile stress-strain curves to both constitutive equations that are used in ALSIM.

To summarize, the objective of this chapter is three-fold:

1. Obtain detailed knowledge of the mechanical behavior (such as the strength of material, ductility and constitutive parameters) in the sub-solidus temperature regime (between 400 and 465 °C).
2. Analyze the change in the failure mechanism of the tested samples as the alloy approaches the solidus temperature. This is to assess the possibility of crack arrest or sub-critical crack propagation of the formed HT in the sub-solidus regime.
3. Complete the constitutive parameters of ALSIM in the sub-solidus temperature regime. We do this by fitting the obtained constitutive data with the available constitutive equations in ALSIM and analyze the best constitutive equation available in ALSIM to represent the material behavior in the sub-solidus regime.

3.2 Experimental procedure

The constitutive behavior (tensile mechanical properties at different strain rates) of the alloy was obtained with a Gleeble 3800 thermo-mechanical simulator produced by Dynamic System Incorporated. The tensile test specimens were machined directly from the AA7050 billet in the as-cast condition (Figure 3.1). The specimens were heated by Joule-heating from room temperature up to 400 °C with a heating rate of 5 °C/s and then up to the test temperatures (see Table 3.1 for the test-condition matrix) with a heating rate of 1 °C/s [3]. The temperature of the specimens was measured and controlled by thermocouples spot-welded to the center of the specimens (Figure 3.2). The strain is measured using a diametrical dilatometer. Once the specimens reached the test temperature, they were kept at that temperature for 40 s to ensure a steady-state temperature distribution and then uniaxially deformed in tensile.

For each temperature point, we obtained tensile data from three different strain rates (refer to Table 3.1 for the test-condition matrix). These values were chosen to cover the strain-rate conditions that occur during DC-casting [11]. For each combination of temperature and strain rate, we repeated the test three times to obtain the statistical behavior of the alloy under the testing condition.

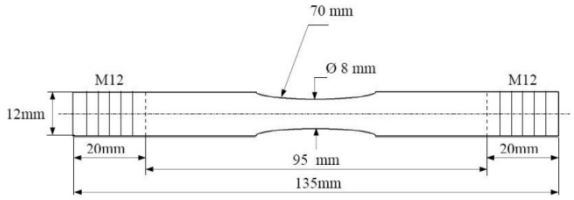

Figure 3.1 Tensile sample geometry [7, 8].

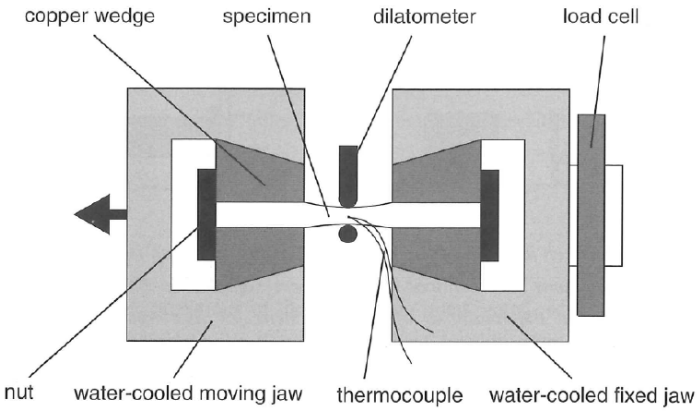

Figure 3.2 Schematic view of the experimental setup [7, 11].

Table 3.1 Tensile test matrix: Combination between temperature and strain-rates and the number of tests per combination of temperature and strain-rates.

Temperature (°C) / Strain-rate (s^{-1})	400	420	440	450	455	460	465
0.0005	3	3	3	3	3	3	3
0.005	3	3	3	3	3	3	3
0.05	3	3	3	3	3	3	3

To analyze the fracture surface, the tested samples were directly taken to the microscopy facility. A Jeol JSM-6500F scanning electron microscope (SEM) was employed to observe the microstructure of the tested samples.

3.3 Results

3.3.1 Tensile mechanical behavior

Figure 3.3 shows the true stress and true strain curve tested with a strain rate of 0.05 s^{-1} at different test temperatures. This figure shows that the strength of the alloy decreases as temperature increases. Moreover, the alloy becomes less ductile as the temperature increases. From the shape of the curves, in general, both hardening and flow stress behavior is observed. The curves reach a peak value and then decrease to a steady-state stress value where the alloy subsequently fails (shown by the steep drop in strength). From this figure, we can also see that the length of the steady-state regime also decreases as temperature increases.

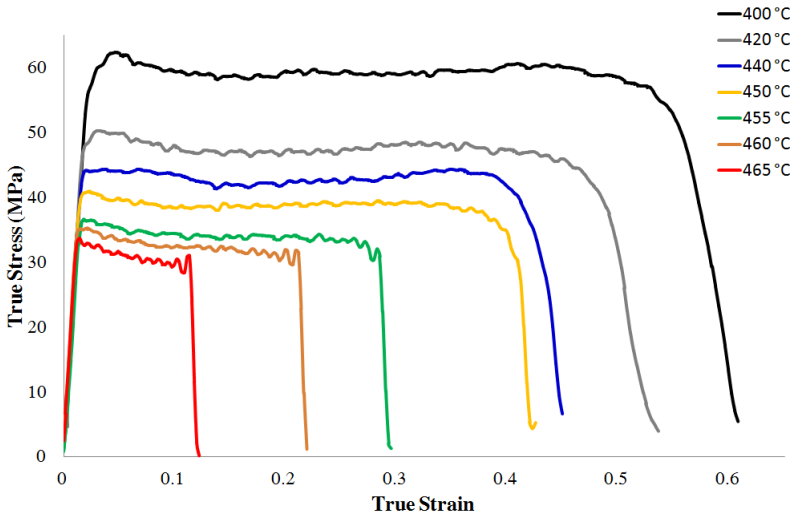

Figure 3.3 Stress–strain curves at different temperatures from 400 to 465 °C, tensile strain at a strain rate of 0.05 s^{-1}.

Figure 3.4 shows an example of stress and strain curves obtained at 400 °C at three different strain rates. The three repeated tests at the same strain rate show that the test results are reproducible. As the alloy has reached a steady-state condition, it is in a relatively ductile state, which can be clearly distinguished from the brittle behavior reported below 200 °C [8].

In order to use the obtained data like the stress and strain curves shown in Figure 3.3 and Figure 3.4, for constitutive equation fitting that will be used for the ALSIM database, we need to have a quantification value for the strength of the alloy at each test condition (combination of temperature and strain rate). In the current investigation, we use the steady-state flow stress (SSFS) as the measure for the strength of the alloy. A SSFS value is

obtained as the stress average in the deformation range where the stress of the alloy reaches the steady-state after it has passed its peak stress. The SSFS of the three repeated tests for each combination of temperature and strain rate are averaged to obtain a SSFS value for each combination. An example of the SSFS value for the alloy deformed with a strain rate of 0.005 s^{-1} is shown by the thick dashed grey line in Figure 3.4.

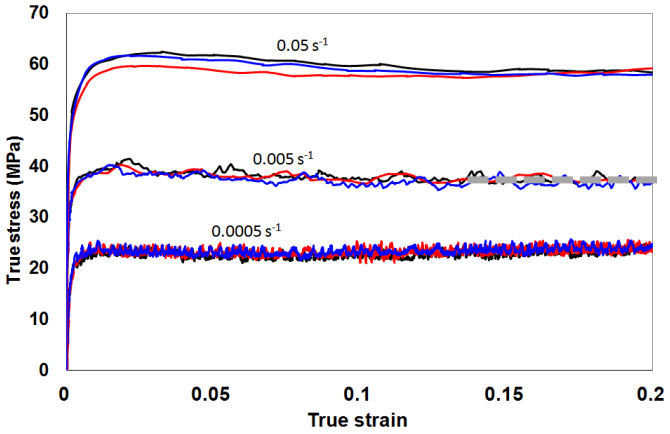

Figure 3.4 Stress–strain curve at a temperature of 400 °C, strained at different strain rates. An example of steady-state flow stress is shown in thick dashed grey line at a strain rate of 0.005 s^{-1}.

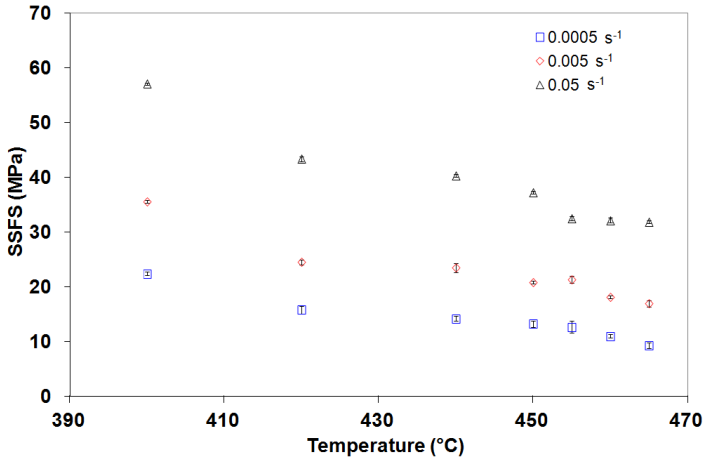

Figure 3.5 The dependency of the steady-state flow stress (SSFS) on testing temperature and strain rate.

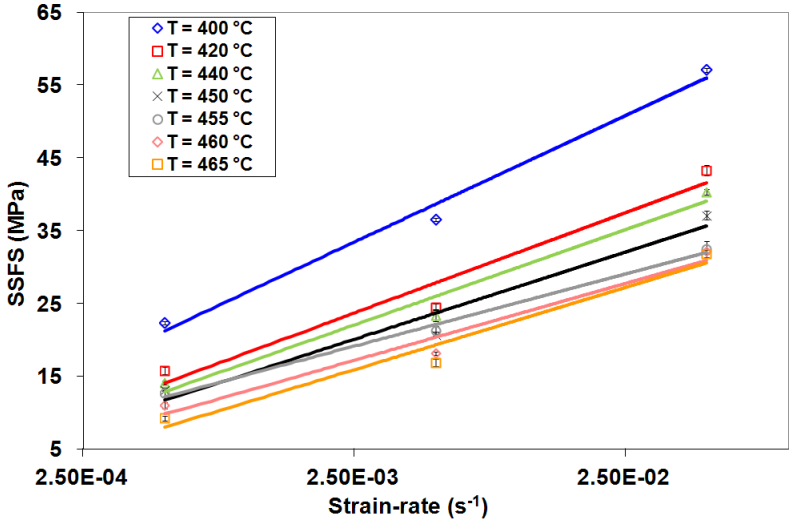

Figure 3.6 Trend of strain-rate sensitivity with respect to different test temperatures.

Figure 3.5 confirms that indeed the SSFS decreases as the temperature increases. From this plot, it is shown that all data obtained from the three different strain rates follow the same trend. This figure shows the most significant SSFS drop is between 400 °C and 420 °C, which is rather unexpected since it is still relatively far from the solidus point. Then, from 420 °C to the solidus point (465 °C), the change is more gradual.

Figure 3.6 shows that in this temperature regime the SSFS increases with the strain rate. Moreover, as the temperature increases the alloy becomes less strain-rate sensitive, as indicated by the decrease of the slope in Figure 3.6. Error bars are shown in both Figure 3.5 and Figure 3.6, but they are smaller than the marker used to plot the data points.

Despite our statement that the alloy is still noticeably ductile due to the possibility of SSFS value measurements, we observed that the ductility of the alloy decreases as the temperature increases. In general, the fracture strain (Figure 3.7), defined at the start of the steep drop in stress after the steady-state stress regime on the stress-strain curve, decreases as the temperature and the strain rate increase. This also can be interpreted as the alloy becoming less ductile at higher temperatures and strain rates. The trends for fracture strain changes above 450 °C; the decrease in ductility is steeper above 450 °C as compared to lower temperatures.

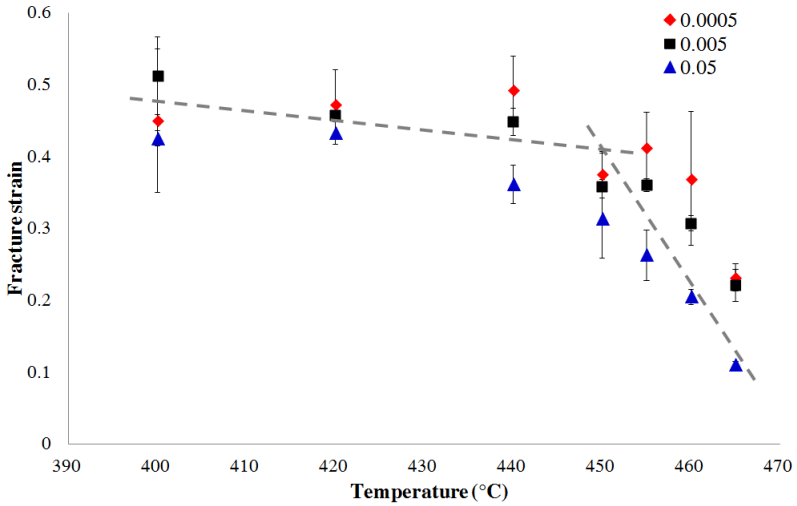

Figure 3.7 Fracture strain at different temperatures and strain rates. The dashed grey lines show the trend in fracture strain with respect to temperature and its change at approx. T = 450 °C.

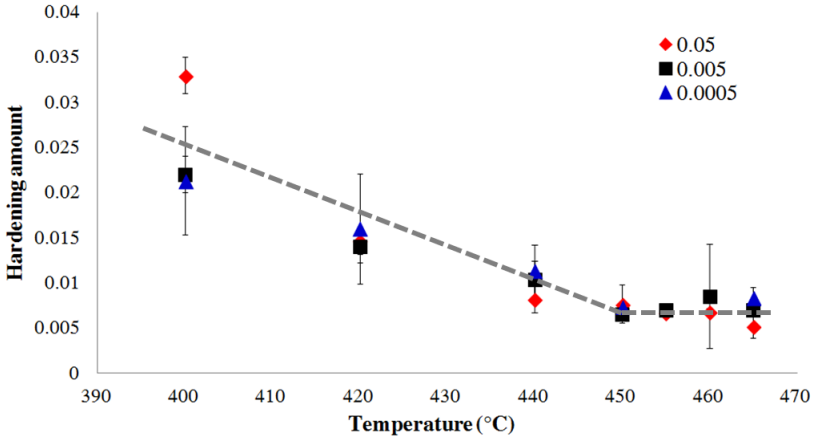

Figure 3.8 Amount of hardening (from the proportionality limit up to the peak stress) in strain units at different temperatures and strain rates. The grey dashed line shows the trend discontinuity in hardening at around 450 °C.

Figure 3.8 shows the amount of hardening with respect to different temperatures and strain rates. The amount of hardening is defined as the amount of strain from the end of the proportionality limit up to the maximum stress on the stress–strain curve. This figure shows that hardening decreases as the temperature increases, and it reaches a saturation strain value of approximately 0.0075 starting from 450 °C.

3.3.2 Fracture surface analysis of tested samples

Figure 3.9 shows the fracture surfaces after tensile testing at 400 °C at different strain rates and magnifications. At 400 °C and the lowest strain rate – 0.0005 s^{-1} (Figure 3.9a and Figure 3.9b), in general the failure mode is mixed between intergranular and ductile transgranular. However, from this picture, we see that the dominant fracture mode is ductile transgranular. This is shown by the sharp features at the separation sites (last connection point before failure occurs) and dimples. Moreover, such features are also observed at the highest strain rate – 0.05 s^{-1} (Figure 3.9c and Figure 3.9d), so we did not see many feature differences between these two strain rates. At higher magnification, however, at lower strain rates (Figure 3.9b), we see broken eutectic phases with fine striation lines (red arrows in Figure 3.9b). While at the highest strain rate, there are no striation marks observed, but dimples (hole-like features) are the dominant features along with steps-like features.

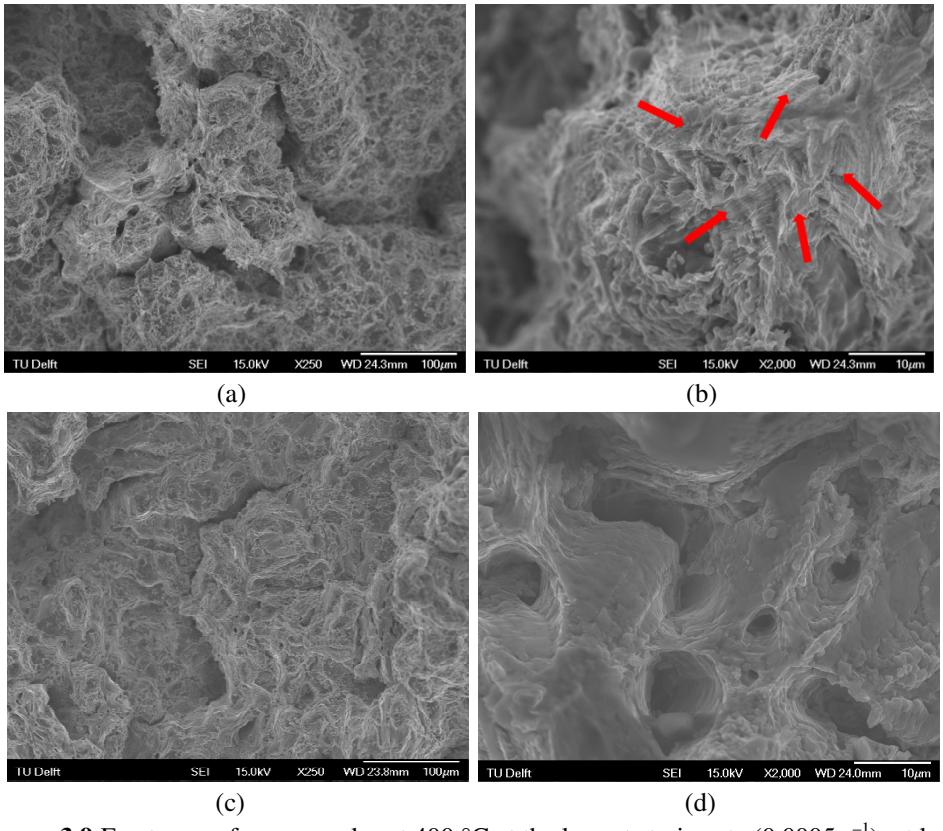

Figure 3.9 Fracture surface examples at 400 °C at the lowest strain-rate (0.0005 s^{-1}); at low magnification (a) and high magnification (b) and the highest strain-rate (0.05 s^{-1}); at low magnification (c) and high magnification (d).

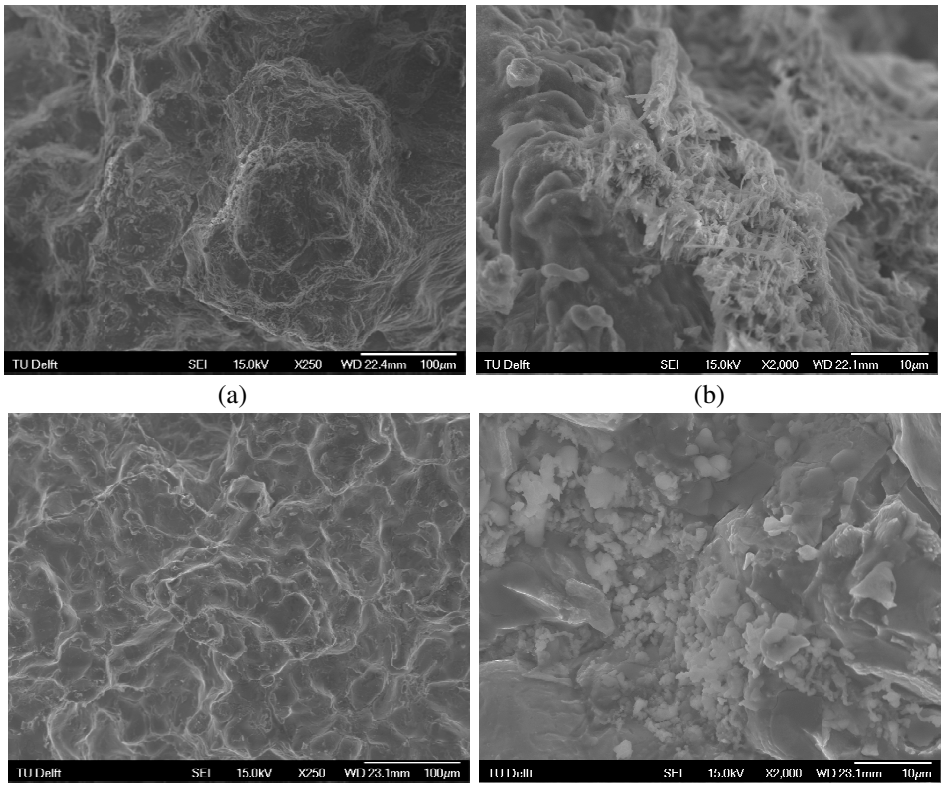

Figure 3.10 Fracture surface examples at 465 °C at the lowest strain rate (0.0005 s^{-1}); at low magnification (a) and high magnification (b) and at the highest strain rate (0.05 s^{-1}); at low magnification (c) and high magnification (d).

Figure 3.10 shows the fracture surfaces after tensile testing at 465 °C for different strain rates and magnifications. From these pictures, we observe that the main fracture mode is intergranular ductile, irrespective of strain rates. The most significant difference between these two strain rates at this temperature is the morphology of the eutectics (brighter phases) in Figure 3.10b and Figure 3.10d. Figure 3.10b shows that the lowest strain rate produces elongated eutectics phases (whiskers) while the higher strain rate produces more globular or rounded eutectic phases (Figure 3.10d).

From Figure 3.11a, we observe that at 440 °C, although the intergranular fracture mode starts to be visible, there are still some ductile transgranular sites (some sharp edges observed at the separation points – red ellipses in Figure 3.11). However, at 455 °C, the fracture mode becomes predominantly intergranular (Figure 3.11b). This signifies the change in the dominant fracture mode happens between these two temperature points.

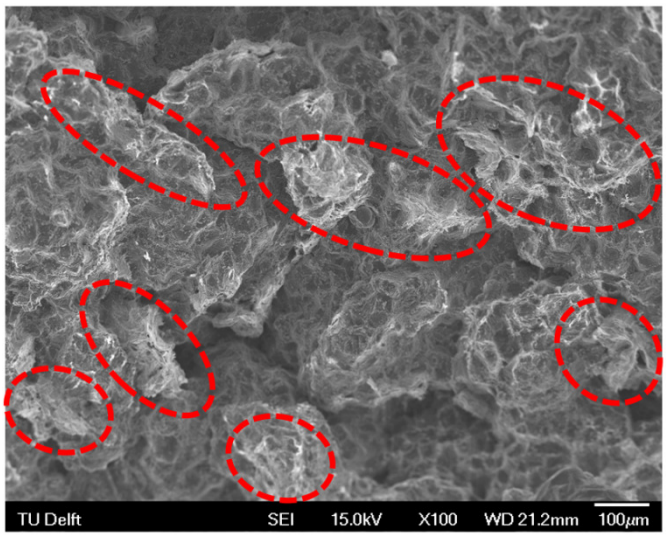

(a)

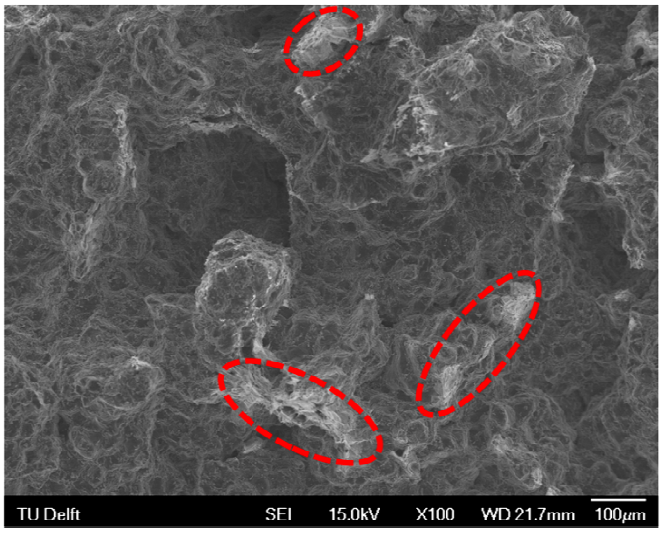

(b)

Figure 3.11 SEM fracture surface of tensile tested samples at a strain rate of 0.0005 s^{-1}, at temperatures of 440 °C (a) and 455 °C (b). The area within red ellipses shows the ductile transgranular fracture features.

3.3.3 Constitutive parameters

3.3.3.1 Fitting of extended Ludwik parameters

The results of constitutive behavior (true stress – true strain curves at different temperatures and strain rates) that we showed in Section 3.3.1 can be fit with the extended Ludwik equation (Eq. 2.17). The equation parameters were extracted through an in-house built MATLAB routine.

Figure 3.8 shows that there is still some amount of hardening from 400 °C to 450 °C. Therefore, in this range we can fit the hardening regime (from the proportionality limit up to the maximum stress at the end of hardening) using the extended Ludwik equation. The result of the fitting in this temperature range is shown in Table 3.2 while the fitting value from its lower temperature counterpart is shown in Table 3.3 [12, 13].

Table 3.2 Constitutive parameters from extended Ludwik fitting (from Eq. 2.17) obtained in this study.

Temperature (°C)	r	m	K
400	0.12 ± 0.02	0.16 ± 0.06	146 ± 51
420	0.12 ± 0.04	0.17 ± 0.10	120 ± 70
440	0.10 ± 0.04	0.14 ± 0.06	88 ± 31
450	0.10 ± 0.03	0.15 ± 0.08	84 ± 36

Table 3.3 Constitutive parameters obtained of AA7050 from extended Ludwik fitting at lower temperature regime [12, 13].

Temperature (°C)	r	m	K
20	0.42 ± 0.02	-0.2 ± 0.02	774 ± 32
100	0.38 ± 0.01	-0.16 ± 0.03	626 ± 13
200	0.21 ± 0.006	-0.03 ± 0.005	392 ± 11
300	0.11 ± 0.007	0.03 ± 0.007	199 ± 4.5
400	0.09 ± 0.01	0.15 ± 0.009	174 ± 5

From the value shown in Table 3.2, we can see that both the hardening (r) and strain-rate sensitivity parameter (m) do not vary much as the temperature increases and the values are comparable with the data from the highest temperature of the lower temperature database (Table 3.3). However, the consistency of the alloy (K) decreases as temperature increases, which follows the trend of the data from the lower temperature regime. This show the constitutive parameters that we obtained in the sub-solidus temperature regime are relatively continuous with its lower temperature counterpart [12, 13].

3.3.3.2 ALSIM sub-solidus constitutive parameters

From Figure 3.8 and the result from Section 3.3.3.1, we can see that between 400 and 450 °C the amount of hardening is significantly small compared to that in the lower temperature

regime (below T = 400 °C) [1], while the flow-stress behavior is dominant. Therefore, for the ALSIM database, we fit the data for the entire sub-solidus regime (400 – 465 °C) using the creep-law equation (Eq. 2.16) to simplify the condition. From the fitting of SSFS versus temperature, we obtained the creep-law parameters as follows: σ_0 = 0.01 MPa, $\dot{\varepsilon}_0$ = 3.22 · 10^{-4} s^{-1}, Q = 185 kJ/mol and n = 4.39. This constitutive database of sub-solidus regime from our AA7050 results can be used to replace the database of Al-2% Cu [14] in the sub-solidus regime (400 – 465 °C) which was previously used in the simulations shown on Chapter 2.

Table 3.4 shows the comparison of the apparent activation energy (Q) and the stress exponent (n) of different alloys. From this table, we can see that our AA7050 has relatively high activation energy and it has the highest stress exponent compared to other types of alloys.

Table 3.4 Comparison on activation energy (Q) and the stress exponent (n) of the creep law constitutive parameters from AA7050 with other pre-existing alloy data.

Alloy → Parameters	AA7050	Al-2% Cu [14]	AA5182 [15, 16] AC*	AA5182 [11] HG**	AA1050 [15]	AA3004 [15]
Q (kJ/mol)	185	154	125	174	157	194
n	4.39	3.8	3.44	1.35	3.84	3.6

*AC = as-cast; **HG = homogenized

3.4 Discussion

The small scatter of the SSFS measurement represents good repeatability of the tests, thus providing us with confidence in the representation data for the constitutive parameter extraction. From the strain-rate sensitivity point of view, other works reported that for similar alloys – 7XXX-series [9, 10] and for other aluminum alloys [2, 15, 17, 18] – as the alloy approaches solidus point, the strain-rate sensitivity of the alloys is positive. Additionally, the result in our study is also supported by the strain-rate sensitivity trend from previous research on the AA7050 in the lower temperature regime [12].

In general, from Figure 3.3 the shape of stress–strain curves in this temperature regime corresponds with the ductile behavior, which is quite common at high temperatures [9, 10, 18]. However, we observed that in the sub-solidus regime, the ductility decreases as the temperature increases (Figure 3.7), which is counter-intuitive but this phenomenon is also observed in other works [2, 12]. It can be suggested that such a phenomenon occurs because as temperature increases and approaches the solidus point, the material becomes weaker thus promotes the coalescence process of the formed voids and may eventually lead to failure.

From Figure 3.7, we observe that in sub-solidus regime there are two different trends of ductility and a change in the ductility versus temperature slope around 450 °C (T_{switch}) – a shallower ductility slope below this temperature and a steeper ductility slope above this point. This condition might be explained by a change in failure mechanisms at this temperature. Below this temperature, the alloy fails mostly in a ductile transgranular manner (Figure 3.9). Just below T_{switch} (at T = 440 °C), from the fractograph in Figure 3.11a, although ductile intergranular fracture already starts, ductile transgranular fracture still exists. Just above T_{switch}, (at T = 455 °C) the alloy mostly fails in a ductile intergranular manner; although some minor patches of ductile transgranular failure are still present (Figure 3.11b). As the temperature increases to approximately 465°C, the failure mostly occurs through the intergranular ductile mechanism. This is because as the alloy approaches solidus, the weakest point is represented by the intermetallic phases between the grain boundaries (eutectic phases), thus the deformation mostly occurs there. Moreover, from Figure 3.8, we can also see that the hardening diminished as it approaches T_{switch}. This is supported by the shape of stress and strain curves in Figure 3.3. Above T_{switch} there is hardly any hardening visible. This suggests that there is an intrinsic change in the mechanical behavior of the alloy in terms of response to tensile deformation at around T_{switch}. One possible explanation of the drop in ductility above T_{switch} is due to the weak bond strength between the eutectic phases and the aluminum matrix which is reported in another work on an as-cast aluminum alloy in the vicinity of the solidus point [19]. This may also explain the reason that the main fracture mode above T_{switch} is changed to intergranular instead of transgranular. Another possible explanation of this ductility drop is because of the contribution of the local pre-melting of the eutectic phases at the grain boundaries [20]. However, this occurrence is rather unlikely because the T_{switch} is approximately 15 °C below the solidus point of AA7050. As a note, the relationship between diminishing of strain-hardening coefficient and the start of the sharp drop in ductility at T_{switch} is still not clear.

In addition to the points above, we observed that at solidus, the morphology of the eutectic phase after fracture is also strain-rate dependent. When we tested the samples with the lowest strain rate (0.0005 s^{-1}, Figure 3.10b), we see that the eutectic phase exhibits a whisker-like morphology, which is also observed by other research at low strain-rate tensile testing [21]. It is suggested that this feature is a micro-superplasticity phenomenon. At the highest strain rate (0.05 s^{-1}, Figure 3.10d), the eutectics have a droplet shape. This may suggests that at this strain rate, when the deformation took place in the grain boundaries, the eutectic did not have sufficient time to elongate and compensate for the deformation.

We only obtained the constitutive parameters using the extended Ludwik equation up to 450 °C because, even though from Figure 3.8 there is some hardening available in the sub-solidus regime, above 440 °C the amount saturates at a relatively insignificant value. In

Figure 3.3, no hardening is actually visible in the stress–strain curve above 440 °C. The reason that the hardening coefficient (r) saturates instead of decreasing to zero is because beyond this temperature (440 °C) the hardening regime is very short, thus the number of data points to be fit is reaching the limit of the measurement resolution, and therefore it always produces very low but non-zero value.

From the creep-law parameters obtained in section 3.3.3.2, our AA7050 produces relatively high values for both the apparent activation energy (Q) and the stress exponent (n) in comparison to the other aluminum alloys showed in Table 3.4. However, the Q value of our alloy (185 kJ/mol) is within the value range of other 7XXX-series alloy. For example, an extruded AA7075 produces value around 131 kJ/mol [18], another work reports that aged AA7075 and AA7150 have values between 155 and 162 kJ/mol [22] and a solution treated AA7012 shows 200–230 kJ/mol [23], while an as-cast AA7020 is reported to have 173.8 kJ/mol [24]. When compared to other AA7050 with different processing routes, our alloy has a lower Q compared to the as-rolled AA7050 that produces 256.6 kJ/mol [9]. Meanwhile, our alloy has a higher Q compared to the homogenized AA7050, which have values between 160 and 170 kJ/mol for different homogenization routes [25, 26]. As for the stress exponent (n), when compared to other 7XXX alloys, results on AA7075 give a stress exponent of 6.7 [18], while an as-cast AA7020 produces a value of 5.63 [24]. These results show that the 7XXX-family alloys demonstrate relatively high stress exponents compared to other aluminum alloy series shown in Table 3.4. From the result above, we suggest that the values of both Q and n are sensitive not only to the change of alloying element amounts but also to the different processing route histories [11, 25].

Due to the low-ductility and low-strength regime between $T_{solidus}$ and T_{switch}, this regime might become a preferential regime for an existing defect such as a micro HT or pore to sub-critically propagate, especially since in this temperature range the thermal stress on the billet rapidly increases [1, 13]. This condition may promote the propagation of pre-existing solidification defects. However, as the temperature decreases below T_{switch}, there is a significant increase in ductility as the alloy cools down before it eventually becomes brittle below 200 °C [8]. The ductile phase between T_{switch} and 200 °C may stabilize the crack growth, thus hindering and possibly arresting further crack propagation before it becomes a trigger for a catastrophic CC. From these findings, we may suggest that the wider temperature range between $T_{solidus}$ and T_{switch}, is more likely to be the range where sub-critical crack propagation occurs, hence increasing the CC susceptibility of the alloy during DC casting.

3.5 Conclusions

In this chapter, we presented a study on the tensile mechanical behavior of an AA7050 in the sub-solidus temperature range (between 400 °C up to the solidus 465 °C). From the results of this study, we obtained a detailed understanding of the tensile mechanical properties, such as the strength of the alloy (via SSFS value), strain-rate sensitivity and ductility, as well as the failure mechanism of the alloy in this temperature regime. Additionally, we obtained the constitutive parameters of the alloy using both available constitutive equations of the ALSIM model. From the results obtained in this chapter, we draw the following conclusions:

1. The SSFS value and strength of the alloy, in general, decrease as the temperature increases. This trend supports the results from previous works on an AA7050 alloy performed at lower temperatures [8, 12].
2. In the sub-solidus temperature range (between 400 °C and 465 °C), the SSFS increases with the strain rate. This supports the earlier result that at a sufficiently high temperature (relatively near the solidus point), the alloy exhibits positive strain-rate sensitivity (strength increase with the strain rate) [12].
3. The ductility of the alloy in this temperature regime decreases as the temperature increases; this phenomenon is also observed on other works [2, 12]. This may be due to the fact that as the alloy approaches solidus, it becomes weaker, thus favors the coalescence process of the formed voids and eventually leads to failure.
4. There is a change in the ductility slope at approximately T_{switch}, which also reveals the preferential modes of failure below and above this temperature. Below T_{switch}, the alloy fails mostly in the ductile transgranular mode while above T_{switch}, the alloy fails mostly in the ductile intergranular mode.
5. The constitutive parameters that we fit using extended Ludwik equation in the temperature regime where some hardening is available (from 400 °C up to 450 °C) is obtained and the value is continuous with the result of AA7050 at lower temperature range (between room temperature and 400 °C) [12].
6. As the flow stress behavior is dominant and hardening is insignificant in this temperature regime, we obtained ALSIM database through fitting of creep law parameters. The values of obtained parameters (Q and n) are relatively comparable with other 7XXX-series alloys.
7. The low strength and low ductility regime accompanied by the rapid increase in thermal stress [1, 13] between T_{switch} and $T_{solidus}$ may become a preferential regime for a sub-critical propagation of the pre-existing solidification defects (e.g. micro HT and pores). Thus, we may suggest that the width of this temperature range also influences the CC susceptibility.

References

[1] Lalpoor, M., Eskin, D. G., and Katgerman, L., "Cold-cracking assessment in AA7050 billets during direct-chill casting by thermomechanical simulation of residual thermal stresses and application of fracture mechanics", *Metallurgical and Materials Transactions A* (2009), 40A, pp. 3304-13.
[2] Colley, L. J., Wells, M. A., Maijer, D. M., "Tensile properties of as-cast aluminum alloy AA5182 close to the solidus temperature", *Materials Science and Engineering A* (2004), 386, pp. 140-8.
[3] Subroto, T. A. S., Miroux, A. G., Eskin, D. G., Katgerman, L., "Constitutive behaviour of an as-cast AA7050 alloy in the sub-solidus temperature range", *IOP Conference Series: Materials Science and Engineering* (2011), 27, pp. 012074.
[4] Nagaumi, H., "Prediction of internal crack in high strength Al-Mg-Si alloy" In: Proceedings of The 8th International Conference on Aluminium Alloys (ICAA8), Gregson, P. J., Harris, S. (Eds.), Cambridge, UK, (2002), pp. 71-6.
[5] Nagaumi, H., Umeda, T., "Prediction of internal cracking in a direct-chill cast, high strength, Al-Mg-Si alloy", *Journal of Light Metals* (2002), 2, pp. 161-7.
[6] Subroto, T., Miroux, A., Eskin, D. G., Ellingsen, K., Marson, A., M'Hamdi, M., Katgerman, L., "Tensile mechanical behavior of as-cast AA7050 alloy in the super-solidus temperature range", In: *13th International Conference on Fracture (ICF-13)*, Beijing, China (2013), pp. 2528-36.
[7] Lalpoor, M., "Study of cold cracking during DC-casting of high strength aluminum alloys", [Ph.D. Thesis] (2010), Delft University of Technology.
[8] Lalpoor, M., Eskin, D. G., Katgerman, L., "Fracture behavior and mechanical properties of high strength aluminum alloys in the as-cast condition", *Materials Science and Engineering A* (2008), 497, pp. 186-94.
[9] Hu, H. E., Zhen, L., Yang, L., Shao, W. Z., Zhang, B. Y., "Deformation behavior and microstructure evolution of 7050 aluminum alloy during high temperature deformation", *Materials Science and Engineering A* (2008), 488, pp. 64-71.
[10] Jin, J. S., Wang, X. Y., Hu, H. E., Xia, J. C., "High-temperature deformation behavior and processing map of 7050 aluminum alloy", *Metals and Materials International* (2012), 18, pp. 69-75.
[11] Van Haaften, W. M., "Constitutive behavior of aluminum alloys", [Ph.D. Thesis] (2002), Delft University of Technology.
[12] Lalpoor, M., Eskin, D. G., Katgerman, L., "Constitutive parameters, mechanical properties and failure mechanism in DC-cast AA7050 billets", In: *12th International Conference on Fracture (ICF-12)*, Ottawa, ON, Canada (2009), pp. 407-15.
[13] Lalpoor, M., Eskin, D. G., Katgerman, L., "Cold cracking development in AA7050 direct chill-cast billets under various casting conditions", *Metallurgical and Materials Transactions A* (2010), 41A, pp. 2425-34.
[14] Ludwig, O., Drezet, J. M., Martin, C. L., Suéry, M., "Rheological behavior of Al-Cu alloys during solidification: Constitutive modeling, experimental identification, and numerical study", *Metallurgical and Materials Transactions A* (2005), 36, pp. 1525-35.

[15] Van Haaften, W. M., Magnin, B., Kool, W. H., Katgerman, L., "Constitutive behavior of as-cast AA1050, AA3104, and AA5182", *Metallurgical and Materials Transactions A* (2002), 33, pp. 1971-80.
[16] Ludwig, O., Drezet, J. M., Ménésès, P., Martin, C. L., Suéry, M., "Rheological behavior of a commercial AA5182 aluminum alloy during solidification", *Materials Science and Engineering A* (2005), 413-414, pp. 174-9.
[17] Alankar, A., Wells, M. A., "Constitutive behavior of as-cast aluminum alloys AA3104, AA5182 and AA6111 at below solidus temperatures", *Materials Science and Engineering A* (2010), 527, pp. 7812-20.
[18] Jenab, A., Karimi Taheri, A., "Evaluation of low strain rate constitutive equation of 7075 aluminium alloy at high temperature", *Materials Science and Technology* (2011), 27, pp. 1067-72.
[19] Couto, K. B. S., Claves, S. R., Van Geertruyden, W. H., Misiolek, W. Z., Goncalves, M., "Effects of homogenisation treatment on microstructure and hot ductility of aluminium alloy 6063", *Materials Science and Technology (Short communication)* (2005), 21, pp. 263-8.
[20] Chattopadhyay, K., Goswami, R., "Melting and superheating of metals and alloys", *Progress in Materials Science* (1997), 42, pp. 287-300.
[21] Giraud, E., Suery, M., Coret, M., "Mechanical behavior of AA6061 aluminum in the semisolid state obtained by partial melting and partial solidification", *Metallurgical and Materials Transactions A* (2010), 41, pp. 2257-68.
[22] Sheppard, T., Jackson, A., "Constitutive equations for use in prediction of flow stress during extrusion of aluminium alloys", *Materials Science and Technology* (1997), 13, pp. 203-9.
[23] Cerri, E., Evangelista, E., Forcellese, A., McQueen, H. J., "Comparative hot workability of 7012 and 7075 alloys after different pretreatments", *Materials Science and Engineering A* (1995), 197, pp. 181-98.
[24] Liu, Q. J., Fang, G., "Analysis of constitutive behaviours and processing map of 7020 aluminium alloy", *Materials Science and Technology* (2010), 26, pp. 1088-94.
[25] Deng, Y., Yin, Z., Huang, J., "Hot deformation behavior and microstructural evolution of homogenized 7050 aluminum alloy during compression at elevated temperature", *Materials Science and Engineering A* (2011), 528, pp. 1780-6.
[26] Liu, S., You, J., Zhang, X., Deng, Y., Yuan, Y., "Influence of cooling rate after homogenization on the flow behavior of aluminum alloy 7050 under hot compression", *Materials Science and Engineering A* (2010), 527, pp. 1200-5.

Chapter 4

TENSILE MECHANICAL PROPERTIES AND CONSTITUTIVE PARAMETERS AT SUPER-SOLIDUS TEMPERATURE REGIME

4.1 Introduction

In order to minimize the occurrence of hot tearing (HT), it is critical to understand the mechanical properties of the alloy in the solidification regime below the rigidity temperature [1]. The constitutive response of the semi-solid phase to the tensile stresses is critical in controlling many solidification defects such as HT and porosity, see e.g. [2]. This is because tensile stress is the dominant stress mode related to HT during DC casting.

In this chapter, we investigate the tensile mechanical behavior of the alloy starting from the rigidity temperature until the alloy is fully solid. For an AA7050, from a solidification contraction experiment, it is known that thermal stress starts to be appreciable at 559 °C [3] or based on JMat-Pro® calculations, this temperature corresponds approximately to a solid fraction of 0.85. Therefore, a series of tensile experiments is carried out from this solid fraction until the alloy is fully solid (super-solidus temperature regime) where HT is most likely to occur [4-6].

From the tensile constitutive behavior of the alloy, we quantified the mechanical behavior of the alloy in the super-solidus regime such as strength and ductility at different solid fractions. We also tested the alloy with two different pulling speeds to study the strain-rate sensitivity of the alloy. After the tests were done, we also observed the failure mechanism of the tested samples through fracture surface analysis using a scanning electron microscope (SEM) at different solid fractions. It was reported that in the semi-solid regime there are different mechanical regimes (i.e. brittle and ductile) [6, 7], therefore, it is also interesting to observe this phenomenon in our AA7050.

Additionally, we know from Chapters 1 and 2 that ALSIM is also lacking a constitutive behavior database in the semi-solid regime for the AA7050. In this chapter, we also extract the semi-solid constitutive parameters based on the ALSIM semi-solid constitutive model described in Chapter 2 using the result of the semi-solid tensile tests.

The constitutive parameters were selected by comparing the tensile force-displacement curves obtained from the experimental tensile tests with the result from numerical thermo-mechanical tensile tests that are built using ALSIM. Using this method, we select the constitutive parameters that provide us with a good fit of the force value between numerical and experimental tensile tests in the semi-solid temperature range. From these results, we find that it is feasible to obtain reasonable constitutive parameters by utilizing a simple numerical thermo-mechanical model.

Additionally, by obtaining these constitutive parameters, we are not only completing the semi-solid mechanical database of AA7050 but also get detailed insight of the semi-solid behavior with respect to HT susceptibility of the alloy.

4.2 Experiment and constitutive parameters extraction procedure

4.2.1 Mechanical testing procedure

The specimens were tested using a set-up developed at SINTEF Materials and Chemistry with an Instron 5944 series tensile test machine equipped with a 2-kN load cell. The specimen was heated up using an induction heating coil system. The temperature in the center of the specimen was controlled by a Eurotherm™ temperature controller. The schematic of the tensile test setup is shown in Figure 4.1 and the geometry of the tensile specimen is shown in Figure 4.2. The notch near the end of the specimen is designed to reduce the heat flow out of the specimen by the water-cooled surface, thus flattening the temperature gradient across the specimen.

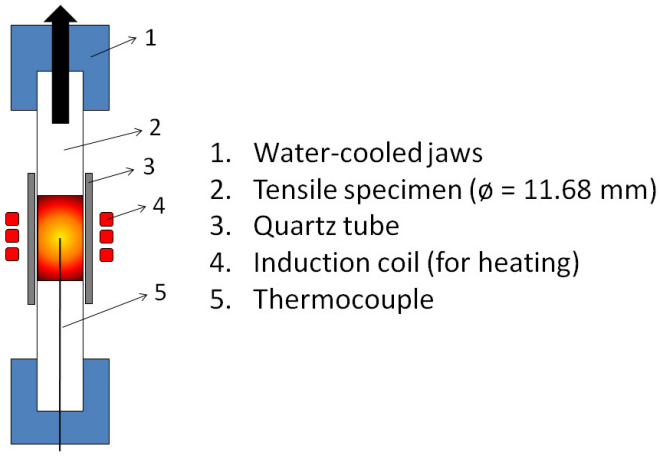

Figure 4.1 Tensile test setup schematics.

A quartz-glass tube coated with boron nitride aerosol on the inside was used to enclose the center part of the sample in order to avoid liquid breakout during the full melt phase. The coating was intended to prevent the sticking of the liquid aluminum onto the quartz tube which might affect the force measurement due to the added friction resistance. The experimental cycle (for both re-melt and mechanical testing temperature) is shown in Figure 4.3.

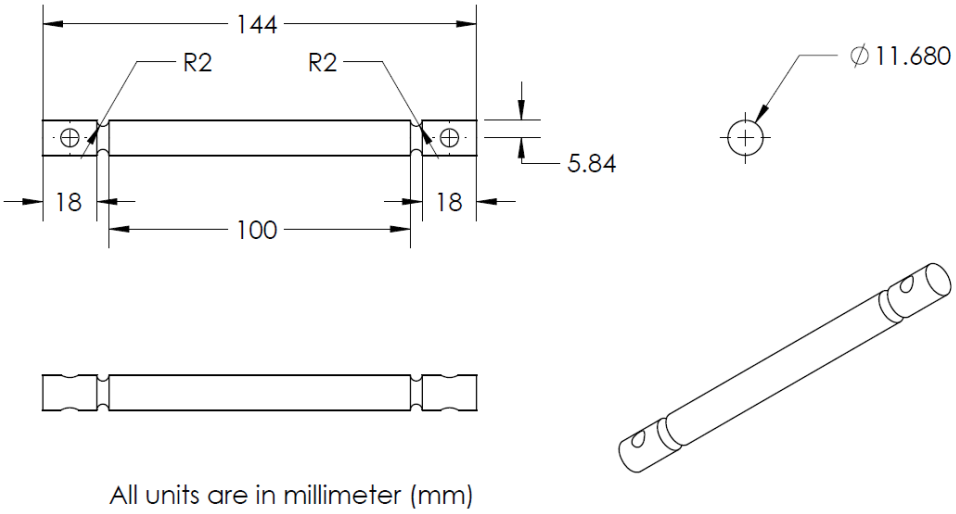

Figure 4.2 Tensile test sample geometry.

First, we heated the sample from room temperature up to T_{max} = 635 °C, which is just above the liquidus of our AA7050 alloy based on the calculation of JMat-Pro® software (Figure 1.2). Then we held the sample at T_{max} for 60 s to assure that the central mid-length part of the specimen was fully liquid. Subsequently, we cooled down the sample to the test temperature with a cooling rate of 1 °C/s. We then held the sample at this test temperature for approximately 90 s to let the temperature in the specimen stabilize. Then, we performed the mechanical tensile testing of the sample at a certain displacement rate until the force value was approximately zero after the fracture.

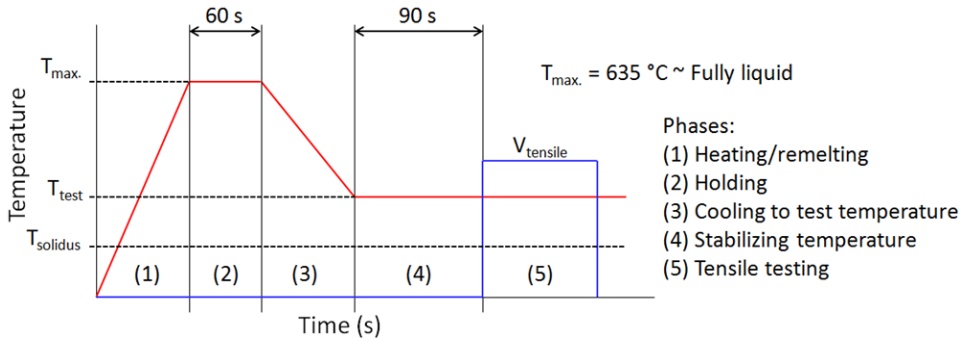

Figure 4.3 Isothermal tensile test cycle; thermal (red line) and mechanical (blue line).

The reason we opted for a re-melt experiment (imitating real solidification) instead of a re-heating experiment (going directly from room temperature to the tensile test temperature) is because the morphology of the liquid distribution is different using these two routes even though the tensile test takes place at the similar solid fraction. This leads to different observed mechanical strengths [7, 8].

We also performed the tests with two different pulling speeds (or displacement rates), slow and fast (see Table 4.1). The lowest chosen speed was 0.2 mm/min because below this displacement-rate, the liquid parts of the alloy start to stick to the quartz tube and may increase the friction force and increase the possibility of measurement error. To study the displacement-rate sensitivity of the alloy in this temperature regime, we thus chose the other pulling speed with an order of magnitude higher (2 mm/min).

As hinted in section 4.1, the test temperatures that we used in this work correspond to solid fractions (f_s) between 0.85 and 1.0. We took data at several points within this range: 0.85, 0.88, 0.9, 0.94, 0.97, 0.99 and 1.0, or in terms of temperature: 550, 520, 485, 475, 473, 470 and 465 °C, respectively – see Table 4.1. The solidification path of this alloy was calculated by JMat-Pro® software and is shown in Figure 1.2. For each combination of the test (temperature–displacement rate), we repeated the test at least three times to obtain statistical information. The fracture surface of the samples was treated similarly to the sub-solidus samples from Chapter 3: Those were observed in a Jeol JSM-6500F SEM at the tip of the failed specimens.

Table 4.1 Tensile plan matrix and the number of the test performed at different test conditions.

Testing temp. (°C) / Disp.-rate	465 (f_s=1.00)	470 (f_s=0.99)	473 (f_s=0.97)	475 (f_s=0.94)	485 (f_s=0.90)	520 (f_s=0.88)	550 (f_s=0.85)
$2 \cdot 10^{-1}$ mm/min	3	3	3	3	3	3	3
$2 \cdot 10^{0}$ mm/min	0	3	0	3	3	0	0
Number of test :	30						

4.2.2 Constitutive parameters extraction procedure

To describe the semi-solid properties of the alloy, ALSIM uses the constitutive equations described in Chapter 2 (Eq. 2.1 – 2.16). From the internal function of the semi-solid constitutive equation (Eq. 2.10 – 2.14), the constitutive parameters that need to be extracted and optimized are the rheological parameters p, α_0, α_1, g_s^{coal} and k; because the parameters

of solid part of the alloy (represented by creep law properties – Eq. 2.15 and 2.16) $\sigma_0, \dot{\varepsilon}_0, Q$ and n were already obtained in Chapter 3. In this chapter, we focus on obtaining the constitutive parameters for the semi-solid part of the constitutive model by utilizing ALSIM package.

The flow chart of the constitutive parameter extraction procedure is shown in Figure 4.4. As a requirement, we need two sets of information that should be obtained experimentally. First, the tensile force-displacement curves of the alloy at different solid fractions. Second, we need the temperature distribution across the length of the sample at various solid fractions where the tensile tests are carried out. After we obtain those two pieces of information, there are two steps needed to obtain the constitutive parameters of the alloy. We start by making a temperature distribution model using ALSIM and verify the results with the calibrated temperature. Then, on the geometry with the modeled temperature distribution, we carry out numerical tensile tests and perform optimization to find the constitutive parameters that have the best fit with respect to the experimental tensile test data (lowest error between numerical and experimental force-displacement curves).

The reason it is necessary to build a model of the temperature distribution along the sample is because the length of the mushy zone is different at different test temperatures. We know that in any mechanical test, deformation mostly occurs in the weakest part of the sample, i.e. in the semi-solid region because this part has significantly weaker mechanical strength compared to the fully solid part [9, 10]. Therefore, a realistic temperature distribution along the sample is critical for obtaining accurate values of the constitutive parameters. We built a simple thermal model of the sample using ALSIM that focuses on the main heat transport phenomena: heating by induction coil and cooling by both a water-cooled surface and air cooling from the ambient temperature. The aim of this model is to have a steady-state temperature distribution along the sample length where the center mid-length of the sample has the test temperature while heat is being constantly extracted by the cooling surfaces.

To reduce the calculation time, we make a 2D thermal model and only need to simulate a quarter-part of the sample due to axis symmetry. The geometry of the sample is taken from the gauge-length of the sample, which is represented as a rectangular section with a length of 50 mm (from the center to the end of the gauge length – before the notch) and width of 5.84 mm. To simulate heat generation, which in the experiment is done by induction heating, we specify a layer of source-term (a specific region in the simulation geometry that supplies heat to the system) in the surface area around the mid-length of the sample. The power given by the source term is regulated in such a way that the temperature in the central mid-length of the sample resembles the test temperature. For the heat extraction phenomenon, the main heat extraction comes from the cooling surface at the end of the sample and the secondary heat extraction is carried out by the air cooling from the surface

of the sample. The water temperature and ambient room temperature resembles the experimental conditions: Water temperature is 8 °C and room temperature is 20 °C. The illustration of the thermal model and its parameters is shown in Figure 4.5. This model is then compared to experimental temperature measurements specifically done for this purpose. These tests were done with conditions corresponding to some of the test temperatures specified in Table 4.1. In the experiment, we measured the distribution on the centerline along the length of the sample – we measured temperature at 4 different points; at 0 mm, 12 mm, 24 mm and 39 mm-off the mid-length. Additionally, we also obtained the radial temperature distribution of the sample by measuring the temperature at the central mid-length and 5 mm off-center in the mid-length of the sample. From this measurement, we adjust the model parameters (dimension of the source term, water heat transfer coefficient or HTC_{water} and air heat transfer coefficient or HTC_{air}) such that a good qualitative fit between the model and the measured temperature is obtained. These parameters will be shown in section 4.3.3.1.

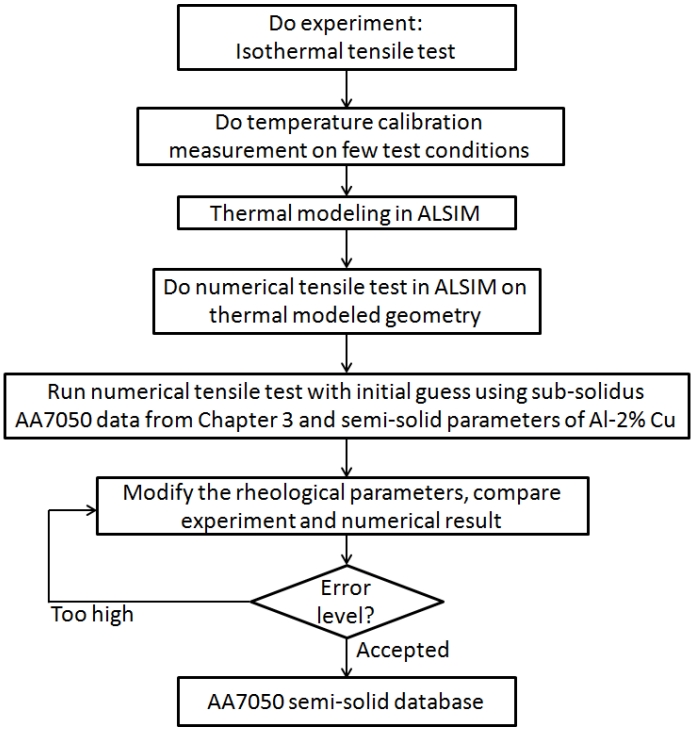

Figure 4.4 Flow chart of semi-solid constitutive parameter extraction using ALSIM.

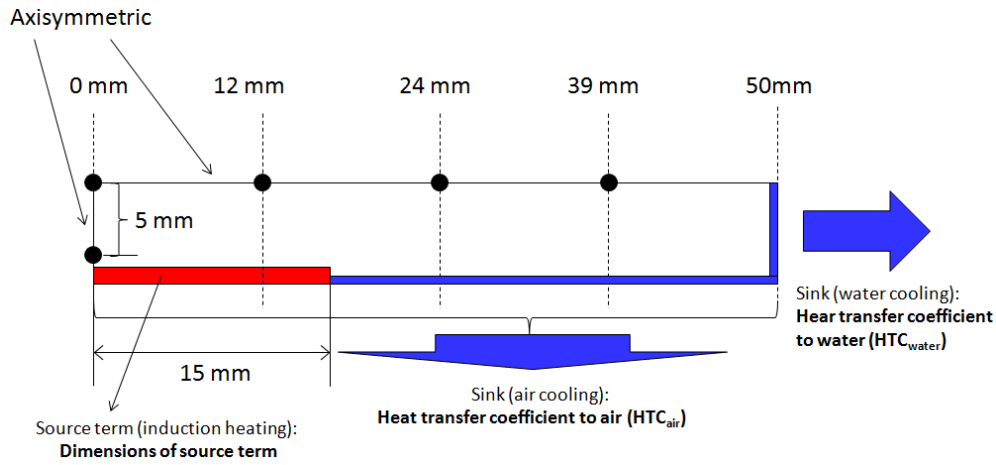

Figure 4.5 Thermal model illustration along with model parameters. The black dots represent the temperature measurement points on both experiment and numerical model.

After we obtain the temperature distribution across the model geometry from the numerical model, the geometry is used as the template geometry where we performed the numerical tensile test for each solid fraction. The numerical tensile test model is also built using ALSIM. The tensile displacement-rate used on the simulation is half of the experimental counterpart because the geometry of the simulation is only half the total gauge length of the specimen. We use the AA7050 alloy parameters of the creep-law obtained in Chapter 3 for the solid part of the semi-solid sample. For the semi-solid part, we use the Al-2% Cu semi-solid database [11] as the initial guess. This is not only due to its availability, but also from the literature [12] this alloy is considered to be susceptible to HT similarly to our AA7050 alloy. Using this setting, we run the numerical tensile test and then compare the resulting force-displacement curve between the numerical and experimental results. Subsequently, we modify the semi-solid constitutive parameters and then run the test again. We repeat this until the force-displacement curve produced by the numerical test gives a good qualitative fit with respect to the experimental counterpart. However, the constitutive parameters that need to be fitted are not solid-fraction or temperature dependent. Therefore, we have to select one set of parameters (p, α_0, α_1, g_s^{coal} and k) that produce a reasonable global error for all solid fractions in the semi-solid regime.

4.3 Results

4.3.1 Tensile mechanical behavior

From the tensile tests, we obtained force–displacement curves at different temperature points and displacement rates. The force–displacement curves with a displacement rate of 0.2 mm/min are shown in Figure 4.6 and Figure 4.7 – this separation is done because of the large scale difference of the force values at this displacement rate. While the plot with a displacement rate of 2 mm/min is shown in Figure 4.8.

Figure 4.6 and Figure 4.7 show that at the displacement rate of 0.2 mm/min, the height of the peak force in general decreases as the solid fraction reduces. In addition, the shape of the curve also changes significantly from $f_s = 1.0$ (when the alloy is fully solid) to $f_s = 0.97$ (refer to Figure 4.6) and then it changes again as the solid fraction decreases further, from $f_s = 0.97$ down to $f_s = 0.85$ (refer to Figure 4.7). Such a transition in the force–displacement curve can be interpreted as a change in the deformation mechanism. From Figure 4.6 and Figure 4.7, we observed two mechanical property transitions. First, the alloy behavior changes from ductile at $f_s = 1.0$ to brittle at $f_s = 0.97$. The sharp drop in ductility and strength at $f_s = 0.97$ informs us that the alloy fails in a brittle manner. The second transition in the mechanical behavior of the material occurs when the solid fraction of the alloy decreases from $f_s = 0.97$ to $f_s = 0.85$. As the solid fraction decreases, the end part of the curve (after peak force) changes, i.e. the slope of the curve is not as steep at $f_s = 0.85$ as it is at $f_s = 0.97$ and the slope gradually becomes shallower as the solid fraction decreases. Finally at the lowest solid fraction in this test series ($f_s = 0.85$), the curve resembles a shallow symmetric hump with a long ‘tail’.

A similar change in the force–displacement curve is also observed at a displacement rate of 2 mm/min. As shown in Figure 4.8, at $f_s = 0.99$, the force exhibits a sharp drop after the sample reaches the fracture point, which is interpreted as brittle behavior of the alloy. As the solid fraction decreases to $f_s = 0.94$, the peak force significantly decreases despite the similar curve shape with the preceding case. The main shape distinction is that the curve at $f_s = 0.94$ has a ‘tail’ after the sharp drop. At $f_s = 0.90$, the peak force is reduced even more and the shape of the force–displacement curve is significantly changed as compared to the two other curves at this displacement rate.

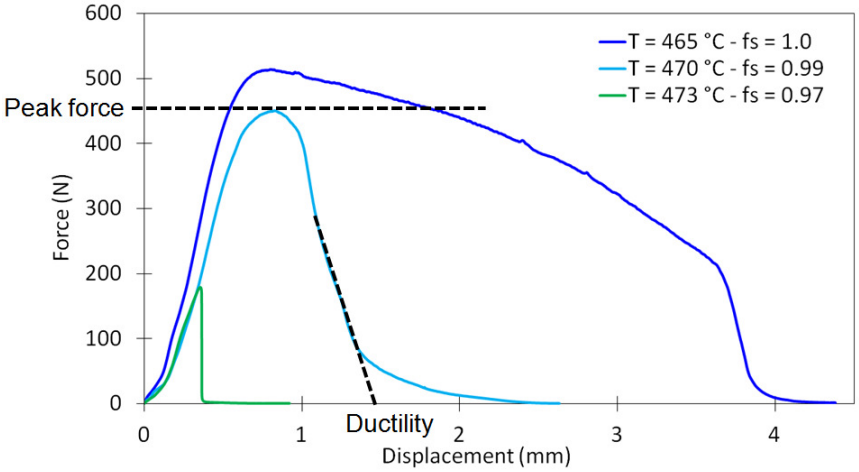

Figure 4.6 Force-displacement curves at low displacement rate (0.2 mm/min) at higher solid fractions ($f_s \geq 0.97$).

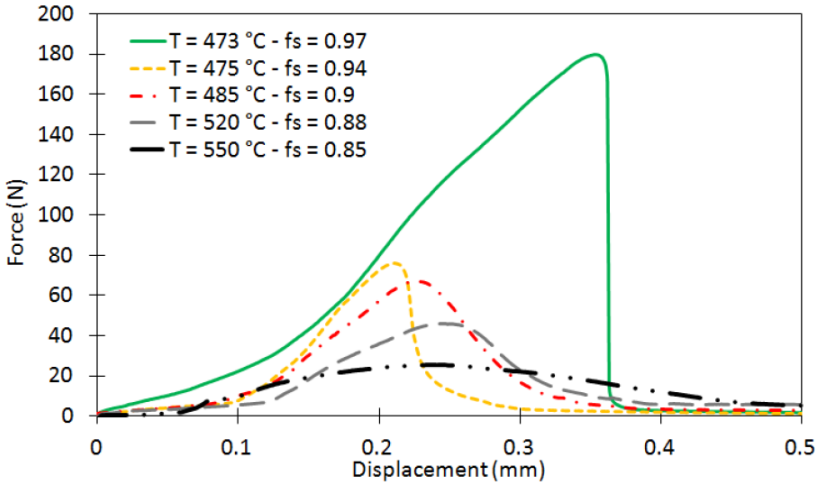

Figure 4.7 Force-displacement curves at low displacement rate (0.2 mm/min) at lower solid fractions ($f_s \leq 0.97$).

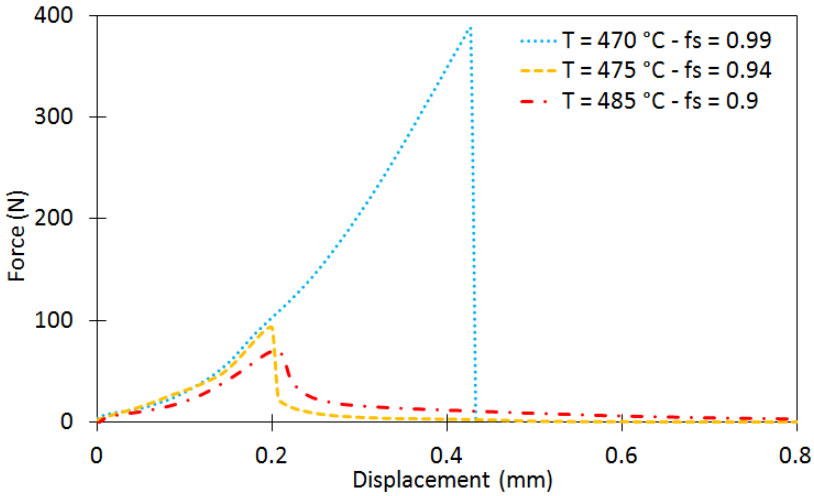

Figure 4.8 Force-displacement curves at high displacement rate (2.0 mm/min).

Figure 4.9 shows an example of test repeatability at the lowest solid fraction from the test series – f_s = 0.85. We can see that the load-displacement curves are generally grouped together especially from the load building phase up to the displacement of 0.3 mm (shortly after the peak force reached) and diverges afterwards. This shows the high quality of the test results despite the presence of significant liquid fraction in the sample.

We use peak force and ductility as the quantification of the mechanical behavior of the alloy. Peak force is described as the maximum force value in the force-displacement curve and ductility is described as the intersection between the force equals zero axis and the extrapolation of the last linear regime after the peak force before the sample completely failed. This definition of ductility is selected in this study because in some of the obtained tensile test data, after the peak force there is quite a significant elongation achieved before the force reaches complete zero. This condition may not represent the real physical phenomenon and could interfere with the data analysis. An example of both the peak force and ductility is shown in Figure 4.6.

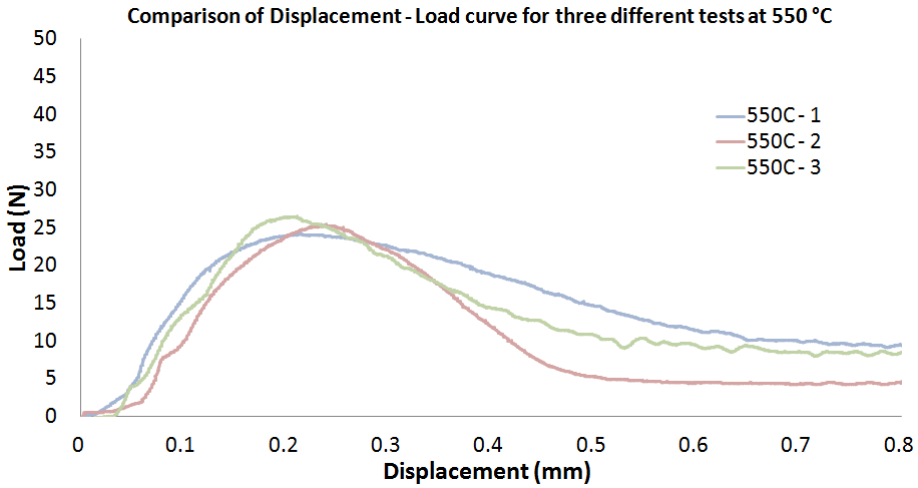

Figure 4.9 Example of test repeatability. Three tests are done at the lowest solid fraction of this test series with the low displacement rate (0.2 mm/min).

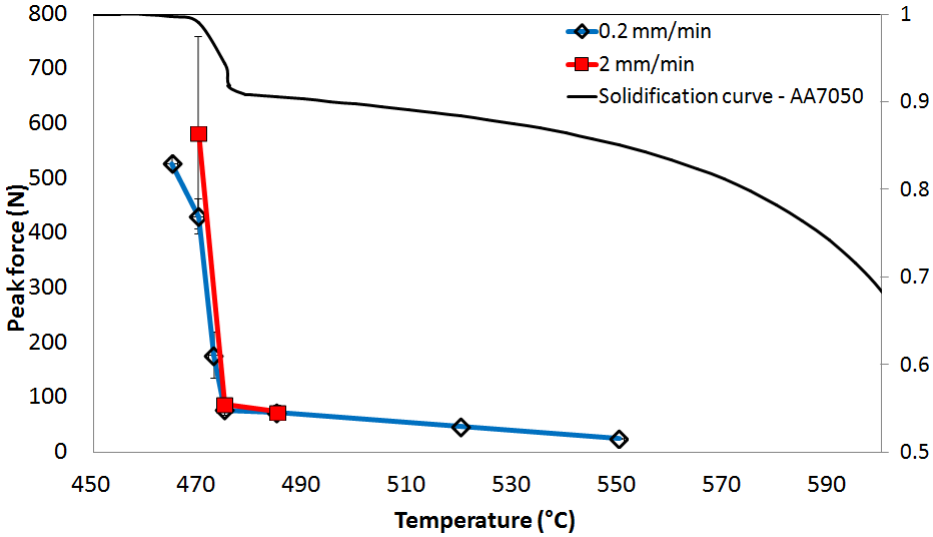

Figure 4.10 Peak force at different temperature and the comparison with respect to solid fraction (black line). Each peak force point is the average of three tests and some of the error bars are smaller than the size of the data points.

The evolution of the peak force of the alloy with respect to the temperature is shown in Figure 4.10. As an example, on displacement rate of 0.2 mm/min, the minimum engineering peak stress is obtained at $f_s = 0.85$ with a value around 0.23 MPa (25 N) while the maximum engineering peak stress is obtained at $f_s = 1.0$ with value around 4.92 MPa

(527 N). For both displacement rates, the peak force rapidly increases as the temperature is lowered below 475 °C. Therefore, we can argue that grain coalescence starts between f_s = 0.94 and f_s = 0.97. The temperature range from 475 to 470 °C also coincides with the brittle fracture behavior and the eutectic solidification domain (see Figure 1.2). One also notices that the alloy starts to become displacement-rate sensitive with decreasing test temperature.

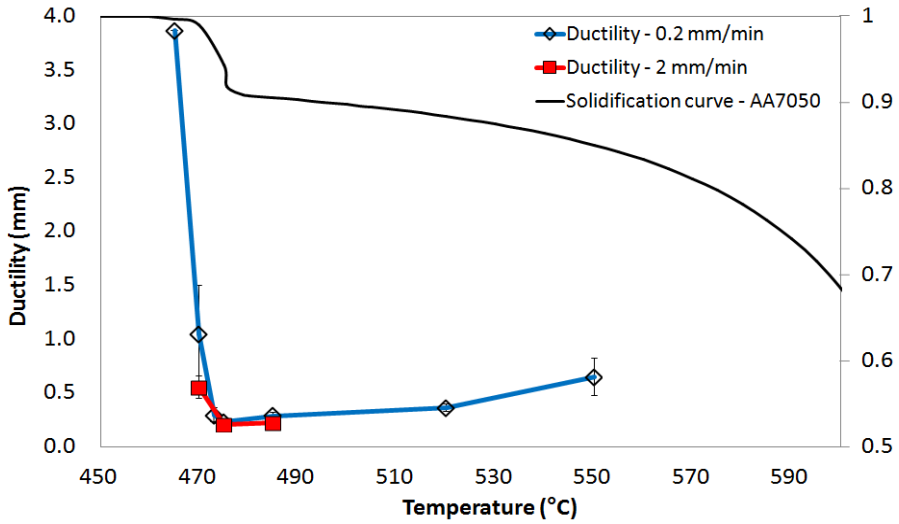

Figure 4.11 Ductility at different temperature and the comparison with respect to solid fraction (black line). Each ductility point is the average of three tests and some of the error bars are smaller than the size of the data points.

The ductility of the alloy at different temperature points is shown in Figure 4.11. For both displacement rates, one can see that the ductility of the alloy starts to drop significantly as the temperature increases above 465 °C. The lowest ductility value for both displacement rates was found at a temperature of 475 °C or f_s = 0.94, which corresponds, according to the solidification path in Figure 1.2, to the beginning of the eutectic solidification. As the temperature increases further above 475 °C, the ductility starts to develop gradually up to 550 °C. This observation resembles the shape of the classical brittle temperature range curves [6].

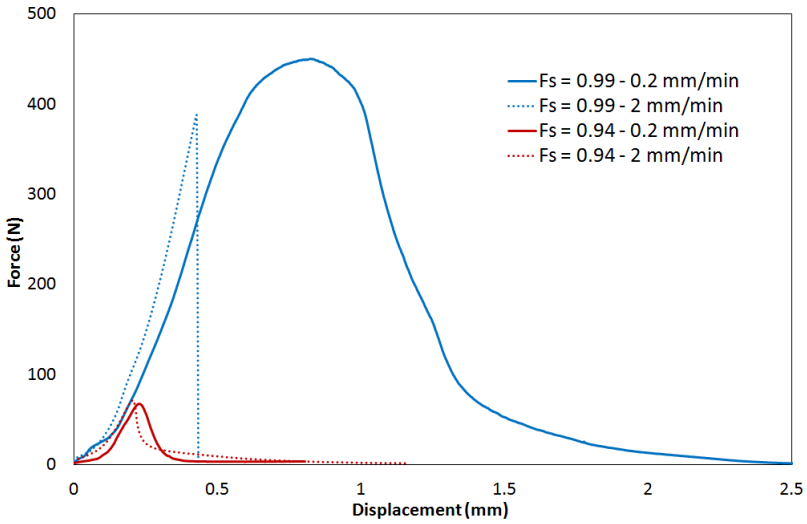

Figure 4.12 Displacement rate sensitivity at two solid fractions. Before coalescence (f_s = 0.94) and after coalescence (f_s = 0.99).

Figure 4.12 shows that there is not much strain rate sensitivity observed either by the force-displacement curve or from other mechanical properties (Figure 4.10 and Figure 4.11), between the solid fraction before (f_s = 0.94) and after grain coalescence (f_s = 0.99). The displacement rate has a small effect on the mechanical behavior. The main difference is that at 470 °C the tests at 2 mm/min gave a brittle behavior while at 0.2 mm/min some tests showed a brittle behavior while other tests gave a ductile response. At a temperature of 475 °C, there is a slight change in the curve shape with different displacement rates. The most significant change is the shape of the curve after the peak force was reached. At the lower displacement rate, the decrease is more gradual compared to the slope at 2 mm/min. This behavior is reasonable, because at 0.2 mm/min, the alloy has more time to compensate the deformation.

4.3.2 Fracture surface analysis

To analyze the failure mechanisms at different solid fractions, we performed SEM analysis on the fracture surfaces of the tested samples at four different test conditions, i.e. at two deformation rates and at solid fractions of 0.99 and 0.94, reflecting the transition from brittle to ductile behavior (see Figure 4.6 – Figure 4.8). From the fracture analysis performed, we found that in general, the fracture mode is mixed between inter-granular (with dendritic morphology) and intra-granular, irrespective of solid fractions and displacement rates used during the test. An example of the fracture surface is shown in Figure 4.13. The sample in that figure was tested at f_s = 0.94 with tensile speed of 2 mm/min. In that figure, the area within the blue rectangles represents the transgranular-like

features while the area within red ellipses reflects the dendritic intergranular fracture mode. Features that possibly attest for broken solid bridges (encircled by dashed red ellipses in Figure 4.14a) were mostly found starting at $f_s = 0.94$ and above. At lower solid fractions ($f_s \leq 0.94$), for both displacement rates, the interdendritic liquid raptures [13] (features within the dashed red ellipses in Figure 4.14b) are commonly observed. Interestingly, such interdendritic liquid features are rarely found at the higher solid fractions.

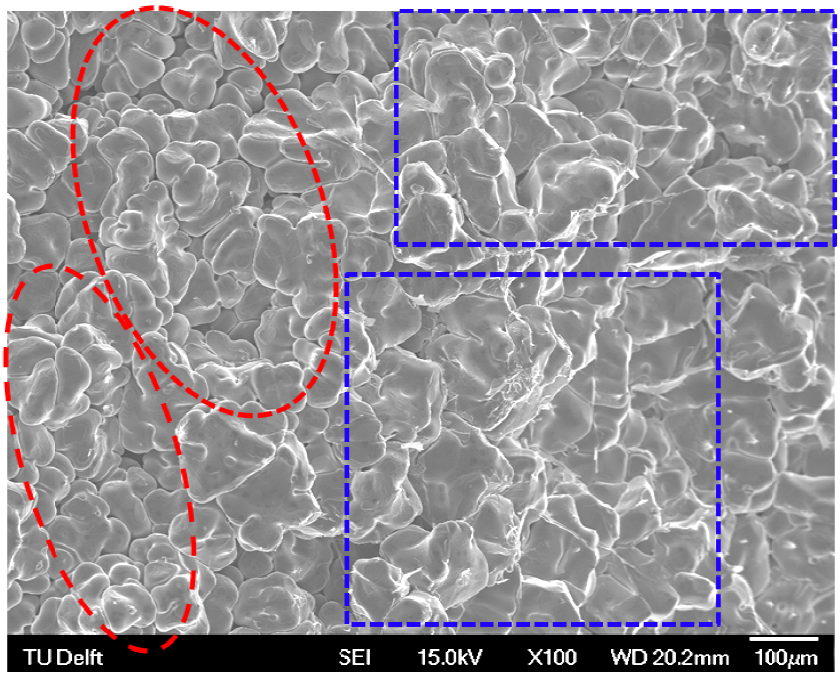

Figure 4.13 Typical fracture surface observed in the tensile tested samples in the super-solidus temperature regime – mixed fracture mode. Area within the dashed blue square represents the intragranular-like features. While the area within the dashed red ellipses represents the dendritic intergranular features. This SEM picture is taken from the sample tested at $f_s = 0.94$ and displacement rate of 2 mm/min.

Figure 4.14c shows the morphology of the solidified interdendritic liquid at the higher solid fraction ($f_s = 0.99$) and slow displacement rate (0.2 mm/min). While Figure 4.14d shows the morphology of the solidified interdendritic liquid phase at similar solid fraction but with the fast displacement rate (2 mm/min). The shape differences could be explained as the interdendritic liquid has more time to deform and rearrange at slower displacement rate compared to the faster one.

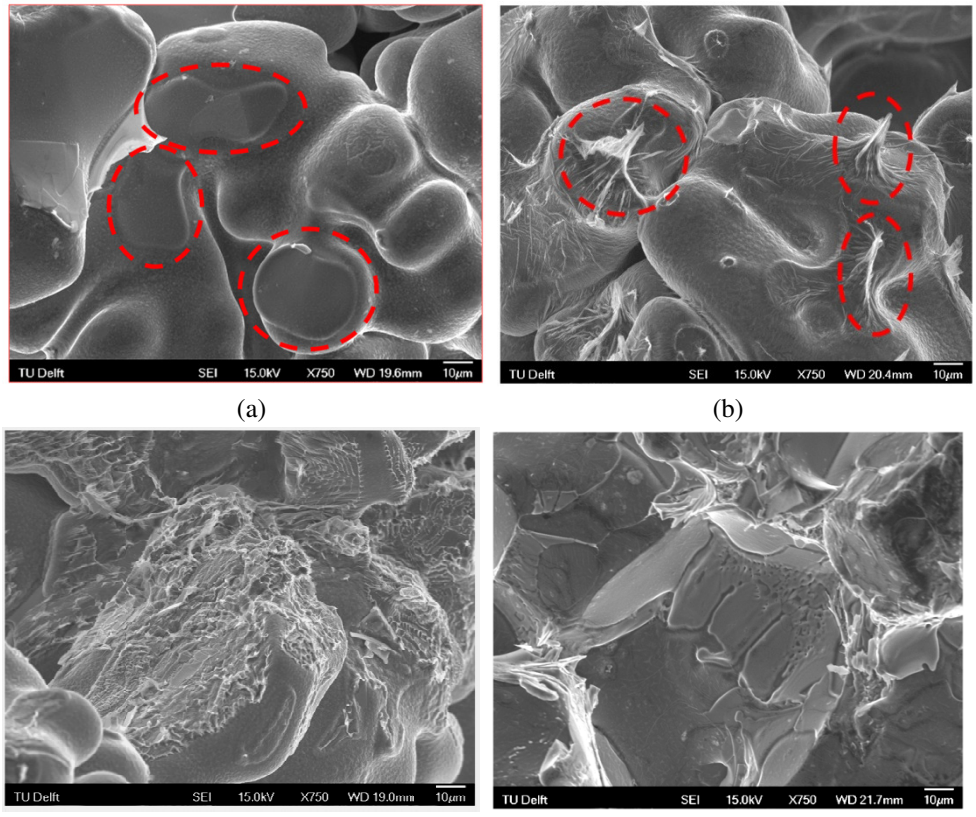

Figure 4.14 Broken solid bridges (encircled by dashed red ellipses), commonly observed features starting from $f_s = 0.94$ and above (a). Common feature at lower solid fraction ($f_s \leq 0.94$); broken liquid bridges (raptures) encircled by dashed red ellipses (b). Typical eutectic layer morphology at higher solid fraction ($f_s = 0.99$) with slower displacement rate (0.2 mm/min) (c) and typical eutectic layer morphology at higher solid fraction but with faster displacement rate (2 mm/min) (d).

4.3.3 Semi-solid constitutive parameters extraction

4.3.3.1 Temperature field comparison

We obtain the good qualitative fit between the thermal model and the measured temperature described in section 4.2.2 using the following values for the dimensions of the source term: length of 15 mm and width of 0.6 mm. The heat transfer coefficient to water and air-cooling are HTC_{water} = 1000 W/m^2 and HTC_{air} = 10 W/m^2, respectively. Table 4.2 shows the temperature difference between the measured and modeled temperature ($T_{meas.}$- T_{model}) at different test temperatures along the length of the sample using these model parameters. All of the experimentally measured temperatures have an error bar of ± 4 °C due to

measurement uncertainty during the thermocouple calibration process. From this table, we can see that the highest temperature difference between the model and the measurement is found at the test temperature of 485 °C instead of at the extremities of the test temperatures (T = 550 °C and T = 460 °C).

Table 4.2 Difference between measured temperature ($T_{meas.}$) and modeled temperature (T_{model}) in the axial length (center of the sample) at different temperatures in the mid-length of the sample.

Dist. From center-> Center temp.(°C) ↓	($T_{meas.}$- T_{model}) 12 mm	($T_{meas.}$- T_{model}) 24 mm	($T_{meas.}$- T_{model}) 39 mm
550	1.4	1.1	-7
485	-3.9	-9.3	-14.7
473	-0.6	-2.5	-6.5
460	0.4	1.6	-4.5

Figure 4.15 shows an example of thermal modeling using ALSIM when the center of the sample is at f_s = 0.88. Figure 4.15a shows the temperature distribution where red corresponds to higher temperatures and blue to lower temperatures. Figure 4.15b shows the solid fraction based on the temperature distribution from Figure 4.15a. The result of the model shows that the biggest temperature gradient is along the length of the sample – lower temperature toward the water-cooled surfaces and there is almost no temperature gradient to the radial direction (approximately 2 °C). This finding is supported by the temperature calibration measurement; the temperature difference between the center and 5 mm off the center of the sample mid-length is approximately 2 °C. This shows a good correlation between the temperature measurement and the model.

From the thermal modeling, we can estimate the length of the semi-solid regime in the sample. This regime is defined as the length between the mid-length of the sample and the point where f_s = 1.0 (solidus). Based on the thermal model, Figure 4.16 shows the length of the mushy zone in the sample at different solid fractions. The length specified in that figure is for the full gauge length of the sample instead of the model geometry (the length of the model geometry is half the complete sample gauge-length). From the trend, we can see that the length of the mushy-zone decreases as solid fraction increases with a significant drop between f_s = 0.88 and f_s = 0.9 as a direct consequence of the solidification path shape.

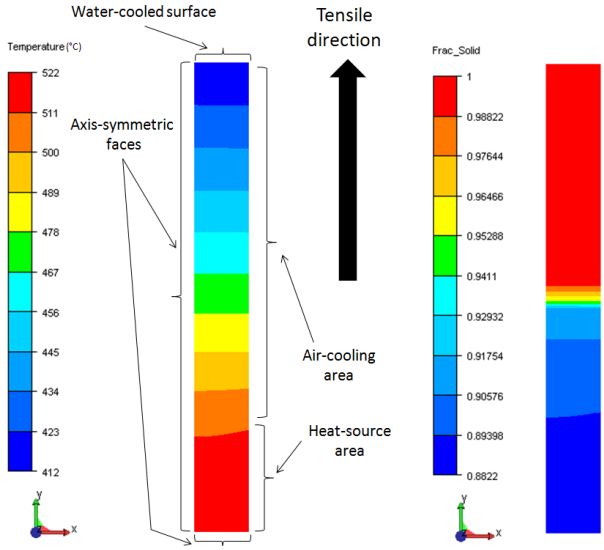

Figure 4.15 Example of thermal modeling using ALSIM when the center of the sample is at $f_s = 0.88$. Comparison between temperature (a) and solid fraction (b) distribution.

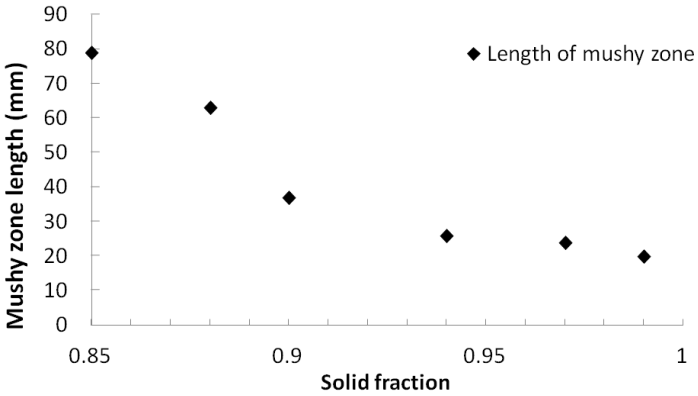

Figure 4.16 Length of mushy zone for the entire gauge-length of the sample for different solid fraction based on thermal model.

4.3.3.2 Numerical vs. experimental tensile test

The numerical tensile test in ALSIM takes place on a geometry that has been temperature modeled as described in section 4.3.3.1. From that section, we found that the temperature difference between the center and the surface of the sample is insignificant. Therefore, for simplicity, in the mechanical part of the simulation, we only use the axial temperature distribution along the sample. The example of comparison between the solid fraction and

effective strain distribution in the sample of a numerical tensile test at a solid fraction of 0.9 is shown in Figure 4.17. This figure shows that most of the strain took place in the mushy part of the sample (the region of the sample where solid fraction is below 1.0).

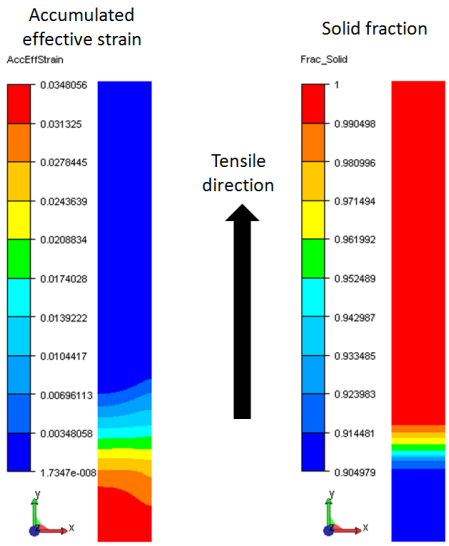

Figure 4.17 Example of strain (left) calculation result at $f_s = 0.9$ with comparison to the location of the mushy zone based on the solid fraction distribution (right).

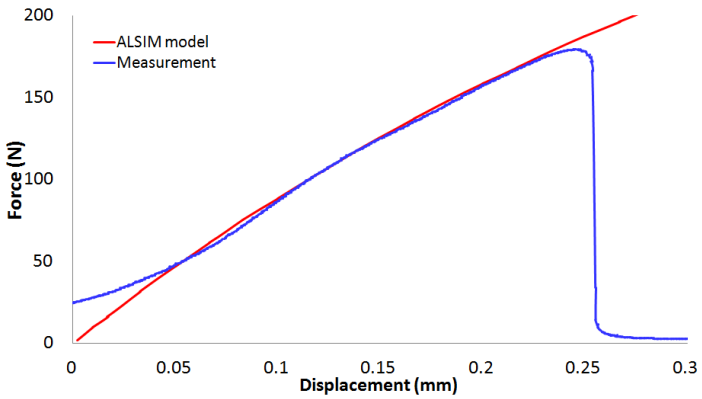

Figure 4.18 An example of an individual (single-curve fit) comparison between numerical tensile test (red line) and an experimental data (blue line) on solid fraction of $f_s = 0.97$ with displacement-rate of 0.2 mm/min.

An example of an individual fit (single-curve fit) comparison of the force-displacement curve between the numerical and experimental tensile test results for a single test (at a solid fraction of 0.97 with a displacement rate of 0.2 mm/min) is shown in Figure 4.18. The

fitting is aimed at capturing the force-displacement curve starting from the highest slope at the beginning of the deformation up to the peak force of the curve. This is because the shallow slope at the beginning of the force displacement curve (see Figure 4.6 – Figure 4.8) is considered to be predominantly due to machine initialization rather than material behavior. Figure 4.18 shows that the semi-solid constitutive model is able to capture the load development part of the curve. However, as mentioned in section 4.2.2, since the semi-solid parameters are not solid fraction (or temperature) dependent, we need to select a set of parameters that allows us to obtain a reasonable global minimum error. An example of a good global fit of the semi-solid parameters plotted at different solid fractions and compared to its experimental counterpart is shown in Figure 4.19. The fitting results are comparable with the results obtained for other alloys using a similar constitutive equation, such as: Al-2% Cu [11] and AA5182 [14].

Figure 4.19 shows that using the obtained set of parameters, from $f_s = 0.9$ and below, the results from numerical tests underestimate the experimental forces while above $f_s = 0.9$, the results from numerical tests tend to overestimate the experimental forces. Additionally, aside from the trade-offs that are made to attain global minimum deviation, the shape of the curve from the semi-solid constitutive equation are not completely comparable to the shape of experimental curves at every solid fraction, especially at the higher solid fractions (above 0.97). Despite its drawbacks, the model reasonably captures the material behavior for solid fractions below 0.99.

4.3.3.3 Constitutive parameters

From the constitutive parameters extraction results shown in section 4.3.3.2, we obtained the semi-solid constitutive parameters for the AA7050. The obtained semi-solid parameters are as follows: $p = 0.08$, $\alpha_0 = 13.65$, $\alpha_1 = 0.0116$, $g_s^{coal} = 0.94$ and $k = 10$. Table 4.3 shows the comparison of the constitutive parameters from different alloys that were also described using similar semi-solid constitutive models such as used in ALSIM. From this result, we can see that AA7050 has the lowest 'p' value while having the highest value of 'α_0' and the value of 'α_1' is between the other two alloys.

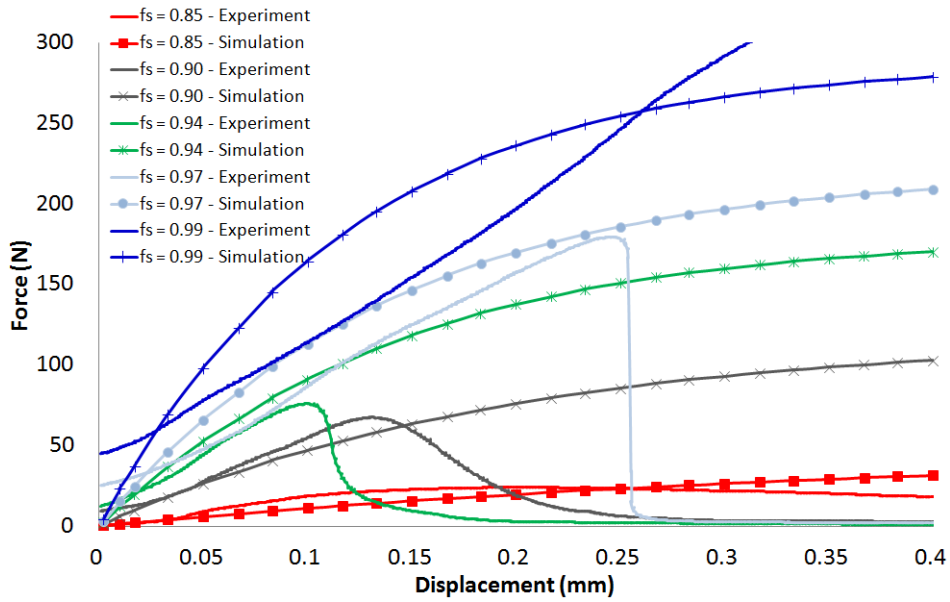

Figure 4.19 Example of simultaneous fitting at different solid fractions (global fit).

Table 4.3 Comparison of the AA7050 semi-solid constitutive parameters for different alloys described using ALSIM semi-solid constitutive equation (Eq. 2.12 – Eq. 2.14).

Parameters / Alloys	p	α_0	α_1
AA5182 [14, 15]	0.315	10.54	0.0632
Al–2% Cu [11]	0.11	4.45	0.0107
AA7050	0.08	13.65	0.0116

To compare the semi-solid constitutive behavior of different alloys in terms of tensile force-displacement curves, we plot the tensile response for each alloy shown in Table 4.3 using numerical tensile test setup in ALSIM (shown in section 4.3.3.2) at different solid fractions with a pulling speed of 0.1 mm/min. We found that for AA7050, there is only a small difference in the resulting simulated force when the additional tensile condition is taken into account (Eq. 2.14); the force value that is obtained using $\alpha(g_s,X)$ for all stress state (Eq. 2.13) is lower than the simulations that are using the activated tensile condition $\alpha(g_s,X)$ (Eq. 2.14). The largest force difference at semi-solid state is found at f_s = 0.99 and the value from all stress state simulation is around 20 N lower (or around 10% lower at this force value) than the activated tensile condition counterpart. Figure 4.20 shows the tensile response comparison between Al–2% Cu and AA7050. While Figure 4.21 shows the comparison between AA5182 and AA7050.

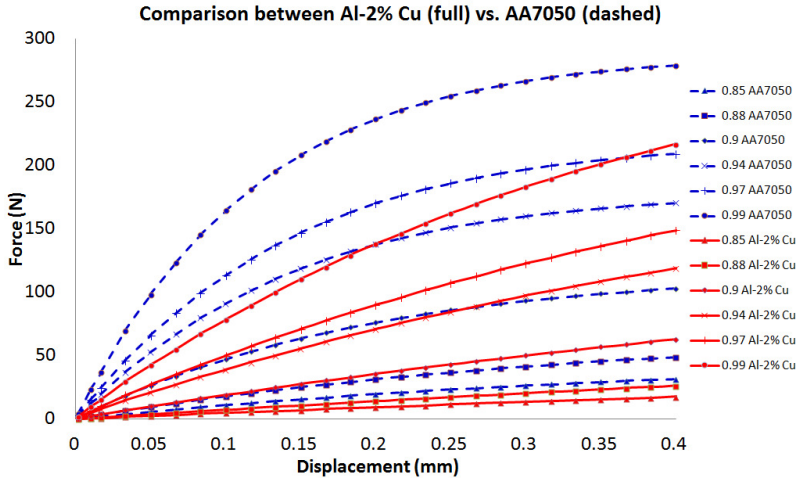

Figure 4.20 Comparison of modeled tensile response at different solid fractions between Al–2% Cu (full lines) and AA7050 (dashed lines).

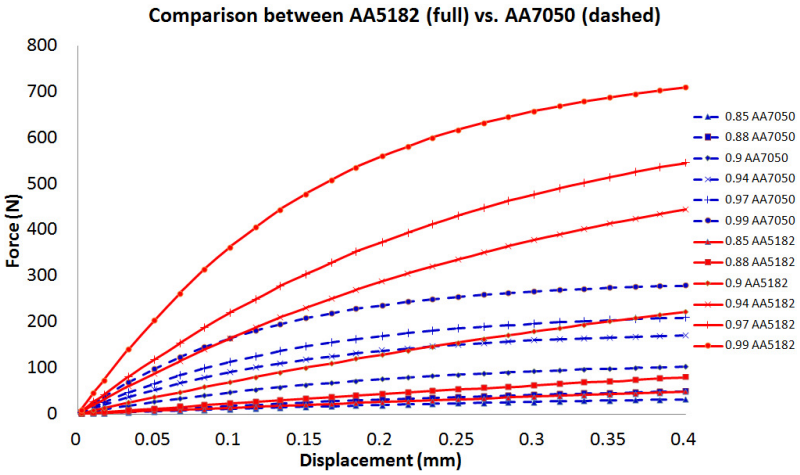

Figure 4.21 Comparison of modeled tensile response at different solid fractions between AA5182 (full lines) and AA7050 (dashed lines).

Figure 4.20 and Figure 4.21 show that the AA7050 alloy is stronger than an Al–2% Cu alloy (Figure 4.20) but it is weaker that the AA5182 alloy (Figure 4.21) in the semi-solid state. It is clear that the strength and load development characteristics (the quickness of the alloy to reach high force values with respect to displacement) are different for the three different alloys. The difference in both strength and behavior becomes more significant as the solid fraction increases, especially starting above f_s = 0.88. In terms of strength, the AA7050 alloy is comparable to the Al–2% Cu alloy but the load development characteristic

is clearly different – AA7050 alloy is quicker to reach high force values compared to Al–2% Cu which has a slower load development mode. In comparison with AA5182, the AA7050 alloy has a relatively similar load development characteristic – relatively quick increase in load at lower displacement and saturation as the displacement increases. However, it is clear that the AA5182 alloy is stronger than the AA7050, especially at higher solid fractions.

4.4 Discussion

The results show that the mechanical testing at super-solidus temperatures is reproducible. Figure 4.9 demonstrates that in the load development portion of the curve (from where the alloy starts to gain strength up to the peak stress of the curves), the shape of the curves is similar and the difference between different tests is relatively low (within approximately 5 N). This measure gives us good confidence in the obtained results of the measurements.

From the evolution of the force-displacement curves at different solid fractions shown in Figure 4.6, Figure 4.7 and Figure 4.8, we can deduce the evolution of the mechanical behavior of the alloy at different solid fractions and relate it to the solidification process. Generally, the evolution of the mechanical behavior is comparable with the solidification process described in previous works [4, 5, 16]; at the beginning of solidification, when there is still a significant amount of liquid in the system, the alloy is still ductile. At lower temperature, when feeding becomes difficult, the alloy becomes brittle and prone to HT. After the dendrites have coalesced, the alloy becomes stronger and it can resist thermal stress and the development of HT. Moreover, the shape and evolution trend of the force-displacement curves obtained in this work by tensile testing is similar to those reported on other alloys [11, 14]. From those figures mentioned above, as the solid fraction decreases, the length of the force 'tail' (after the force-displacement curve reaches the peak force) increases irrespective of displacement rate used for the test. This might be caused by the increasing presence of the liquid phase within the sample during the test. Another possible explanation is that the main mechanism of deformation is grain boundary sliding thanks to the presence of sufficient interdendritic liquid surrounding the grains at lower solid fractions [6].

From the result in Figure 4.10, we observe that the grain coalescence occurs approximately between a solid fraction of 0.94 and 0.97. This value is supported by other works on different aluminum alloys [7, 8, 11, 14, 16, 17]. Additionally, from Figure 4.11 we also find that the temperature range between solid fractions of 0.9 and 0.97 has the lowest ductility of the entire test regime. This also corresponds to the suggestion given in a previous work [8]; liquid feeding stops at approximately $f_s = 0.9$ and in this solid fraction regime the grains

have not yet coalesced, therefore the semi-solid material is not yet strong enough to resist developing HT.

In terms of deformation rate sensitivity, we observe that there are not many differences in terms of the force-displacement curve shape (Figure 4.12), peak force (Figure 4.10) or ductility (Figure 4.11) for tests conducted with different displacement rates. This might be correlated to the similarities of the fracture surface features, mixed intragranular-like and dendritic intergranular at both solid fractions; below (at f_s = 0.94) and above grain coalescence (at f_s = 0.99). However, the difference in peak stress and ductility at different displacement rates starts to increase with solid fraction. This might be because at higher solid fractions, there are already more solid bridges connecting the dendrites (e.g. features shown in Figure 4.14a), thus the alloy gains a behavior approaching the one observed in the sub-solidus regime; with greater strain-rate sensitivity [10, 18]. Additionally, this condition can also be linked with the increase of error-bar width with solid fraction. This could be explained as the strength of the alloy in the semi-solid state not only depends on the solid fraction but also depends on the distribution of the formed damage and/or redistributed eutectics.

Some interesting results are also found in the fracture surface analysis. For instance, the mixed fracture surface features: dendritic intergranular (within red ellipses in Figure 4.13) and transgranular (within blue squares in Figure 4.13) irrespective of the solid fraction and displacement-rate during the test. One possible explanation for this phenomenon is that the dendritic intergranular features are a result of separation of the part of the sample that is covered by the liquid fraction while the intragranular-like features are the results of the separation of welded grains or solid bridges. Therefore, the possible reason for these mixed fracture-features in the entire semi-solid range are because in the solid fraction range where we carried out the tests, even at the lowest solid fraction (f_s = 0.85), the alloy already has an appreciable load. This means some of the dendrites already linked together (and were able to transmit loads), thus, the occurrence of intragranular-like separation is possible. On the lower solid fraction side i.e. below coalescence point ($f_s \leq 0.94$), liquid bridge raptures as shown in Figure 4.14b are commonly observed. Such rapture morphology is also observed in previous works on semi-solid deformation [9, 13, 19].

Another interesting fracture surface feature that we observed is that at high solid fraction (at f_s = 0.99), the morphology of the eutectic is deformation-rate dependent. The tests at lower displacement rate (0.2 mm/min) show that the eutectic is more elongated and produces filament-like features. This feature is also observed in the higher temperature portion of the sub-solidus regime (commonly visible starting at 455 °C – Chapter 3) at a strain-rate of 0.0005 s^{-1}. This could be explained as the micro-superplasticity behavior observed by Takayama *et al.* [20] in the AA7475 alloy near the solidus temperature. The morphology of

the micro-superplasticity feature in Figure 4.14c is comparable to the morphology reported at the moderate strain-rate given in Takayama *et al*.'s work ($2.8 \cdot 10^{-3}$ s^{-1}) which is similar to the slower displacement rate we use in the semi-solid regime tensile test (0.2 mm/min). The whiskers produced in the tests at $f_s = 0.99$ are shorter compared to the tests at 465 °C at 0.0005 s^{-1} (in Chapter 3). This might be explained by the trend of superplasticity given in previous works [8, 20] that the length of the filaments decreases as the pulling speed increases because if the displacement rate is too high, the viscous flow becomes unstable and the filament cannot form. However, the length of the filament that we found in this work is relatively short compared to the result by Giraud [8] in the AA6061 alloy with a faster pulling rate. This also might be due to the chemical composition of AA6061 is quite different from our AA7050 alloy, whereas that difference is less compared to the AA7475-type alloys.

Based on the thermal model that we built in ALSIM, we found that the most sensitive parameters influencing the temperature distribution along the axis of the sample are the heat transfer coefficient (to water-cooled surface) and the dimension of the heat-source. This is in accordance with the theory since the main thermal influence in the experiment is the heat generated by the heating-coil and heat extraction by the water-cooled surface. This result shows that by using a simple thermal model, we are able to perform a constitutive parameter extraction with reasonable quality. Thus, in the future, we may be able to reduce the need to perform temperature calibration measurements at every solid-fraction where the tests are carried-out (i.e. we only need to do thermal calibration measurements at the highest and the lowest test temperatures), saving time and resources. For future development of this thermal model, we suggest increasing the level of realism in the model, for example, by using a temperature (or solid fraction) dependent heat transfer coefficient.

From the comparison between the temperature calibration measurement and the thermal model in Table 4.2, we see that the difference is relatively small up to two thermocouples off the mid-length (12 mm and 24 mm from the mid-length). These two points are considered important because most of the mushy zone is formed within this part of the sample especially at solid fractions important for HT development – above $f_s = 0.9$ the length of mushy zone is below 24 mm (Figure 4.16).

Figure 4.18 shows that the semi-solid constitutive model in ALSIM can capture the important parts of the force-displacement curve such as the load development part up to the peak force. Such a figure shows that we can obtain quite a good fit between experimental and numerical force-displacement curve in an individual fit. However, for the global fit (Figure 4.19), at lower solid fraction ($f_s < 0.94$) the simulated force is underestimating the experimental result while it is the other way around at higher solid fractions. This shows

that an accuracy compromise (from each individual fit) has to be made to obtain a set of parameters that produce global minimum error.

The shape of the constitutive model curves however, resembles the experiment only for certain solid fractions (Figure 4.19), the shape of the force-displacement curves having reasonable fit below a solid fraction of 0.99, where the HT initiation process mainly occurs. Above $f_s = 0.97$, the grains have coalesced and thus HT initiation becomes difficult (less liquid is available as initiation points) but the HT propagation mechanism is more dominant.

The current semi-solid constitutive model in ALSIM is able to reasonably capture the semi-solid behavior of aluminum alloys, especially at the load development phase. However, Figure 4.6 – Figure 4.8 and also other works on tensile semi-solid constitutive behavior of aluminum alloys [11, 14] shows that damage development phase (the decrease in force value after peak is reached) is also important because it is directly linked to the propagation of the formed HT. Therefore, for future development, perhaps an implementation of damage development model, for instance the de-cohesion model developed by Mihanyar *et al.* [21] would be an ideal continuation for further ALSIM development.

The result of the semi-solid constitutive parameter extraction in Table 4.3 shows that the AA7050 alloy has relatively different parameters, hence different mechanical behavior, compared to the two other alloys (AA5182 [14, 15] and Al–2% Cu [11]). The internal variables; C^* (function of p) and α (function of α_0 and α_1) define the cohesion rate (Eq. 2.2) of the alloy during the solidification process which in turns defines the alloy strength. This explains the results of numerical tensile simulation shown in Figure 4.20 and Figure 4.21; AA7050 is weaker than AA5182 but it is stronger than Al-2% Cu. The fact that AA7050 has lower k values compared to the other aluminum alloys (i.e. AA5182 and Al-2% Cu [11, 14]) shows that for AA7050 (in the tensile stress mode), the strength increase around the grain coalescence point occurs more gradually. In terms of HT susceptibility, Al–2% Cu is known to be susceptible to HT [12] due to its relatively wide solidification range (around 105 °C) and the high thermal contraction onset temperature (starting at approximately $f_s = 0.9$ [22]) compared to AA5182. Although the latter alloy has a wider solidification range (around 185 °C) compared to the Al–2% Cu alloy, this alloy has a lower thermal contraction onset temperature (starts at around $f_s = 0.93$). The solidification range for Al–2% Cu and AA5182 for this comparison is obtained from Scheil's calculation with the ThermoCalc package using the TTAL7 database. Moreover, AA5182 has a stronger semi-solid tensile strength compared to Al–2% Cu and AA7050. The AA7050, on the other hand, has a relatively wide solidification range (170 °C) and has a higher onset temperature for thermal contraction than both Al–2% Cu and AA5182. However, the semi-solid strength of the AA7050 is higher than Al–2% Cu. In general, for billet castings, Al–2% Cu [12] and

AA7050 [23] are known to be susceptible to HT. Therefore, we may suggest that, apparently, for an alloy to be susceptible to HT, not only should it have a wide solidification range, but it also needs to have a higher thermal contraction onset temperature (starting at lower solid fractions). Additionally, the tensile mechanical strength in the semi-solid state also influences the HT susceptibility of an alloy because this characteristic defines the capability of an alloy to resist HT development.

The results from ALSIM thermal simulations allow us to approximate the length of the mushy zone (Figure 4.16), where most of the deformation that contributes to HT development takes place. This information combined with the ductility measurement at each solid fraction (Figure 4.11), can be used to obtain an estimation of engineering fracture strain; a ratio between ductility and the length of the mushy zone at different solid fractions (Figure 4.22). A potential utilization of this engineering fracture strain data is a HT susceptibility estimation through the comparison with linear-contraction data from thermal-contraction experiments as described in the literature [3, 22, 24-28]. The thermal-contraction data may be converted into a strain value, thus an experimental-based HT susceptibility measure, such as in the works of Novikov [4, 6] and Magnin [29], could be obtained.

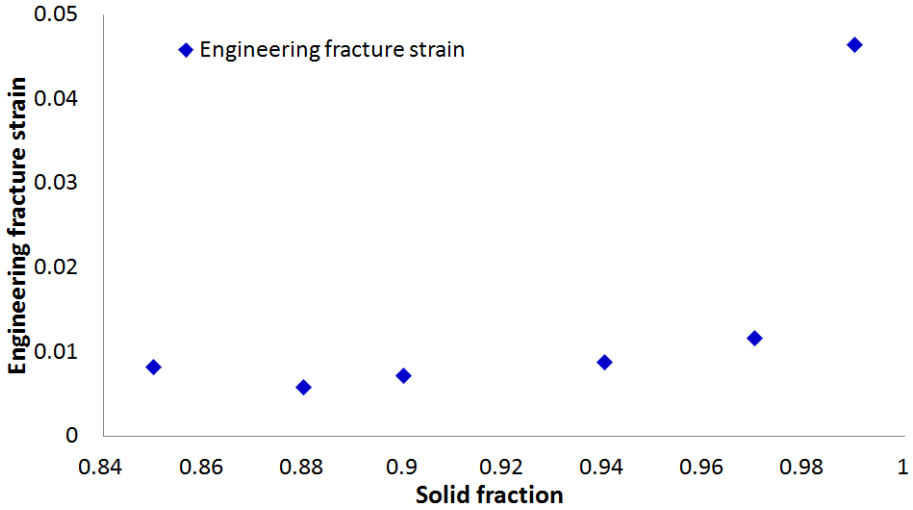

Figure 4.22 Engineering fracture strain (strain when fracture occurs) at different solid fractions.

In this chapter, we showed that a simple ALSIM thermo-mechanical model combined with temperature calibration measurements and experimental tensile test data is a reasonable method to extract constitutive parameters for the semi-solid constitutive model described in Chapter 2. From the results in this chapter and Chapter 3, we have not only completed the

database of the AA7050 alloy but also gained insight into the tensile constitutive behavior, which is necessary to understand the mechanisms of the connection between hot and cold crack. Therefore, with the full data set of the AA7050 alloy in the database, we expect to have simulation results with better accuracy for DC casting of this alloy. Moreover, we can also check the sensitivity of ALSIM with respect to different materials because this topic is important for ALSIM's long-term development. The need of a material database sensitivity analysis is also supported by our findings in Table 4.3 and Figure 4.20 that the AA7050 alloy and Al–2% Cu have different semi-solid mechanical characteristics, thus we expect significant differences in the simulation results.

4.5 Conclusions

In this chapter, we have performed a detailed study of the tensile constitutive behavior such as strength (peak force), ductility and failure mechanisms through SEM fracture surface analysis of the AA7050 alloy in the semi-solid state. Moreover, we also obtained the constitutive parameters for the semi-solid constitutive model for ALSIM described in Chapter 2 by making a thermal model and performing numerical tensile tests in ALSIM. From the results and analysis that we have, we obtain conclusions as follows:

1. From the shape of the force–displacement curves, we found that in the range of $f_s = 1.0$ (fully solid) to $f_s = 0.85$, the alloy has three different mechanical behavior regimes: ductile (between $f_s = 1.0$ and $f_s = 0.99$), brittle (between 0.99 and 0.9) and ductile again (between 0.9 and 0.85).
2. The grain coalescence in AA7050 occurs between $f_s = 0.94$ and $f_s = 0.97$. This is signified by the sharp increase in peak force between the mentioned solid fractions.
3. The alloy produces a ‘classically’ shaped brittle temperature range curve with the minimum ductility reached at 475 °C, and the alloy again gains ductility as the liquid fraction increases in the alloy.
4. The alloy has almost no displacement rate sensitivity in terms of peak force at high temperatures (below $f_s = 0.94$) but it has a positive displacement rate sensitivity starting at $f_s = 0.94$ and at higher solid fractions.
5. From SEM fracture surface analysis of samples that are tensile tested in the super-solidus temperature regime (e.g. shown in Figure 4.13), it is found that in general the fracture mode is mixed between inter- and intra-granular. Additionally, at higher solid fractions, the morphology of the eutectic is different at different displacement rates (Figure 4.14c and Figure 4.14d). Sites that resemble necking of interdendritic liquid were observed in samples that were tested at lower solid fractions (Figure 4.14b), independent of the displacement rate used during the test.

6. Behavior of AA7050 in the semi-solid regime is different compared to the other two alloys reported elsewhere. AA7050 is stronger compared to Al–2% Cu but weaker compared to AA5182. This result shows that the AA7050 alloy and Al–2% Cu have different semi-solid characteristics, thus a comparison of a full scale DC casting simulation needs to be done to justify the simulation results done in Chapter 2.
7. The HT susceptibility of an alloy is not only influenced by the width of solidification range but also by the mechanical characteristics in the semi-solid state, such as the onset temperature of thermal contraction, strength and ductility.

References

[1] Suéry, M., "Rheological behavior of various Al alloys during solidification", In: *International Conference on Advances in Metallic Materials and Manufacturing Processes for Strategic Sectors (ICAMPS 2012)*, Trivandrum, India (2012), pp. 35-42.
[2] Phillion, A. B., "Hot tearing and constitutive behavior of semi-solid aluminum alloys", [Ph.D. thesis] (2007), The University of British Columbia.
[3] Lalpoor, M., Eskin, D. G., Katgerman, L., "Thermal expansion/contraction behavior of AA7050 alloy in the as-cast condition relevant to thermomechanical simulation of residual thermal stresses", *International Journal of Materials Research* (2011), 102, pp. 1286-93.
[4] Eskin, D. G., "Physical Metallurgy of Direct Chill Casting of Aluminum Alloys (Advances in Metallic Alloys)", CRC Press, Taylor & Francis group, LLC (2008).
[5] Eskin, D. G., Katgerman, L., "A quest for a new hot tearing criterion", *Metallurgical and Materials Transactions A* (2007), 38A, pp. 1511-9.
[6] Eskin, D. G., Suyitno, Katgerman, L., "Mechanical properties in the semi-solid state and hot tearing of aluminium alloys", *Progress in Materials Science* (2004), 49, pp. 629-711.
[7] Fabrègue, D., Deschamps, A., Suéry, M., Poole, W. J., "Rheological behavior of Al-Mg-Si-Cu alloys in the mushy state obtained by partial remelting and partial solidification at high cooling rate", *Metallurgical and Materials Transactions A* (2006), 37, pp. 1459-67.
[8] Giraud, E., Suery, M., Coret, M., "Mechanical behavior of AA6061 aluminum in the semisolid state obtained by partial melting and partial solidification", *Metallurgical and Materials Transactions A* (2010), 41, pp. 2257-68.
[9] Subroto, T., Miroux, A., Eskin, D. G., Ellingsen, K., Marson, A., M'Hamdi, M., Katgerman, L., "Tensile mechanical behavior of as-cast AA7050 alloy in the super-solidus temperature range", In: *13th International Conference on Fracture (ICF-13)*, Beijing, China (2013), pp. 2528-36.
[10] Subroto, T. A. S., Miroux, A. G., Eskin, D. G., Katgerman, L., "Constitutive behaviour of an as-cast AA7050 alloy in the sub-solidus temperature range", *IOP Conference Series: Materials Science and Engineering* (2011), 27, pp. 012074.
[11] Ludwig, O., Drezet, J. M., Martin, C. L., Suéry, M., "Rheological behavior of Al-Cu alloys during solidification: Constitutive modeling, experimental identification, and numerical study", *Metallurgical and Materials Transactions A* (2005), 36, pp. 1525-35.
[12] Suyitno, A., Eskin, D. G., Savran, V. I., Katgerman, L., "Effects of alloy composition and casting speed on structure formation and hot tearing during direct-chill casting of Al-Cu alloys", *Metallurgical and Materials Transactions A* (2004), 35 A, pp. 3551-61.

[13] Rappaz, M., Drezet, J. M., Grasso, P. D., Jacot, A., "Hot tearing and coalescence: Two deeply-connected phenomena", In: *The Tenth International Conference on Modeling of Casting, Welding and Advanced Solidification Processes (MCWASP X)*, Destin, FL, USA (2003), pp. 53-60.
[14] Ludwig, O., Drezet, J. M., Ménésès, P., Martin, C. L., Suéry, M., "Rheological behavior of a commercial AA5182 aluminum alloy during solidification", *Materials Science and Engineering A* (2005), 413-414, pp. 174-9.
[15] Van Haaften, W. M., Magnin, B., Kool, W. H., Katgerman, L., "Constitutive behavior of as-cast AA1050, AA3104, and AA5182", *Metallurgical and Materials Transactions A* (2002), 33, pp. 1971-80.
[16] Sweet, L., Easton, M. A., Taylor, J. A., Grandfield, J. F., Davidson, C. J., Lu, L., Couper, M. J., Stjohn, D. H., "Hot tear susceptibility of Al-Mg-Si-Fe alloys with varying iron contents", *Metallurgical and Materials Transactions A* (2013), 44, pp. 5396-407.
[17] Mathier, V., Grasso, P. D., Rappaz, M., "A new tensile test for aluminum alloys in the mushy state: Experimental method and numerical modeling", *Metallurgical and Materials Transactions A* (2008), 39 A, pp. 1399-409.
[18] Alankar, A., Wells, M. A., "Constitutive behavior of as-cast aluminum alloys AA3104, AA5182 and AA6111 at below solidus temperatures", *Materials Science and Engineering A* (2010), 527, pp. 7812-20.
[19] Farup, I., Drezet, J. M., Rappaz, M., "In situ observation of hot tearing formation in succinonitrile-acetone", *Acta Materialia* (2001), 49, pp. 1261-9.
[20] Takayama, Y., Tozawa, T., Kato, H., "Superplasticity and thickness of liquid phase in the vicinity of solidus temperature in a 7475 aluminum alloy", *Acta Materialia* (1999), 47, pp. 1263-70.
[21] Mihanyar, S., Mo, A., M'Hamdi, M., Ellingsen, K., "Modeling of de-cohesion and the initiation of hot tearing in coherent mushy zones of metallic alloys", *Metallurgical and Materials Transactions A* (2011), 42, pp. 1887-95.
[22] Eskin, D. G., Suyitno, Mooney, J. F., Katgerman, L., "Contraction of aluminum alloys during and after solidification", *Metallurgical and Materials Transactions A* (2004), 35 A, pp. 1325-35.
[23] Lalpoor, M., Eskin, D. G., and Katgerman, L., "Cold-cracking assessment in AA7050 billets during direct-chill casting by thermomechanical simulation of residual thermal stresses and application of fracture mechanics", *Metallurgical and Materials Transactions A* (2009), 40A, pp. 3304-13.
[24] Stangeland, A., Mo, A., Eskin, D., "Thermal strain in the mushy zone for aluminum alloys", *Metallurgical and Materials Transactions A* (2006), 37, pp. 2219-29.
[25] Eskin, D. G., Katgerman, L., "Thermal contraction during solidification of aluminium alloys", In: *10th International Conference on Aluminium Alloys (ICAA-10)*, Vancouver, Canada (2006), pp. 1681-6.
[26] Stangeland, A., Mo, A., Nielsen, Ø., Eskin, D., M'Hamdi, M., "Development of thermal strain in the coherent mushy zone during solidification of aluminum alloys", *Metallurgical and Materials Transactions A* (2004), 35 A, pp. 2903-15.
[27] Suyitno, Eskin, D. G., Katgerman, L., "Thermal contraction of AA5182 for prediction of ingot distortions", *Key Engineering Materials* (2006), 306-308 II, pp. 977-82.

[28] Zhang, L., Eskin, D. G., Lalpoor, M., Katgerman, L., "Factors affecting thermal contraction behavior of an AA7050 alloy", *Materials Science and Engineering A* (2010), 527, pp. 3264-70.
[29] Magnin, B., Maenner, L., Katgerman, L., Engler, S., "Ductility and rheology of an Al-4.5%Cu alloy from room temperature to coherency temperature", *Materials Science Forum* (1996), 217-222, pp. 1209-14.

Chapter 5

SENSITIVITY ANALYSIS OF ALSIM WITH RESPECT TO MECHANICAL PROPERTIES OF ALUMINUM ALLOYS

5.1 Introduction

An advanced crack prediction model that is able to capture the geometry and specific location of the formed hot tear (HT) needs to be developed in order to reveal the connection between hot tearing and cold cracking (CC). It was suggested in Chapter 2 that ALSIM model that we use for direct-chill (DC) casting simulation has a potential to do this. Therefore, ALSIM may serve as the basis for such an advanced cracking model. Since this model has to take into account the HT occurrence on different length scales [1], ALSIM model has to be quite sensitive to different factors that influence HT formation.

As reported in the previous works, a good HT criterion should be able to predict the HT susceptibility to varying different process parameters during DC casting, for example: alloy composition, casting speed, sensitivity to the start-up regime etc. [2, 3]. Even though it was reported in Chapter 2 that ALSIM is sensitive to different casting parameters such as casting speed and inlet feeding geometry, at the moment there is no information regarding ALSIM's sensitivity to mechanical properties of different alloys.

In ALSIM these mechanical properties are described by the constitutive equations presented in Chapter 2. The values of the parameters of these equations for a given alloy form a set, which we will call “materials properties database” or “materials database” in this chapter. To obtain this database, the data from the experiment needs to be fitted to ALSIM's constitutive equation as presented in Chapter 2. The methods of obtaining such a materials database at different temperature ranges has been either presented in the previous chapters (Chapter 3 and Chapter 4) or shown in the previous work by Lalpoor [4].

From the result of Chapter 4, we see that the semi-solid constitutive behavior for Al-2% Cu (that is usually used as a substitute for different Al alloys in ALSIM) [5] and that of AA7050 (the alloy of our interest) are different (Figure 4.20). Therefore, we need to analyze the sensitivity of ALSIM model with respect to the semi-solid materials database to verify the accuracy of the casting simulation that we carried out in Chapter 2. Additionally, we need to observe the difference in simulation results (especially those with direct relationship to HT and CC susceptibility estimation) caused by different semi-solid materials database, as this is the temperature regime where HT forms.

In this chapter, we focus our study on observing the change in the themo-mechanical calculation results from ALSIM simulation, such as first principal stress and the results of both crack susceptibility estimators by utilizing different combinations of constitutive parameters (materials databases) at different temperature ranges; semi-solid state and fully solid (hardening) state. Several materials databases that we utilize for this analysis are the AA7050 database obtained in Chapter 3 and Chapter 4, and the mechanical properties

databases from other alloys available in the literature [5-7]. Moreover, we also construct and utilize an artificial materials' database to see the response of ALSIM model to an alloy that has an extremely different mechanical characteristic.

The result from this chapter will provide information on ALSIM model readiness for the development of an advanced cracking model. Additionally, the conclusion from this chapter may help the industry minimize the development cost of a new alloy database by pointing out the temperature regime of the model where the material database gives the most significant impact to the result of the simulation.

5.2 Simulation setup and cases

As mentioned in Section 5.1, our main goal in this chapter is to observe the sensitivity of ALSIM model with respect to different material databases at different temperature ranges; semi-solid and fully-solid (hardening) regime. In this work the semi-solid materials database represents the mechanical behavior of the alloy in both the sub-solid temperature regime (Chapter 3) and the super-solid temperature regime (Chapter 4). Meanwhile, the fully-solid (hardening) materials database represents the mechanical behavior of the alloy between room temperature and merge properties temperature (T_{merge} = 410 °C, with T_0 = 390 °C for AA7050) [6, 8]. To carry out the analysis, we use three different DC casting scenarios described in Chapter 2; hot-tearing (HT), cold-cracking (CC) and healthy cases.

Because we intend to study the materials database sensitivity during the DC casting simulation, we used the same simulation settings as described in section 2.2.3 (AA7050 properties) for each casting scenario. In this chapter, we only modify the materials databases of the alloy at different temperature regimes for different casting scenarios.

Table 5.1 shows the list of simulations that we carried out for the materials database sensitivity analysis. As seen from that table, we ran ALSIM simulations with the three different casting scenarios described in Chapter 2 (HT, CC and healthy case). The results of trials 1–3 have been presented in Chapter 2 and the simulations that we ran using the newly obtained materials database from Chapter 3 and Chapter 4 (i.e. using database of AA7050 in both semi-solid and fully solid (hardening) part of the temperature regime) are shown in trials 4–6. Moreover, we also ran simulations with additional materials databases: AA7050XTR in the additional HT scenario (trial 7) and AA1050 for the additional CC scenario (trial 8). These two additional databases were chosen because of their stark difference in mechanical characteristics from the existing materials databases that are readily available (i.e. Al–2% Cu [5] and AA7050).

AA7050XTR is an artificial semi-solid materials database based on the constitutive parameters of AA7050 that we obtained in Chapter 4. From the obtained parameters, some of the rheological parameters (variables that have significant influences on the force saturation level and the load development characteristics) such as p, α_0 and α_1 are multiplied by 10 to flaunt the difference (for comparison, the values in the standard AA7050 database are shown in Table 4.3). Thus, for AA7050XTR, the values of p, α_0 and α_1 are 0.8, 136.5 and 0.116, respectively. As a results the internal variables C^* and α will be increased and the cohesion of the material represented by the internal variable C will be also higher than for AA7050 for the same solid fraction. To show the difference in the tensile mechanical behavior between AA7050 and AA7050XTR databases, we plot in Figure 5.1 the tensile test curves at different solid fractions using the tensile numerical test simulator described in Chapter 4 (in Figure 4.20 and Figure 4.21).

Table 5.1 List of the simulations ran along with the materials database used in each simulation.

Simulation ID	Case	Material database	
		Semi-solid (including sub-solid)	Fully solid (hardening)
Trial 1	Healthy	Al-2% Cu [5]	AA7050
Trial 2	Cold-cracking (CC)	Al-2% Cu [5]	AA7050
Trial 3	Hot tearing (HT)	Al-2% Cu [5]	AA7050
Trial 4	Healthy	AA7050	AA7050
Trial 5	CC	AA7050	AA7050
Trial 6	HT	AA7050	AA7050
Trial 7	HT	AA7050XTR	AA7050
Trial 8	CC	AA7050	AA1050 [7]

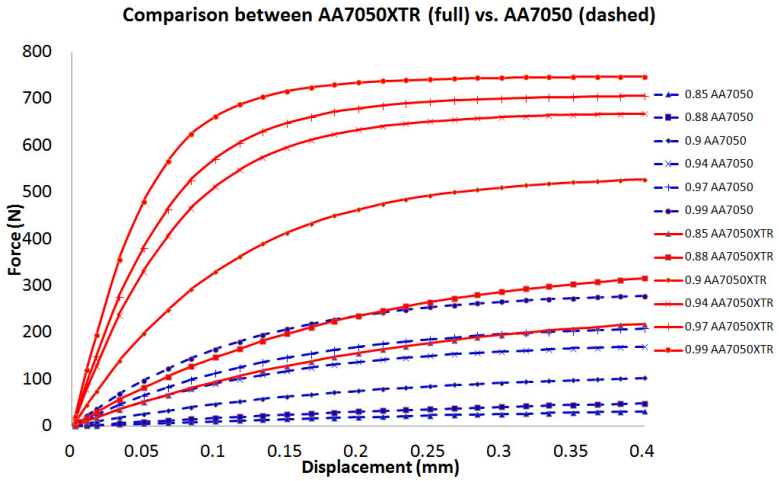

Figure 5.1 Comparison of the tensile force-displacement of semi-solid behavior between AA7050XTR (full lines) and AA7050 (dashed lines).

For the fully solid (hardening) regime database, the AA1050 database is selected because of its stark contrast to the mechanical properties of AA7050 [7, 9]. AA1050 is a member of a high-purity wrought aluminum alloy family and known to be significantly weaker than AA7050 [10]. By using these two additional mechanical property databases with different mechanical characteristics compared to the available materials databases, we can properly observe the difference on the mechanical calculation response.

For the sake of uniformity, we discuss and compare all the simulation results in this chapter at the steady state of the DC casting process, i.e. when the distance between the surface of the liquid aluminum and the billet bottom just above the starting block is approximately 750 mm.

5.3 Simulation results

5.3.1 Results of mechanical calculation

The comparison of the first principal stress result for the simulation cases that use the complete AA7050 materials database; i.e. uses AA7050 materials databases on both semi-solid and fully solid (hardening) temperature ranges, is shown in Figure 5.2a–c (or trials 4–6, respectively). Comparison with simulations using the semi-solid Al–2% Cu materials database (trials 1–3, Figure 2.5a–c) shows that the first principal stress distributions on each corresponding casting scenario, for example between the HT case obtained in Chapter 2 (trial 3) and the HT case with the complete AA7050 database (trial 6), are similar. Moreover, there is only small difference in terms of maximum and minimum first principal

stress between the cases with semi-solid Al–2% Cu materials database (trials 1–3) and semi-solid AA7050 materials database (trials 4–6). In all cases, the maximum and minimum value difference between the corresponding casting scenarios is within approximately 5 MPa.

To observe the effect of different semi-solid materials database, we compare trial 6 (AA7050 – Figure 5.2c) and trial 7 (AA7050XTR – Figure 5.2d). Both trials are utilizing HT scenario. From this comparison, we observe a small difference in terms of the first principal stress result. Not only are the stress distribution and the minimum stress value similar, but also the difference between the maximum stress values is relatively low (within 3 MPa).

The most significant difference in terms of the first principal stress calculation occurs when we change the fully solid (hardening) materials database. For this analysis, we use the CC scenario as the test-bed (the same base case used in Chapter 2) for the comparison. Based on the result from trial 2 (shown in Chapter 2) and trial 5 (Figure 5.2b), this casting scenario produces the highest first principal stress value among other casting scenarios. Thus, we think this selection is optimal to observe the effect of different fully solid (hardening) materials databases. To observe this effect, we compare trial 5 (AA7050 – Figure 5.2b) and trial 8 (AA1050 – Figure 5.2e). From this comparison, we see the resulting first principal stress is significantly different. Although the stress distribution is seemingly similar, trial 8 produces a significantly lower stress (with a maximum stress of 47 MPa and minimum stress of –1.5 MPa) compared to trial 5.

5.3.2 Results of cracking susceptibility estimation

5.3.2.1 Hot tearing

The HT susceptibility measure in ALSIM is represented by the integrated critical strain (ICS) – higher values represent higher susceptibility of certain regions in the billet to HT (see Chapter 2). Figure 5.3 shows the comparison of ICS values for different simulation cases. From assessment of comparable casting scenarios (e.g. between trial 1 and trial 4, between trial 2 and trial 5 etc. – the simulation results for trial 1,2 and 3 is shown in Chapter 2 – Figure 2.6), we did not see any significant difference in terms of the ICS value nor the spatial distribution. For the comparison of the HT scenario, there is also not much difference in the ICS calculation result with respect to different semi-solid databases; Al–2% Cu (trial 3 – Figure 2.6c), AA7050 (trial 6 – Figure 5.3c) and AA7050XTR (trial 7 – Figure 5.3d). From Figure 5.3, we can see that the simulations that utilize full AA7050 mechanical database produces the same ICS trend at different casting case as found in Chapter 2 (Figure 2.6), the healthy (Figure 5.3a) has the lowest ICS compared to CC (Figure 5.3b) and HT (Figure 5.3c) cases, while HT has the highest ICS value of all cases.

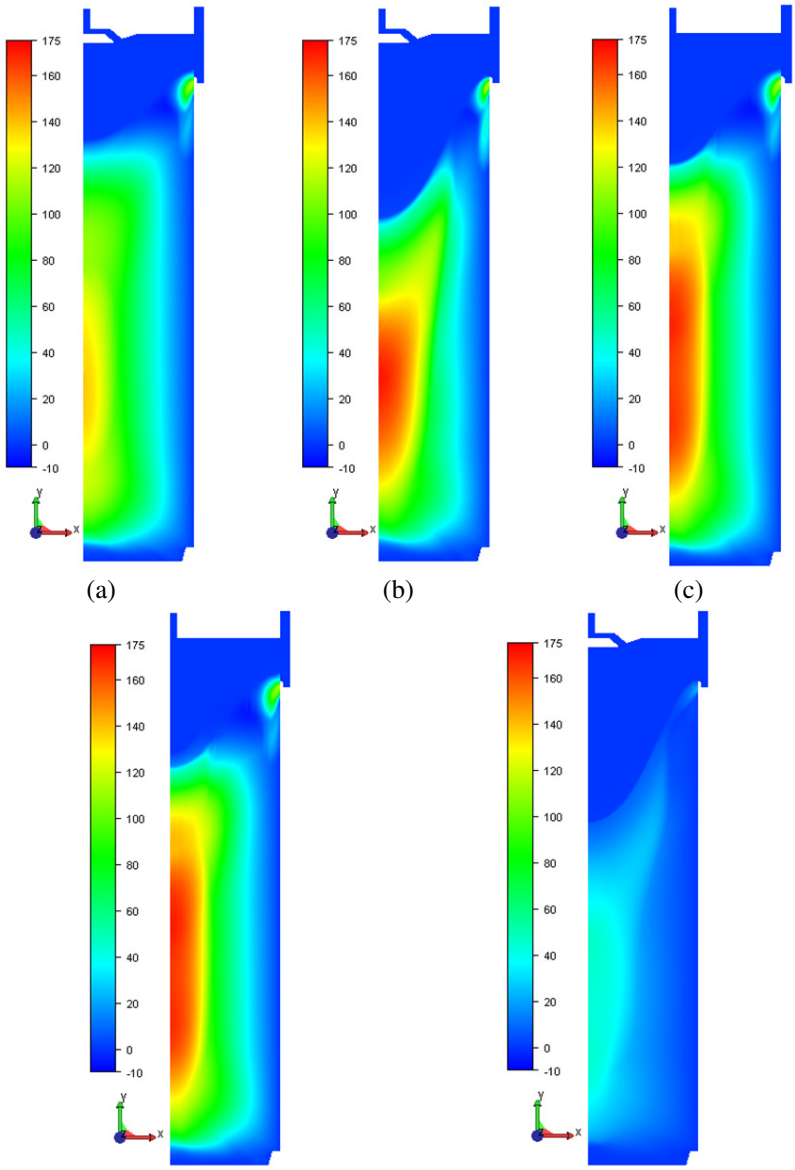

Figure 5.2 Comparison of first principle stress calculations (unit in MPa) on different casting scenarios and materials database. Simulation that uses complete AA7050 materials databases; trial 4 (a), trial 5 (b) and trial 6 (c). Simulation that uses AA7050XTR on semi-solid database, trial 7 (d). Simulation that uses AA1050 at the fully solid (hardening) part of the database, trial 8 (e). The results from trials 1–3 are presented in Chapter 2 (Figure 2.5).

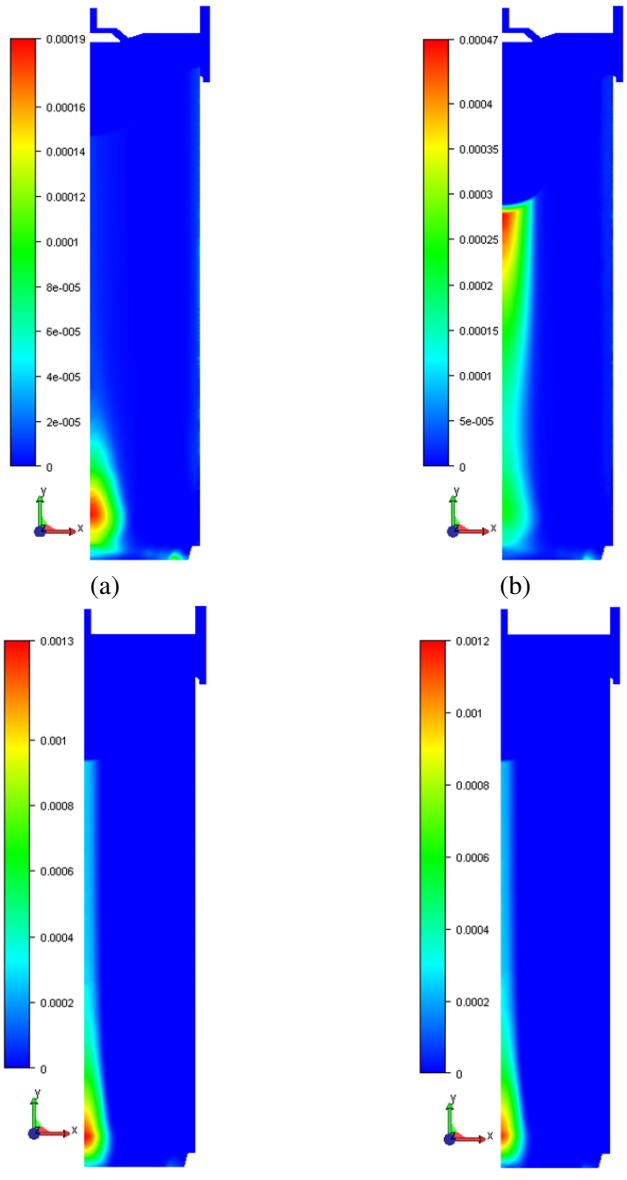

Figure 5.3 Comparison of integrated critical strain (ICS) value on different casting scenarios and materials databases. Simulation that uses complete AA7050 materials databases; trial 4 (a), trial 5 (b) and trial 6 (c). Simulation that uses AA7050XTR on semi-solid database; trial 7 (d). The results from trials 1–3 are presented in Chapter 2 (Figure 2.6).

Figure 5.4 shows the ICS value comparison of simulation cases with different semi-solid databases (Al–2% Cu, AA7050 and AA7050XTR). This plot is taken at the centerline of the billet starting from just above the bottom block up to billet height of 500 mm. We observe that the ICS value has a similar trend for all semi-solid databases; there is a peak value in the start-up phase and subsequently the value decreases, becoming stable at a value around 0.00025. The figure also shows that the simulations with the semi-solid Al–2% Cu database (trial 3) and the AA7050 database (trial 6) have a comparable ICS value. However, the result of the simulation with the AA7050XTR database (trial 7) shows a slightly lower overall ICS value compared to the two other HT simulations (trials 3 and 6).

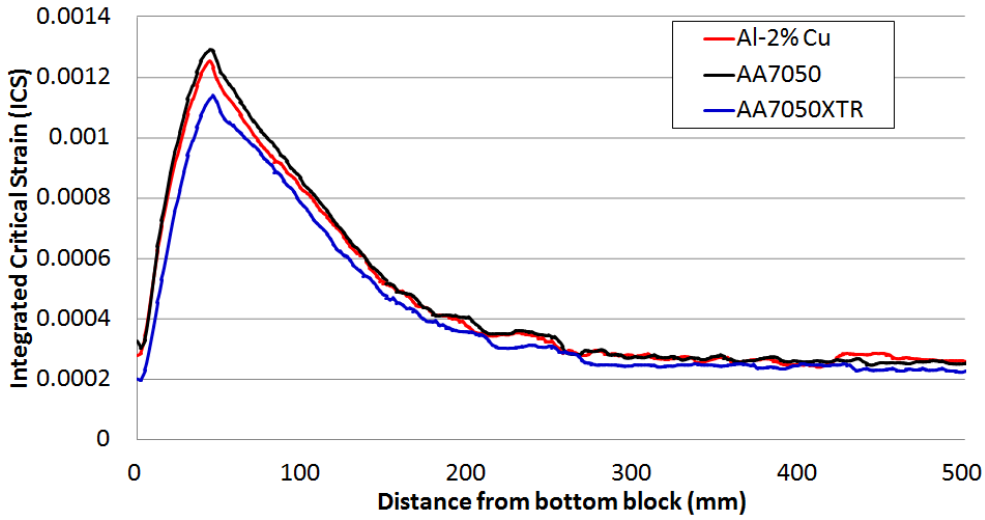

Figure 5.4 ICS value comparison with different semi-solid databases; Al–2% Cu (trial 3), AA7050 (trial 6) and AA7050XTR (trial 7). This plot is taken at the centerline of the billet starting from above the bottom block up to billet height of 500 mm. These simulations presented in this figure are utilizing the HT casting scenario.

5.3.2.2 Cold cracking

As described in Chapter 2, the cold-crack susceptibility in ALSIM model is represented by the critical crack size (CCS) value – a lower value represents a higher susceptibility of the region in the billet to CC. Figure 5.5 shows the comparison of CCS values from different simulation cases (trials 4–8).

Figure 5.5a, b and c (trials 4, 5 and 6 respectively) show the results of the CCS calculation on simulations that utilize the semi-solid AA7050 database. To see the effect of semi-solid materials database towards the CC susceptibility estimation, we then compare the results of these trials with the results of simulation cases that use Al–2% Cu semi-solid materials

database (trials 1–3, Chapter 2). From this comparison, we see the trend of the CCS value distribution is similar for each comparable casting scenario (e.g. comparison between trials 1 and 4, trials 2 and 5 etc.).

We also analyzed the difference in CCS values between three HT cases that utilize different semi-solid databases (Al–2% Cu – trial 3, AA7050 – trial 6 and AA7050XTR – trial 7). This is done by plotting the CCS values from center of the billet to the surface of the billet at 350 mm above the bottom block (steady-state casting state). From this analysis, we found that the change in the semi-solid materials database does not affect the CCS calculation result.

The most significant change in the CCS value occurs when we changed the fully solid (hardening) materials database into the AA1050 (trial 8 – Figure 5.5e) as compared to the trial with AA7050 materials database (trial 5 – Figure 5.5b). This comparison is done on CC casting scenario. From trial 8 (Figure 5.5e), we observe the area that is susceptible to CC (blue colored region of the billet in Figure 5.5) is significantly smaller than the simulation that utilized complete AA7050 materials database (trial 5 – Figure 5.5b). Moreover, the lowest CCS value increases to around 25 mm instead of the single digit value produced in the result of trial 5 (Figure 5.5b). This result shows the simulation using AA1050 in the fully solid (hardening) materials database has a lower CC susceptibility compared to the simulations that use the AA7050 database in the same temperature regime.

5.4 Discussion

The results from Section 5.3 and Chapter 2 show that, in general, ALSIM is sensitive to different materials databases. The results in Figure 5.2 and Figure 5.5 show that by changing the fully solid (hardening) materials database into AA1050, the first principal stress result and consequently, the CC susceptibility of the alloy, decrease significantly. This is because AA1050 is known as a soft alloy with relatively low strength [7] and high ductility [11] as compared to AA7050 [9]. Moreover, this also supports the fact that CC is more prone to occur in high strength aluminum alloys [12]. This shows that ALSIM model is sensitive with respect to different material databases in the fully-solid (hardening) regime.

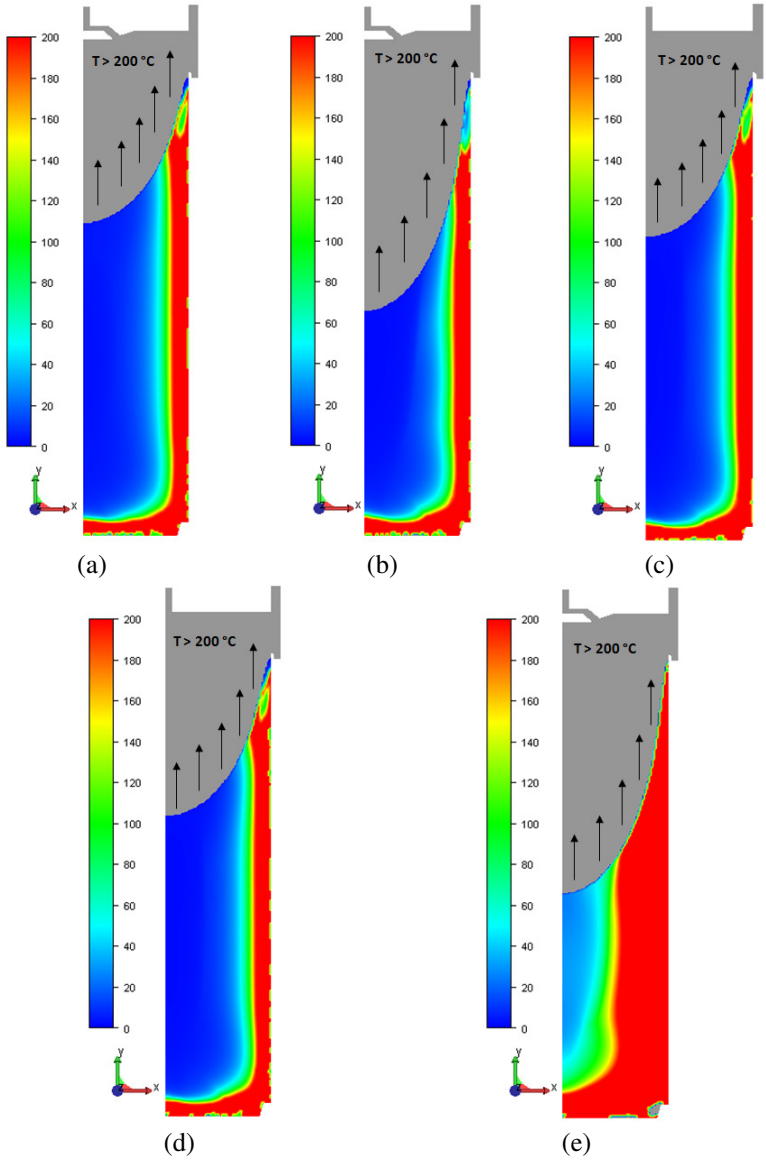

Figure 5.5 Comparison of the critical crack size value or CCS (unit in mm) on different casting scenarios and materials database. Simulation that uses complete AA7050 materials databases; trial 4 (a), trial 5 (b) and trial 6 (c). Simulation that uses AA7050XTR on semi-solid materials database; trial 7 (d) and simulation that uses AA1050 on the fully solid (hardening) materials database; trial 8 (e). The results of CCS calculation from trial 1 – 3 are presented in Chapter 2 (Figure 2.8).

On the other hand, Figure 5.2 and Figure 5.3 show that changing the semi-solid materials database does not bring about significant changes in the first principal stress results and the HT susceptibility calculation (ICS). This result is quite interesting, as we have expected to have noticeable differences because of quite different constitutive parameters in the tested semi-solid databases.

To gain insight into this finding, let us take a closer look at the results of the mechanical calculation in the mushy zone, especially between the rigidity point – where the alloy begins to have an appreciable mechanical property (f_s = 0.85) and the solidus point (f_s = 1.0). This is the solidification regime where HT are usually formed [13, 14]. As a representative case, we select the HT casting scenario because it gives the highest ICS peak value among all casting scenarios. Figure 5.6 shows an illustration of our analysis. We made a plot along the centerline of the billet at the deepest part of the sump, starting from f_s = 0.85 up to the solidus point f_s = 1.0. In this figure, we show the amount of solid fraction with respect to different positions of the sump. From this illustration, Figure 5.7 and Figure 5.8 show the results of the radial strain-rate and radial stress calculations, respectively, for HT casting scenarios with different semi-solid material databases.

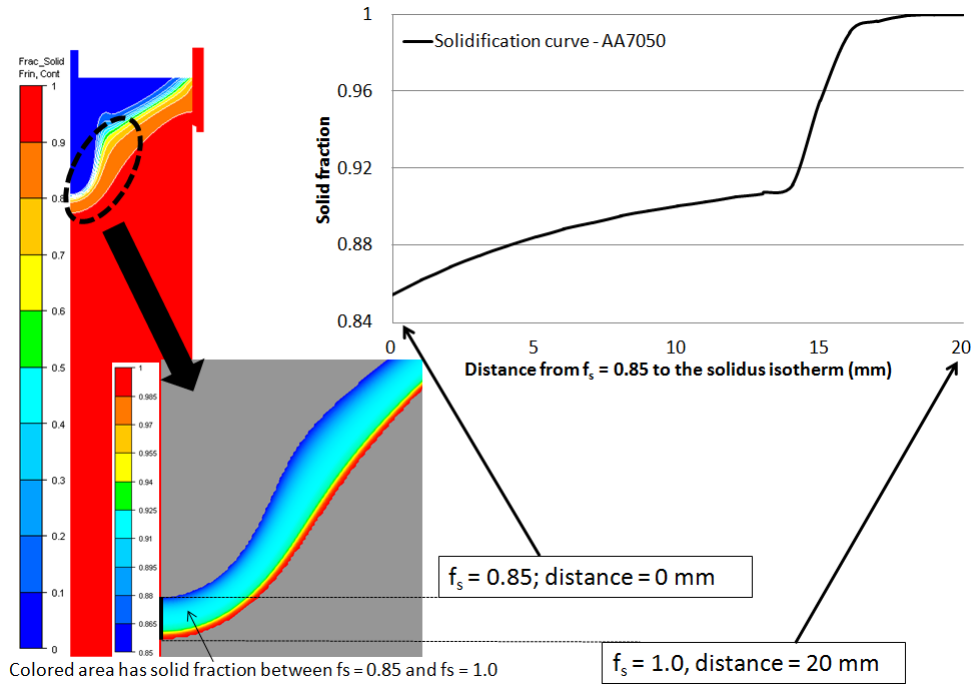

Figure 5.6 Illustration of the detailed analysis at the end part of the mushy-zone of the alloy during DC casting.

Figure 5.7 shows that, in this part of solidification range, all three semi-solid databases have comparable values of the strain rate (between 0 and 0.0002 s^{-1}). In general, the trends from the different databases are similar; at lower solid fraction, the strain-rate is relatively high and it decreases as the solid fraction increases. Then it approaches zero when the fully solid state is reached. As the alloy cools down further beyond the solidus point (when the value of the horizontal axis in Figure 5.7 is higher than 20 mm), the strain rate increases again. This could be due to the significant strength buildup as the alloy becomes fully solid [6]. The same figure shows that Al–2% Cu and AA7050 result in similar values. Meanwhile, the simulation with the AA7050XTR database produces the lowest strain-rate of all the databases. This might be because AA7050XTR is stronger compared to the two other materials (Figure 5.1), therefore, it deforms less under similar casting conditions.

This result also explains the reason the AA7050XTR database produces the lowest ICS value among the other databases. The ICS formulation (Eq. 2.18 in Chapter 2) shows this value is an accumulation of strain during the time when it is prone to HT (from f_s = 0.9 to f_s = 0.99). This might also explain the correlation between the semi-solid strength of the alloy with its susceptibility to HT. This is under assumption that we are comparing alloys with similar thermo-physical properties (e.g. thermal conductivity, solidification path, liquid viscosity and the onset temperature of mechanical contraction, etc.).

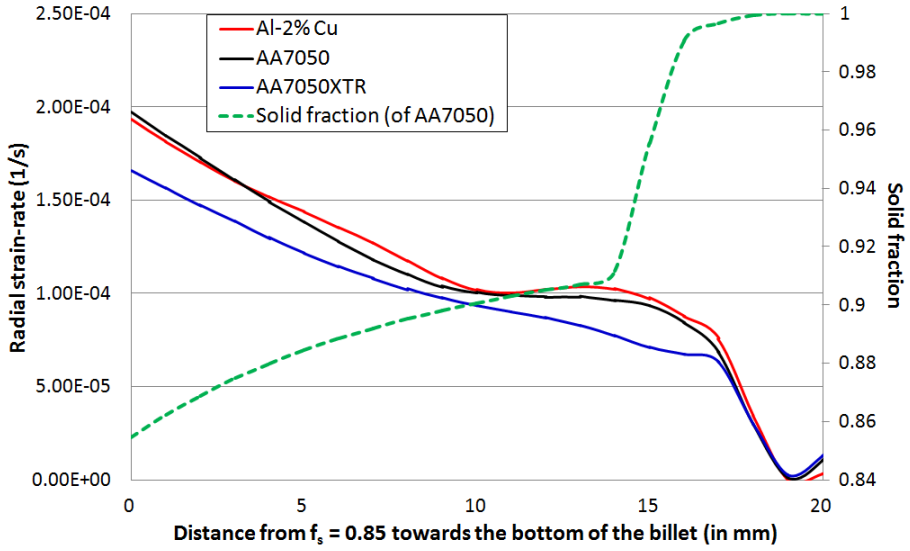

Figure 5.7 Plot of radial strain-rate calculation result from HT simulations with different semi-solid materials databases (Al-2% Cu – trial 3, AA7050 – trial 6 and AA7050XTR – trial 7) as compared to its respective solid fraction at different position of the sump.

Figure 5.8 shows the radial stress evolution at different locations along the sump for three different semi-solid databases. In general, all databases result in a similar trend; the radial stress increases with the solid fraction. Additionally, there is a significant increase in the stress value as the alloy approaches the fully solid state. This phenomenon reflects grain coalescence commonly observed in the last portion of solidification [15-19]. However, in this result, the sharp increase in stress occurs fairly late, near the end of solidification. This comparison suggests that the behavior of the radial stress evolutions with the solid fractions for Al–2% Cu and AA7050 is relatively similar. AA7050XTR, however, has different stress development characteristics compared to the other alloys. This alloy has a steeper stress slope even at the lower solid fraction (before the sharp transition) and has a higher overall stress value for all solid fractions. This is understandable, because from Figure 5.1, AA7050XTR is clearly stronger compared to the AA7050, which has a comparable strength with Al–2% Cu (Figure 4.20). Figure 5.8 also shows that AA7050 has approximately twice higher stress value compared to Al–2% Cu throughout the mushy-zone. This supports our finding in Chapter 4 (Figure 4.20) that AA7050 is stronger than Al-2% Cu. This observation shows that ALSIM is fairly responsive to the different semi-solid mechanical materials databases. Furthermore, the stress values at different solid fractions from the ALSIM simulation are of the same order of magnitude than the experimental stress values derived in Chapter 4 from Figure 4.10.

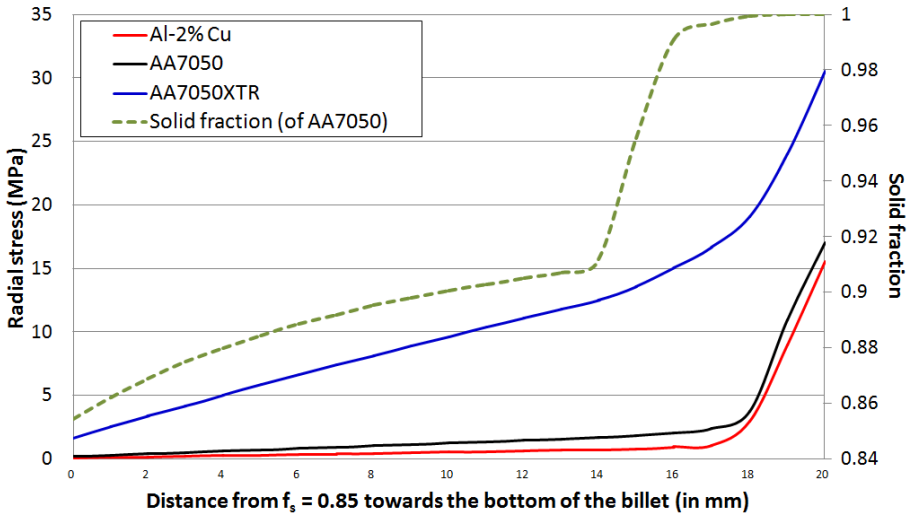

Figure 5.8 Plot of radial stress calculation from HT simulations with different semi-solid mechanical properties (Al-2% Cu – trial 3, AA7050 – trial 6 and AA7050XTR – trial 7) as compared to its respective solid fraction at different position of the sump.

There are two possible factors that may change the results of semi-solid calculation: First, the casting conditions (e.g. cooling condition and casting geometry) because this factor

defines the width of the semi-solid phase. Second is the onset of thermal contraction temperature. Although we use the same temperature (AA7050) for all trial cases shown in this chapter and Chapter 2, this variable defines the amount of time that the alloy has to spend in the semi-solid state (below rigidity temperature). This amount of time is proportional to the utilization time of the semi-solid materials database. Therefore, longer time corresponds to the larger impact on the simulation.

The results from Section 5.3 (Figure 5.5) show that the CC criterion (CCS) in ALSIM is fairly sensitive with respect to different alloy properties and the results correlate with the experimental findings [7, 11]. Therefore, this criterion is ready to be used as a part of the cracking criterion to observe the connection between HT and CC. However, the HT criterion (ICS) seems to be lacking in sensitivity to different mechanical behaviors (Figure 5.4). As Figure 5.1 and Figure 5.3 illustrate that strong mechanical property difference between AA7050 and AA7050XTR does not translate in any significant ICS differences. This suggests that ALSIM HT susceptibility estimator needs improvement. One possible explanation is that the studied DC casting process is predominantly a strain (and strain-rate) –controlled process (i.e. the displacements of the boundary of the mushy zone are controlled by the casting geometry, water cooling, etc). This would explain the result shown in Figure 5.7 that for alloys of different mechanical characteristics, the strain-rate is relatively similar. This also explains the reason that the ICS is sensitive with respect to different casting conditions (as shown in Chapter 2, Figure 2.6 and Figure 2.7b). However, we found that ALSIM semi-solid mechanical model is sensitive with respect to different materials database because the stress calculation result differs for different materials database (see Figure 5.8). This means that ALSIM is sensitive to different materials database but ICS, which is a strain based criterion, is not sufficient to capture the HT susceptibility for different materials. Therefore, the current HT criterion in ALSIM needs to be completed so it is able to capture the HT susceptibility of different alloys with different mechanical behavior.

The findings in this chapter not only reveal additional development points for ALSIM but are also beneficial to the industrial application of ALSIM. From the result, we may offer a suggestion to industry for building materials databases of new industrial alloys. Particularly, for alloys that are not susceptible to HT, the semi-solid materials database is not the most critical information needed for the simulation (i.e. semi-solid mechanical database originated from the same alloy family may be used). This way, the development cost of the new materials database could be reduced.

5.5 Conclusions

From the results and analysis of ALSIM model sensitivity with respect to different materials databases for the different temperature ranges that we carried out in this chapter, we can draw several conclusions as follows:

1. In general, ALSIM model is fairly sensitive with respect to different materials databases. This is shown by the results of the stress calculation in the semi-solid temperature regime (Figure 5.8) and the comparison between the different materials databases in the fully solid (hardening) state, e.g. the first principal stress for trial 5 (Figure 5.2b) and trial 8 (Figure 5.2e).
2. The simulation variables that may influence the semi-solid mechanical calculation are the casting conditions (e.g. casting geometry, casting speed and cooling rate, etc.), transition region and mushy zone widths, onset temperature of thermal contraction and solidification behavior of the alloy. These factors may define the width of the semi-solid regime where such materials databases are utilized for calculation.
3. The CC criterion (CCS) which takes into account the first principal stress calculation from ALSIM [6, 20-22] is quite sensitive to different materials database, especially at the fully solid (hardening) temperature regime. Thus, in terms of materials database sensitivity, the CC criterion is ready to be part of the cracking criterion for observing the connection between HT and CC.
4. Although ALSIM HT criterion is sensitive to different casting parameters (e.g. casting speed and inlet geometry, as explained in Chapter 2), this criterion is not particularly sensitive with respect to different material properties. Therefore, alongside ICS, it needs a complementary HT criterion that is material properties dependent. This way, ALSIM model can be used as a host for the advanced cracking model.
5. For alloys and casting setups that do not result in HT senstive conditions (e.g. by having extended semi-solid regime), the semi-solid materials database is not critical for estimating the mechanical behavior of the ingot during casting. Therefore, for the development of materials databases of new industrial alloys, it would be more efficient to focus on obtaining the fully-solid (hardening) materials database.

References

[1] Eskin, D. G., Katgerman, L., "A quest for a new hot tearing criterion", *Metallurgical and Materials Transactions A* (2007), 38 A, pp. 1511-9.
[2] Farup, I., Mo, A., "Two-phase modeling of mushy zone parameters associated with hot tearing", *Metallurgical and Materials Transactions A* (2000), 31, pp. 1461-72.
[3] Suyitno, Kool, W. H., Katgerman, L., "Hot tearing criteria evaluation for direct-chill casting of an Al-4.5 pct Cu alloy", *Metallurgical and Materials Transactions A* (2005), 36, pp. 1537-46.
[4] Lalpoor, M., "Study of cold cracking during DC-casting of high strength aluminum alloys", [Ph.D. Thesis] (2010), Delft University of Technology.
[5] Ludwig, O., Drezet, J. M., Martin, C. L., Suéry, M., "Rheological behavior of Al-Cu alloys during solidification: Constitutive modeling, experimental identification, and numerical study", *Metallurgical and Materials Transactions A* (2005), 36, pp. 1525-35.
[6] Lalpoor, M., Eskin, D. G., and Katgerman, L., "Cold-cracking assessment in AA7050 billets during direct-chill casting by thermomechanical simulation of residual thermal stresses and application of fracture mechanics", *Metallurgical and Materials Transactions A* (2009), 40A, pp. 3304-13.
[7] Van Haaften, W. M., Magnin, B., Kool, W. H., Katgerman, L., "Constitutive behavior of as-cast AA1050, AA3104, and AA5182", *Metallurgical and Materials Transactions A* (2002), 33, pp. 1971-80.
[8] Fjær, H. G., Mo, A., "ALSPEN-A mathematical model for thermal stresses in direct chill casting of aluminum billets", *Metallurgical Transactions B* (1990), 21, pp. 1049-61.
[9] Lalpoor, M., Eskin, D. G., Katgerman, L., "Fracture behavior and mechanical properties of high strength aluminum alloys in the as-cast condition", *Materials Science and Engineering A* (2008), 497, pp. 186-94.
[10] ASM International Handbook Committee, "ASM handbook, Volume 2", Materials Park, OH, USA, ASM International (1990).
[11] Li, X., He, L., Cao, Y., Zhu, P., Guo, Y., Cui, J., "Effects of microporosity on the tensile properties of aluminum alloy", *Advanced Materials Research* (2012), 422, pp. 627-31.
[12] Drezet, J. M., Phillion, A. B., "As-cast residual stresses in an aluminum alloy aa6063 billet: Neutron diffraction measurements and finite element modeling", *Metallurgical and Materials Transactions A* (2010), 41, pp. 3396-404.
[13] Eskin, D. G., "Physical Metallurgy of Direct Chill Casting of Aluminum Alloys (Advances in Metallic Alloys)", CRC Press, Taylor & Francis group, LLC (2008).
[14] Eskin, D. G., Suyitno, Katgerman, L., "Mechanical properties in the semi-solid state and hot tearing of aluminium alloys", *Progress in Materials Science* (2004), 49, pp. 629-711.
[15] Fabrègue, D., Deschamps, A., Suéry, M., Poole, W. J., "Rheological behavior of Al-Mg-Si-Cu alloys in the mushy state obtained by partial remelting and partial solidification at high cooling rate", *Metallurgical and Materials Transactions A* (2006), 37, pp. 1459-67.
[16] Giraud, E., Suery, M., Coret, M., "Mechanical behavior of AA6061 aluminum in the semisolid state obtained by partial melting and partial solidification", *Metallurgical and Materials Transactions A* (2010), 41, pp. 2257-68.

[17] Mathier, V., Grasso, P. D., Rappaz, M., "A new tensile test for aluminum alloys in the mushy state: Experimental method and numerical modeling", *Metallurgical and Materials Transactions A* (2008), 39 A, pp. 1399-409.
[18] Phillion, A. B., Thompson, S., Cockcroft, S. L., Wells, M. A., "Tensile properties of as-cast aluminum alloys AA3104, AA6111 and CA31218 at above solidus temperatures", *Materials Science and Engineering A* (2008), 497, pp. 388-94.
[19] Subroto, T., Miroux, A., Eskin, D. G., Ellingsen, K., Marson, A., M'Hamdi, M., Katgerman, L., "Tensile mechanical behavior of as-cast AA7050 alloy in the super-solidus temperature range", In: *13th International Conference on Fracture (ICF-13)*, Beijing, China (2013), pp. 2528-36.
[20] Lalpoor, M., Eskin, D. G., Katgerman, L., "Cold cracking development in AA7050 direct chill-cast billets under various casting conditions", *Metallurgical and Materials Transactions A* (2010), 41A, pp. 2425-34.
[21] Lalpoor, M., Eskin, D. G., Ruvalcaba, D., Fjær, H. G., Ten Cate, A., Ontijt, N., Katgerman, L., "Cold cracking in DC-cast high strength aluminum alloy ingots: An intrinsic problem intensified by casting process parameters", *Materials Science and Engineering A* (2011), 528, pp. 2831-42.
[22] Eskin, D. G., Lalpoor, M., Katgerman, L., "Cold cracking during direct-chill casting", In: *Light Metals, TMS*, San Diego, CA, USA (2011), pp. 669-74.

Chapter 6

FORMATION OF A HOT TEAR UNDER CONTROLLED SOLIDIFICATION CONDITIONS

6.1 Introduction

Progress in predicting the cold cracking (CC) occurrence was recently made using a fracture mechanics approach [1, 2]. The developed criterion for this type of crack states that solidification defects that survive until the ingot is fully solid could become the initiation point of CC if they exceed a critical crack size. It was also suggested that the presence of under-developed or microscopic (micro) hot tear (HT) could increase the CC susceptibility in an ingot [3]. This is because such a micro HT could acts as an initiation point of the catastrophic CC. However, the validation of this assumption is yet to be done because it requires the presence of a HT defect with known size prior to the CC testing. So far, the method to fully control the formation of HT (to a quantitative level) is not yet available. Therefore, the development of an experimental technique that would allow creating a HT under controlled conditions is needed and will be the subject of this chapter.

Recent experimental advances give the possibility to perform high-resolution and in-situ observation of HT [4-6]. However, most of these studies are directed toward the development of HT up to complete failure. Our main focus is on the contrary, on undeveloped HT that remains within the billet and could act as a nucleation point for a catastrophic CC.

The purpose of this chapter is to demonstrate an experimental technique that has potential to control the size of the formed micro HT by controlling test parameters such as cooling rate and deformation rate in a small-scale casting process. The sizes and location of created HT are measured by X-Ray microtomography (XMT) technique after full solidification of the sample. Subsequently, such samples with formed HT within can be used for a test that simulates CC occurrence at lower temperature. The result from such a test can be used to verify the existing CC criterion [7]. This verification experiment is the main subject of Chapter 7.

6.2 Experimental design

The complete verification experiment on the connection between HT and CC is divided into four phases as shown in Figure 6.1. In the first phase (I), we need to produce samples with a controlled amount of HT within the sample. We carry out this task by performing a controlled solidification experiment. Our task in the next phase (II) is to characterize the formed HT within the samples produced in the previous step. To complete this task, we utilize XMT technique to perform a 3-D reconstruction of the HT within the samples. After we obtain the 3-D images, we need to quantify the formed HT. Image analysis technique is used to complete this task (III). After we possess both the HT samples and the quantitative information of the formed HT on each sample, we carry out room temperature tensile tests

on those HT samples (IV) to simulate the CC occurrence. This is to validate the existing CC criterion [8] using the assumption of HT as the crack initiation point with the information obtained in the previous phase (III). Phases (I) and (II) are the main focus of this chapter, whereas phases (III) and (IV) will be covered in Chapter 7.

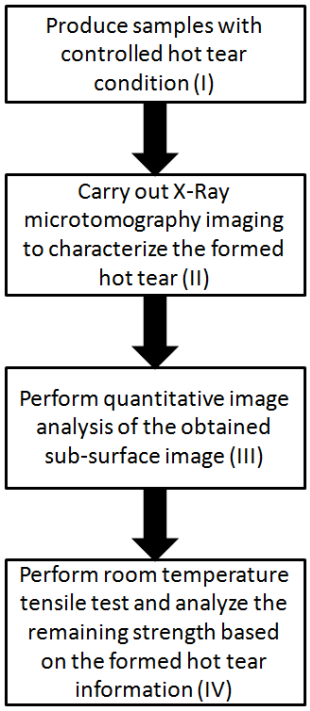

Figure 6.1 Flow chart of the experimental phases on verification of the connection between HT and CC.

6.2.1 Mechanical experimental setup

The experiment for phase (I) (Figure 6.1) is carried out at the SIMaP - GPM2 laboratory in Grenoble INP, France. The setup used for the tests is schematically depicted in Figure 6.2a and the photo of the setup is shown in Figure 6.2b. An Adamel DY34 machine equipped with a 2 kN load cell was utilized. The samples were machined from the billet as cylinders with a diameter of 9.5 mm and length of 120 mm. Additional features such as holes at 29 mm off the mid-length were machined on the sample for the water-cooling purposes (Figure 6.2). The temperature during the test was controlled by a Eurotherm^{TM} temperature controller and measured by a K-type thermocouple of 0.5 mm diameter located at mid-length of the sample at a depth of 2 mm from the surface.

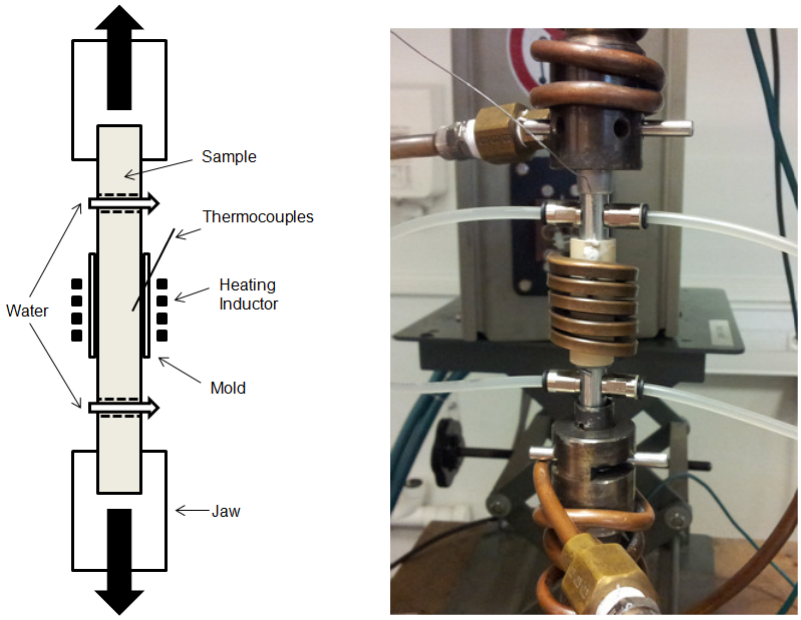

(a) (b)

Figure 6.2 Schematics (a) and a photograph (b) of the experimental setup for the formation of HT.

The testing cycle of the experiment follows Figure 6.3. First, the sample was heated by induction to the fully liquid state or $T_{liquidus}$ (635 °C) with a heating rate of 2 °C/s. Since the ends of the sample were cooled down by water circulation, a temperature gradient developed along the length of the sample with the hottest point at mid-length where the temperature was recorded. During heating, the thermal expansion of the sample was accommodated by the displacement of the jaw, thus minimizing the imposed force to the sample (Phase – I in Figure 6.3). When the center of the sample reached the liquidus temperature, it was held for 30 s to stabilize the temperature gradient (II). At this point, the jaw displacement due to thermal expansion of the sample was about 0.82 mm. Subsequently, the sample was cooled down at controlled cooling rates that resembled the cooling rates at the center part of a billet during DC casting: between 0.1 and 1.0 °C/s. Two types of jaw displacement modes have been used during this phase (III). For the first setting, named "constrained", the jaw movement was locked so that the force was built up due to thermal contraction. In the second setting, force compensation was provided by moving the jaws towards each other at a constant speed to reduce the force generated by the thermal contraction. The compensation speeds, or displacement compensation rates, used in this work were between 0.00018 mm/s and 0.0009 mm/s. In both cases, when the temperature reached the solidus temperature ($T_{solidus}$ = 465 °C), the force level in the sample

was minimized and the sample was cooled down to room temperature at the same cooling rate (IV). The force minimizing step at the last phase was also to ensure that only HT were produced inside the sample and that such a defect did not develop further during cooling in the fully solid state. At the end of the test, the sample length increased on average by 0.21 mm. All of the variables of the experiment (temperature, jaw displacement and load) were recorded in real time during the test.

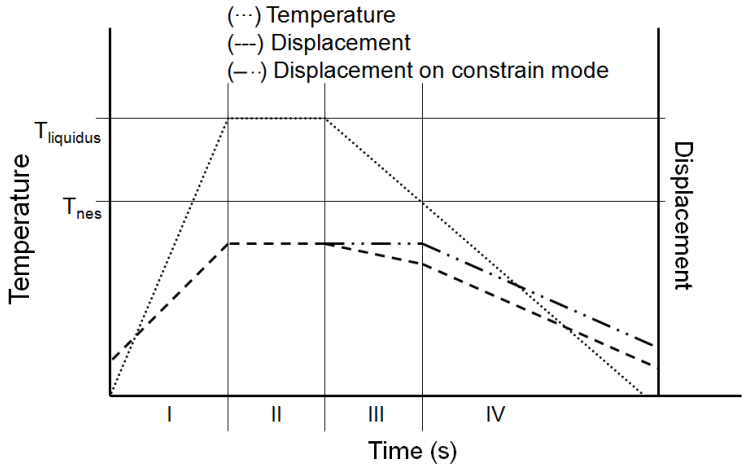

Figure 6.3 Thermal and mechanical test cycle of the experiment.

We made separate tests to observe the axial and radial temperature distribution in the sample during the heating cycle of the test as shown in Figure 6.3. In these tests, we simulate the heating phase, holding at near solidus temperature (460 °C) and then cooling with prescribed cooling rates similar with the thermo-mechanical tests. To observe the axial temperature distribution, we used two thermocouples along the center-axis; one was at the mid-length and the other was 10 mm off the mid-length. Using linear extrapolation to $T_{liquidus}$, the temperature at 10 mm off mid-length was approximately 96 °C lower than at the mid-length. To observe radial temperature distribution, we did a test with two thermocouples at the mid-length of the sample; one was placed at the center-axis and the other placed 2 mm below the surface. From such a test, in the heating phase, there was not much temperature variation (in the end of the heating phase, by linear extrapolation to $T_{liquidus}$, the temperature at the center-axis was 5 °C lower as compared to the temperature at 2 mm below the surface). During the holding phase, the center of the sample was approximately 3.5 °C cooler than at 2 mm below the surface. However, there was electromagnetic stirring effect on the liquid phase of the alloy caused by the induction coil that might have helped to homogenize the temperature distribution across the radial direction. We also measured the difference of cooling rate between the center-axis and 2 mm below the surface during the cooling phase. The average cooling rate is homogeneous

between the center-axis and 2 mm below the surface − the difference of the average cooling rate between these two points was approximately 0.005 °C/s independent of the used cooling rates. This accuracy is good compared to the used cooling rates.

6.2.2 Hot tear characterization via X-Ray microtomography

To characterize the formed HT, we need a characterization technique that is able to perform non-destructive three-dimensional (3-D) reconstruction of the sub-surface condition of a solid sample. Moreover, this method also has to be sensitive with respect to material density in order to distinguish between void (formed HT) and matrix (sample). Therefore we select XMT method to complete this task [9]. To carry out the 3-D reconstruction, we use the Phoenix Nanotom® X-Ray microtomography scanner [10] located in the Civil Engineering and Geoscience Faculty of Delft University of Technology. The picture of the instrument and the general schematics of the XMT method are shown in Figure 6.4.

We carry out the imaging of the central part of the tested samples, where the re-solidification process and most deformation take place. During the rotation of the sample over 360°, 1440 transmission images were recorded. The voxel size of the image was set to 5 µm (length of each side). After data acquisition, 3-D images of the sample were reconstructed using VG Studio 2.0 software. Further image analysis in this work was carried out using Fiji image analysis software [11].

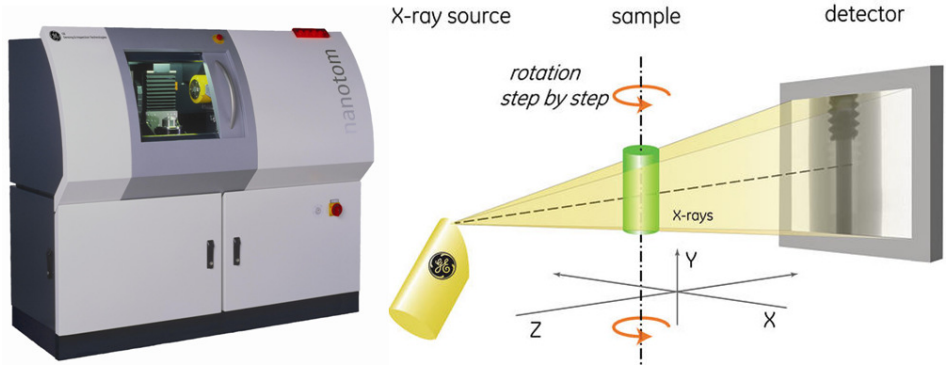

Figure 6.4 X-ray microtomography experimental setup and the basic concept of X-ray tomography imaging [10].

6.3 Results

6.3.1 Mechanical response

When the sample reaches phase III (refer to Figure 6.3) and starts cooling down while being constrained, we typically observe the start of mechanical response at approximately 600°C (solid fraction or $f_s = 0.7$). The load starts to be appreciable around 575°C ($f_s = 0.8$) and will gradually develop as the solid fraction increases. Solid fractions are calculated from the temperature measured at mid-length using JMat-Pro® software. Figure 6.5a shows for different cooling rates the average force value at different solid fractions from at least four tests. Several stages can be distinguished from the slope of force increase; in general, between $f_s = 0.8$ and 0.85, the slope is shallow and such a slope becomes steeper between $f_s = 0.85$ and 0.9, it subsequently becomes shallow again between $f_s = 0.9$ and 0.97 (in this regime, the engineering stress or σ_E is between 0.14 and 0.24 MPa), and then finally above $f_s = 0.97$ it increases again up to $f_s = 1.0$ (at this point σ_E is between 0.21 and 0.28 MPa). We also observe from the data that the lowest cooling rate (0.1 °C/s) produces the highest force as the solid fraction increases above 0.88.

Figure 6.5b shows that the measured force in the force-compensation mode is lower than in the constrained mode. Additionally, this figure also demonstrates a typical force shootout at the end of solidification (at approximately $f_s = 0.97$). This may indicate an advanced grain coalescence point, thus giving the alloy a significantly stronger structure.

6.3.2 X-Ray microtomography imaging

Figure 6.6 demonstrates that the XMT technique can provide detailed microstructure information based on the density of different phases of the alloy. Air or void spaces appear in black, the aluminum matrix is represented by grey, while eutectic phases that contain heavier elements, for instance Al_2CuMg (S-phase), $Al_2Mg_3Zn_3$ (T-phase) and $MgZn_2$ (M-phase) [12, 13], appear as lighter grey.

At the lowest cooling rate in the series (0.1 °C/s) in the constrained mode (Figure 6.6a), we observe the accumulation of eutectic phases in the center part of the sample (within dashed ellipse of Figure 6.6a) and small voids with typical size roughly between 150 and 300 μm within the eutectic region. This finding is coherent with the result in previous observation [6]. At the highest cooling rate (1.0 °C/s) in the constrained mode (Figure 6.6b), the HT damage is well developed and the sample is almost torn apart. Furthermore, eutectic phase is uniformly distributed in the solidified volume. In addition, the propagation of the initiated HT has already taken place in the sample as the crack crosses the entire sample diameter and only a few bridges link the two parts of the sample. Figure 6.6c shows that as the cooling rate decreases to 0.5 °C/s, the eutectic feeding becomes more active than in the

case of 1 °C/s, thus compensating some part of the deformation and acting as the "last glue" that prevents the sample from being completely torn apart by the HT.

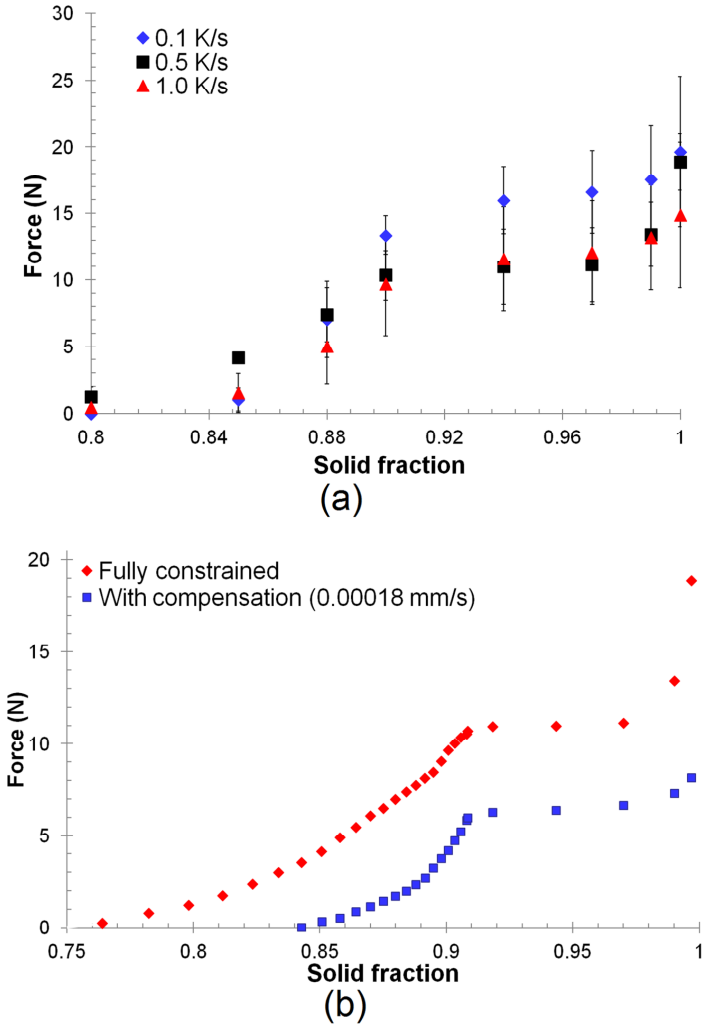

Figure 6.5 Average measured forces versus solid fractions during cooling of constrained samples at three cooling rates (a) and the comparison of averaged force–displacement curves at 0.5 °C/s in the fully constrained and compensation modes (b).

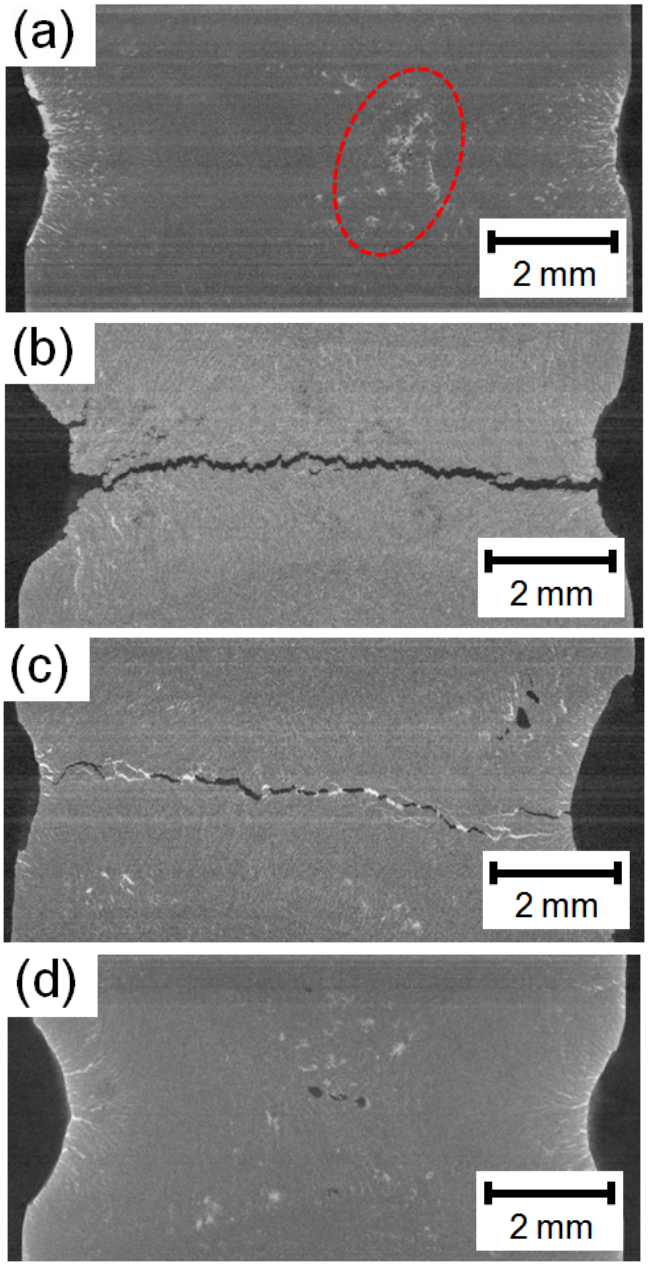

Figure 6.6 Examples of axial cross section imaged by XMT of samples tested under different conditions: (a) 0.1 °C/s constrained; (b) 1.0 °C/s constrained; (c) 0.5 °C/s constrained; and (d) 0.5 °C/s with compensation.

When the force compensation is applied during the test at a moderate cooling rate (0.5 °C/s, Figure 6.6d), HT development is much reduced. Such compensation technically is a displacement applied at a constant rate in the opposite direction to the thermal contraction, thus reducing the severity of HT development. In such a condition, we can still see some bright patches in the vicinity of the created void signifying that eutectic feeding is active to heal the void formation. Additionally, at this cooling rate, the formation of eutectic distribution does not differ much between constrained (Figure 6.6c) and the compensated condition (Figure 6.6d); the eutectic patches exist at various locations and do not necessarily clustered as for the lowest cooling rate (within red ellipse in Figure 6.6a).

We perform 3-D reconstruction of voids in the area within the bounding box (5 x 5 mm and 3 mm in height) that is smaller than the sample cross section (9.5 mm) and encapsulates the central and the most deformed area of the samples (Figure 6.7a). Figure 6.7b – Figure 6.7e show the result of 3-D void reconstruction of samples tested at different conditions; the voids are represented by white objects, and the aluminum matrix is the background. In Figure 6.7b, we observe that due to the extended eutectic feeding seen in Figure 6.6a, such a testing condition produces only a small amount of void space. While in Figure 6.7c and Figure 6.7d, we observe a planar HT, which has such severity that we could not use these samples for further experimentation. Figure 6.7e shows that the complete geometry of the voids that appear as a simple shape in two-dimensional (2-D) cross section, actually having much more complex geometry if we extend the analysis to the third dimension. Additionally, from the 3-D void reconstruction, we see that the cracks in Figure 6.7c and Figure 6.7d extend to the surface of the bounding box while in Figure 6.7b and Figure 6.7e, voids are rather encapsulated and not connected directly with each other.

6.4 Discussion

From Figure 6.5a, the appreciable load is recorded at solid fraction of approximately 0.8. This is supported by results from the previous research that AA7050 start to acquire mechanical strength at around the similar solid fraction [14]. Moreover, the force shoot-out starting at $f_s = 0.97$ shown in both Figure 6.5a and Figure 6.5b could be interpreted as grain coalescence phenomenon as it has also been observed elsewhere [15]. Indeed, grain coalescence in AA6061 was found to start approximately at $f_s = 0.97$ which is in a good agreement with the result in this experiment and our previous work in AA7050 [16], which is approximately at the end of the eutectic solidification (please refer to Figure 1.2).

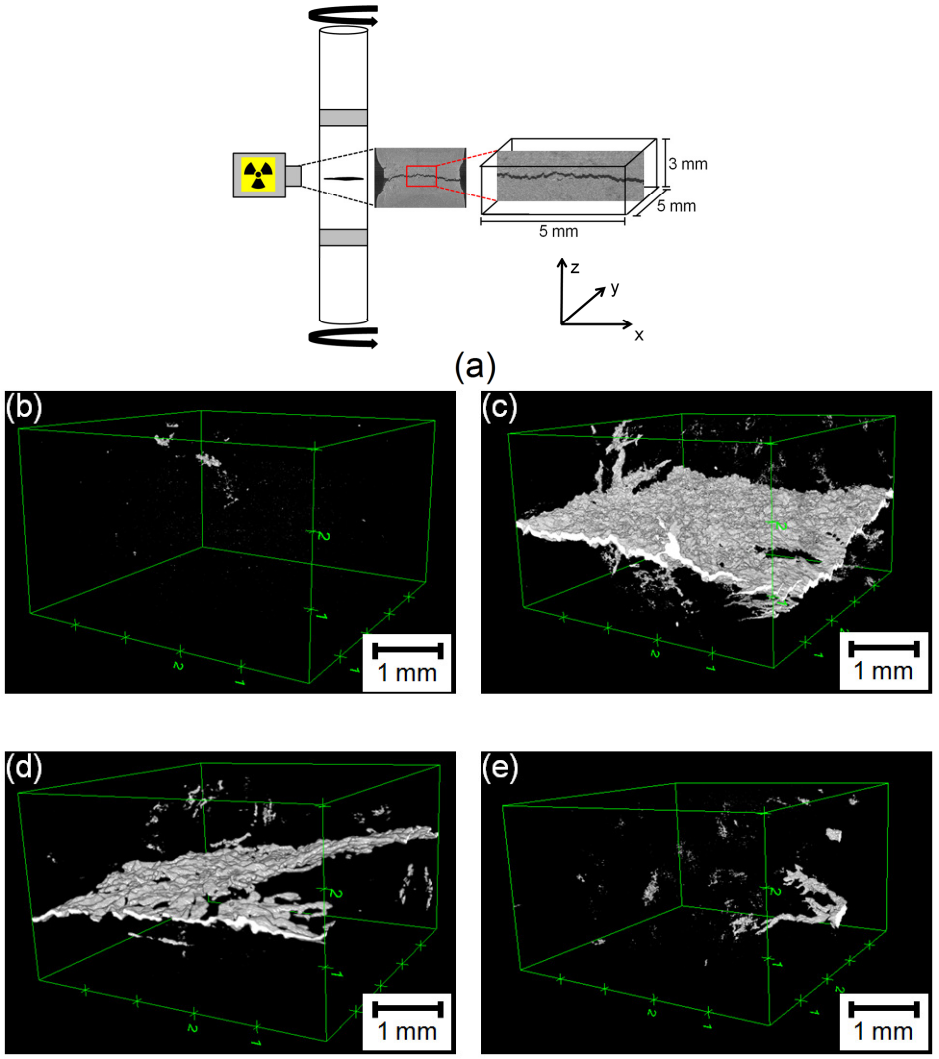

Figure 6.7 Position of the bounding box with respect to the sample (a). The 3-D void space reconstruction of the XMT data from samples with different testing conditions: (b) 0.1 °C/s constrained; (c) 1.0 °C/s constrained; (d) 0.5 °C/s constrained; and (e) 0.5 °C/s with compensation. White objects are voids and black background represents the matrix.

One possible explanation of the constrained condition resulting in a higher force value compared to the compensated one observed in Figure 6.5b is because the compensated condition has a lower strain rate compared to the constrained test. Thus, due to the viscoplastic effect, it results in the lower exerted force. In addition, the mush feeding is better compared to the constrained test due to the lower strain rate exerted onto the sample.

By decreasing the strain-rate we also decrease the amount of strain exerted on the semi-solid part of the sample during solidification. From Figure 4.6 – Figure 4.8 (after the machine initialization part of the curve), we see that the force strongly increases with displacement (hence strain), especially at higher solid fraction (above $f_s = 0.9$) as the load development curves are steeper in these solid fractions as compared to the lower solid fractions. Thus, small difference in displacement produces significant difference in exerted force. Furthermore, different literatures [17-20] also show that strain is an important variable that affects HT formation, and hence may explain lower amount of formed HT at compensated conditions.

Figure 6.5a and Figure 6.5b show that although the force depends on the testing conditions, the shapes of the force vs. solid fraction curves are similar – the force increases up to $f_s = 0.9$ and then flattens up to $f_s = 0.97$ to finally increase again up to fully solid state ($f_s = 1.0$). Figure 6.8 depicts a schematic description of these different mechanical regimes. In region 1, the material mainly starts to build up the mechanical strength due to grain locking and welding (formation of solid bridges). Since there are quite sufficient amounts of liquid phase present between the grains, even though HT initiates, it can still be healed by the liquid phase. As the material continue to solidify (region 2), the force starts to level-off and forms a plateau between $f_s = 0.9$ and $f_s = 0.97$. We can suggest that at the beginning of the plateau – at approximately $f_s = 0.9$ (region 2A), HT initiate. Other works [15, 21] report that $f_s = 0.9$ is the end of interdendritic feeding regime, which means beyond such a solid fraction, crack healing by liquid feeding will be difficult due to the discontinuous feeding path. Then, as solidification progresses, the force level continues to be flat up to $f_s = 0.97$ (region 2B). This phenomenon suggests a balancing act between the increase of intrinsic material strength due to the increase of solid fraction and the propagation of the initiated HT. This is also supported by our previous work [16] which showed that the lowest ductility occurs between $f_s = 0.9$ and $f_s = 0.97$. It corresponds to the area called brittle temperature range where the material is prone to HT [17]. Then as solid fraction increases over 0.97 (region 3), the force increases again. As explained earlier in this sub-section, in this region, the material enters the advanced coalescence regime and it has sufficient strength to resist HT propagation until it is fully solid. This finding is also supported by other studies [15, 16] where the advanced coalescence in aluminum alloys of series 6061 and 7050 was found to be at approximately $f_s = 0.97$.

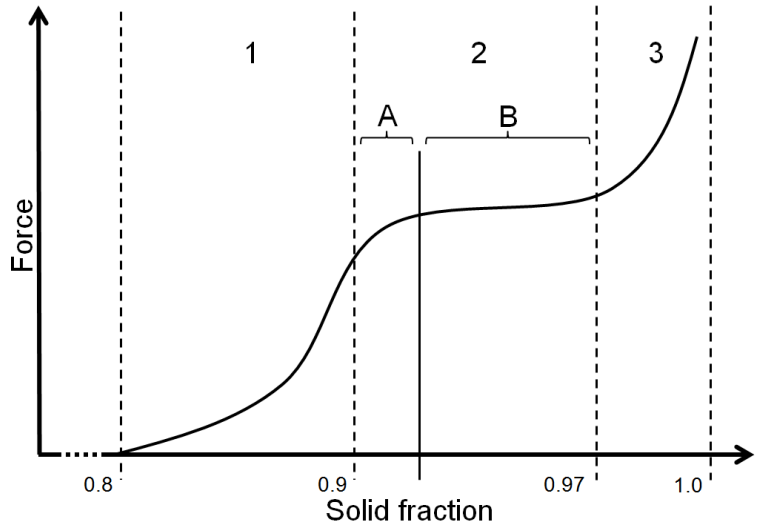

Figure 6.8 Different mechanical regions in the force versus solid fraction curve.

In addition, Figure 6.5a shows that the error bars generally become larger as the solid fraction increases. This becomes significant starting from a solid fraction of 0.88. This is because at lower solid fractions (i.e. below $f_s = 0.88$), there are still open feeding channels with approximately homogeneous width and spatial distribution. The strength of the material is mainly governed by the amount of solid fraction. However, as the material reaches the end of interdendritic feeding (i.e. around $f_s = 0.9$), the strength of the material not only depends on the solid fraction but also depends on the distribution of the formed cracks or redistributed eutectics. These features have less homogeneous distribution in terms of location and size within the sample and can vary from test to test, thus giving a wider range of mechanical response.

Figure 6.6 shows that the amount of formed HT decreases with decreasing the cooling rate. Meanwhile, the amount of eutectic feeding increases with decreasing the cooling rate. This could be explained because at a lower cooling rate, the microstructure has enough time to respond to the deformation. This is shown by the sample tested with the lowest cooling rate (Figure 6.6a) that has the least void. Moreover, we can see that the feeding continues in the eutectic solidification regime with the enriched remaining liquid, leading to the formation of some bright patches and only a small number of voids are produced in that area. Such structure features are called healed microcracks [22]. For the sample tested at 1.0 °C/s, the structure may not have adequate time to respond to the deformation and redistribute eutectic liquid to heal the created void therefore it has the most severe HT (Figure 6.6b). One possible explanation of the observation that at a moderate cooling rate (on both

constrained conditions; Figure 6.6c and Figure 6.6d), the eutectic patches are not clustered as compared to the lowest cooling rate (Figure 6.6a) in a common area but rather clustered throughout the sample might be as follows: With a higher cooling rate, the HT are formed more progressively at different locations on the sample. Thus, the eutectic also distributes accordingly.

Summarizing the results from different testing conditions, we can suggest that this alloy is sensitive to cooling rate. This is shown by less damaged structure produced at the lowest cooling rate (0.1 °C/s) owing to the extended eutectic feeding and on the other hand, the remarkable amount of HT damage developed at the highest cooling rate (1.0 °C/s). The reason that the major HT has developed at such a cooling rate, which is considered relatively low for DC casting [23], is the limited size of the liquid metal reservoir, which is linked to the size of the melted zone in the samples, whereas in the DC casting case the liquid aluminum is continuously added to the sump, improving the feeding of the mush. The fact that the most of HT development reflects the highest cooling rate rather than the largest force shows that the role of feeding and deformation rate (cooling rate) may be determining in the HT development [24-26].

The substantial increase in complexity of the produced HT geometry from 2-D (Figure 6.6d) to 3-D (Figure 6.7e) analysis flaunts the importance of a full 3-D reconstruction of the HT. This is because we will need to use such a complex geometry as the CC initiator when using the samples for validation of the existing CC criterion [27].

The results on damage characterization (Figure 6.6 and Figure 6.7) along with the results on force development (see Figure 6.5) allow us to conclude that it is possible to semi-quantitatively estimate the amount of HT inside the sample during the test. If the force development is relatively low throughout the process, more damage is developed as the alloy accommodates the stress by developing voids and cracks; and vice versa.

From the force–temperature measurements and 3-D reconstruction of XMT images, we propose a HT development map that represents different testing regimes associated with the extent of HT by varying two test variables: cooling rate and displacement compensation rate. Figure 6.9 is the map based on the present experimental data. The first regime is compression where the compensation rate exceeds the full-compensation rate, thus negative or compression force in the force–temperature measurement is produced. Full-compensation rate is the compensation rate needed to keep the force equal to zero and such a value depends on the cooling rate of the experiment. In this regime, there can be no HT since the pressure is positive inside the mush. The second regime can be called the micro-HT regime. In this regime, the compensation rate is just below the full-compensation rate thus producing a limited amount of HT. There are two sub-regimes of the micro-HT regime

– low cooling rate with none to low compensation rate regime (type – I in Figure 6.9) and high cooling rate with medium to high compensation rate (type – II in Figure 6.9). For the former sub-regime, the low amount of HT is owing to the sufficient feeding condition while the latter is due to the low total strain rate (also strain) exerted by the sample due to the compensation condition. These two sub-regimes are distinguished by the final distribution of eutectic phase as explained above. The next regime represents macroscopic HT (macro-HT) development, thus rendering the samples unusable for further experimentation. The final regime is complete fracture where the compensation rate is significantly lower than the full-compensation rate. The boundaries between these regimes may vary for different alloys and also not necessarily have a sharp transition or divided linearly as HT is inherently a complex and nonlinear phenomenon [24, 26].

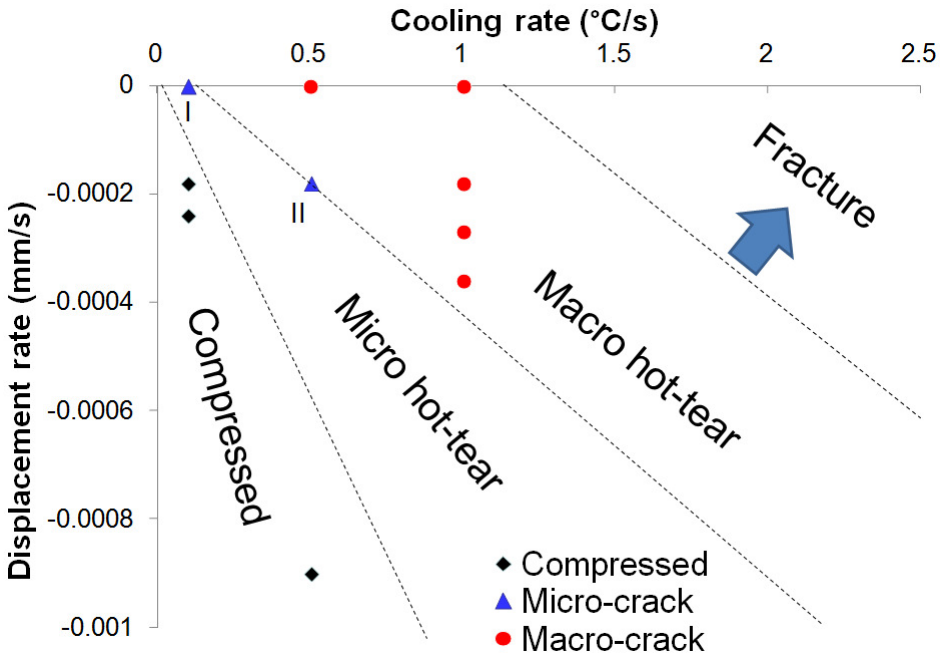

Figure 6.9 Map of regimes of HT formation as a function of two experimental variables, cooling rate and compensation rate.

The settings in the micro-HT regime are suitable to produce a controlled HT that can be used for further CC validation experiment. A sample produced in this regime can be subsequently machined to a smaller diameter in order to remove the layer containing the drilled hole where the thermocouple was placed. Then, such a sample can be tensile tested at room temperature. The goal of this test, which will be presented in Chapter 7, is to see the correlation between the size and geometry of the produced micro HT (obtained from

quantitative image analysis of XMT data) with respect to the room temperature fracture strength. Such information can be further used to validate the existing CC criterion [7, 8, 27].

In addition, the experimental method described in this chapter not only has the potential to produce samples with controlled HT severity, but also could be used as a relatively simple technique to measure the HT susceptibility of different aluminum alloys. Therefore, this method would be beneficial for industrial application, especially for the development of new alloys. This may help the cast house to find the optimum production process parameters to minimize HT occurrence of such new alloys during casting.

6.5 Conclusions

In this chapter, we have demonstrated an experimental method that has potential to control HT development in a small-scale solidification process. Such a method is needed to produce samples for the validation of the connection between HT and CC. From the results and the analysis that we have done in this chapter, we can conclude several points as following:

1. From the obtained results, we suggest that, when it comes to HT development, the cooling rate and feeding of the mushy zone during solidification may be more important variables as compared to the exerted force.
2. From the result in Figure 6.5, we propose that there are three different mechanical regimes during solidification as described in Figure 6.8: First, grain locking and material strength buildup (region 1). Second, the HT initiation (region 2A) and propagation (region 2B). The third regime signifies the grain coalescence phase where the strength of the alloy increases significantly (region 3).
3. The substantial increase of complexity in HT geometry from 2-D (Figure 6.6d) to 3-D (Figure 6.7e) analysis signifies the importance of a complete 3-D reconstruction of the formed HT. Especially, this information is going to be key information in the existing CC criterion [27] because it will be used as the assumption of the crack initiation point.
4. By controlling two variables during solidification, i.e. cooling rate and compensation rate, we propose four regimes that signify the level of formed HT: compressed, micro-HT, macro-HT and failure.
5. The method demonstrated in this chapter opens up a possibility for a relatively simple characterization technique to measure the HT susceptibility for different types of alloys.

References

[1] Eskin, D. G., Lalpoor, M., Katgerman, L., "Cold cracking during direct-chill casting", In: *Light Metals, TMS*, San Diego, CA (2011), pp. 669-74.
[2] Subroto, T., Miroux, A., Mortensen, D., M'Hamdi, M., Eskin, D. G., Katgerman, L., "Semi-quantitative predictions of hot tearing and cold cracking in aluminum DC casting using numerical process simulator", *IOP Conference Series: Materials Science and Engineering* (2012), 33, pp. 012068.
[3] Lalpoor, M., Eskin, D. G., ten Brink, G., Katgerman, L., "Microstructural features of intergranular brittle fracture and cold cracking in high strength aluminum alloys", *Materials Science and Engineering A* (2010), 527, pp. 1828-34.
[4] Phillion, A. B., Hamilton, R. W., Fuloria, D., Leung, A. C. L., Rockett, P., Connolley, T., Lee, P. D., "In situ X-ray observation of semi-solid deformation and failure in Al-Cu alloys", *Acta Materialia* (2011), 59, pp. 1436-44.
[5] Puncreobutr, C., Lee, P. D., Hamilton, R. W., Cai, B., Connolley, T., "Synchrotron tomographic characterization of damage evolution during aluminum alloy solidification", *Metallurgical and Materials Transactions A* (2013), 44, pp. 5389-95.
[6] Terzi, S., Salvo, L., Suéry, M., Limodin, N., Adrien, J., Maire, E., Pannier, Y., Bornert, M., Bernard, D., Felberbaum, M., Rappaz, M., Boller, E., "In situ X-ray tomography observation of inhomogeneous deformation in semi-solid aluminium alloys", *Scripta Materialia* (2009), 61, pp. 449-52.
[7] Lalpoor, M., Eskin, D. G., and Katgerman, L., "Cold-cracking assessment in AA7050 billets during direct-chill casting by thermomechanical simulation of residual thermal stresses and application of fracture mechanics", *Metallurgical and Materials Transactions A* (2009), 40A, pp. 3304-13.
[8] Lalpoor, M., Eskin, D. G., Katgerman, L., "Cold cracking development in AA7050 direct chill-cast billets under various casting conditions", *Metallurgical and Materials Transactions A* (2010), 41A, pp. 2425-34.
[9] Salvo, L., Suéry, M., Marmottant, A., Limodin, N., Bernard, D., "3D imaging in material science: Application of X-ray tomography", *Comptes Rendus Physique* (2010), 11, pp. 641-9.
[10] http://www.ge-mcs.com/en/radiography-x-ray/ct-computed-tomography/nanotom-s.html, (2014).
[11] Schindelin, J., Arganda-Carreras, I., Frise, E., Kaynig, V., Longair, M., Pietzsch, T., Preibisch, S., Rueden, C., Saalfeld, S., Schmid, B., Tinevez, J. Y., White, D. J., Hartenstein, V., Eliceiri, K., Tomancak, P., Cardona, A., "Fiji: An open-source platform for biological-image analysis", *Nature Methods* (2012), 9, pp. 676-82.
[12] Mondolfo, L. F., "Aluminum alloys: Structure and properties", London-Boston, Butterworths & Co Ltd (1976).
[13] Robson, J. D., "Microstructural evolution in aluminium alloy 7050 during processing", *Materials Science and Engineering A* (2004), 382, pp. 112-21.
[14] Lalpoor, M., Eskin, D. G., Katgerman, L., "Thermal expansion/contraction behavior of AA7050 alloy in the as-cast condition relevant to thermomechanical simulation of residual thermal stresses", *International Journal of Materials Research* (2011), 102, pp. 1286-93.

[15] Giraud, E., Suery, M., Coret, M., "Mechanical behavior of AA6061 aluminum in the semisolid state obtained by partial melting and partial solidification", *Metallurgical and Materials Transactions A* (2010), 41A, pp. 2257-68.
[16] Subroto, T., Miroux, A., Eskin, D. G., Ellingsen, K., Marson, A., M'Hamdi, M., Katgerman, L., "Tensile mechanical behavior of as-cast AA7050 alloy in the super-solidus temperature range", In: *13th International Conference on Fracture (ICF-13)*, Beijing, China (2013), pp. 2528-36.
[17] Eskin, D. G., Suyitno, Katgerman, L., "Mechanical properties in the semi-solid state and hot tearing of aluminium alloys", *Progress in Materials Science* (2004), 49, pp. 629-711.
[18] Magnin, B., Maenner, L., Katgerman, L., Engler, S., "Ductility and rheology of an Al-4.5%Cu alloy from room temperature to coherency temperature", *Materials Science Forum* (1996), 217-222, pp. 1209-14.
[19] Won, Y. M., Yeo, T. J., Seol, D. J., Kyu Hwan, O. H., "A new criterion for internal crack formation in continuously cast steels", *Metallurgical and Materials Transactions B* (2000), 31, pp. 779-94.
[20] M'Hamdi, M., Mo, A., Fjær, H. G., "TearSim: A two-phase model addressing hot tearing formation during aluminum direct chill casting", *Metallurgical and Materials Transactions A* (2006), 37, pp. 3069-83.
[21] Fabrègue, D., Deschamps, A., Suéry, M., Poole, W. J., "Rheological behavior of Al-Mg-Si-Cu alloys in the mushy state obtained by partial remelting and partial solidification at high cooling rate", *Metallurgical and Materials Transactions A* (2006), 37, pp. 1459-67.
[22] Suyitno, Eskin, D. G., Katgerman, L., "Structure observations related to hot tearing of Al-Cu billets produced by direct-chill casting", *Materials Science and Engineering A* (2006), 420, pp. 1-7.
[23] Eskin, D. G., "Physical Metallurgy of Direct Chill Casting of Aluminum Alloys (Advances in Metallic Alloys)", CRC Press, Taylor & Francis group, LLC (2008).
[24] Van Haaften, W. M., Kool, W. H., Katgerman, L., "Hot tearing studies in AA5182", *Journal of Materials Engineering and Performance* (2002), 11, pp. 537-43.
[25] Suyitno, Kool, W. H., Katgerman, L., "Hot tearing criteria evaluation for direct-chill casting of an Al-4.5 pct Cu alloy", *Metallurgical and Materials Transactions A* (2005), 36A, pp. 1537-46.
[26] Eskin, D. G., Katgerman, L., "A quest for a new hot tearing criterion", *Metallurgical and Materials Transactions A* (2007), 38A, pp. 1511-9.
[27] Lalpoor, M., Eskin, D. G., Ruvalcaba, D., Fjær, H. G., Ten Cate, A., Ontijt, N., Katgerman, L., "Cold cracking in DC-cast high strength aluminum alloy ingots: An intrinsic problem intensified by casting process parameters", *Materials Science and Engineering A* (2011), 528, pp. 2831-42.

Chapter 7

QUANTITATIVE ANALYSIS OF FORMED HOT TEAR AND ITS EFFECT TO COLD CRACKING SUSCEPTIBILITY

7.1 Introduction

In Chapter 6 we have demonstrated a technique that has a potential to control the formation of hot tear inside a sample. This technique is required for the verification experiment to study the connection between hot tear (HT) and cold crack (CC). In that chapter, we also have obtained three dimensional (3-D) images of the formed HT in the sample by utilizing X-ray microtomography (XMT) imaging method. At this point, we have both the pre-HT samples and 3-D XMT images of those samples. Therefore, in this chapter, we mainly focus on the quantitative crack characterization using the XMT image data obtained in Chapter 6 (phase III in the flow chart of Figure 6.1) and the measurement of the remaining tensile strength of the pre-HT samples at the room temperature (phase IV in the flow chart of Figure 6.1), where the CC usually occurs.

To quantify the size and the geometrical characteristics of the formed HT in the sample, we use image analysis of the obtained 3-D XMT images. An image analysis is a widely used method to extract important information from available image data in different research fields for example as object recognition in artificial intelligence field, medical science and material sciences [1-3]. In recent years, this analysis method is also used to analyze the obtained 3-D tomography images and carry out quantification of the complex-shaped entities such as formed voids and non-equilibrium (eutectic) phases of a solidified sample [4-7]. In this chapter, we employ image analysis technique to carry out quantitative characterization of the formed voids using the obtained 3-D image data of the samples produced by the experiment described in Chapter 6 (pre-HT samples).

After we obtain the quantitative information of the formed voids on the pre-HT samples, we carry out room temperature tensile tests of those samples until they fail. The tensile stress generated in the test is used to simulate the residual stress developed in the billet during casting and cooling down process. The aim of this test is to correlate the fracture stress (the maximum stress when the sample fails) and the size of the formed HT based on the image analysis observation. This correlation is used to justify the connection between HT and CC i.e. whether the presence of micro-HT in the sample could increase the susceptibility of the alloy to CC. Moreover, we also review the validity of the existing CC criterion [8] when we use the assumption of micro HT as the CC initiator. We close this chapter by discussing some additional possible connection mechanisms between HT and CC on top of the existing one [9], and also the possible improvement of the existing CC criterion in the future.

7.2 Verification method

The samples with different HT conditions were produced from a controlled solidification experiment described in Chapter 6. However, in this chapter, we only focus on samples with micro-HT condition. This condition is selected because our focus is the underdeveloped HT in the sample. Figure 6.9 shows that there are two types of micro HT samples; Type-I where, qualitatively, the produced void is minimum and the eutectic (non-equilibrium phase) feeding focuses in the void area (Figure 6.7b). The other is Type-II where, qualitatively, there are more produced voids (Figure 6.7e) compared to the Type-I samples and the eutectic patches are more widely distributed throughout the sample. These two types of micro-HT are categorized based on different processing variables; Type-I samples are solidified with cooling-rate of 0.1 °C/s with fully constrained condition, while Type-II samples are solidified with cooling-rate of 0.5 °C/s with compensation speed of 0.00018 mm/s. Please see Chapter 6 for more details on the processing method.

In this chapter, we focus our analysis on the micro-HT samples of both types (Type-I and Type-II, see Figure 6.9). We tested five Type-I samples (Sample ID: I-1 to I-5) and four Type-II samples (Sample ID: II-1 to II-4). As a reference and comparison to the micro-HT samples, we tested four healthy samples. These samples are machined directly from the DC cast billet and no HT is present in the sample.

7.2.1 Quantitative image analysis procedure

The series of XMT images obtained in Chapter 6 enables us to reconstruct the sub-surface condition of the pre-HT samples in 3-D. To be able to analyze the connection mechanism between HT and CC through critical crack size, we need to quantify the formed voids, for example the geometry and the orientation of the voids. This is because the existing CC criterion uses the critical crack size of the crack initiator to predict the maximum stress that can be sustained by the material before CC takes place.

As seen from Figure 6.7b, Type-I samples typically have minimum number of void formed in the sample, thus the defect can be assumed as pore or solidification shrinkage. On the other hand, Type-II samples (Figure 6.7e) shows features closer to a HT morphology (e.g. branching-type voids) [10]. Since we are interested in studying micro-HT as the CC initiator, we focus the quantitative image analysis on the Type-II samples.

The quantitative image analysis is carried out by utilizing an image analysis toolbox (Analysis3D) developed by Salvo *et al.* in the Institut Polytechnique de Grenoble (INP Grenoble), France [11]. This toolbox is built as a plug-in on ImageJ software [12, 13]. We perform the image analysis on a HP Z800 workstation with Intel Xeon ® processors series

W5590 (total of 4 cores) with 24 Gb of random access memory (RAM). Figure 7.1 shows flow-chart of the image processing steps.

Before the quantitative image analysis takes place, a series of pre-processing steps need to be done on the obtained images (steps 2 – 4 in Figure 7.1). This is because the original image quality produced by the XMT characterization is not ideal for quantitative characterization. For example, there are image noises from the image acquisition process and the borders between entities (i.e. between void and matrix) are not sharp. This could introduce error to the image analysis result. The graphical example of the pre-processing steps is shown in Figure 7.2.

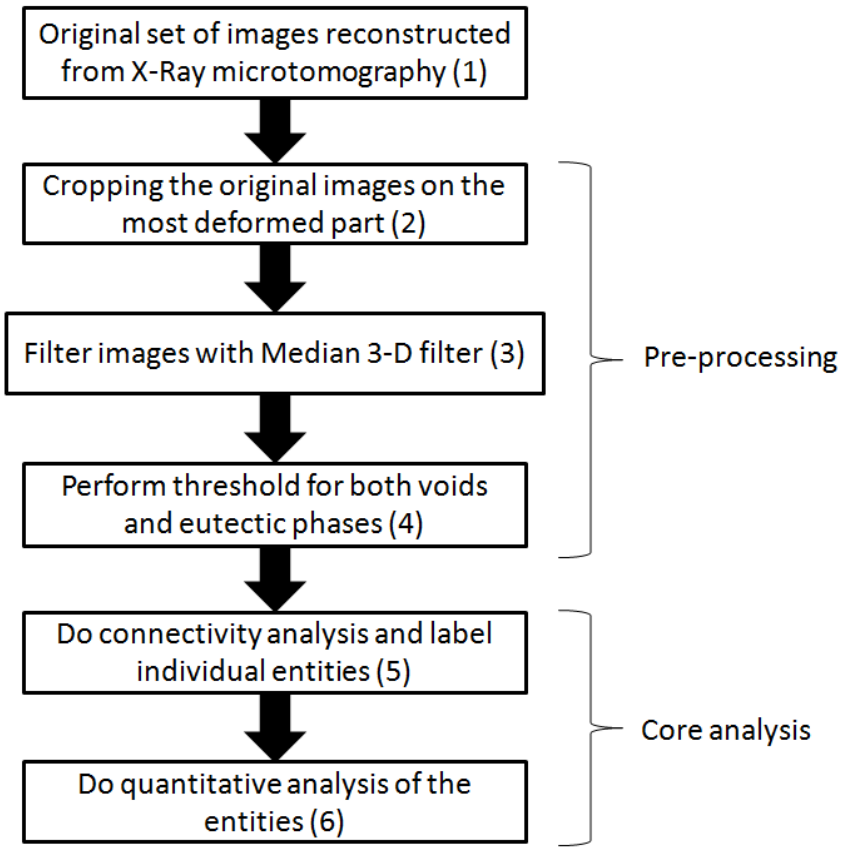

Figure 7.1 Flow chart of steps of image processing to obtain quantitative information from the XMT images.

The pre-processing steps are described as follows: First, we focus the quantitative image analysis on the most deformed part of the sample as shown in the Figure 6.7a (a square box

with 5 mm on each side with 3 mm height). Therefore, we crop this part from the original image to obtain an analysis box (step 2 in Figure 7.1). An example of a cross-section view from an analysis box as compared to the original sample is shown in Figure 7.2a. (the analysis box is the region within the red-dashed square). The cross-section of the cropped volume (analysis box) from the original sample is shown in Figure 7.2b. The cropped volume is then filtered using a median filter in 3-D with radius of 2 voxels (step 3 in Figure 7.1). Median filter is selected because of its ability to reduce image noise (smoothening) while simultaneously preserve the sharpness of the boundaries between entities unlike the common smoothening procedure [14]. The example of the filtered volume is shown in Figure 7.2c. Subsequently, we perform threshold (color segmentation) for different entities on the filtered volume; voids and eutectics (step 4 in Figure 7.1). These two entities are shown as dark region and lighter grey region respectively in Figure 7.2a - Figure 7.2c. The matrix is represented with grey regime in the same figures. Threshold process is in principle making a colors segment of each desired entities. An example of segmented void regime is the area covered in red shown in Figure 7.2d. An example of segmented eutectic regime is the area covered in red shown in Figure 7.2e. After segmentation process, the image is then converted into a binary-type image. An example of a void segmentation in the binary image format is shown in Figure 7.2f; the white area represents void and black area is the rest of the sample. The conversion to binary image format is to simplify the case and hence makes the further analysis more efficient.

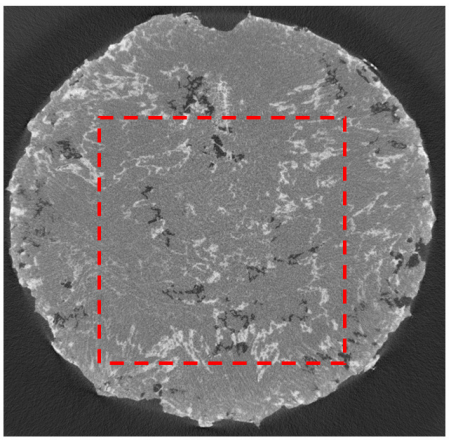

(a)

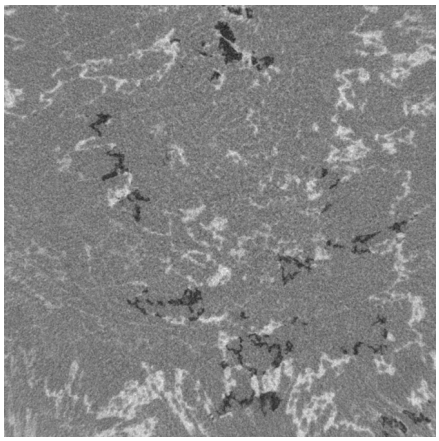

(b)

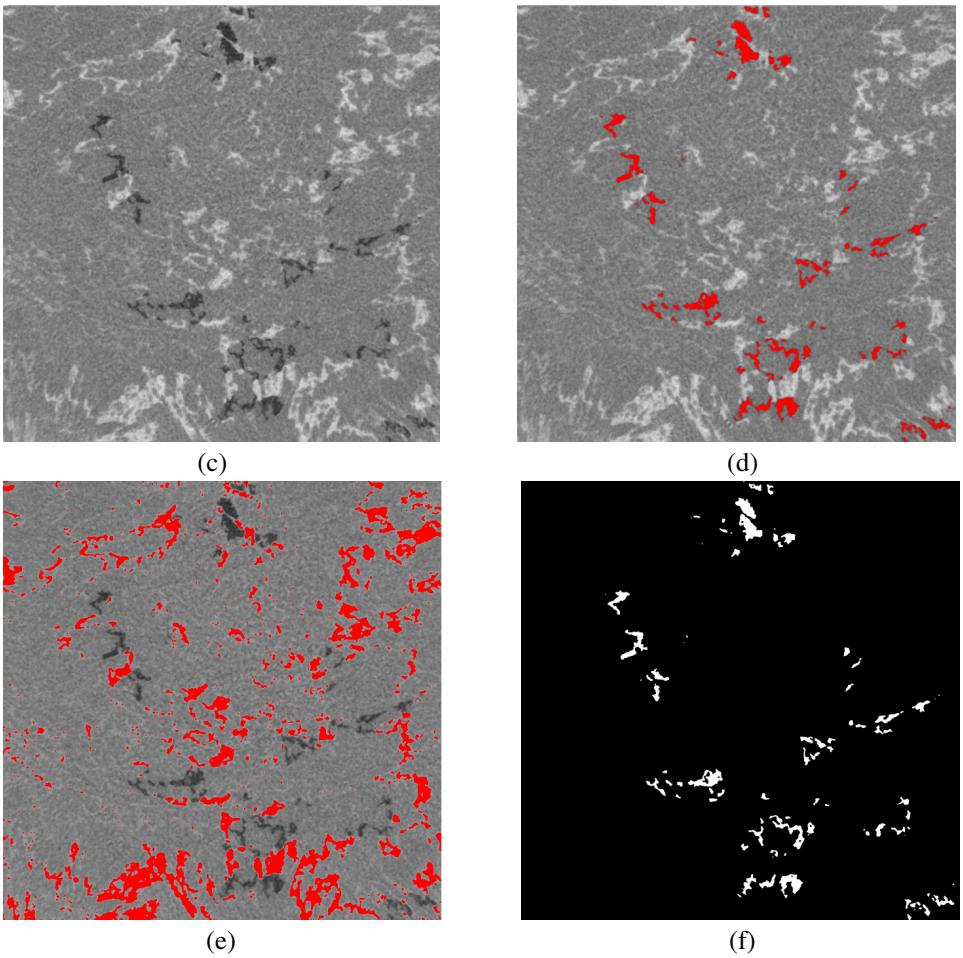

(c) (d)

(e) (f)

Figure 7.2 Graphical representation of image analysis pre-processing steps. Start with image cropping from the original image of the sample, cropped region is within the red-dashed square – square side: 5 mm (a). Example of the cross section of the cropped volume (b). Filtered image using Median 3D filter of the cropped regime (c). Void-segmented area (area covered in red) from the filtered image (d). Eutectic-segmented area (area covered in red) from the filtered image (e). Binary image format of the void-segmentation, white area represents void and the black area represent the rest of the sample (f).

After pre-processing steps are completed, we perform connectivity analysis of the entities. Starting from this step, we only focus on analyzing the voids, because the goal of this chapter is to quantify the dimensions of the formed HT and study its influence to the CC occurrence via the critical crack size. A void is considered as an individual void if it is not directly connected with other void space, i.e. separated by other entities (i.e. eutectic or matrix). Such a void will receive its own individual label (designation for further

processing). During the labeling process, we also filter the voids that interest us based on their size. We use the criterion as follows: If an individual entity has a volume smaller than 100 voxels, such entity will be erased (step 5 in Figure 7.1). This filtering step is aimed to filter image noises that are not eliminated by the median filter. On each of the individually labeled void, we perform a series of quantitative image analysis. These are for example, calculation of the volume of the void, determination of bounding box that encapsulates the void and the orientation of the void with respect to the axes of the sample (step 6 in Figure 7.1). A detailed description of these calculations will be given in Section 7.3.1. Aside from performing calculation on individual voids, we also perform the calculation of void and eutectic volume fraction with respect to the total volume of the analysis box.

7.2.2 Mechanical testing procedure

During the experiment where we introduce HT to the sample (Chapter 6), we drill a hole 2 mm deep on the sample to place the thermocouple which is utilized to measure the temperature of the sample during the test. Furthermore, the mid-length part of the sample is re-solidified during the test, thus producing low surface quality in this part of the sample. Because of these conditions, we need to reduce the initial diameter of the sample to minimize mechanical properties modification caused by these artifacts. By reducing the diameter of the initial sample, we remove the thermocouple-hole feature and simultaneously improve the surface quality of the sample in the mid-length regime. This way, we ensure the tensile mechanical properties are only affected by the re-solidification phenomena, such as the presence of HT on the sample.

Electric discharge machining (EDM) is selected as the machining technique to reduce the diameter of the sample. This is because on the contrary to the common machining method, for example milling and cutting, EDM does not introduce mechanical force to the sample. Therefore, the original geometry of the formed HT is preserved. The final shape of the sample is a cylindrical dog-bone shaped sample with a total length of 50 mm and the length of the reduced section is 28 mm. The diameter of the end part of the sample is 8 mm while the diameter of the reduced section is 5 mm. The details of the machined sample geometry are shown in Figure 7.3.

Before the pre-HT samples are tensile tested, we carry out surface observation using a stereo microscope and verify the result with the XMT images to inspect for any presence of HT or voids that are continuous to the surface of the machined (final) sample geometry. All samples have remnants of propagated HT or voids that connected to the surface.

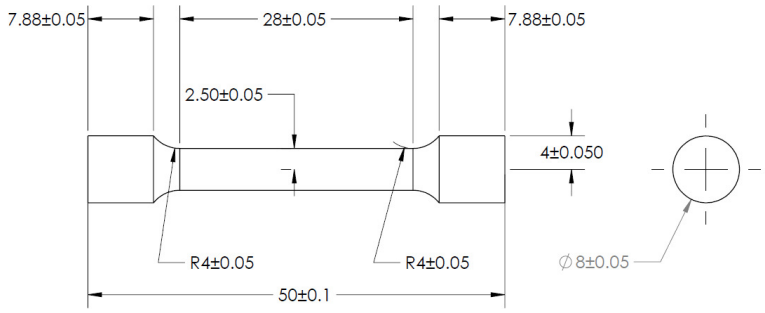

Figure 7.3 The final geometry of the sample machined by EDM.

We performed the room temperature tensile test on an Instron mechanical testing machine (series 5500R) equipped with a 10kN load cell. To connect the tensile sample with the jaws of the testing machine, we designed a special adapter that is able to hold the neck of the sample and connect it to the jaws of the testing rig as shown in Figure 7.4a. This adapter is designed to be self-aligned, thus minimizing multi-axial loading on the sample. This way we can assume the stress acting on the sample during testing has only the tensile component.

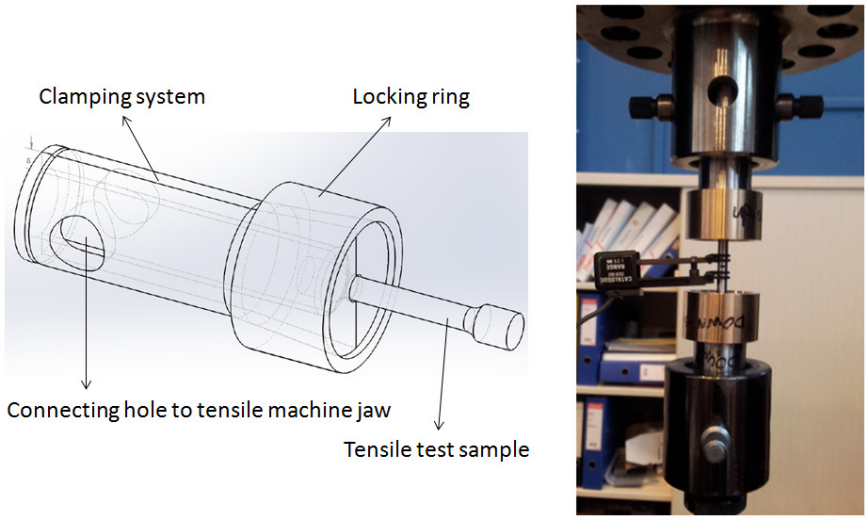

(a) (b)

Figure 7.4 Schematics of the adapter that connects the tensile sample and the test rig (a). A photograph of the experiment (b). Such a picture (b) shows the strain of the sample is measured by an extensometer.

We define the gauge length of the sample as 8 mm and the strain is measured in the gauge area using an extensometer (Figure 7.4b). During the placement of extensometer, we ensure the mid-length of the sample is between the two extensometer arms. We test the samples using displacement rate of 0.0035 mm/s (or equivalent to strain rate of 0.005 s^{-1}). This value is selected because it is within the strain rate of the billet during DC casting [15]. We tested the sample with a constant displacement rate until the sample fails and the load is almost zero. The load, displacement and strain are measured in real time.

7.3 Results

7.3.1 Quantitative image analysis of the pre hot-tear samples

Figure 7.5 shows the comparison between the void fraction (blue bars) and eutectic fraction (red bars) of the Type-II samples. The void fraction is defined as the total volume of voids divided by the total volume of the analysis box. The same principle is used for defining the eutectic counterpart. This figure shows that the void fraction of all samples with this type is between 0.2% and 0.6% from the total volume analyzed. While for the eutectic fraction, it is between 1 % and 1.9 % of the total volume analyzed. In all cases, the total amount of eutectic fraction is significantly higher than the void fraction inside the sample.

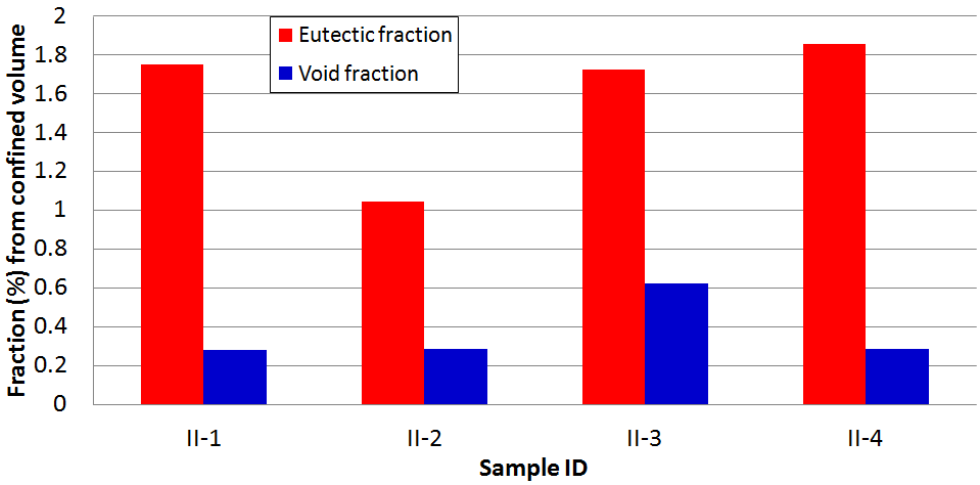

Figure 7.5 Comparison between void fraction and eutectic fraction of Type-II samples.

There are several quantitative characteristics that we would like to know about the individual voids. These are for example, the orientation of the void with respect to the cross-section plane of the sample and the dimensions of the bounding box that encapsulates each individual voids.

In the controlled solidification experiment described in Chapter 6, the main stress direction is parallel to the tensile axis (thermal stress). Therefore, the formed HT theoretically should have the longest axis normal to the tensile direction, or parallel to the cross-section plane of the sample. However, in reality, as shown in Figure 6.7, the formed voids do not always have their longest axis perfectly aligned with the cross-section plane of the sample. From those figures, the formed voids have complex shapes and have multiple branches. This does not resemble a classical crack shape [16].

The image analysis program [11] is able to calculate the volume and the coordinates of the bounding box for each individual void. The program first calculates the center of mass and the main inertia axes of the void ($\mathbf{V_1}$, $\mathbf{V_2}$ and $\mathbf{V_3}$ on Figure 7.6a). The inertia axis that corresponds to the highest inertia is designated as $\mathbf{V_1}$ and the axes that give second and lowest inertia are designated as $\mathbf{V_2}$ and $\mathbf{V_3}$ respectively (the direction of $\mathbf{V_3}$ is into the paper on Figure 7.6a). All of these local axes are perpendicular to each other. The deviation between $\mathbf{V_1}$ and the tensile axis of the sample – see Figure 7.6b (and also between the plane formed by $\mathbf{V_2}$ and $\mathbf{V_3}$ and the cross-section plane of the sample) is denoted by the angle θ (Figure 7.6a). The plane formed by the vectors $\mathbf{V_2}$ and $\mathbf{V_3}$ is henceforth designated as the void-orientation plane. The bounding box of each void is described using the local coordinate axes of the voids ($\mathbf{V_1}$, $\mathbf{V_2}$ and $\mathbf{V_3}$). The bounding box is defined as a box that encapsulates the extreme points of the void in its local inertia axes. An example of a bounding box representation of a two dimensional (2-D) void is shown in Figure 7.6a. dV_1 and dV_2 is the length of the bounding box in the direction of $\mathbf{V_1}$ and $\mathbf{V_2}$ respectively.

Since the main stress direction is parallel to the tensile axis of the sample (Figure 7.6b) , we expect to have a Mode-I cracking or opening-type fracture [17] in the cross-section plane. Therefore, in the remainder of this chapter we confine our analysis to the voids that have the longest axis oriented parallel to the sample cross-section plane. We define that a void has its longest axis oriented parallel to the cross-section plane when the vector component in the direction of tensile axis (in the original coordinate system, Figure 7.6b) of $\mathbf{V_1}$ has larger value compared to its counterpart in $\mathbf{V_2}$ and $\mathbf{V_3}$. For description simplicity, the voids that fulfill this category are hereafter designated as the oriented voids.

To be noted, not all of the voids present in the sample fall into oriented-void category. From the result of image analysis (Figure 7.7), only half of the total amount of voids within the analysis box in Type-II samples is oriented voids (blue bars on Figure 7.7, f_{oriented} in Eq. 7.1). In Eq. 7.1, $N_{oriented}$ is the number of oriented void in the sample and $N_{total\ void}$ is the total number of void present within the analysis box. However, since the volume of the voids has an influence on the remaining strength of the sample, we calculate the total volume fraction from the oriented voids ($f_{oriented\_vol}$ in Eq. 7.2). In this equation, $V_{total\ void}$ represents the total volume of all voids present within the analysis box and V_i is the volume of the *i*-th oriented

void. From the volume fraction calculation, we obtained that the oriented voids make at least 80% of the total void fraction (red bars on Figure 7.7). This condition shows that the voids with the larger volumes are oriented parallel to the cross-section plane of the sample.

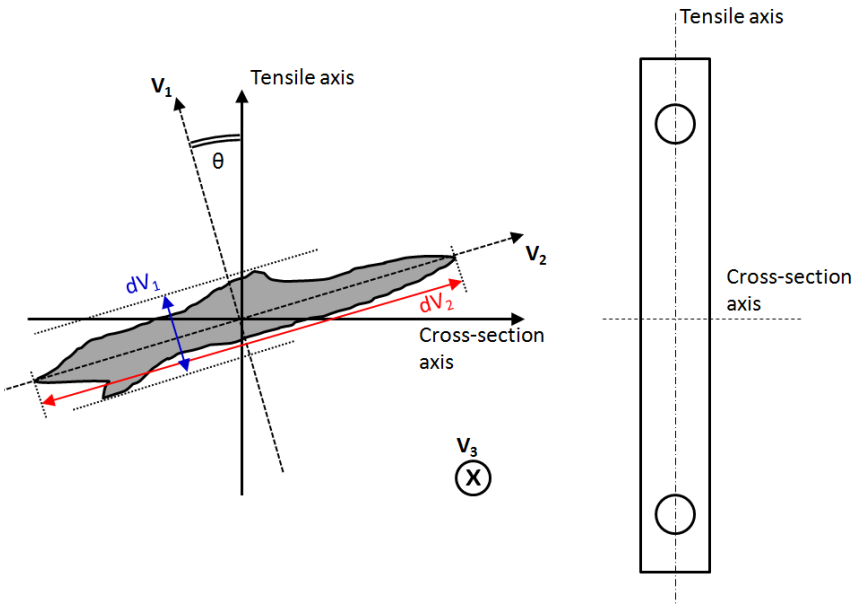

(a) (b)

Figure 7.6 Illustration of the local coordinate axes and bounding box of an individual void (a) and the comparison to the sample original coordinate axes (b).

$$f_{oriented} = \frac{N_{oriented}}{N_{total\ void}} \times 100\% \tag{7.1}$$

$$f_{oriented\_vol} = \left(\frac{1}{V_{total\ void}} \sum_{i}^{N_{oriented}} V_i\right) \times 100\% \tag{7.2}$$

However, the orientations of the "oriented" voids are not necessarily perfectly parallel with the cross-section plane. Blue bars in Figure 7.8 shows that the average deviation between the void-orientation plane and the cross-section plane of the sample (θ in Figure 7.6a) varies from sample to sample. The values span between approximately 20° and 35°.

The existing CC criterion [8] states that the only stress component that has an effect on the void is the one perpendicular to the void-orientation plane. Although during the mechanical test described in Section 7.2.2, the main stress that is introduced to the sample is parallel to the tensile axis of the sample, we know from Figure 7.8 (blue bars) that the oriented voids within the sample are not necessarily perfectly parallel to the cross-section plane of the sample. As the tensile stress assumed only affects the geometrical component of the void

that is perfectly aligned to the sample cross-section plane, we need to project the length of the voids obtained via the bounding box information (dV_2 and dV_3) to the cross-section plane using the deviation angle (θ in Figure 7.6a) of each void.

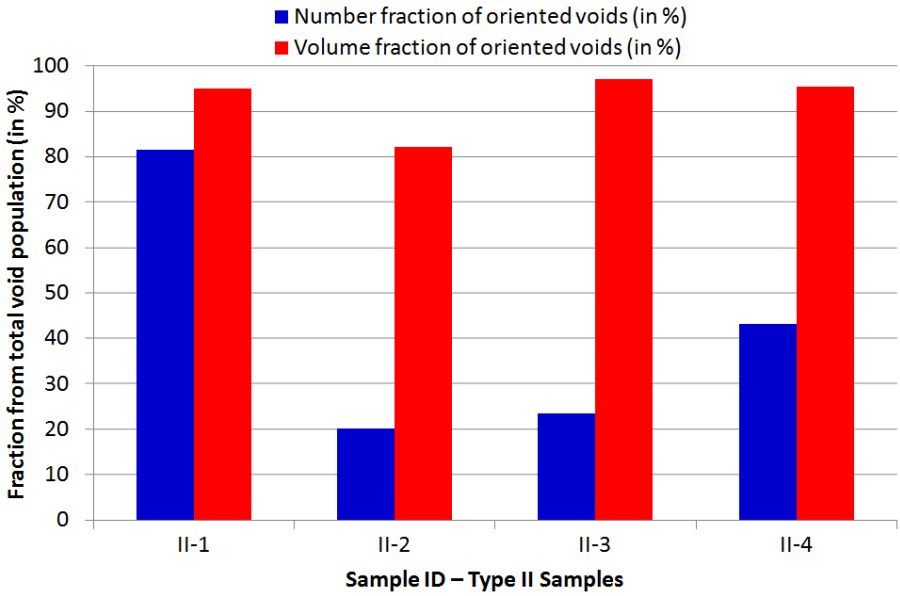

Figure 7.7 Number fraction of the oriented void (blue bars) with respect to the total number of voids. Volume fraction of the oriented voids (red bars) with respect to the total volume of voids.

Because the lengths of the bounding box in the void-orientation plane (dV_2 and dV_3) are not necessarily the same, we approximate the void shape in its orientation plane as a circular geometry to approach the crack initiation shape as described in the existing CC criterion (penny shape). The diameter of the circle is estimated by using the definition of equivalent circular diameter (ECD). The effective ECD is defined as the equivalent diameter obtained from the area constructed by the lengths of the bounding box in the void-orientation plane projected to the cross-section plane. The effective thickness of the void is defined as the length of the bounding box in $\mathbf{V_1}$ direction projected to the tensile axis of the sample. The average ratio between the effective ECD and the effective thickness of the voids for Type-II samples are shown in Figure 7.8 (red bars). This ratio obtained through the projected plane is the same as the ratio from the non-projected plane due to the elimination of the θ. Such a figure shows that the ratio for different Type-II samples is ranging between 2.3 and 3.1.

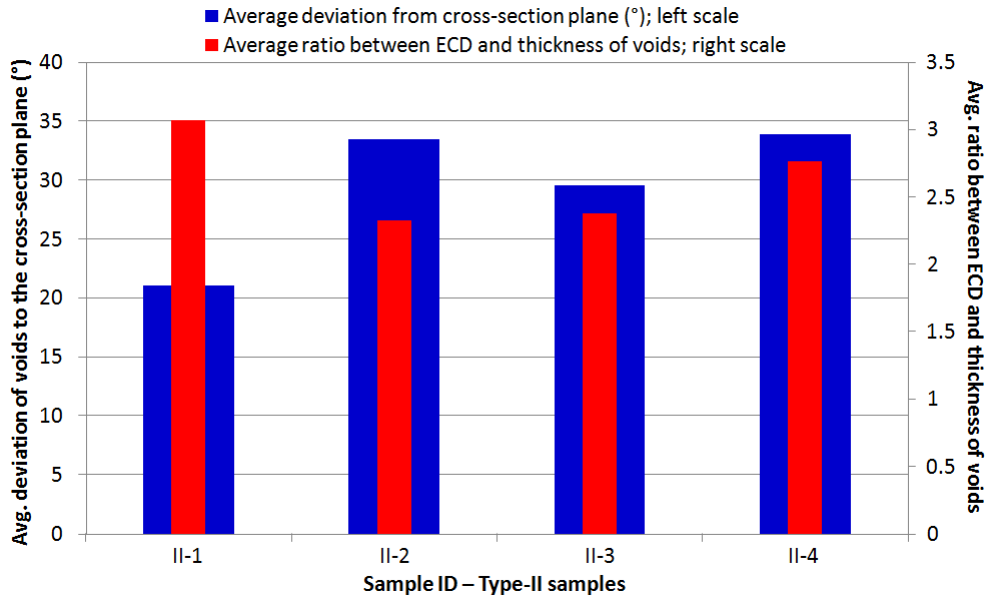

Figure 7.8 Average deviation between the void-orientation plane and sample cross-section plane (blue bars). Average ratio between the ECD and the thickness of the void (red bars).

The frequency distribution of void size (via effective ECD) on the Type-II samples is shown in Figure 7.9. This is a relative frequency and it is defined as the number of oriented-voids for each size range (e.g. between 101 and 200 µm) divided by the total number of the oriented-voids. From this result, we see that more than half of the oriented voids have effective ECD below 400 µm and in average each sample has four large voids with effective ECD above 1000 µm.

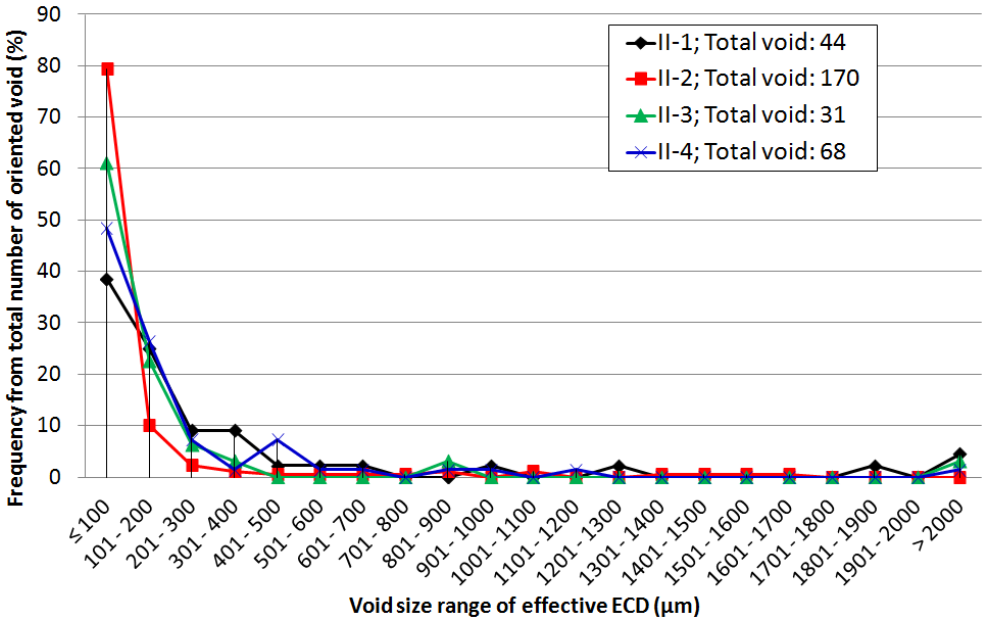

Figure 7.9 Frequency distribution of effective diameter of the formed voids for different Type-II samples.

The formed solidification damage in Type-I samples have more characteristics of porosity instead of HT (Figure 6.7b); i.e. the void does not have extended branches (as compared to the HT in Figure 6.7c – Figure 6.7e) and/or is not continuous across the sample. From semi-quantitative image analysis of the XMT image data, we found that the size of the largest void, defined here as the maximum length of the void along the two cross-section axes (in the plane parallel to the sample cross-section plane), for each sample is rather considerable; 1150 µm, 1020 µm, 860 µm, 860 µm and 660 µm for sample I-1, I-2, I-3, I-4 and I-5 respectively. However, the number of such a large void is significantly low on each sample as compared to the Type-II samples.

7.3.2 Mechanical testing results

From the mechanical test, we determined several tensile mechanical properties of the pre-HT samples. Those are namely: fracture stress, fracture strain and the modulus of elasticity for every sample. We define fracture stress as the point where the sample reaches its maximum strength just before brittle fracture takes place (before the stress value starts to decrease). Fracture strain is defined as the tensile strain where the fracture takes place. Modulus of elasticity is defined as the average slope between stress and strain, when the alloy is in its elastic mechanical regime.

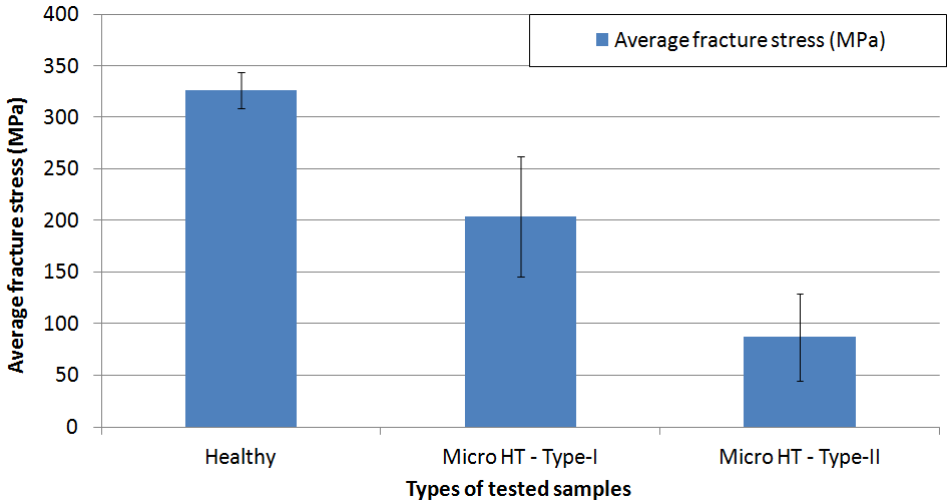

Figure 7.10 Comparison of average fracture stress for different types of tested samples.

Figure 7.10 shows the average fracture stress for different types of tested samples. The healthy samples have an average fracture stress of 326 MPa while Type-I and Type-II micro HT samples have an average fracture stress of 204 MPa and 87 MPa respectively. From this result, we observed a significant drop of the strength of the alloy on both types of the samples but Type-II has worse tensile strength compared to the Type-I samples. The same figure also shows that the voids inside the Type-I samples reduce the strength of the alloy to approximately 63% of its healthy strength. While in the Type-II samples, the strength reduces to 27% of its healthy strength. Figure 7.11 shows the average fracture strain for different types of tested samples. We see that the fracture strain of healthy samples is approximately 1.24%. The fracture strain is severely reduced when voids are present in the samples (both types of micro HT samples). Type-II samples have lower average fracture strain (approximately 0.12%) compared to Type-I samples (approximately 0.32%). This shows reduction by 74% and 90% in the average fracture strain for Type-I and Type-II samples respectively from the average fracture strain of the healthy samples. Figure 7.12 shows the modulus of elasticity for different types of tested samples. This figure shows that the values on different types of samples are approximately similar. The values span between 64 and 72 GPa for different types of samples and the average value from the these different samples is 69 GPa, which agrees well with the Young's modulus of aluminum alloys. From visual observation on the tested samples, almost all of the micro HT samples (both types) fail in the mid-length of the samples. This location is the re-solidified area on the sample and hence the location where we expect the solidification defects to form.

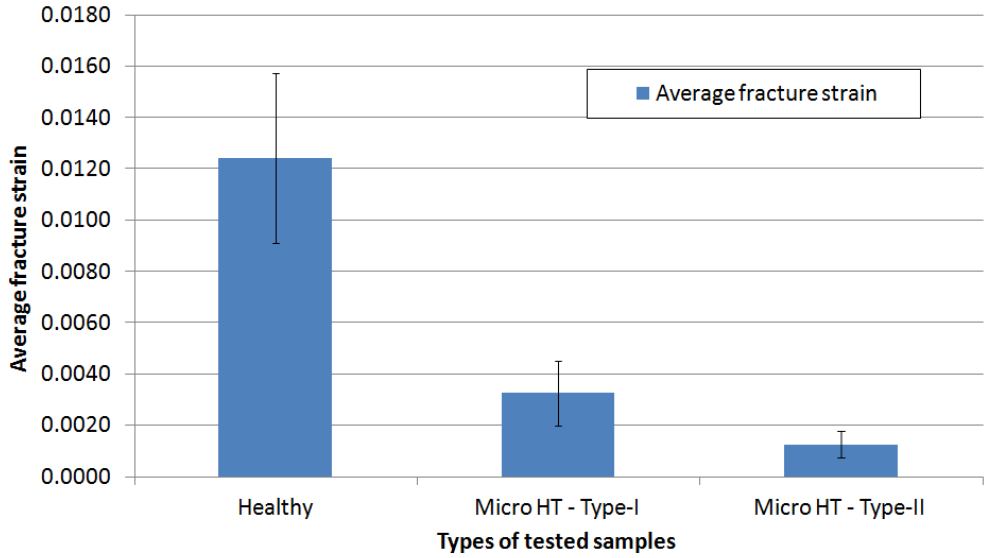

Figure 7.11 Comparison of average fracture strain for different types of tested samples.

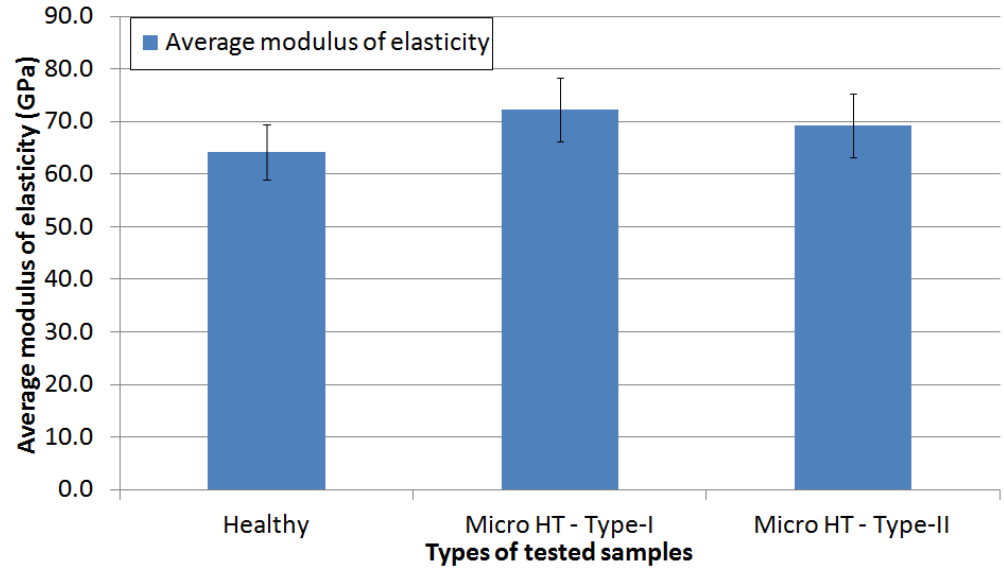

Figure 7.12 Comparison of average modulus of elasticity for different types of tested samples.

7.3.3 Discussion

7.3.3.1 Quantitative imaging on formed hot tear

In general, the image analysis technique that we employed is quite effective to quantify different features of the formed voids in the pre-HT samples because it can estimate the geometrical characteristics of each void relatively fast. As an example, for sample II-2 (this sample has the highest number of individual voids) the calculation takes approximately 2 minutes to analyze the entire analysis box starting from labeling of the entities until the quantitative characterization calculation is completed.

As briefly discussed in Section 7.3.1, Figure 7.7 shows that the larger or the main voids are oriented perpendicular to the main stress direction (tensile direction of the sample) and the average deviation between the void-orientation plane and the sample cross-section plane is at most around 35° (blue bars in Figure 7.8). These results suggest that the formed voids with larger volumes in our samples are likely to be HT [18, 19]. This is also supported by the observation of the branching morphology of typical formed voids (e.g. in Figure 6.7e and Figure 7.2f). This is characteristic of HT [10]. This may suggest that the remaining voids are either pores that are produced during re-solidification or image noises that are introduced during data acquisition process because their orientation plane is not perpendicular to the thermal stress direction.

7.3.3.2 Room temperature tensile test of pre hot tear samples

The results shown in Section 7.3.2 signify that we have good confidence in the test results. This can be seen from several different aspects. For instance, the healthy samples (reference samples) always give the highest fracture stress and fracture strain. Also these values decrease according to the severity of the HT inside the sample, which is logical. The average fracture stress of the healthy samples from this test agrees with the room temperature tensile stress similar AA7050 alloys [20]. The average fracture strain of the healthy samples is 1.24%, which proves that our AA7050 is a CC-prone alloy [20, 21]. Moreover, the measured modulus of elasticity of the alloy from all types of tested samples is close to reference Young's modulus for an AA7050, which is 70.3 GPa [22]. We can be confident that the measured properties of the micro-HT samples represent the mechanical properties of the re-solidified (HT) alloy because almost all of the micro-HT samples (of both types) fail in the mid-length where microstructure modification due to re-solidification takes place.

Figure 7.10 demonstrates that the average fracture stress for different types of the tested samples is clearly different. This can be explained, because qualitatively (from Figure 6.7) Type-II samples typically have more voids compared to the Type-I samples. However, the most distinctive difference between healthy samples and the micro HT samples are revealed through the fracture strain value. Figure 7.11 shows that even though on the Type-I samples

the remaining strength of the samples decreases to 63% from its healthy value, the strain immediately reduces to 26% from its healthy value. Meanwhile, Type-II samples severely lose its capability to withstand strain even though the samples still have remaining strength of approximately 27% from its healthy value. This shows the sample ductility reduces significantly due to the re-solidification process. This phenomenon may be caused by the interplay of two different mechanisms. The first is because of the presence of the formed HT and other voids in the samples. The second is due to local embrittlement of the alloy as a result of the abundance presence of the eutectic phase (red bars in Figure 7.5) within the sample, formed by preferential feeding channels [23].

7.3.3.3 Connection between solidification damage and cold cracking

The results that we obtained in this chapter verify the connection between HT and CC. This is indicated by the significant strength reduction of the sample when a relatively small solidification defect is present in the sample (i.e. in Type-I samples). As discussed in the previous section, the redistribution of the eutectics plays a significant role in lowering the ductility of the sample and may promote alloy susceptibility to CC. This result verifies that eutectic phase indeed embrittles the material by lowering its ductility as suggested by Lalpoor [23]. However, the presence of significant eutectic amount that occurs in the pre-HT samples might be overestimated as compared to the DC casting case. This is because in DC casting process of a billet, the liquid metal reservoir is abundant, thus may provide better mass feeding instead of the eutectic feeding to heal the formed voids. Thus, in DC casting case, the embrittlement effect due to the concentration of eutectic phase in the structure should be lower as compared to the pre-HT samples.

The previous work [9] suggested that the connection mechanism between the two types of cracks is the possible transformation of the HT to a CC due to the significant change in the stress states in the billet (CCS becomes lower) in the just fully solidified condition [24]. The solidification defects that are formed in the course of solidification and survived throughout the entire solidification process become the initiator of CC [25]. As the billet continues to cool down and passes the temperature point where alloy loses its ductility (below 200 °C) [20], the alloy becomes extremely brittle and thus catastrophic CC initiated by the formed solidification defect took place. From the result and observation that we obtained in this work, we can suggest an additional possible mechanism that may support the connection between HT and CC. This aforementioned mechanism is sub-critical micro-HT propagation in the sub-solidus temperature regime (between 450 and 465 °C). As shown in Chapter 3, in the sub-solidus temperature regime, the alloy has low strength and low ductility while simultaneously sustaining a surge increase in residual stress [8]. However, the extent of this propagation should be moderate due to the short temperature range and it depends on the produced strain rate on the billet. This is because we know from Chapter 6, strain rate is an important variable for HT development. However, even

though the extent of the crack propagation may not be significant, it may cause coalescence of the formed micro-HT or other voids in the sub-solidus temperature range [17, 26]. This may be possible because (as we observe from Figure 7.9) of the presence of multiple micro-HT and other voids in the sample. This coalescence phenomenon could increase the total crack initiator size and worsen the strength of the alloy in response to the stress buildup in the billet when it is cooled down.

In the existing CC criterion [8] (Eq. 2.19 and 2.20 in Chapter 2) the crack initiator is described as a single defect. Therefore, for quantitative validation of the criterion, we assume the largest HT in the sample acts as the crack initiator. The K_{IC} value at the room temperature is obtained through the previous work [24] which is 8.9 $MPa \cdot m^{1/2}$, and from other previous work [8] we assume first the crack initiator geometry to be penny-shaped (Eq. 2.19 in Chapter 2). The effective ECD value of the largest HT in the sample is used to calculate the theoretical fracture stress value. The comparison between theoretical (red bars) and the measured fracture stress (blue bars) is shown in Figure 7.13. Because the pre-tensile test observation shows that all of the samples have solidification damage (either HT or pore) that is continuous to the surface of the sample and it was reported that the presence of surface [27] and/or near-surface crack [28] could worsen the materials properties further, in the same figure we also calculate the theoretical fracture stress assuming a thumbnail-shaped crack (Eq. 2.20) (black bars in Figure 7.13).

Figure 7.13 show the theoretical values (both with penny-shaped and thumbnail-shaped approximation) are always higher than the measured fracture stress value for Type-II samples. There are two possible hypotheses for this result: (1) as we see in Figure 7.5 and explained in the preceding paragraphs, the abundance of eutectic fraction in the sample may play a considerable role in worsening of the mechanical properties of the alloy. (2) Figure 7.9 shows that when HT formed in the sample, it is usually not formed individually. These multiple cracks may work collectively to reduce the strength of the sample even further and thus giving significantly lower measured fracture stress. Because we expect lower amount of eutectic phase presence in the billet during the DC casting case due to the presence of abundant liquid metal reservoir, the latter hypothesis suggests there is a critical oversimplification in the existing CC criterion.

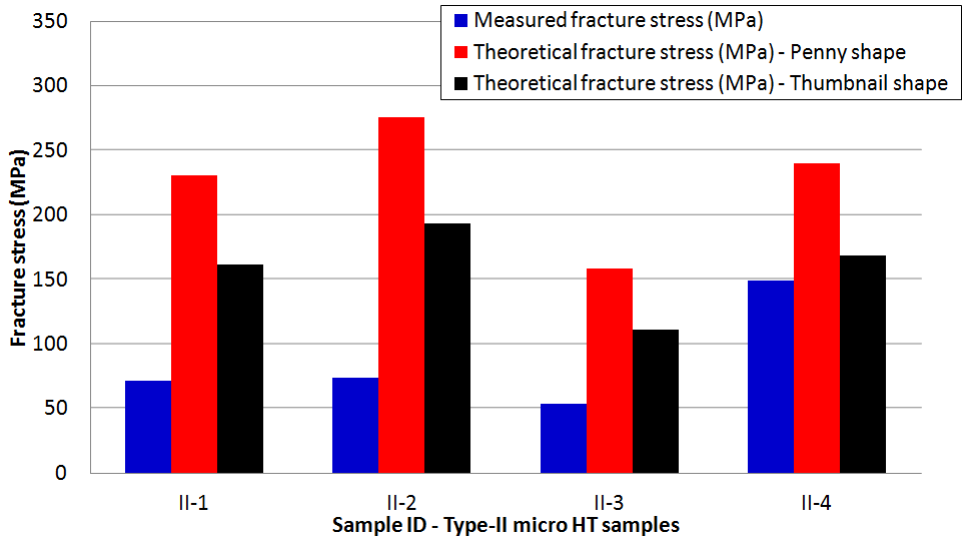

Figure 7.13 Comparison between theoretical and measured fracture stress for Type-II samples.

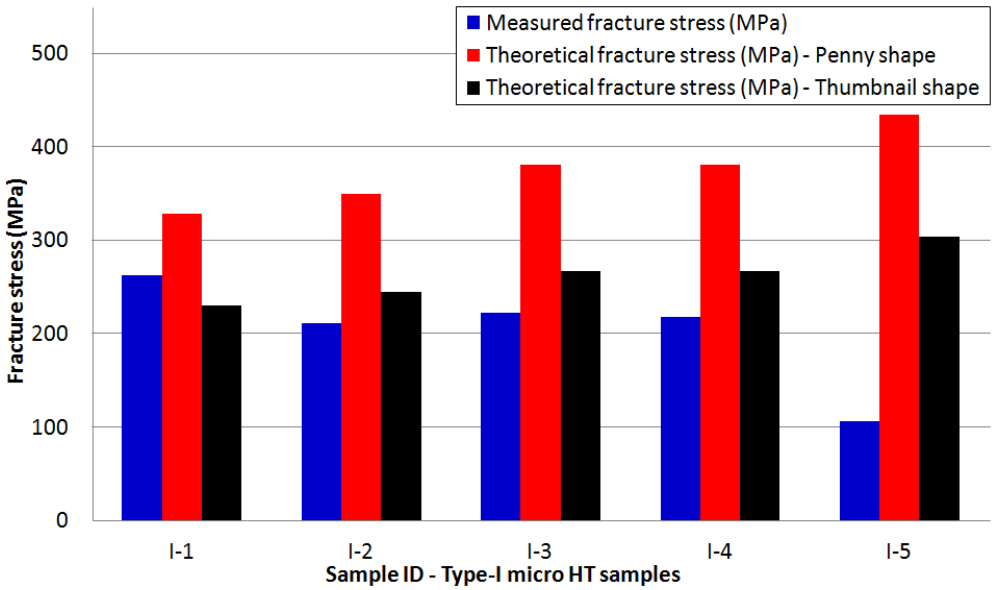

Figure 7.14 Comparison between theoretical and measured fracture stress for Type-I samples.

From Figure 7.10, we see that the pores that are formed on Type-I samples can rather significantly reduces the strength of the sample, thus it might also be worth to compare the measured fracture stress (Figure 7.14, blue bars) and its theoretical estimation. We obtained the theoretical value using the largest void size of Type-I samples (Section 7.3.1) as the crack initiator. The red bars in Figure 7.14 shows the estimated value for penny shaped case and the black bars in the same figure shows the estimated value for the thumbnail shaped counterpart. In this figure, in general we see that the theoretical fracture stress is still higher than the measured ones. However, estimation using thumbnail-shape crack initiator produces a closer value to the measured ones. This is logical because all of the samples have pre-existing surface damage before tensile tested. This suggests that the current CC criterion can, for this type of sample, approximate the experimental value in a fairly good manner. The current CC criterion assumes an individual defect as the crack initiator, thus the damage condition in Type-I samples (the number of the formed void is significantly low and the geometry is relatively simple as compared to the formed HT in Type-II samples) could provide a better approximation for the criterion. This condition is also supported by the previous work where the existing CC criterion is sufficient to predict CC occurrence when the crack initiator is an individual entity, for instance an oxide or inclusion [25, 29].

However, when the crack initiator is a micro-HT (i.e. Type-II samples), we saw that in general; the theoretical estimation is much higher than the measured value (Figure 7.13). Therefore, there are several aspects in the current CC criterion that should be improved. From the point of view of the number of crack initiators, the existing CC criterion uses only a single defect as the crack initiator. Meanwhile, our result shows that HT is usually formed in clusters (not necessarily formed as a large single entity – Figure 7.9). This demonstrates that the existing criterion neglects other HT and voids that potentially could participate in further worsening of the mechanical properties of the billet. From the aspect of the crack initiator geometry, the existing CC criterion uses penny-shape geometry [8]. In reality, HT has much more complex geometry (see Figure 6.6 and Figure 6.7). Moreover, from Figure 7.8 (red bars), in average, the ratio between ECD and the crack thickness is approximately 2.6. This shows HT have finite thickness, hence penny-shaped geometry may not be the best approximation as the crack initiator geometry. A possible starting point for improvement in this direction is to use an ellipsoid shape as the crack initiation geometry [30]. One other suggestion for the improvement of the criterion is to include a spatial distribution factor of the formed HT as part of the criterion. Different spatial distributions of HT, e.g. either void closely clustered or widely spread, may provide different effect on the material strength, even though the total void fraction is similar.

The suggested explanation on the connection between HT and CC discussed earlier in this section also supports our hypothesis regarding the interpretation of the ALSIM simulation of the cold cracking casting case in Chapter 2. The micro-HT that may form during the

entire casting process (based on ICS calculation in Figure 2.7b especially at the steady state) might act as the initiation points of catastrophic CC. However, with the current version of crack estimation of ALSIM (on both HT and CC), the quantitative description of the crack connection is difficult to be captured properly by ALSIM. Moreover, the result shown earlier in this chapter suggests that the quantitative description of HT (geometry and location) may significantly affect the mechanical properties in the lower temperature regime and hence, the CC susceptibility. These drawbacks are what the ALSIM cracking criteria are currently lacking of. This situation provides motivation to develop a crack criterion that is able to capture both the geometry and the location of the formed HT. The concept of a cracking model that is able to quantitatively capture the connection between HT and CC will be the main subject of Chapter 8.

7.4 Conclusions

In this chapter, we focus on the quantitative characterization of the formed HT in the samples produced in Chapter 6. Additionally, we also carried out room temperature tensile test of such pre-HT samples and measured the remaining strength and ductility of the samples. The combination of information obtained on both analyses helped us to verify the connection between HT and CC. From the analysis done in this chapter, we have conclusions as follows:

1. Image analysis is an effective and efficient method to quantify the characteristics of the formed HT on obtained 3-D images. The result of this analysis is not only useful to gain insight into the general characteristics of the sample (i.e. the void and eutectic fraction) but it is also useful to perform quantitative analysis of the formed HT (e.g. the effective ECD value of the largest HT in the sample) which enables us to estimate the theoretical fracture stress via the existing CC criterion.
2. We verify the connection between HT and CC. This is shown by the significant decrease in sample strength in the room temperature due to the presence of relatively small solidification defects (Type-I samples) and the strength worsens in the presence of micro-HT (Type-II samples).
3. Additional possible connection mechanism other than the significant decrease of the fracture stress in the presence of solidification defect [8] is the sub-critical crack propagation in the sub-solids temperature regime (when the strength and ductility of the alloy are low). Moreover, possible micro-HT and/or void coalescence caused by this sub-critical propagation may further decrease the capability of the billet to resist CC.

4. The significant reduction of the fracture strain might be caused by the interplay between the formed HT and the embrittlement caused by the abundant presence of non-equilibrium phases in the sample when it is in its brittle state (below 200°C).
5. Although the existing CC criterion could provide a reasonable estimation for samples with a limited number of crack initiator (i.e. an individual large pore in Type-I samples), this criterion is not sufficient for predicting the CC occurrence if we assume HT as the crack initiators. There are several additional factors that might be improved for better CC prediction accurracy. One is to modify the number of crack initiation points because the current CC criterion uses the description of a single defect as the crack initiator and HT is usually not formed individually (Figure 7.9). Another point is to improve the realism of crack initiator geometry because HT have a more complex geometry compared to the classical crack shape [16].
6. ALSIM needs a better HT criterion that would be able to capture the quantitative description of the formed HT as the geometry and location of these HT may provide a significant impact to the CC susceptibility of the billet.

References

[1] Wojnar, L., "Image analysis : applications in materials engineering", Boca Raton, FL, USA, CRC Press (1999).
[2] Zhao, W., Chellappa, R., Phillips, P. J., Rosenfeld, A., "Face recognition: A literature survey", *ACM Computing Surveys* (2003), 35, pp. 399-458.
[3] Robb, R. A., Hanson, D. P., Karwoski, R. A., Larson, A. G., Workman, E. L., Stacy, M. C., "ANALYZE: A comprehensive, operator-interactive software package for multidimensional medical image display and analysis", *Computerized Medical Imaging and Graphics* (1989), 13, pp. 433-54.
[4] Maire, E., Buffière, J. Y., Salvo, L., Blandin, J. J., Ludwig, W., Létang, J. M., "On the application of X-ray microtomography in the field of materials science", *Advanced Engineering Materials* (2001), 3, pp. 539-46.
[5] Salvo, L., Cloetens, P., Maire, E., Zabler, S., Blandin, J. J., Buffière, J. Y., Ludwig, W., Boller, E., Bellet, D., Josserond, C., "X-ray micro-tomography an attractive characterisation technique in materials science", *Nuclear Instruments and Methods in Physics Research, Section B: Beam Interactions with Materials and Atoms* (2003), 200, pp. 273-86.
[6] Salvo, L., Suéry, M., Marmottant, A., Limodin, N., Bernard, D., "3D imaging in material science: Application of X-ray tomography", *Comptes Rendus Physique* (2010), 11, pp. 641-9.
[7] Puncreobutr, C., Lee, P. D., Hamilton, R. W., Cai, B., Connolley, T., "Synchrotron tomographic characterization of damage evolution during aluminum alloy solidification", *Metallurgical and Materials Transactions A* (2013), 44, pp. 5389-95.

[8] Lalpoor, M., Eskin, D. G., Katgerman, L., "Cold cracking development in AA7050 direct chill-cast billets under various casting conditions", *Metallurgical and Materials Transactions A* (2010), 41A, pp. 2425-34.
[9] Lalpoor, M., "Study of cold cracking during DC-casting of high strength aluminum alloys", [Ph.D. Thesis] (2010), Delft University of Technology.
[10] Campbell, J., "Complete casting handbook : metal casting processes, metallurgy, techniques and design", Oxford, UK; Waltham, MA, Elsevier Butterworth-Heinemann (2011).
[11] Boulos, V., Fristot, V., Houzet, D., Salvo, L., Lhuissier, P., "Investigating performance variations of an optimized GPU-ported granulometry algorithm", In: *6th Annual Conference on Design and Architectures for Signal and Image Processing (DASIP 2012)*, Karlsruhe, Germany (2012), pp. 36-41.
[12] Rasband, W. S., "ImageJ", U. S. National Institutes of Health, Bethesda, Maryland, USA, http://imagej.nih.gov/ij/, (1997-2014).
[13] Schindelin, J., Arganda-Carreras, I., Frise, E., Kaynig, V., Longair, M., Pietzsch, T., Preibisch, S., Rueden, C., Saalfeld, S., Schmid, B., Tinevez, J. Y., White, D. J., Hartenstein, V., Eliceiri, K., Tomancak, P., Cardona, A., "Fiji: An open-source platform for biological-image analysis", *Nature Methods* (2012), 9, pp. 676-82.
[14] Blanchet, G. C. M., "Digital signal and image processing using Matlab", London; Newport Beach, CA, ISTE Ltd. (2006).
[15] Van Haaften, W. M., "Constitutive behavior of aluminum alloys", [Ph.D. Thesis] (2002), Delft University of Technology.
[16] Callister, W. D., "Materials science and engineering : an introduction", New York, Wiley (2000).
[17] Janssen, M., Zuidema, J., Wanhill, R. J. H., "Fracture mechanics", Delft, The Netherlands, Delft University Press (2002).
[18] Rappaz, M., Danzig, J. A., "Solidification", CRC Press, Taylor & Francis group, LLC (2009).
[19] Eskin, D. G., Katgerman, L., "A quest for a new hot tearing criterion", *Metallurgical and Materials Transactions A* (2007), 38 A, pp. 1511-9.
[20] Lalpoor, M., Eskin, D. G., Katgerman, L., "Fracture behavior and mechanical properties of high strength aluminum alloys in the as-cast condition", *Materials Science and Engineering A* (2008), 497, pp. 186-94.
[21] Livanov, V. A., Gabidullin, R. M., Shipilov, V. S., "Continuous Casting of Aluminum Alloys", Metallurgiya, Moscow, (1977).
[22] ASM International Handbook Committee, "ASM handbook, Volume 2", Materials Park, OH, USA, ASM International (1990).
[23] Lalpoor, M., Eskin, D. G., ten Brink, G., Katgerman, L., "Microstructural features of intergranular brittle fracture and cold cracking in high strength aluminum alloys", *Materials Science and Engineering A* (2010), 527, pp. 1828-34.
[24] Lalpoor, M., Eskin, D. G., and Katgerman, L., "Cold-cracking assessment in AA7050 billets during direct-chill casting by thermomechanical simulation of residual thermal stresses and application of fracture mechanics", *Metallurgical and Materials Transaction A* (2009), 40A, pp. 3304-13.

[25] Lalpoor, M., Eskin, D. G., Ruvalcaba, D., Fjær, H. G., Ten Cate, A., Ontijt, N., Katgerman, L., "Cold cracking in DC-cast high strength aluminum alloy ingots: An intrinsic problem intensified by casting process parameters", *Materials Science and Engineering A* (2011), 528, pp. 2831-42.
[26] Eskin, D. G., "Physical Metallurgy of Direct Chill Casting of Aluminum Alloys (Advances in Metallic Alloys)", CRC Press, Taylor & Francis group, LLC (2008).
[27] Atluri, S. N., Kathiresan, K., "3D analyses of surface flaws in thick-walled reactor pressure-vessels using displacement-hybrid finite element method", *Nuclear Engineering and Design* (1979), 51, pp. 163-76.
[28] Murakami, Y., Miwa, K., Kanetake, N., Tada, S., "Effect of casting defects distribution on the beginning of tensile fracture in semi-solid injected magnesium AZ91D alloy", *Magnesium Technology* (2013), pp. 271-4.
[29] Eskin, D. G., Lalpoor, M., Katgerman, L., "Cold cracking during direct-chill casting", In: *Light Metals, TMS*, San Diego, CA, USA (2011), pp. 669-74.
[30] Tada, H., Paris, P. C., Irwin, G. R., "The stress analysis of cracks handbook", New York, ASME Press (2000).

Chapter 8

TOWARDS QUANTITATIVE CRACK PREDICTION IN ALUMINUM DIRECT-CHILL CASTING PROCESS

8.1 Introduction

In Chapter 7, we showed that undeveloped or micro hot tears (HT) could significantly reduce the strength of the alloy at room temperature, where it is prone to cold cracking (CC). This validates the connection between HT and CC. From the result of Chapter 2, we see an indication that ALSIM is able of capturing the connection between these two types of cracks. Thus, the next step is to model the connection between these cracks.

As explained in Chapter 2, the current version of ALSIM HT criterion is only able to provide a relative HT susceptibility of the ingot and it is unable to capture the dimension of the formed HT. This is a critical drawback as the necessary input for ALSIM CC criterion requires the size of the micro-HT as the crack initiator. This suggests that the current ALSIM release could not quantify the connection between HT and CC using its existing cracking criteria.

As described elsewhere [1] and to the best of the author's knowledge, up to now there are no HT criteria that are able to provide the exact dimension and position of the formed HT [2-4]. The main challenges to model this phenomenon are the complexity and non-linearity of the HT [1]. An example of the non-linearity of HT formation is shown in Figure 8.1 on X-Ray microtomography (XMT) images of the cross-section of the sample at the mid-length of four different samples produced through a controlled solidification process (Chapter 6). All of the samples are produced with similar solidification conditions; cooling-rate of 0.5 °C/s and compensation rate of 0.00018 mm/s. In this figure, the voids are shown in dark areas, non-equilibrium phases are shown in light grey areas and aluminum matrix are shown in grey areas. This figure shows that even though in general the total amount of formed HT in the sample is qualitatively comparable, the locations and dimensions of the formed HT are different for different samples. This shows the difficulty of predicting the exact location and dimension of HT using a deterministic or classical crack prediction model. However, as suggested in our previous work [5] and also in Chapter 7, the different spatial distributions of the formed HT in the system may provide dissimilarity of the alloy strength at room temperature. Therefore, it is necessary to predict the location and dimension of the HT as accurately as possible. One potential way to capture these phenomena is to model the crack formation through a stochastic process.

Nowadays, non-linear and stochastic-based models are commonly utilized in different research fields. Some examples related to the field of materials science are; modeling the evolution of a multi-phase microstructure [6], probabilistic approaches in fracture mechanical problems [7] and modeling of microstructure formation during the solidification process [8-10]. Although a predictive description of HT formation has been successfully done recently by Sistaninia *et al.* [11, 12] through the development of a

granular model [13, 14], the main objective of this project is to develop the ALSIM model further so that it can capture the connection between HT and CC by means of extending its existing cracking prediction capabilities.

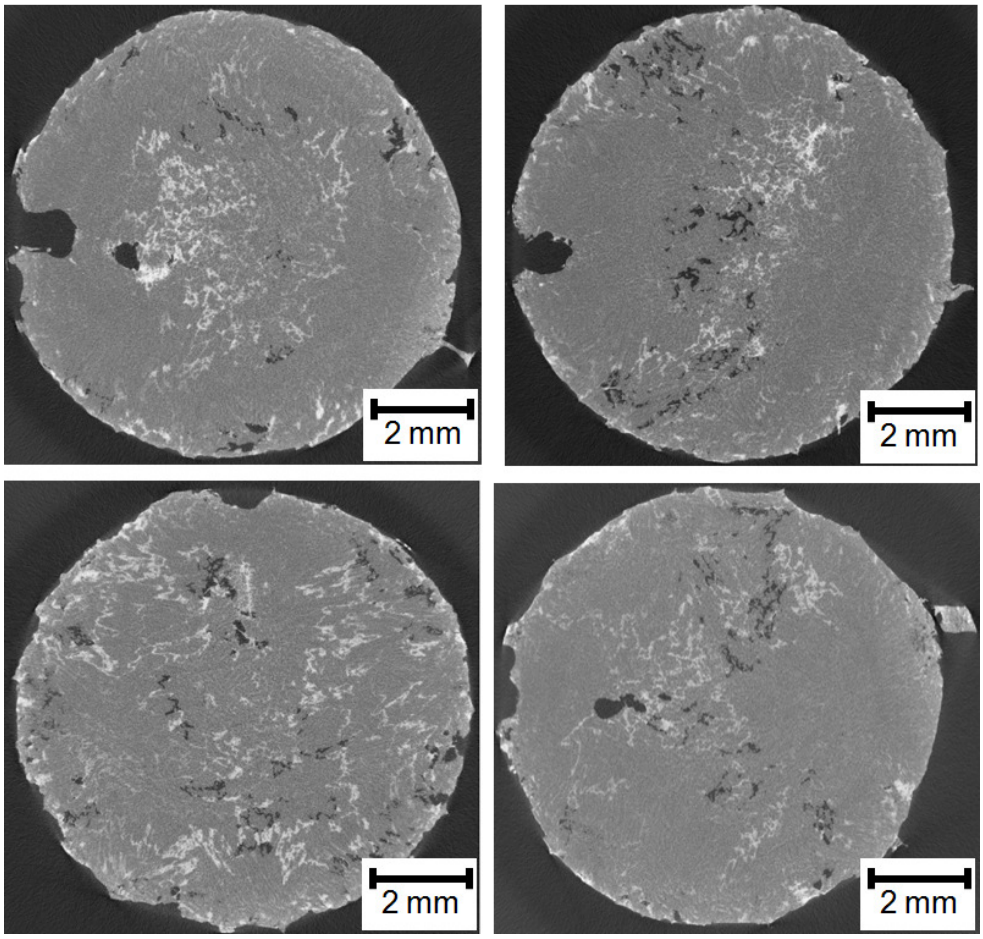

Figure 8.1 Comparison of the formed HT location and dimension of different samples produced through similar processing conditions; 0.5 °C/s and compensation rate of 0.00018 mm/s. The voids are shown in dark areas, non-equilibrium phases are shown in light grey areas and aluminum matrix are shown in grey areas.

We believe that a probabilistic approach could be used to quantitatively model the formation of HT because DC casting in industry is a repetitive process, thus a cast house can generate significant quantities of historical data necessary for tuning and validating the probabilistic model. The data that we are interested in from the cast house are from the

ingot production log which gives the cracking status of the produced ingot (cracked or healthy) at different casting conditions. This data, in combination with the simulation results produced by the ALSIM model, will be the foundation of our new HT model.

The aim of this chapter is to show the possibility of using a probabilistic approach to carry out a quantitative prediction of HT formation. In this chapter, we propose a concept of a new HT model that has the potential to estimate the dimension, location and the statistical occurrence of the HT, thus providing the necessary input for the existing CC criterion. For this stage of the model development, we limit ourselves to a conceptual level and for the example case we only provide a simple mathematical-level implementation of the model. This concept will act as a framework for future development of a new type of HT criterion that is able to perform quantitative prediction of HT formation.

The potential advantage of the new HT model is not only that it is able to capture the connection between HT and CC in a quantitative manner, but it may also provide a tool for selecting the optimal process conditions to produce ingots with the lowest cracking probability through modeling, which historically has been done through trial and error.

8.2 Model description

8.2.1 Modeling the connection between hot tearing and cold cracking

The flow chart of the modeling concept for the connection between HT and CC is shown in Figure 8.2. The main input to the new HT model is the result of a DC casting simulation case produced by ALSIM (step 1 in Figure 8.2). As described in Chapter 2 and shown in our previous work [15], ALSIM is able to produce simulation output in the form of different physical fields. These are, for example, temperature, solid fraction, fluid flow and mechanical fields. For simplification, in this version of the model development, the new HT model will only act as a post-processor (HT prediction is not carried out during the simulation of the casting case).

In our model we assume that a CC needs a micro-HT as the crack initiator. Therefore, for the new HT model, we focus the analysis on the section of the ingot that is prone to both HT and CC. This overlapping region is henceforth called the analysis area (step 2 in Figure 8.2). The graphical example of the analysis area in the ALSIM simulation output is the area within the dashed black ellipse in Figure 8.3a (taken from the simulation of the healthy case in Chapter 2). To confine the analysis area, a criterion needs to be defined. For example: We may choose to limit our view to the area with an ICS value > $0.5 \cdot ICS_{max\text{-}HT}$ (highest ICS value on the HT simulation case, from the result of Chapter 5 it is equal to 0.0013). This is because on HT side, at ICS > 0.00065, we expect some micro-HT already formed. From the

CC side, we focus on the regime where CCS is lower than 10 mm, because the previous work determined that the size of the CC initiator is around 7 mm [16, 17]. While these cutoff values are reasonable initial guesses, these values can be replaced with more realistic ones during further study.

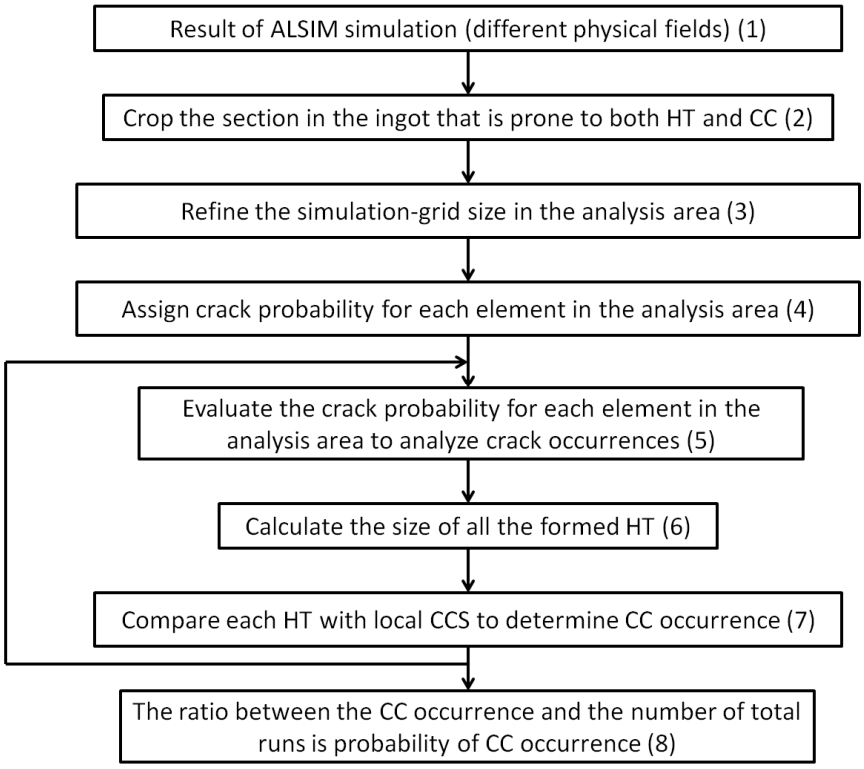

Figure 8.2 The general flow chart of the model to capture the connection between HT and CC.

To improve the resolution of the HT modeling, the simulation grid size in the analysis area is refined from the initial grid size to the length scale of micro-HT (step 3 in Figure 8.2). For example, if the standard simulation grid size is a square with 1 mm on each side, a refinement to 0.2 mm would be sufficient to represent the resolution of the micro-HT. This is because the result from Chapter 7 shows that a void with a diameter of approximately 0.6 mm could significantly reduce the room-temperature strength of the alloy, therefore, a grid size that is comparable to that length scale is needed to capture the void properly and a finer grid size should improve the accuracy of the model prediction.

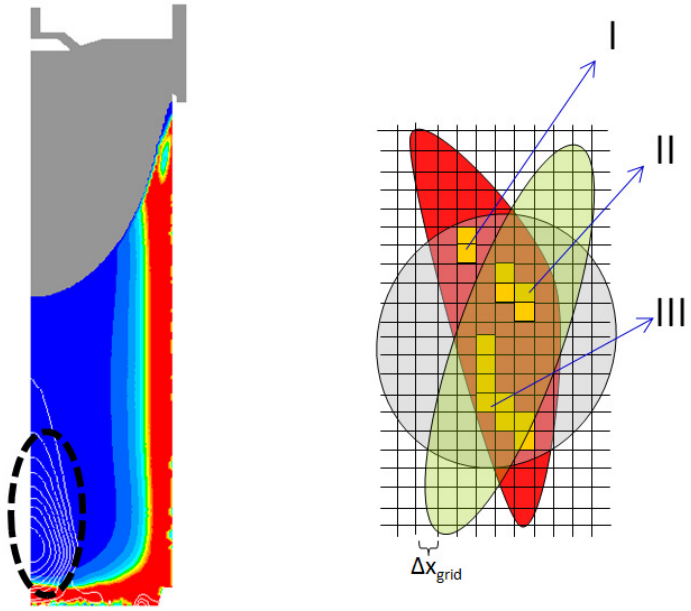

(a) (b)

Figure 8.3 Graphical representation of the area in the billet that is prone to both HT and CC (analysis area), within the black ellipse; colored region represents CC susceptibility (blue is highly susceptible and red is otherwise) while the white isolines signify the susceptibility to HT (the closely-distanced circular isolines above the bottom block show high susceptibility to HT) (a). An illustration of the layers of different physical fields on the analysis area, cracked elements (yellow-filled elements) and the definition of individual cracks (I, II and III) (b).

The next step is assigning cracking probability to each element in the analysis area (step 4 in Figure 8.2). From the literature, the trends of the recent HT criteria suggest that HT formation is a result of a combination of different physical phenomena that occur during solidification [4, 18, 19]. For example, in ALSIM [4], the HT susceptibility is defined as the cumulative strain that occurs during bad feeding conditions. This shows that there is an interdependency between different physical phenomena with respect to the formation of HT and we will take that into account in this model. Details on the formulation of the relationship between physical phenomena will be the main discussion of Section 8.2.2. The cracking probability of each element depends on the values of the physical fields at that specific element.

The next step is to evaluate the cracking probability in each of the elements in the analysis area (step 5 in Figure 8.2). The outcome of this evaluation step for each element is binary: Either that specific element cracks or it does not.

The subsequent step (step 6 in Figure 8.2) is to calculate the dimension (i.e. length) of the formed HT based on the result of evaluation procedure in the previous step. An illustration of the layers of different physical fields on the analysis area, cracked elements and the description of individual HT are shown in Figure 8.3b. From that figure, different ellipses with different colors represent different physical fields and the yellow-filled elements represent cracked elements. An individual HT is defined as an uninterrupted connection of cracked elements. I, II and III are considered individual HT because they are not directly connected with each other. The length of each HT is defined by the number of the connected cracked elements multiplied by the individual (refined) grid size in the analysis area (Δx_{grid} in Figure 8.3b).

After we obtained the length of all the formed HT from the previous step, the next step is to compare each formed HT length with the critical crack size (CCS) value at the location where the HT is formed (step 7 in Figure 8.2). If the formed HT exceeds the CCS obtained from the ALSIM calculation, then CC will occur. From macroscopic point of view, e.g. through ALSIM simulation, a set of physical field values can be used to represent the outcome of a certain solidification process. However, from more microscopic-level observation, for example as shown in Figure 8.1, different HT configurations (in terms of HT dimension and location where it forms) can be obtained when repeating the experiment with the same set of solidification conditions. Because we would like to capture the different possibilities of HT formation through statistical analysis, we need to run step 5 to 7 in Figure 8.2 multiple times. One set of these steps is henceforth designated as a trial run.

The ultimate output of the complete model is the probability of CC occurrence on a DC casting case based on a set of casting conditions as the inputs. This CC occurrence probability is defined as the ratio of the number of CC occurrences (if the formed HT exceeds the CCS value) and the total number of trial runs used in the model (step 8 in Figure 8.2).

To illustrate the implementation of the essential parts of this model (step 5 to 7 in Figure 8.2), in Section 8.3 we show a mathematical-level implementation in a simplified one dimensional (1-D) system.

8.2.2 Modeling the relationship between physical phenomena

In section 8.2.1, we mentioned that there is interplay between different physical phenomena during solidification that results in the formation of HT. Although, in general, there are many physical phenomena during solidification that influence HT formation (e.g. feeding [20, 21], strain rate [19], dendrite arms spacing (DAS) [22], stress [23], etc.), previous studies suggest that these phenomena have varying levels of significance or weight with respect to HT formation [1, 5]. For instance, it is generally accepted that feeding is one of

the most critical parameters of HT formation. This is because if the mush is under good feeding condition, it may be difficult for HT to form due to the liquid metal healing. If the feeding is bad, the strain rate is considered quite important because the higher it is, the shorter the time for the alloy to react and compensate to the deformation. There are also other variables that are suggested to depend on each other to affect the HT formation. These are, for example, stress and DAS [22-24] (assuming DAS is proportional to the grain size [25]). However, the detailed correlation between these two phenomena with respect to HT susceptibility of the alloy is still not clear, thus, further investigation on this topic is needed. From our previous work, we suggest that strain rate is more important than the amount of produced stress for the formation of HT [5].

An example of how one might formulate the crack probability for each element in the analysis area from the various physical phenomena mentioned above is shown in Eq. 8.1.

$$P_{total} = P(p_{feeding}) \times (c_A \cdot P(\dot{\varepsilon}_{rr}) + (c_B \cdot P(\sigma_{rr}) \times P(DAS))) \quad \textbf{(8.1)}$$

P_{total} is the total cracking probability or the joint cracking probability of each element based on the values of different physical fields. P_{total} has a value between 0 (no probability to crack) and 1 (crack always occurs). The joint cracking probability is obtained through the combination of individual cracking probability functions (CPF) of different physical phenomena. For example, the CPF for feeding pressure in Eq. 8.1 is described as $P(p_{feeding})$, while $\dot{\varepsilon}_{rr}, \sigma_{rr}\ and\ DAS$ are the radial strain rate, radial stress and dendrite arms spacing (DAS), respectively. For strain-rate and stress, we only take into account the radial component of the variable because the mechanical deformation generated in this direction is considered as the main mode of HT formation in a billet [26]. c_A and c_B are weight component for different groups of physical fields that can be tuned to signify the importance of different groups of physical phenomena. For completion, we have to normalize these weight components so the maximum value of P_{total} is 1. This formulation is simplified and further study of the relationship between different physical phenomena still needs to be done. However, the aim of this section is to show the method to formulate the relationship between different physical phenomena mathematically, in order to construct the cracking probability of the elements in the analysis area.

The CPF of each physical field is described as the relationship between the physical field value and the cracking probability at that certain physical field value. The shape of the CPF is unique for each physical field. It depends on their influence and contribution to HT formation. In this model, the values of physical fields are produced through ALSIM simulation at different process conditions and the shape of CPF could be defined either through hypothesis of physical phenomena or by fitting to statistical data from the cast house. Simple examples to define CPF through both methods are shown in Figure 8.4.

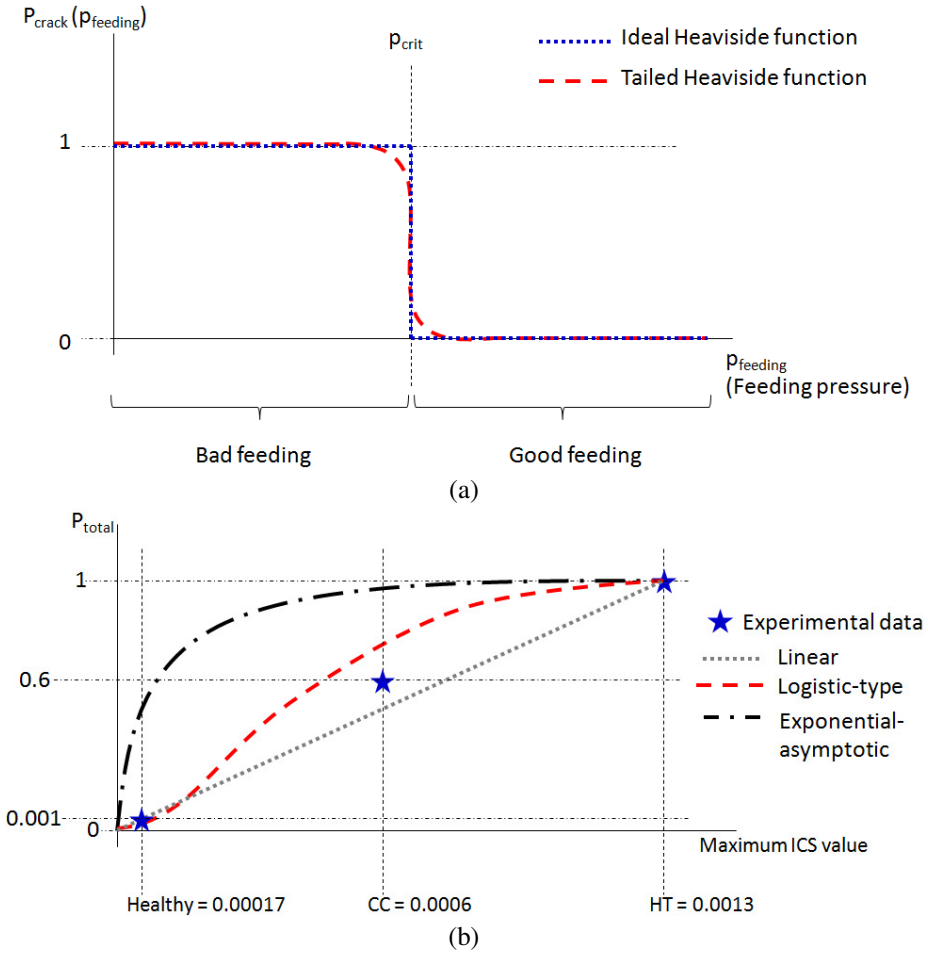

Figure 8.4 Two methods to define the shape of the cracking probability function (CPF) of individual physical fields. One method is to use a hypothesis of physical phenomenon; in this case, feeding (a). A second method is fitting to statistical data from the experiment (i.e. production data from the cast house) (b).

For the first method (hypothesis of physical phenomenon), let us take an example of a physical phenomenon that is commonly described in available HT criteria as a threshold-like condition [4, 19]: feeding condition. To specify the bad feeding condition, we frequently use a critical pressure value (p_{crit}) [19]. This means if a specific element experiences feeding difficulties, i.e. the feeding pressure becomes lower than p_{crit} at some stage during solidification, there is a chance of HT to occur in such an element. Thus a step (Heaviside) function (dotted blue line in Figure 8.4a) would be appropriate to represent the CPF of this phenomenon. However, in practice, there are major difficulties to define an

absolute critical value (i.e. critical feeding pressure) and some events may occur in the vicinity of the absolute value [27]. Therefore, to improve the realism of the function, we suggest of using a tailed Heaviside function for representing the CPF of this phenomenon (dashed red line in Figure 8.4a).

The other method is to construct CPF by fitting the experimental data from a repeated casting process (for example from the production log of the cast house) and relate them with the result of ALSIM simulation. For the fitting example, we use the maximum integrated critical strain (ICS) values from the benchmark casting cases presented in Chapter 2 as the example data points. The maximum ICS value for healthy, CC and HT cases are 0.00017, 0.0006 and 0.0013 respectively. Because we only performed one trial cast for each casting condition we have to make an assumption for the cracking probability for each casting case. For the healthy case, we will assume that the crack probability is significantly low (i.e. 0.001). As discussed in Chapter 2, the CC may be started by the micro-HT, therefore we specify the crack probability for CC case as 0.6. For this model, it is important to specify the maximum threshold value. For this example, we assume that the casting conditions of the HT case will always resulting in catastrophic HT. Therefore, we specify the cracking probability of the HT case as 1. From these three data points (plotted as blue stars in Figure 8.4b), we can carry out a fitting procedure through different function types. Different function examples are shown in Figure 8.4b; linear (grey dotted line), logistic-type (red dashed line) and exponential asymptotic (black dashed and dotted line). Naturally, other types function outside these examples can also be used to obtain the best fitting from the experimental data. From this figure, an optimum fit would be obtained if a larger number of experimental data is used for the analysis. The shape of the CPF or the type of function that offer the best fit to the experimental data may reveal the influence of different physical phenomena with respect to the HT formation.

8.3 Implementation example of the model in a simplified 1-D system

8.3.1 Model setting

For an implementation example of the model, we only provide a mathematical-level implementation in a simple system. In this example, we only focus on the main part of the model which describes the probabilistic evaluation of the HT formation (steps 5–7 in Figure 8.2). The aim of this example is to show the implementation steps and the capability of this model to provide the statistical distribution of the dimension (i.e. length) and the location of the formed HT based on different combinations of physical fields as the model input.

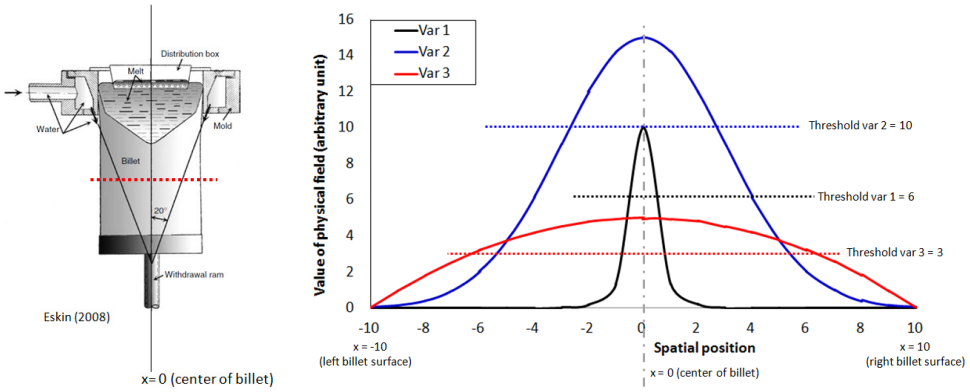

(a) (b)

Figure 8.5 Assumption of the 1-D system for the example case, a horizontal slice of the billet, red dashed line (adapted from [28]) (a). Spatial distribution value of different physical fields and the comparison between the values of each physical field and its threshold value (b).

The geometry that we use for this example is a 1-D system. Let us assume that we take a horizontal slice from a billet (red dotted line in Figure 8.5a). This geometry has 21 elements with equal size. For simplification, in this example we use non-physical (dummy) values for the physical fields that can be produced by the ALSIM simulation. For each physical field, we use different value distributions as shown by different colored lines in Figure 8.5b. In this figure, we choose the spatial distribution value to be maximum at the center of the billet as compared to the surface. This is because we know from the literature, the values of some physical phenomena that influence the HT formation increase toward the center of the billet [3, 15, 25].

At the current stage of the model development, the detailed relationship between physical phenomena with respect to HT formation is not yet studied. Therefore, for this example, we assume that each physical phenomenon is independent from the others. The relationships between physical phenomena for this case are described in Eq. 8.2. We define the CPF of all physical fields as an idealized step function (dotted blue line in Figure 8.4a) and each physical field has its own unique threshold value (i.e. if the value of the field is bigger than the threshold, the outcome of CPF is 1, otherwise it is 0). The comparison between the values of each physical field and its threshold value is shown in Figure 8.5b.

$$P_{total}(x) = c_1 \cdot P(\mathrm{var}_1(x)) + c_2 \cdot P(\mathrm{var}_2(x)) + c_3 \cdot P(\mathrm{var}_3(x)) \quad \textbf{(8.2)}$$

$P_{total}(x)$ is the total cracking probability at x and the value of each weight component (c_1, c_2 and c_3) is also normalized so that the maximum value of $P_{total}(x) = 1$. Since we assume that each physical field has an equal weight, Eq. 8.2 can be re-written as Eq. 8.3.

$$P_{total}(x) = 0.33 \cdot P(\text{var}_1(x)) + 0.33 \cdot P(\text{var}_2(x)) + 0.33 \cdot P(\text{var}_3(x)) \quad \textbf{(8.3)}$$

From the comparison between the field values and the thresholds of the different fields shown in Figure 8.5b, the spatial distribution of cracking probability for an individual physical field is depicted in Figure 8.6a. The spatial distribution of the joint cracking probability of three variables ($P_{total}(x)$) is shown in Figure 8.6b. From those figures we see that the joint cracking probability at the center of the billet ($x = 0$) is the highest because the CPF value of each physical field is 1. The joint cracking probability decreases as it moves to the surface because the number of physical fields with CPF equal to 1 decrease and eventually disappear as it reaches the surface of the billet. This is because in the sub-surface, the values of the physical fields are always below its threshold.

The next step is to perform the evaluation of cracking probability on every element in the system. In one trial run, we check each element in the system once. The crack probability evaluation algorithm for one trial run is shown in Figure 8.7. We use a uniformly-distributed random number generator (rand) for evaluating the crack probability of each element. This evaluation method may be referred to as a statistical simulation. As mentioned in the previous section, the outcome of the evaluation is binary; either crack (1) or not crack (0). A series of contiguous elements that have been identified as cracked form one HT. To obtain the statistical distribution of the length of formed HT, we need to do a multiple trial runs. In this example, we perform 10 trial runs.

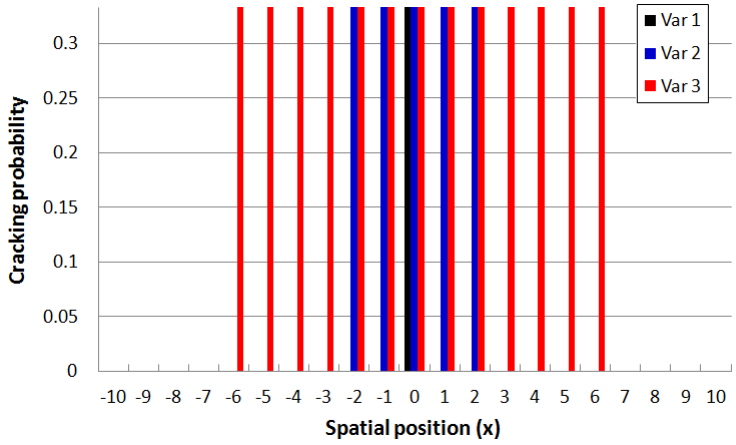

(a)

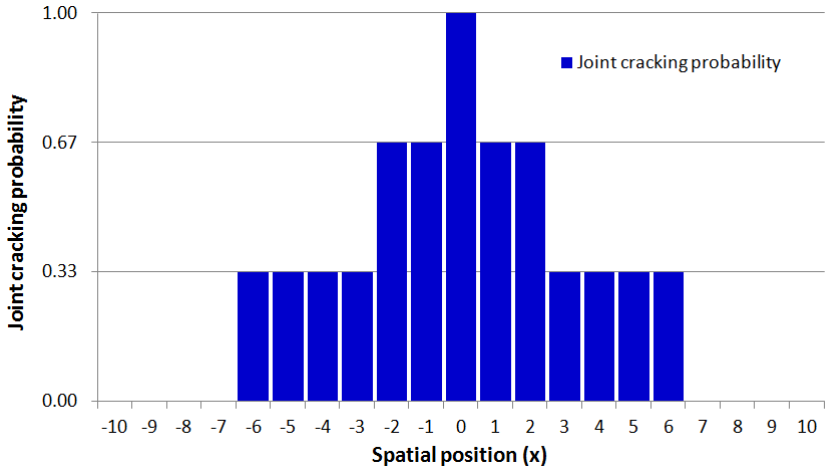

(b)

Figure 8.6 Spatial distribution of cracking probability for each physical field (a) and spatial distribution of joint cracking probability for three physical fields (b).

```
for x = -10:10  %Checking all spaces
    Px(var1,var2,var3) = 0.33*P(var1) + 0.33*P(var2) + 0.33*P(var3); %Define joint cracking probability
    if (rand < Px(var1,var2,var3))  %Probabilistic check
        crack(x) = 1; %Crack occurs
    else
        crack(x) = 0; %Crack not occurs
    end
end
```

Figure 8.7 Crack probability evaluation algorithm for one trial run.

8.3.2 Results

Figure 8.8a shows the map of the cracked elements (blue dots) on different spatial positions (horizontal axis) at different trial runs (vertical axis). In general, the trend of cracking occurrence is highest at the center and gradually decreases as it goes toward the surface as formulated by the joint cracking probability distribution in Figure 8.6b. Also from Figure 8.8a, we see that even though the probability of cracking at spatial positions is following the joint probability distribution, the length of the formed crack and its location is not always similar for different trial runs. For example, although generally the position of the longest cracks usually occurs around the center of the billet, there are a few of relatively long cracks that are formed a bit off the center of the billet. This result shows that the proposed model is able to represent the randomness of crack occurrence. Figure 8.8a shows that from 10 trial runs, the longest crack formed has the length of 5 elements (continuously neighboring dots enclosed in the red labels in the same figure) and it has 20% chance of occurrence because it only occurs in trial 2 and 9. The next longest crack has a length of 4 (continuously neighboring dots enclosed in the blue labels in the same figure) and the chance of having this length of crack and more is 80% (it occurs in every trial except trial 6 and 8).

From this result, we may also observe the statistical crack occurrence for different crack length. Figure 8.8b shows that the probability for finding shorter cracks in the entire system is higher as compared to longer cracks. This result supports the trend from the experimental result observed in Chapter 7 (Figure 7.9).

8.4 Discussion

As shown in Section 8.3.2, the proposed model has a potential to provide the length, location and statistical distribution of HT lengths using the relation between different physical fields as its input. The output of this model is the critical input for the existing CC criterion in ALSIM. By inserting the result of the new HT model to the existing CC criterion, we can obtain the probabilistic occurrence of CC. For instance, if the CCS is 5 then the chance of CC occurrence is only 20%. However, if the CCS is 4, then the CC occurrence increases to 80%. The implementation of this new HT model in ALSIM could allow ALSIM to capture the connection between HT and CC, and provide us with quantitative measure of the CC occurrence in a DC casting simulation. However, in the future, we suggest carrying out larger number of trial runs because 10 trial runs are deemed insufficient to capture the steady-state statistical behavior of the system. This is because Figure 8.6b shows that the joint cracking probability between x = -6 and x = 6 is continuously above zero. Thus, theoretically, the longest possible crack that can occur in

this system is 13. Since the occurrence probability of this event is extremely low and we only use low number of trial runs, the event does not show in this example.

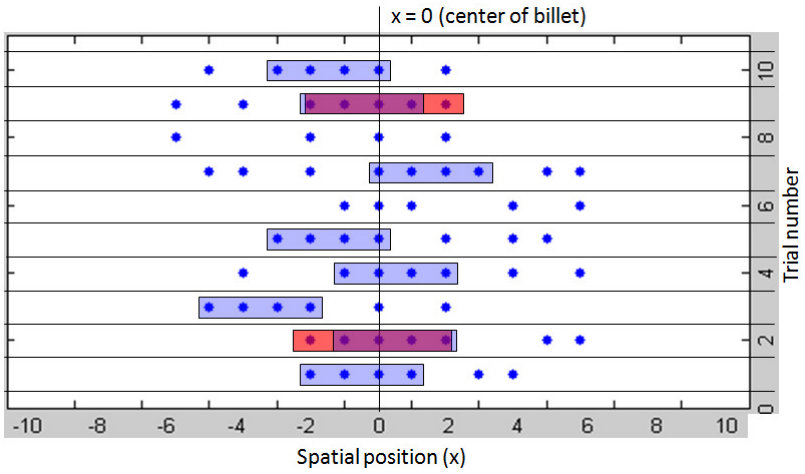

(a)

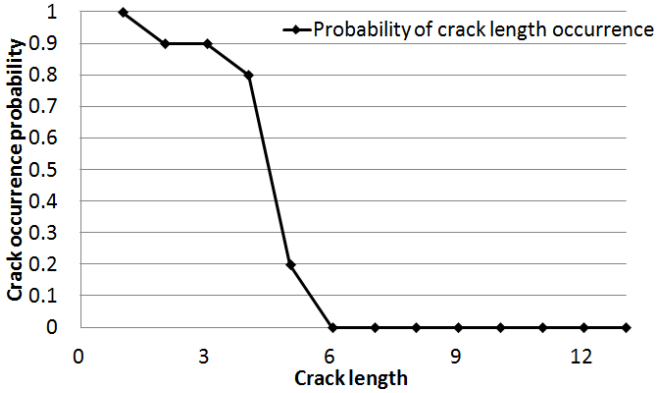

(b)

Figure 8.8 Result of probabilistic crack evaluation on spatial positions with 10 trial runs, blue dots represents cracked elements (a). Probability of finding crack with a minimum length on the system from 10 trial runs (b).

For a simple 1-D system shown in Section 8.3.2, it is possible to extract an analytical solution of a simple cracking event, i.e. the occurrence probability of a single crack with a finite length in the entire system. However, in reality, for example in the DC casting case or in the small-scale solidification experiment (experiment shown in Chapter 6), the conditions of the system are much more complex compared to the given example. The possible examples of the increased system complexity are as follows:

1. The increase in the system dimension, for example to two dimensions (2-D) or even three dimensions (3-D).
2. The formulation of the relationships between physical phenomena that influence the HT formation will be more complex because more physical phenomena will be taken into account.
3. The shape of CPF of each physical field may not be as straightforward as the step function defined in the example case.
4. The analysis area (cropped regime in the ALSIM simulation that is prone to both HT and CC) would not necessarily have a simple geometrical shape (e.g. rectangular or spherical). This is because the shape of the analysis area will depends on different process conditions of casting and it may be irregular.

The complexities mentioned above may pose difficulties in formulating an analytical solution for finding the crack probability in the entire analysis area. Therefore a statistical simulation method, for instance the one shown in the example case may provide more practical solution compared to the effort of deriving an analytical solution of a highly complex system. Additionally, by using this simulation technique, we are also able to extract the possible locations of each formed HT within the analysis area and, thus, can derive the relative distances between individual HT. This information may be useful to study the spatial distribution effect of the formed HT with respect to the room temperature strength as discussed in Chapter 7.

If we increase the level of complexity of the system as described in the previous paragraphs, calculating the length of each formed HT would be not as straightforward as shown in the example. Therefore, for future research, we suggest developing an additional technique to calculate the crack dimension, for example using an image-based percolation method [29], and integrate it to the new HT model. Alternatively, the image analysis method that we use to quantify the HT geometry in Chapter 7 [30] could also be utilized to quantify the dimension of the formed HT. This is because the crack distribution map as shown in Figure 8.8a has a binary value, thus comparable to a binary-type image shown in Figure 7.2f as a preferred input for the image analysis.

Before this model is fully operational for predicting the cracking outcome of the DC casting process, there are two necessary steps that need to be carried out. These steps are as follows:

1. We need to improve the formulation on the relationship between physical fields as described in Eq. 8.1. Although the formulation described in such an equation includes the main phenomena of HT formation, it is still too simple. In reality, HT is a highly complex process and it involves a significant number of physical

phenomena during solidification [1]. Therefore, to capture the real HT formation, the formulation needs to be improved.

2. We need to specify the shape of the CPF and fine-tune the weight constants of each physical field. This is because these factors represent the degree of influence of each physical phenomenon with respect to the HT formation. The methods to obtain this information are described in 8.2.2; either through theoretical hypothesis of physical phenomenon or by fitting of the statistical data from the production line in combination with the result of ALSIM simulation.

After the steps described in the previous paragraph have been carried out, another possible development is to verify the validity of the model at different length scales. One possible way to study this is to make an ALSIM simulation of the HT formation experiments described in Chapter 6 and then optimize the new HT model parameters (i.e. CPF and weight constants) for this experiment. Subsequently, we cross-check the predicted HT result with the obtained 3-D XMT images of the pre-HT samples. The difference between model parameters of different length-scale cases (DC casting and the small scale solidification experiments) may reveal the length-scale sensitivity of the new HT model.

Despite the relative simplicity of this model, it has the potential to provide us with the dimension, location and statistical occurrence of the HT length. There are several ways to improve upon this model further, to give it more realism and useful predictive capabilities:

1. As suggested in Chapter 3 and Chapter 7, sub-critical HT propagation may be an important mechanism of the connection between HT and CC. Therefore, future developments of the model should take into account the propagation mechanism of the formed HT.
2. Capturing the HT formation in ‘real-time’ and taking into account the HT propagation mechanism during solidification, would require implementation of this model in ALSIM simulation of DC casting (not as a post-processor).
3. A better method to predict the threshold value of HT occurrence should be developed. So far, we define this threshold value by using the ALSIM simulation result that is produced from the casting conditions that always give a HT outcome (i.e. HT casting case in Chapter 2).

The examples shown above should be included in the roadmap of the future model development.

8.5 Conclusions

In this chapter, we propose a concept of a new HT model that can be implemented in ALSIM for capturing the connection between HT and CC. From the work and analysis that we carried out in this chapter, we obtain some conclusions as following:

1. From the result of a mathematical-level implementation, we show that the proposed HT model has a possibility to provide quantitative information of HT occurrence such as the dimension (i.e. length), location and statistical occurrence of the HT length.
2. The output of the new HT model can be used as an input to the existing CC criterion and ultimately it will provide us with the statistical occurrence of the CC. This will enable ALSIM to capture the connection between HT and CC.
3. Although the formulation in Eq. 8.1 includes the main physical phenomena that are responsible for HT formation (e.g. feeding and strain-rate), in reality, HT is a highly complex phenomena, therefore to truly capture the HT phenomena, the formulation needs to be improved such as by taking into account more physical phenomena that are responsible for HT formation and clarifying the relationship between all of the involved phenomena.
4. To obtain the shape of CDF and the optimum weight constant for each individual physical field, two methods for obtaining these values are suggested. These are either via a theoretical hypothesis of known physical phenomena or through fitting of the statistical data from the production line in combination with the result of ALSIM simulation. The obtained information may explain the contribution of different physical phenomena with respect to the HT formation.
5. For a highly complex system, a simulation technique to evaluate the crack probability is preferred over the analytical solution due to practical reasons. Moreover, the simulation technique is also able to provide the possible locations and dimension of the formed HT, and thus raises the possibility to study the spatial distribution effect of the formed HT towards the room temperature strength of the alloy as suggested in Chapter 7.

References

[1] Eskin, D. G., Katgerman, L., "A quest for a new hot tearing criterion", *Metallurgical and Materials Transactions A* (2007), 38A, pp. 1511-9.
[2] Eskin, D. G., Suyitno, Katgerman, L., "Mechanical properties in the semi-solid state and hot tearing of aluminium alloys", *Progress in Materials Science* (2004), 49, pp. 629-711.
[3] Suyitno, Kool, W. H., Katgerman, L., "Hot tearing criteria evaluation for direct-chill casting of an Al-4.5 pct Cu alloy", *Metallurgical and Materials Transactions A* (2005), 36, pp. 1537-46.

[4] M'Hamdi, M., Mo, A., Fjær, H. G., "TearSim: A two-phase model addressing hot tearing formation during aluminum direct chill casting", *Metallurgical and Materials Transactions A* (2006), 37, pp. 3069-83.
[5] Subroto, T., Miroux, A., Bouffier, L., Josserond, C., Salvo, L., Suéry, M., Eskin, D. G., Katgerman, L., "Formation of Hot Tear Under Controlled Solidification Conditions", *Metallurgical and Materials Transactions A* (2014), 45, pp. 2855-62.
[6] Holm, E. A., Srolovitz, D. J., Cahn, J. W., "Microstructural evolution in two-dimensional two-phase polycrystals", *Acta Metallurgica Et Materialia* (1993), 41, pp. 1119-36.
[7] Provan, J. W., "Probabilistic fracture mechanics and reliability", Dordrecht; Boston, M. Nijhoff (1987).
[8] Boettinger, W. J., Coriell, S. R., Greer, A. L., Karma, A., Kurz, W., Rappaz, M., Trivedi, R., "Solidification microstructures: recent developments, future directions", *Acta Materialia* (2000), 48, pp. 43-70.
[9] Rappaz, M., Gandin, C. A., "Probabilistic modelling of microstructure formation in solidification processes", *Acta Metallurgica Et Materialia* (1993), 41, pp. 345-60.
[10] Charbon, C., Jacot, A., Rappaz, M., "Three-dimensional probabilistic modelling of equiaxed eutectic solidification in the presence of convection", *Materials Science and Engineering A* (1993), 173, pp. 143-8.
[11] Sistaninia, M., Drezet, J. M., Phillion, A. B., Rappaz, M., "Prediction of hot tear formation in vertical DC casting of aluminum billets using a granular approach", *JOM* (2013), 65, pp. 1131-7.
[12] Sistaninia, M., Phillion, A. B., Drezet, J. M., Rappaz, M., "A 3D coupled hydro-mechanical granular model for the prediction of hot tearing formation", *IOP Conference Series: Materials Science and Engineering* (2012), 33, pp. 012070.
[13] Vernède, S., Dantzig, J. A., Rappaz, M., "A mesoscale granular model for the mechanical behavior of alloys during solidification", *Acta Materialia* (2009), 57, pp. 1554-69.
[14] Vernède, S., Jarry, P., Rappaz, M., "A granular model of equiaxed mushy zones: Formation of a coherent solid and localization of feeding", *Acta Materialia* (2006), 54, pp. 4023-34.
[15] Subroto, T., Miroux, A., Mortensen, D., M'Hamdi, M., Eskin, D. G., Katgerman, L., "Semi-quantitative predictions of hot tearing and cold cracking in aluminum DC casting using numerical process simulator", *IOP Conference Series: Materials Science and Engineering* (2012), 33, pp. 012068.
[16] Lalpoor, M., Eskin, D. G., Ruvalcaba, D., Fjær, H. G., Ten Cate, A., Ontijt, N., Katgerman, L., "Cold cracking in DC-cast high strength aluminum alloy ingots: An intrinsic problem intensified by casting process parameters", *Materials Science and Engineering A* (2011), 528, pp. 2831-42.
[17] Eskin, D. G., Lalpoor, M., Katgerman, L., "Cold cracking during direct-chill casting", In: *Light Metals, TMS*, San Diego, CA, USA (2011), pp. 669-74.
[18] Suyitno, W. H., Kool, W. H., Katgerman, L., "Integrated approach for prediction of hot tearing", *Metallurgical and Materials Transactions A* (2009), 40, pp. 2388-400.
[19] Rappaz, M., Drezet, J. M., Gremaud, M., "A new hot-tearing criterion", *Metallurgical and Materials Transactions A* (1999), 30, pp. 449-55.

[20] Feurer, U., "Influence of Alloy Composition and Solidification Conditions on Dendrite Arm Spacing, Feeding and Hot Tearing Properties of Aluminum Alloys", In: *International Symposium of Quality Control of Engineering Alloys and the Role of Metals Science*, Delft, The Netherlands (1977), pp. 131-45.
[21] Katgerman, L., "A Mathematical Model for Hot Cracking of Aluminum Alloys During D.C. Casting", *Journal of Metals* (1982), 34, pp. 46-9.
[22] Pekguleryuz, M. O., Lin, S., Ozbakir, E., Temur, D., Aliravci, C., "Hot tear susceptibility of aluminium-silicon binary alloys", *International Journal of Cast Metals Research* (2010), 23, pp. 310-20.
[23] Dickhaus, C. H., Ohm, L., Engler, S., "Mechanical Properties of Solidifying Shells of Aluminum Alloys", *Transactions of the American Foundrymen's Society* (1993), pp. 677-84.
[24] Li, S., Sadayappan, K., Apelian, D., "Role of grain refinement in the hot tearing of cast Al-Cu alloy", *Metallurgical and Materials Transactions B* (2013), 44, pp. 614-23.
[25] Eskin, D. G., Zuidema, J., Savran, V. I., Katgerman, L., "Structure formation and macrosegregation under different process conditions during DC casting", *Materials Science and Engineering A* (2004), 384, pp. 232-44.
[26] Phillion, A. B., "Hot tearing and constitutive behavior of semi-solid aluminum alloys", [Ph.D. thesis] (2007), The University of British Columbia.
[27] Schmitt, W., Wellein, R., "Model of the flaw size distribution in welds", *Nuclear Engineering and Design* (1982), 71, pp. 293-4.
[28] Eskin, D. G., "Physical Metallurgy of Direct Chill Casting of Aluminum Alloys (Advances in Metallic Alloys)", CRC Press, Taylor & Francis group, LLC (2008).
[29] Yamaguchi, T., Nakamura, S., Saegusa, R., Hashimoto, S., "Image-based crack detection for real concrete surfaces", *IEEJ Transactions on Electrical and Electronic Engineering* (2008), 3, pp. 128-35.
[30] Boulos, V., Fristot, V., Houzet, D., Salvo, L., Lhuissier, P., "Investigating performance variations of an optimized GPU-ported granulometry algorithm", In: *6th Annual Conference on Design and Architectures for Signal and Image Processing (DASIP 2012)*, Karlsruhe, Germany (2012), pp. 36-41.

Chapter 9
CONCLUDING REMARKS AND OUTLOOK

9.1 Concluding remarks

From the previous study on cold cracking (CC) prediction, it was suggested that undeveloped or micro hot tear (HT) may acts as the initiation point of CC. However, this phenomenon was not yet experimentally validated and the connection mechanism between HT and CC was also not yet studied in details.

In the last few decades, numerical process simulator has been commonly used to minimize the occurrence of ingot cracking in the industrial DC casting process. In this study, we use ALSIM as the process modeller. ALSIM is a multi-physics finite-element based model that is fine tuned to optimize the aluminium DC casting process. Although ALSIM is relatively well developed with available criteria for susceptibility estimation for both types of casting cracks, the cracking prediction capability in ALSIM has not yet reached its full potential, for example, it cannot provide a quantitative crack prediction and thus needs to be improved.

At the beginning of this project, we showed that the current version of ALSIM (ALSIM 6) is sensitive to different casting parameters and it is able to qualitatively estimate the formation of both HT and CC of aluminum DC casting process. This validation is performed through benchmarking between trial casts that produced different cast outcomes (healthy, HT and CC) and ALSIM simulations that were ran to mimic those trial casts. In this validation, we also see an indication that ALSIM has the potential to capture the connection between HT and CC. Although there are several aspects that need to be improved (such as improvement of the HT criterion to provide the dimension of the formed crack), the analysis shows that ALSIM possesses the necessary foundations for modelling the connection between HT and CC.

In this work we added new data to ALSIM constitutive database of AA7050 for sub- and super-solidus temperature ranges. Interesting tensile mechanical phenomena was observed for this alloy at temperature around the solidus (465 °C). In the sub-solidus temperature regime (fully solid state, between 400 °C – 465 °C), we see that there is a fast decrease in alloy ductility above 450 °C. This temperature is also the switching point of fracture mechanism from ductile transgranular (below 450 °C) to ductile intergranular (above 450 °C). Additionally, the hardening also reaches a minimum and very low value at the similar temperature point which leads to a conclusion that there is a change in the alloy mechanical behavior at 450 °C. In semi-solid temperature regime, we found that the mechanical behavior of AA7050 is different compared to the other two alloys that have been previously used in ALSIM semi-solid mechanical database. AA7050 is stronger compared to Al–2% Cu but weaker compared to AA5182.

Using the obtained mechanical properties database of AA7050 and the other alloys that are available from the literature, we performed the sensitivity analysis of ALSIM model with respect to different mechanical databases at different temperature regime; semi-solid and fully-solid (hardening). This analysis shows that ALSIM model is sensitive to different mechanical properties databases on both temperature regimes.

From the combination of controlled solidification experiment and three dimensional X-Ray microtomography imaging method (including image analysis), we managed to qualitatively control the formation of HT inside a sample. By altering two variables during the controlled solidification experiment; i.e. cooling rate and compensation rate, we were able to construct a HT map that shows different level of HT severity; healthy (compression state), micro-HT, macro-HT and complete fracture. The samples produced with micro-HT conditions are the ones that are suitable for the verification of the connection between HT and CC.

Connection between HT and CC is experimentally verified. This is shown by significant reduction of the strength and ductility of the alloy at room temperature when micro-HT are present in the material. From the obtained results, there might be two mechanisms that play a role: The presence of the micro HT in the material and the overabundant amount of non-equilibrium phase that is present in the material. We think there might be interplay between these mechanisms that causes detrimental effect to the mechanical properties of the material because non-equilibrium phase is known to reduce the ductility of the material. From this study, we also suggest an additional possible connection mechanism between HT and CC. The previous study on CC prediction states that that CC occurs due to the significant increase in the stress states of the ingot when it is fully solidified and thus a decreased critical crack size. From this study, we suggest there might be sub-critical propagation of the formed micro-HT at the low-strength and low-ductility temperature regime (between 450 and 465 °C) due to the large increase in the stress states of the ingot when it just fully solidified. Since we observed that micro-HT usually does not formed individually, sub-critical propagation of the micro-HT might lead to crack coalescences and ultimately produces larger CC initiator. This condition could increase the CC susceptibility of the ingot.

After validating the connection between HT and CC, the next step is to extend the ALSIM HT criterion capability so it is able to calculate the dimension (i.e. length) of the formed HT. In this study, we proposed a concept of a new HT model based on a stochastic (probabilistic) framework. This model utilizes the result of ALSIM simulation (different physical fields) as the model input. A simplified example that we presented in this study shows that the new HT model has a potential to provide the information regarding probable length and locations of the formed HT in the system. This information is needed by the existing ALSIM CC criterion to predict the crack occurrence. The utilization of the new HT

model would open the possibility for ALSIM to capture the connection between HT and CC and ultimately provide us with a quantitative crack prediction.

9.2 Outlook

Although we have obtained important and new results from this study, there are still some remaining challenges that need to be solved. This is for example the way how ALSIM treats constitutive behaviour in the semi-solid state. The current constitutive model only takes into account the load development process while the experimental results of different alloys at the semi-solid temperature regime show that the damage development phase is quite important for capturing the HT development. Therefore, we need to develop a better constitutive model that takes into account the damage development phase in the semi-solid state.

From this study we also revealed some drawbacks in the existing ALSIM cracking criteria (both HT and CC). The problem on HT side is that although ALSIM current criterion is sensitive to different casting parameters, it is not sensitive to different semi-solid mechanical databases and thus could not capture the HT susceptibility of the different alloys with similar thermo-physical properties (e.g. solidification range). In response to this drawback, for future ALSIM development, we suggest to implement a complementary HT criterion in addition to the existing one. This complementary HT criterion should be materials properties dependent. On the CC side, the existing crack criterion only uses a single crack initiation point and the assumption of crack initiator geometry is oversimplified (e.g. penny-shaped or thumbnail-shaped). From the experimental results, we found that micro-HT does not usually form individually and the micro-HT often has a finite thickness and complex-shaped geometry, e.g. branching crack. The oversimplifications made in the CC criterion reduce the accuracy of the crack prediction.

Further development and implementation of the probabilistic HT model is necessary. In this study, we only propose a concept of the model and there are several steps that need to be carried out before this model is fully operational in ALSIM for estimating the cracking occurrence on DC casting processes. These steps are for example, the clarification of the relationship between the physical phenomena during casting (e.g. stress, strain rate, dendrite arms spacing etc.) and proper formulation of such a relationship for the model. This formulation should be subsequently tuned by fitting the experimental data from the cast house to improve the crack prediction accuracy of the model.

Summary

Direct-chill (DC) casting is one of the most common methods to produce ingots of high-strength aluminum alloys such as an AA7050. Despite of its superior mechanical properties, this alloy is prone to both hot tearing (HT) and cold cracking (CC) during DC casting. HT form above the solidus while CC occurs below the solidus temperature. CC occurrence appears to be random and thus it is difficult to foresee. Moreover, the propagation of CC is usually catastrophic. Thus, not only it decreases the yield of the production and may damage the casting equipments, but it also poses safety hazard to the casting personnel. A previous study on CC indicated this type of crack could start from a solidification defect, for example an inclusion. The same study also suggested that undeveloped or micro hot tear (HT) may also act as CC initiation point but this assumption has not yet being proven. In addition to trials and errors methods, numerical models are more and more considered as relevant tools to find process conditions minimizing the risk of both HT and CC. At the moment, we have a numerical process simulator to simulate aluminium DC-casting process, called ALSIM. Although at its current version (ALSIM 6), ALSIM has criteria to estimate the susceptibility for both HT and CC, it was reported that ALSIM's crack prediction capability has not yet reached its full potential. Therefore, the main goal of this study is four-fold: (1) Verify the connection between HT and CC experimentally. (2) Complete ALSIM materials database for AA7050 for a better crack prediction accuracy. (3) Analyze ALSIM model sensitivity with respect to different DC casting parameters and materials database. (4) Propose a concept of a new crack prediction criterion so that ALSIM could capture the connection between HT and CC quantitatively.

Before developing the connection between HT and CC within ALSIM, we need to make sure that the current version of ALSIM is able to properly estimate the susceptibility of different types of cracks during DC casting. For this validation, we performed benchmark tests between trial casts that produce different cast output (healthy, HT and CC) and ALSIM simulations that mimic those trial casts. For obtaining different cast outputs, we vary two casting parameters; casting speed (in combination with cooling rate) and melt inlet geometry. The analysis shows the output of the ALSIM simulation is in qualitative agreement with the experimental results of the trial DC casting. This verifies that ALSIM is sensitive with respect to different casting parameters. Moreover, the results also indicate that ALSIM has the potential to capture the connection between HT and CC.

ALSIM uses a set of material properties database to simulate the DC casting process. One of the ALSIM drawbacks in the beginning of the project was the incompleteness of the

AA7050 mechanical properties database in the vicinity of the solidus point (T = 465 °C). To complete this database, we performed isothermal tensile tests in both the sub-solidus temperature regime (between 400 and 465 °C) and in the super-solidus temperature regime (when the material is in its semi-solid state but already possesses mechanical strength), i.e. between solid fraction of 0.85 and 1.0 (fully solid). We fitted the result of the tensile tests in respective temperature regimes with the constitutive models implemented in ALSIM to obtain the material property parameters. The focus was on the tensile behavior of the alloy as this loading mode is the main one for the HT formation in the billet. The tensile test results also reveal the mechanical behavior and the failure mechanisms of AA7050 around the solidus point and shed some light on the possible mechanisms of the connection between HT and CC.

In the sub-solidus temperature range, we performed tensile tests at different temperature points (400, 420, 440, 450, 455, 460, 465 °C) and three strain rates (0.05, 0.005, 0.0005 s^{-1}). For each combination of temperature and strain rate, we repeated the tests three times to capture the statistical behavior of the alloy at the test condition. From the test result, we found that the ductility of the alloy decreases as temperature and strain-rate increases. Meanwhile, the strength of the alloy increases with strain rate but it decreases as temperature increases. From the fracture surface assessment, we observed that the main mode of failure gradually changes from ductile transgranular (at 400 °C) to ductile intergranular (at 465°C). In the sub-solidus temperature range, we fitted the tensile constitutive behavior data with both extended-Ludwik equation and creep-law. For the former fit, we found that the obtained constitutive parameters are continuous with the data from the lower temperature regime (room temperature up to 400°C) while for the latter fit, we found that the AA7050 parameters are relatively comparable to the value of other 7XXX series alloys.

In the super-solidus temperature range, we performed tensile test at different solid-fractions (f_s); 0.85, 0.88, 0.9, 0.94, 0.97, 0.99 and 1.0 (fully solid) or in terms of temperature at 550, 520, 485, 475, 473, 470 and 465 respectively. To observe the displacement-rate sensitivity, we did tests at two different displacement rates (0.2 and 2.0 mm/min) for some solid fractions. To assess the statistical behavior of the alloy, for each test conditions, we repeated the test three times. The results show that grain coalescence starts between solid fraction of 0.94 and 0.97. This occurrence is signified by the steep increase in the peak stress as solid fraction increases. The alloy undergoes a typical brittle temperature range behavior – transition from ductile-brittle-ductile as the solid fraction decreases from the fully solid state, with the lowest ductility observed at $f_s = 0.94$. The fracture mode observed from fracture surface analysis is generally mixed between transgranular and interdendritic. We extracted the constitutive parameters by comparing the tensile force-displacement curves obtained from the experimental tensile tests and the result from numerical thermo-

mechanical tensile tests that were built using ALSIM. Using this method, we selected the constitutive parameters that provide a good fit of the force value between numerical and experimental tensile tests in this temperature range. From the fitting, we found that the semi-solid behavior of AA7050 is different compared to the other alloys that were already available in ALSIM semi-solid mechanical database; Al-2% Cu and AA5182. We observe that AA7050 is stronger than Al-2% Cu but weaker than AA5182 in the semi-solid temperature regime.

Using the newly obtained AA7050 materials database, we carried out the sensitivity analysis of ALSIM with respect to different materials database at both temperature regimes (semi-solid and fully-solid). We ran ALSIM simulations using the same set-up as the benchmarking cases but we varied the materials database at different temperature ranges. We assessed the results of both cracking criteria. We conclude that ALSIM model is sensitive with respect to the materials database in both temperature ranges. However, we also found that ALSIM HT criterion has a weak dependency with respect to different materials databases, which is unexpected and shows this criterion needs to be improved.

To experimentally validate the connection between HT and CC, we need to produce samples containing undeveloped HT and then quantify the dimension of these HT. To produce these samples, we used a solidification experiment with controlled conditions. During the solidification, we varied two process parameters namely cooling-rate and constrain conditions. We made sure only HT were formed in the sample by relieving the constraining force as soon as the material is fully solidified and let the sample cool down unconstrained to room temperature. Subsequently, we performed three dimensional imaging on the re-solidified and most deformed part of the sample by using X-Ray microtomography technique and analyzed the image data by image analysis method. From the result of the image analysis, we found that by changing these two process parameters, four regimes of HT can be distinguished based on its severity; compressive, micro-HT, macro-HT and complete fracture. Only the samples with micro-HT conditions were selected for the subsequent tests.

The produced samples with micro-HT were then tensile tested at room temperature, which is the temperature where CC commonly occurs. The result of tensile tests shows significant drop in strength and ductility of the alloy if micro-HT are present in the sample. This verifies the connection between HT and CC. The result from the quantitative image analysis shows that usually HT do not form individually. Moreover, the geometry of the formed HT is not simple (i.e. branching crack) and the approximate ratio between the longest and shortest crack axis is finite (unlike the penny-shaped geometry). These HT features are not taken into account in the crack initiator geometry of the current ALSIM CC

criterion. Therefore, the criterion needs to be improved in order to increase the accuracy of the crack prediction.

One of the most important drawbacks in the current ALSIM HT criterion in the framework of connection between HT and CC is that it cannot provide the dimension of the formed HT. This information is crucial for the CC criterion to decide whether crack will occur. Since HT is a non-linear and complex phenomenon, we propose to capture its formation by using a stochastic (probabilistic) model. The new HT model considers the relationship between different physical phenomena during solidification and utilizes ALSIM simulation result (physical fields) as the model input. From the simple example presented in this study, we illustrate the potential of this new approach to provide probable dimension and location of the formed HT. Although further development is necessary to make this model fully operational in ALSIM, the implementation of this new HT model in ALSIM may offer the possibility of quantitative crack prediction of the connection between HT and CC.

Samenvatting

"Direct-chill (DC)" gieten is een van de meest voorkomende methodes voor de productie van hoogsterke aluminium legeringen, zoals AA7050. Ondanks de superieure mechanische eigenschappen is deze legering gevoelig voor warmscheuren (hot tearing, HT) en koud scheuren (cold cracking, CC) tijdens DC gieten. HT vormen boven de solidus temperatuur, terwijl CC onder solidus temperatuur worden gevormd. CC vorming lijkt willekeurig en is dus moeilijk te voorspellen. Bovendien, de scheurgroei van CC is meestal catastrofaal. Zodoende bedreigt het niet alleen de productie opbrengst en kan het schade veroorzaken aan de gietinstallaties, maar het vormt ook een veiligheidsrisico voor het gieterij personeel. Een eerdere studie naar CC toonde aan dat dit type scheur zou kunnen beginnen met een gietdefect, bijvoorbeeld een insluitsel. Dezelfde studie suggereerde dat onontwikkelde of micro warmscheuren als CC initiatie punt kunnen dienen, maar deze aanname is tot dusver niet bewezen. Naast experimentele methodes worden numeriek modellen meer en meer als relevante instrument toegepast, voor het vinden minimale risico procescondities van HT en CC. Momenteel hebben we een numerieke processimulator om het aluminium DC gietproces te simuleren, ALSIM genaamd. Hoewel in de huidige versie ALSIM 6 de beschikking heeft over criteria om de scheurgevoeligheid voor HT en CC te voorspellen, is er gerapporteerd dat de ALSIM's breuk voorspellende capaciteiten nog niet hun volledig potentiaal hebben bereikt. Daarom is het hoofddoel van deze studie viervoudig: (1)Verifieer het verband tussen HT en CC experimenteel, (2) Complementeer de ALSIM materiaal database voor AA7050 voor een nauwkeuriger voorspelling van breuk, (3) Analiseer de ALSIM model gevoeligheid voor de verschillende DC gietparameters en materiaal databases, (4) Formuleer een concept voor een nieuw voorspellingscriterium voor breuk, zodat ALSIM het verband tussen HT en CC kwantitatief kan vast leggen.

Voordat het verband tussen HT en CC in ALSIM gelegd kon worden, moest eerst bevestigd worden dat ALSIM in staat is de gevoeligheid voor verschillende breuk types gedurende DC casting in te schatten. Voor deze validatie, hebben wij verschillende proefgietingen uitgevoerd met verschillende gietkwaliteit (gezond, HT en CC) en ALSIM berekeningen gedaan die deze proefgietingen simuleren. Om verschillende giet kwaliteiten te verkrijgen hebben we twee giet parameters gevarieerd, giet snelheid (in combinatie met afkoelsnelheid) en smelt toevoer geometrie. De analyse toont aan dat de ALSIM simulatie kwalitatief in overeenstemming is met de experimentele resultaten van de DC proef gietingen. Dit bevestigt dat ALSIM gevoelig is voor verschillende giet parameters.

Bovendien, suggereren de resultaten dat ALSIM de potentie heeft het verband tussen HT en CC te leggen.

ALSIM gebruikt een set materiaal databases om het DC giet proces te simuleren. Een van de nadelen van ALSIM aan het begin van het project was de onvolledigheid van de AA7050 database rond de solidus temperatuur (T=465°C). Om de database te complementeren, hebben we isotherme trekproeven gedaan in zowel het sub-solidus temperatuur gebied (tussen 400 en 465°C) als het super-solidus temperatuur gebied (wanneer het materiaal half-vaste is, maar al mechanische sterkt bezit, d.w.z. tussen fracties vaste fase 0.85 en 1.0 (volledig vast)). Om de materiaal eigenschappen te verkrijgen hebben we constitutieve modellen in ALSIM, toegepast op de trekproef resultaten in de verschillende temperatuur regimes. De nadruk lag op het trekgedrag van de legering aangezien deze spanningstoestand de voornaamste is voor HT formatie in de gietbillet. De trekproef resultaten beschrijven ook het mechanische gedrag en het faal mechanisme van AA7050 rondom het solidus punt en geven inzicht op de mogelijke mechanismen van de koppeling tussen HT en CC.

In het sub-solidus temperatuur regime hebben we trekproeven gedaan bij verschillende temperaturen (400, 420, 440, 450, 455, 460, 465 °C) en drie deformatiesnelheden (0.05, 0.005, 0.0005 s^{-1}). Voor elke combinatie van temperatuur en deformatiesnelheid werd de test in drievoud uitgevoerd om het statistische gedrag van de legering onder de test condities vast te leggen. Uit de test resultaten leiden wij af dat de vervormbaarheid van de legering afneemt als de temperatuur en/of de deformatie snelheid toeneemt. Ondertussen neemt de sterkte van de legering toe met toenemende deformatiesnelheid maar neemt af met toenemende temperatuur. Bij breukvlak analyse hebben we geconstateerd dat het belangrijkste faalmechanisme geleidelijk verandert van ductiel transgranulair (bij 400 °C) naar ductiel intergranulair (bij 465°C). In het sub-solidus temperatuur regime hebben we het constitutief trek gedrag aan zowel de uitgebreide Ludwik vergelijking als aan de kruip-wet gefit. Bij de fitting aan de Ludwik vergelijking vonden wij dat de verkregen constitutieve parameters continue zijn met de parameters uit de lagere temperatuur regimes (kamertemperatuur tot 400 °C), terwijl we voor de kruipwet fitting vonden dat de AA7050 parameters relatief vergelijkbaar zijn met de waarden van andere 7XXX legeringen.

In het super-solidus temperatuur regime hebben we trekproeven uitgevoerd bij verschillende fracties vaste fase (f_s); 0.85, 0.88, 0.9, 0.94, 0.97, 0.99 en 1.0 (volledig vast) of in termen van temperatuur bij respectievelijk 550, 520, 485, 475, 473, 470 en 465 °C. Om de deformatiesnelheid gevoeligheid te observeren, hebben we proeven uitgevoerd bij twee verschillende snelheden (0.2 en 2.0 mm/min) voor enkele fracties vaste stof. Om het statistische gedrag van de legering, voor ieder test conditie, te evalueren hebben we de proeven drie maal uitgevoerd. De resultaten laten zien dat korrel klontering begint tussen

fracties vaste fase 0.94 en 0.97. Het optreden van korrel klontering wordt onderstreept door de sterke toename in pieksterkte naarmate de fractie vaste fase toeneemt. De legering ondergaat een typische temperatuur-regime-gedrags-overgang taai→ bros→ taai naarmate de fractie vaste fase afneemt vanaf de volledig vaste toestand met een minimale vervormbaarheid bij f_s = 0.94. Het gevonden breuktype bij de breukvlak analyse is in het algemeen een mix tussen transgranulair en inter-dendritisch.

We bepaalden de constitutieve parameters door experimentele trekproef curves, en de resultaten van de numerieke ALSIM thermo-mechanische trekproeven, met elkaar te vergelijken. Met deze methode hebben we de constitutieve parameters geselecteerd die een goede fit tussen de numerieke en experimentele trekproeven gaven in dit temperatuur regime. Uit de fit, vonden we dat het halfvaste gedrag van AA7050 afwijkt van de andere legeringen in de ALSIM database; Al-2% Cu en AA5182. We zien dat AA7050 sterker is dan Al-2% Cu maar zwakker is dan AA5182 in het halfvaste temperatuur regime.

Gebruik makende van de nieuw verkregen AA7050 materiaal database, hebben we een gevoeligheidsanalyse van ALSIM met verschillende materiaal databases in beide temperatuur regimes (halfvast en volledig vast) uitgevoerd. We hebben ALSIM simulaties met dezelfde benchmark uitgevoerd, maar hebben de materiaal database bij verschillende temperaturen gevarieerd. We hebben de resultaten van beide breuk criteria beoordeeld. We concludeerden dat het ALSIM model gevoelig is voor de materiaal databases in beide temperatuur regimes. Echter, we vonden ook dat het ALSIM HT criterium weinig afhankelijk is van de verschillende materiaal databases, wat onverwacht is en aantoont dat dit criterium verbeterd moet worden.

Om experimenteel het verband tussen HT en CC te kunnen valideren moesten we monsters met onontwikkelde HT produceren en de dimensies van deze HT kwantificeren. Bij de productie van deze monsters, hebben we gebruik gemaakt van een stollingsexperiment onder gecontroleerde omstandigheden. Gedurende de stolling hebben we twee proces parameters gevarieerd te weten de afkoelsnelheid en de krimpcondities. We hebben er op toegezien dat alleen HT gevormd werden in het monster door de krimpkracht te relaxeren zodra het materiaal volledig gestold was en het monster onbeperkt tot kamer temperatuur te laten afkoelen. Vervolgens hebben we een drie dimensionale afbeelding van het opnieuw gestolde en meest vervormde deel van het monster gemaakt met behulp van röntgen microfotografie en hebben we de afbeelding met beeldanalyse methode geanalyseerd. Uit de resultaten van de beeldanalyse maakten we op dat door variëren van deze twee proces parameters vier verschillende HT regimes onderscheiden kunnen worden in oplopende schaal: compressief, micro-HT, macro-HT en volledige breuk. Alleen de samples met micro-HT omstandigheden werden geselecteerd voor de vervolg tests.

De geproduceerde samples met micro-HT werden aan trekproeven onderworpen bij kamertemperatuur, dit is de temperatuur waarbij CC gewoonlijk voorkomt. De resultaten van de trekproeven toonden significante afnames in sterkte en vervormbaarheid van de legering aan in aanwezigheid van micro-HT. Dit bevestigt het verband tussen HT en CC. De resultaten van de kwantitatieve beeldanalyse laten zien dat HT gewoonlijk niet alleen vormen. Eens te meer is de geometrie van de gevormde HT niet eenvoudig, (i.e. vertakte breuken) en is de benaderde verhouding tussen de langste en kortste breuk als eindig (in tegenstelling tot de penny-vormige geometrie). Deze HT karakteristieken worden niet in rekening genomen in de breuk-initiatie-geometrie van het huidige ALSIM CC criterium. Hieruit volgt dat het criterium verbeterd moet worden om de nauwkeurigheid van de voorspelling voor breuk te vergroten.

Een van de belangrijkste nadelen van het huidige ALSIM HT criterium, in het kader van het verband tussen HT en CC, is dat het geen afmetingen van de gevormde HT kan geven. Deze informatie is kritisch voor het CC criterium om te kunnen bepalen of breuk zal optreden. Aangezien HT een non-lineair en complex verschijnsel is, stellen we voor de vorming van HT door gebruik te maken van een stochastische (probabilistische) aanpak. Het nieuwe HT model houdt rekening met het verband tussen de verschillende fysische verschijnselen gedurende de stolling, en gebruikt het ALSIM simulatie resultaat (temperatuur-, spanningsverdeling etc.) als invoer voor het model. Het eenvoudige voorbeeld dat in dit proefschrift wordt gepresenteerd, toont de geschiktheid aan van deze nieuwe aanpak om mogelijke afmetingen en locatie van de gevormde HT te leveren. Hoewel verdere ontwikkeling nodig is om het model in ALSIM volledig operationeel te maken, zou de implementatie van dit nieuwe HT model in ALSIM de mogelijkheid van een kwantitatieve voorspelling tot breuk mogelijk maken, gebruikmakende van het verband tussen HT en CC.

List of publications

1) **Subroto, T.**, Miroux, A., Bouffier, L., Josserond, Ch., Salvo, L., Suéry, M., Eskin, D. G., and Katgerman, L., Formation of hot tear under controlled solidification conditions. Metallurgical and Materials Transactions A, Vol. 45, 6 (2014), pp. 2855-2862. DOI: 10.1007/s11661-014-2220-6.

2) **Subroto, T.**, Miroux, A., Eskin, D. G., Ellingsen, K., Marson, A., M'Hamdi, M. and Katgerman, L., Tensile mechanical behavior of as-cast AA7050 alloy in the super-solidus temperature range. Proceedings of 13th International Conference on Fracture (ICF13), Vol. 3 (2013), pp. 2528-2536.

3) Zhang, L., Eskin, D. G., Miroux, A., **Subroto, T.** and Katgerman, L., Influence of Melt Feeding Scheme and Casting Parameters During Direct-Chill Casting of an AA7050 Billet. Metallurgical and Materials Transactions B, Vol. 43, 6 (2012), pp. 1565-1573. DOI: 10.1007/s11663-012-9711-x.

4) **Subroto, T.**, Miroux, A., Mortensen, D., M' Hamdi, M., Eskin, D. G. and Katgerman, L., Semi-quantitative predictions of hot tearing and cold cracking in aluminum DC casting using numerical process simulator. IOP Conference Series: Materials Science and Engineering, 33 (2012) 012068. DOI: 10.1088/1757-899X/33/1/012068.

5) Zhang, L., Eskin, D. G., Miroux, A., **Subroto, T.** and Katgerman, L., Effect of inlet geometry on macrosegregation during the direct chill casting of 7050 alloy billets: experiments and computer modelling. IOP Conference Series: Materials Science and Engineering, 33 (2012) 012019. DOI: 10.1088/1757-899X/33/1/012019.

6) **Subroto, T. A. S.**, Miroux, A., Eskin, D. G. and Katgerman, L., Constitutive behavior of an as-cast AA7050 alloy in the sub-solidus temperature range. IOP Conference Series: Materials Science and Engineering, 27 (2011) 012074. DOI: 10.1088/1757-899X/27/1/012074.

Acknowledgments

Without a doubt, this past few years was one of the best parts of my life and I learned tremendously during this time period. The completion of this Ph.D. project and the thesis would not be possible without kind help and contributions from many people around me. Thus I would like to acknowledge them and express my gratitude.

First of all, I am deeply grateful to my promotor Prof. Laurens Katgerman. I greatly appreciate his guidance, continuous encouragement, valuable suggestions and full support throughout my Ph.D. I also would like to express my deepest gratitude to my daily supervisors, Prof. Dmitry Eskin and Dr. Alexis Miroux. Dmitry, it was a great pleasure to work under your supervision. Thank you very much for introducing me to the world of solidification and casting, and also for sharing your insight in writing scientific publications. I am very grateful for your morale support, quick feedback and valuable suggestions regarding my work. As a person who has background mostly in computer simulations, Alexis introduced me to the world of experiments. Alexis, I am very grateful for the time that you invested in mentoring me on various things, starting from designing & constructing experimental setups, data acquisitions to performing data analysis. I want to thank you for your advice, great discussions over different subjects (both scientific and about life in general) and also for all your help on many things over these years. I also would like to extend my gratitude to Prof. Jilt Sietsma for always being very supportive and for helping me in many aspects during my Ph.D. I extend many thanks to our secretaries Olga Wens, Marian Smit, Froukje Prins and Prisca Koelman for all administrative support and help on paperwork.

This research was carried out under project number M42.5.09340 in the framework of the Research Program of the Materials innovation institute (M2i) in the Netherlands (www.m2i.nl). I would like to thank M2i for the financial support for this research project and I want to express my gratitude to the staffs of M2i, Dr. Viktoria Savran, Irina Bruckner, Gitty Bouman, Oscar Ruigrok, Brigitte van Uden and Janneke Curovic for their kindness, help and support. I would like to especially thank Monica Reulink for her morale support, encouragement and help over these years…Hartelijk bedankt Monica!

I extend my great appreciation to Dr. Démian Ruvalcaba (Tata Steel) and Dr.-Ing. Roger Sauermann (Aleris Europe) for their complete support and contribution from the industrial side. Their inputs, suggestions and feedback were highly valuable for me.

Acknowledgments

This Ph.D. project is in close collaboration with SIMaP-GPM2 laboratory of Institut Polytechnique de Grenoble, thus I would like to express my gratitude to Prof. Michel Suéry for the opportunity to carry out extensive testing in the GPM2 laboratory and also for providing us with important suggestions regarding the experiment. Special thanks also to Prof. Luc Salvo for all his help during my stay there and for his support on the quantitative image analysis of the X-Ray microtomography data of the pre-HT samples. To my friend (Dr.) Lionel Bouffier, it was great to work together with you, thanks a lot for sharing your knowledge in high temperature mechanical testing. I wish all the best for your future career, Paris seems like a fitting starting place for you. Charles Josserond, thank you very much for your help on the experimental setup. Jérôme Adrien, thanks for the help on the X-Ray tomography imaging at INSA Lyon. I also would like to thank the members of GPM2 group especially: Matteo, Mathieu, Franck, Xavier, Pawel, Jeremy, Benjamin, Damien, Eduard, Bastien, Denis, Emmanuelle and to Fam. Loic Simonin for all of your help and the good times during my stay there...Merci pour tout!

I also would like to kindly thank Dag Mortensen and Hallvard Fjær for their support and help in debugging and improving the ALSIM simulations. Special thanks to all members of the MINAC community for the useful discussion and suggestions that I obtained during the bi-annual MINAC meeting in Kjeller. We have a fruitful collaboration with SINTEF Materials and Chemistry (Norway) and I would like to extend many thanks to them. Prof. Mohammed M'Hamdi, thank you for giving me the opportunity to visit SINTEF. I would like to also thank Dr. Kjerstin Ellingsen for her help during the experimental planning. Thanks to Andrew Marson for his help during the data acquisition in Trondheim. When I visited SINTEF, I was lucky to have Knut Tveito as my office mate. Thank you for the discussions over different topics and for the advice on numerical modeling...Tusen takk!

I also would like to extend many thanks to the laboratory staffs who provided me with enormous help when I performed my experiments at TU Delft. I would like to especially thank Hans Hofman, Wim Verwaal (CITG), Dr. Ir. Ton Riemslag, Kees Kwakernaak, Sander Leeflang, Sander van Asperen, Frans Bosman, Jan van Etten and Lambert Schipperheijn.

I am also thankful to have wonderful friends and colleague in Materials Science & Engineering Department of TU Delft. These people are Liang Zhang, Kirk, Andrea Bojack, Gautam, Mehdi, Hossein, Hongxiang, Gözde, Goro, Yulia, Abbas, Ron, Francois, Patricia, Lie, Jai, Maria and Cem, Juan-Pablo, Bogdan, Ziggy, Begoña, Pina, Sepideh, Muru, Anand, Michael, Dennis, Emmy, Arnold (thank you for checking my Dutch summary and for translating my propositions), Konstantinos, Marios (also Fani and Nikolas), Ankit, Jun, Alfonso, Richard, Roumen, Leo, Erik, Xiaoqin, Tjerk, Ashwath, Bij-Na, Zaloa, Jan-Henk, Elias, Vera, etc. Thank you very much for all of your help and for the great times.

Before I started my Ph.D, I met many people during my M.Sc study in Applied Physics Department of TU Delft, who provided me help in many ways. I would like to thank them, particularly Dr. Jos Thijssen (Jos, thank you very much for all your help and your guidance during my master thesis), Prof. Lieven Vandersypen, Harm Nieuwestadt (I wish you and Ontipa all the best for the future), Renzo Trip, Ondy Dharma, Marcel Koek, Frans Tilma, Kumel Kagawala, Stephanie Hessing, Oleh Klochan, Lan, Aryo and Lia.

During my stay in the Netherlands, I gained wonderful friends whom made my stay more pleasant and unforgettable. I would like to thank all of them: Kim and Erin McGarrity, I could not thank you enough for all your help over these years. Chris and Vanessa for the advice and discussions on various topics. Fateme and Andy for all the good times - I wish both of you all the best for the present and future times. Joost, a very kind and helpful person in many ways (thanks a lot my friend!), Stefan for his kind advice and for letting me stay at "Château Bretzel" during my visits in Munich, Jeroen (thank you for translating my thesis summary to Dutch) and Jules Heldens for various trips and gaming nights, and to Shirish Baviskar for all the talk about life and for his help on many things. Thanks also to Hélène and Andrea for the Rock and Roll classes and for the amazing trip to Lofoten.

I also would like to express many thanks to Fam. Heru Prabowo (Mas Stevie, Mbak Siska and little Tya). Thank you very much for being my truest friend in the place far away from home. I always keep remembering what we agreed upon "Being grateful of what you have will get you through even the heaviest storm". My gratitude also goes to Fam. Kadaruskan (Pakde Budi and Bude Nola), Fam. Darmin (Oom Selamet and Tante Sylvie), Anil and Orchidea. Thank you very much for all your help.

Finally, I would like to express my sincerest and deepest gratitude to my family in Indonesia. Mom, Dad, Mbak Arie, Mas Doddy (and little Shava) thank you so much for being always there for me. I would not be this far in life without your unconditional love, understanding, continuous encouragement and endless support.

Delft, November 2014

Tungky A. S. Subroto

Curriculum Vitae

Tungky Ariwibowo Sosro Subroto

Born on 8th October 1982

in Bandung, Indonesia

2010 –2014	Ph.D. researcher at Materials innovation institute (M2i), Delft Ph.D. in Materials Science and Engineering, Delft University of Technology, Delft. Title of dissertation: *Connection between hot tearing and cold cracking in DC-casting of AA7050: Experiments and computer simulations.* Supervisors: Prof. ir. L. Katgerman, Prof. dr. D. G. Eskin, and Dr. A. Miroux
2007 – 2009	M.Sc. in Applied Physics, Delft University of Technology, Delft. Specialization: Nanoscience. Title of thesis: *Numerical study of grain growth, heating and stress in an electro-migration bridge.* Supervisors: Dr. J. M. Thijssen and Dr. K. S. McGarrity
2001 –2006	B.Sc. in Physics, Bandung Institute of Technology, Bandung – Indonesia. Specialization: Earth and complex systems physics. Title of thesis: *Estimation of tortuosity and coordination number of 2-D and 3-D artificial rocks formed by random number generator.* Supervisor: Prof. dr. rer. nat. U. Fauzi
1998 – 2001	High school in Mathematics and Natural Sciences, Government high school No. 2 (SMUN 2), Bandung – Indonesia.